A STUDY OF RADAR ASPECT SENSITIVITY IN THE LOWER ATMOSPHERE

A Dissertation

Presented to the Faculty of the Graduate School

of Cornell University

in Partial Fulfillment of the Requirements for the Degree of

Doctor of Philosophy

by

Charles Yann-Ting Chen

May 2001

A STUDY OF RADAR ASPECT SENSITIVITY IN THE LOWER ATMOSPHERE

Charles Yann-Ting Chen, Ph. D.

Cornell University 2001

The goal of this thesis is related to atmospheric temperature measurements using *in situ* techniques in tandem with a direct numerical simulation to better understand the zenith angle dependence of VHF (30-300 MHz) radar backscatter from the atmosphere. We begin our study with a high-resolution balloon-borne *in situ* temperature measurement made over Wichita, KS, in 1995. Very steep vertical temperature gradients were found at the edges of vertical potential steps, regions of near zero vertical potential temperature gradient. We use wavelet analysis to isolate the organized components of the signal and, after subtraction from the original signal, the residual signal is found to have the characteristics of isotropic turbulence. This confirms our hypothesis that the measured temperature profile is a superposition of coherent structures and a background isotropic turbulence. From a radar perspective, we show that this wavelet analysis allows us to predict the radar backscatter as a function of zenith angle from a high-resolution one-dimensional temperature measurement.

Unfortunately, radar measurements were not available at this point. We next explore the cause of aspect sensitivity directly via a multi-instrument investigation of the lower atmosphere over the Jicamarca Radio Observatory (JRO) near Lima, Peru. The joint analysis of radar backscatter and *in situ* measurements of the temperature

structure shows that a combination of Fresnel scattering and turbulence is the most likely explanation for aspect sensitive echoes. Furthermore, the strong backscatter seems to originate from vertical potential temperature steps; such as those observed over Wichita, KS.

Finally, we show that the measured potential temperature steps and the structures seen in a direct numerical simulation (DNS) of a Kelvin-Helmholtz instability (KHI) are remarkably similar. Not only do we find good agreement between the observation and the simulation; the similarity is also seen in the wavelet spectrum, which is the behavior of the wavelet coefficient as a function of scale size. We extend the results from experimental observations and numerical simulation by predicting the characteristic radar backscatter and show that it is consistent with observations.

BIOGRAPHICAL SKETCH

Life for the author begun on October 1976 in Tainan, a city on the southwestern portion of Taiwan. He spent his first eleven years there. In the summer of 1987, he and his family immigrated to the United States to suburban Philadelphia where he learned English from watching cartoons and other favorites such as Knight Rider and The A-Team. During his high school years, he dreamt of becoming an aeronautical engineer. However, due to the thaw of the cold war and a decrease in the research and development aspect of the U.S. defense spending, he instead chose to pursue a degree in electrical engineering. He enrolled at Cornell University in 1994 and earned a B.S. degree in 1997. Having developed a vocation for teaching, the author found himself staying at Cornell University to pursue a Ph. D. On the Easter of 1999, he accepted Jesus Christ as his Lord and Savior and made the people at Tabernacle Baptist Church a part of his life.

Soli deo Gloria.

ACKNOWLEDGEMENTS

I wish to thank my parents and my extended family. This thesis is a testament to their support and encouragement.

I take this opportunity to thank the members of my special committee. Michael Kelley, my chairman, I thank for his guidance and his patience, particularly during the many times where my priorities, particularly between teaching and research, were skewed. His passion for the sciences is inspiring and contagious. I thank Donald Farley for his patience in teaching me about the intricacies of radars. His boundless patience and editing skills are also appreciated. Special thanks to Peter Gierasch for his patience in teaching me about gravity waves and other planetary waves.

I am grateful for Drs. Dorothy Gibson-Wilde and Joe Werne in the application of computer simulated Kelvin-Helmholtz instabilities to this thesis. Their collaboration kicked this thesis up notches!

The experiment and years (thankfully not too many) leading to this thesis were funded by a pot pourri of grants from the National Science Foundation (NSF), Air Force Research Laboratory (AFRL), and Cornell University. I wholeheartedly thank the NSF and AFRL for supporting research of the lower atmosphere, although I do pray for their support to intensify in the future. Of course, any opinions, findings, criticisms, and conclusions expressed in this publication are those of the author and do not necessarily reflect the views of the NSF, the AFRL, or Cornell University.

The results in this thesis were obtained via the help and discussion of many individuals. The collaboration with Dr. Donald Walters from the Naval Postgraduate School is acknowledged. I thank Drs. Ron Woodman and Jorge Chau and the operators at the Jicamarca Radio Observatory (JRO) near Lima, Perú. Their Perúvian hospitability made the work at JRO a blast! Special thanks to Dr. Robert Beland and his balloon team from the AFRL. I also appreciate the valuable insight into the atmospheric dynamics and radar backscatter mechanisms from Drs. Ben Balsley,

Jorge Chau, Dave Fritts, Mercedes Huaman, Greg Nastrom, Dennis Riggin, Jose Rosado-Roman, Jurgen Röttger, Wesley Swartz, and Ron Woodman,

A well deserved thanks to the students that I have taught. They helped develop in me skills that would otherwise lay dormant.

I am grateful for the secretaries on the third floor of Rhodes Hall, Sally Bird, Lisa Gould, Laurie Shelton, and Jamie Wright. They made the daily life of research much more interesting and enjoyable. Thanks to many students of the Space Plasma Physics (SPP) group past and present for enjoyable company and insightful discussions.

Thanks go to the Christians that I have met in the Central New York area, particularly those at the Campus Crusade for Christ, Church of Blodgett Mills, Chinese Bible Study, Fellowship of Christian Singaporeans, and my Ithaca home church: Tabernacle Baptist Church. Their prayer support, encouraging words, loving reproofs, and fellowship are priceless! Thanks to our Lord Jesus Christ. "Now unto him that is able to keep you from failing, and to present you faultless before the presence of his glory with exceeding joy, to the only wise God our Saviour, be glory and majesty, dominion and power, both now and ever. Amen." *Jude* 24-25.

TABLE OF CONTENTS

LIST OF TABLES

LIST OF FIGURES

Chapter 1

Introduction

1.1 The Earth's Atmosphere

The Earth is surrounded by a blanket of air, which we call the atmosphere. It reaches over 560 kilometers from the surface of the Earth; we are only able to see what occurs fairly close to the ground. Early attempts at studying the nature of the atmosphere used clues from the weather, the beautiful multi-colored sunsets and sunrises, the twinkling of stars, and the occasional northern lights, i.e., aurora borealis. With the use of ground-based, airborne, and space borne sensitive instruments, we are able to get a better view of the functioning of our atmosphere.

Information obtained from meteorological satellites and balloon and rocket soundings reveals differences in physical conditions throughout the atmosphere. The atmosphere may be generally divided into two vertical layers. The lower layer, called the homosphere, extends from the earth's surface to about 80 km and has a uniform chemical makeup. The upper level of the atmosphere is the heterosphere, which possesses a variable ion and chemical composition and extends upward from the upper boundary of the homosphere to the edge of outer space.

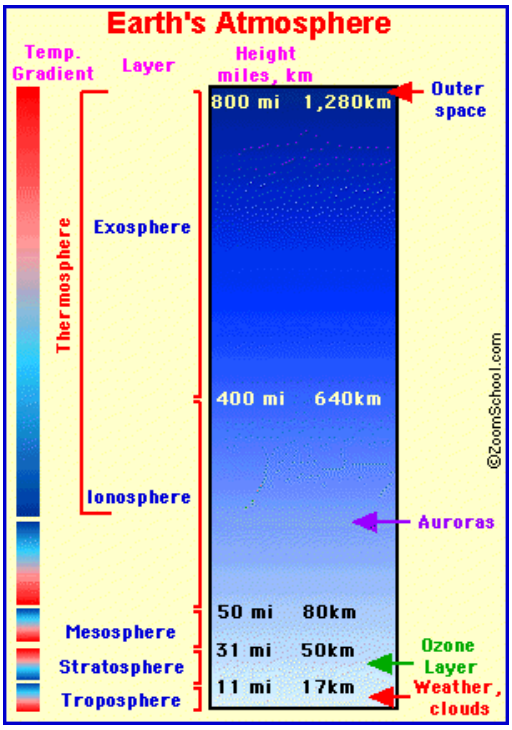

Figure 1.1: Structure of the Earth's atmosphere.

Temperature measurements of the atmosphere reveal a more detailed vertical structure. As Figure 1.1 illustrates, the atmosphere can be divided into four zones: the troposphere, stratosphere, mesosphere, and thermosphere.

The layer closest to the earth's surface is the troposphere. The term is from the Greek *tropo* meaning to turn, which describes the troposphere's mixing and convective characteristics. The troposphere starts at the Earth's surface and extends to 8-15 km high, depending on latitude. This is the densest portion of the atmosphere, containing 75% of the total mass. Tropospheric temperature usually decreases with increased elevation; it is also the layer where the weather occurs, which makes the troposphere, particularly the first few kilometers a primary interest to the meteorologists. The upper boundary of the troposphere, where the atmospheric temperature stops decreasing with elevation, is called the tropopause. Beyond this zone of transition is the stratosphere.

The term stratosphere, a name originated by French scientist Teisserenc de Bort who also coined the term "troposphere", comes from the Greek *strato* meaning horizontally layered [*Greene*, 2000]. This layer starts just above the tropopause and extends to 50 km or so above the surface of the earth. Compared to the troposphere, this part of the atmosphere is less dense. The temperature is nearly constant in the lower levels of the stratosphere and then increases with height. This results in the reduction of vertical motion and overturning; the airflow is mostly horizontal. The stratosphere contains 24% of the mass of the atmosphere. Combined with the troposphere, the two layers account for 99% of the mass of the Earth's atmosphere. In this thesis, we refer to the upper portion of the troposphere, the tropopause, and the lower stratosphere as the lower atmosphere. A thin layer in the upper stratosphere has a high concentration of ozone, a particularly reactive form of oxygen that is responsible for absorbing the ultraviolet radiation from the Sun. The formation of this layer is a delicate matter, since only when oxygen is present in the stratosphere can an ozone layer form and prevent an intense flux of ultraviolet radiation from reaching the surface. The stratopause, a zone of constant temperature with increasing elevation, defines the upper boundary of the stratosphere.

Above the stratosphere is the mesosphere and above that is the ionosphere (or thermosphere) where many atoms are ionized. The mesosphere extends from the top of the stratopause to ~85 km. Temperature falls again in this region. This region and the upper stratosphere, along with the stratopause and the mesopause, are referred to as the middle atmosphere.

The lower portion of the thermosphere, from above the mesopause and extends upward to 600 km, is the ionosphere. Ionosphere is where the aurora borealis takes place and is also responsible for absorbing the most energetic photons from the Sun. The complexity of the structures in the mesosphere and ionosphere is an area of intense interest, particularly when one considers the chemical reactions that take place

in these regions as well as the roles that electrodynamics play in the dynamics of these structures and how they effect satellite communication and power grids [e.g., *Kelley*, 1989]. However, for this thesis, our focus is on the structures of the lower atmosphere, specifically the upper troposphere and the lower stratosphere.

1.2 Our Interest in the Lower Atmosphere

Human beings have always wanted to understand the atmosphere and its dynamics. As early as 2000 years ago, the Greeks observed that the difference in heating between the polar and equatorial regions of the earth is the major force for the general circulation of the atmosphere. In the early portion of the 20th century, although theories of quantum mechanics, special relativity, and radioactive transmutation were born and the atomic theory of matter was confirmed, an interest in the lower atmosphere persists. In 1902, French scientist Teisserenc de Bort, working in his private estate near Paris, conducted a series of balloon experiments that made first measurements of the temperature structure of the upper troposphere, tropopause, and the lower stratosphere [*Greene*, 2000]. With the advent of radars in the first few decades of 20th century for military use and soon after for civilian use, the interest shifted to the atmosphere's interference on radio wave propagation. The current interest is driven in part by curiosity and in part by environmental concerns.

It became apparent in the last few decades that a complete understanding of long-term climatic changes, including possible Sun-weather effects and the effects of anthropogenic contamination, require an understanding of the dynamic processes occurring in regions below the mesopause, i.e., the lower and middle atmosphere. However, it is difficult to probe the atmosphere for heights tens of kilometers above ground, as airplanes and balloons are not able to carry probes to high altitudes. In addition, measurements on a wide range of time scales are needed from instantaneous

species concentrations to seasonal, annual, and long-term transport properties. Measurements by a variety of techniques will be necessary for a satisfactory understanding of the region.

The concern for possible changes in stratospheric ozone concentration produced by the release of fluorocarbons at the surface of the earth has focused attention on the transport processes that operate across the tropopause. There are a handful of processes responsible for the exchange of air masses between the troposphere and the stratosphere, among them the seasonal adjustment of tropopause height, organized synoptic-to-global scale quasi-horizontal motions, large-scale eddy transport in the regions of jet streams, breaking gravity waves, and mesoscale-to-small scale turbulent eddy transport across the tropopause as the primary mechanisms. Each of the transport mechanisms is accessible to observations by radar, as radar can sense remotely the characteristics and dynamics of the atmosphere from near sea level to hundreds of kilometers above that; in practice, some atmospheric dynamics may only be observed by radar.

Radar and balloon-borne instruments are typically used to probe the lower atmosphere with the goal of understanding the atmospheric dynamics. The invention of radar in the early 20th century spurred a wave of interest in the investigation of the lower atmosphere. Early observations of radar returns that could not be attributed to aircraft or precipitation were referred to as "angels" [*Atlas*, 1964], and much speculation surrounded the possible origins of these mysterious targets. By the late 1960s, it became clear that two types of targets were responsible for the returns: 1) discrete targets, such as insects or birds, and 2) extended targets, mainly refractive index inhomogeneities, specifically specular reflection from layered structures in the refractive index field [*Hardy and Katz*, 1969].

In more recent years, a number of radar observatories have made measurements of wind in the vicinity of the tropopause using the refractive index fluctuations produced

by clear air turbulence (CAT) as a tracer of air motion. The radars are generally designed to detect coherent scatter and provide estimates of both the apparent radial velocity (toward the radar) and the intensity of the refractive index fluctuations. To date, most of the observations have been morphological in nature, exploring the occurrence and motion of turbulence in the lower atmosphere. Observations of wind, short-period gravity wave perturbations of the wind profile, and the anisotropy of turbulence in stably stratified regions of the lower stratosphere have been reported [e.g., *Harper and Gordon*, 1980; *Tsuda et al.*, 1997; *Hooper and Thomas*, 1998]. Applications of radar observations to the estimation of turbulence intensity as described by small-scale turbulent eddy dissipation rate have been reported by, e.g., *Sato et al.* [1985] and *Hocking and Mu* [1997]. *Bertin et al.* [1997], *Hocking* [1999], and others also provided estimates of the turbulent eddy diffusion (transport) coefficient based on *in situ* measurements.

Results reported to date show that radar observations, together with simultaneous measurements of temperature obtained from radiosondes, are useful for estimating properties of the small-scale eddy diffusion coefficients, the results of which are in good agreement with the estimates made by *Hocking and Mu* [1997]. However, other mechanisms that affect the eddy diffusion coefficients have yet to be thoroughly investigated, such as annual variation of tropopause height, organized synoptic-scale quasi-horizontal transport, and large-scale eddy transport about the jet stream. These mechanisms, expected to play a significant role in lower to middle atmosphere constituent transport, require careful, coordinated long-duration observations of large-scale air motions by a number of radars capable of continuous observation of the lower stratosphere; radars are the preferred, albeit not the most ideal, tool of observation as they are capable of continuous operation covering heights from near the ground to heights above the tropopause. Some radar, such as the wind profiler, can also be very mobile. *In situ* observations made possible by radiosondes are currently

expensive and mobile lidar units for optical observations of the atmosphere are still being developed [*Balsley*, personal communications; *Kane*, personal communications].

Much about the structures of the lower atmosphere is still poorly understood, partly due to the coarse height resolution of radar measurements and partly due to the lack of *in situ* probes. This lack of understanding is manifested in our inability to explain the observed temperature structures and measured radar backscatter. This thesis focuses on one type of unexplained echo characteristics.

1.3 Goals and Outline of the Thesis

In this thesis, we will examine the structures of the lower atmosphere responsible for aspect sensitivity: the zenith angle dependence of VHF (30–300 MHz) radar backscatter, with the maximum backscatter observed in the vertical direction. This has been observed since the late 1970s [e.g., *Gage and Green*, 1978; *Balsley and Gage*, 1980]. The mechanism(s) causing aspect sensitivity is still a matter of debate. Popular theories are anisotropic turbulence, Fresnel scattering, and Fresnel reflection [e.g., *Chau et al.*, 2000, and references therein]. In this thesis, we advance the understanding of the cause of aspect sensitivity by examining two experimental observations of the lower atmosphere. We support our interpretation of the data with a numerical simulation of a dynamic instability. We will take a top down approach, examining first the structures in the atmosphere as revealed by *in situ* probes followed by the radar observations. We unite the two types of observations by the numerical simulation, which gives added insights into the structures and dynamics of the lower atmosphere. A better understanding of the lower atmosphere will help us model more accurately our effect on the climate and the ozone layer.

This thesis contains nine chapters. Chapter 1, this chapter, introduces the lower atmosphere and briefly outlines the contents of the thesis. Chapter 2 presents a brief historical review of the experimental study of the lower atmosphere. We focus on both observations by radar and balloon-borne *in situ* probes, paying particular attention to the atmospheric temperature and turbulence structures and their relationship to the observed radar backscatter. Past aspect-sensitive observations are summarized. As one of the proposed explanations for aspect sensitivity invokes temperature structures that are created by Kelvin-Helmholtz instability (KHI), a brief discussion of this instability is also included.

We need to understand the structures in the atmosphere first before we can explain aspect-sensitive backscatter. Therefore, we devote Chapter 3 to the analysis of a high-resolution temperature sounding that took place on 5 March 1995 at Wichita, KS. We analyze this one-dimensional temperature dataset not only with the commonly used Fourier transform but also the wavelet transform, a new analysis technique. Chapter 4 presents the data obtained during a multi-instrument investigation of the lower atmosphere at the Jicamarca Radio Observatory (JRO). The two chapters following this are devoted to data analysis. In Chapter 5, we examine the observed aspect-sensitive radar backscatter with *in situ* measurements of temperature and turbulence. Based on the radar and *in situ* data, we conclude our discussion in Chapter 5 with the scattering mechanism(s) most likely to create the observed aspect sensitivity. As turbulence parameters can be computed from the radar data, we compare the turbulence parameters measured by *in situ* probes and the VHF radar. We discuss this in Chapter 6. This helps us understand the background atmospheric conditions in which we observe the aspect-sensitive echoes. In addition, the comparison gives us insight into the limitations of the atmospheric turbulence measurements using radars and *in situ* probes.

The temperature structures, which are observed at Wichita and JRO, closely resemble the vertical temperature structures created by a Kelvin-Helmholtz instability (KHI) at the late stages of its evolution. We devote Chapter 7 to a numerical simulation of a KHI and the comparison between this numerical simulation and the observations. We present in Chapter 8 scattering calculation techniques, developed from the wavelet transform, that will allow us to predict the radar backscatter from an *in situ* temperature measurement. Properties of wavelet transform also allow us to compute the radar backscatter from a low-resolution temperature profile based on our understanding of the measured temperature structures and their relationship with KHI. Finally, in Chapter 9, we present summary comments and suggestions for future research. Appendices are devoted to a brief discussion of turbulence theory, the JRO radiation pattern, and some relevant fluid dynamic terminology discussed in this thesis.

Chapter 2

Review of Aspect Sensitivity and the Kelvin-Helmholtz Instability in the Lower Atmosphere

In the past three decades, scientific attention has been focused on the lower/middle atmosphere where knowledge of its chemistry and dynamics proved inadequate to model accurately the effects of man's activities on the ozone and climate. However, this region of interest, extending from a few kilometers above ground to ~30 km, is difficult to probe. Measurements on a wide range of time scales are needed, from instantaneous species concentrations to seasonal, annual, and longer-term variations in transport properties, for a satisfactory understanding of the region. Efficient methods are needed to measure atmospheric parameters such as wind velocity and turbulent intensity, especially in the troposphere and the stratosphere. One of the most important objectives is to understand the role of stratospheric turbulence in vertical transport phenomena.

Doppler radars operating in the VHF band have revealed some important features about fine-scale structures in the atmosphere. These radars can be used to measure winds, waves, and turbulence parameters in the troposphere and stratosphere by observing the intensity, Doppler shift, and spectral width of the echoes caused by refractive index irregularities. *Woodman and Guillen* [1974] reported wind velocity measurements in the lower stratosphere at a height of 20 km using Doppler radar observations of turbulent scatterers obtained by the 50 MHz Jicamarca radar. Soon after that, it was observed that the echo power depends on the zenith observation angle and is maximized in the vertical direction. This vertical echo enhancement was first noted independently by *Gage and Green* [1978] at 40 MHz and later by *Röttger and Liu* [1978] at 53.5 MHz. Later, many observations were reported, for example, by *Sato et al.* [1985] at 46.5 MHz, *Woodman and Chu* [1989] at 52.2 MHz, and *Hooper and Thomas* [1998] at 46.5 MHz. The phenomenon, usually known as aspect sensitivity, was observed in the lower stratosphere with typical values of enhancement of 10-20 dB above the oblique level and less regularly and less strongly in the troposphere [e.g., *Bolgiano*, 1968; *Hocking and Röttger*, 1983; *Tsuda et al*., 1988]. Similar echo characteristics are also seen in the mesosphere [e.g., *Alcala et al.*, 2001]. Its interpretation is still a subject of controversy in the radar community. Scattering from anisotropic turbulence [e.g., *Gage and Balsley*, 1980] and partial reflection from thin stable layers [e.g., *Röttger and Liu*, 1978] are proposed independently or simultaneously to explain this vertical enhancement.

As aspect sensitivity in the lower atmosphere is not a newly discovered phenomenon, we spend the next few pages reviewing past observations of aspect sensitivity. This leads to a review of the scattering mechanisms and theories developed to explain aspect sensitivity. The ambiguities inherent in radar measurements of the atmosphere are ameliorated when additional instruments are used in concert. In this vein, some pages of this chapter are devoted to the use of *in situ*

atmospheric temperature measurements to predict radar backscatter, as the comparison between the predicted and the measured radar backscatter illuminates the type of scattering mechanism(s) responsible for aspect sensitivity. A recently developed wavelet-based scattering calculation is also discussed.

In the recent years, there is growing evidence that dynamic instabilities such as Kelvin-Helmholtz instabilities (KHI) frequently occur in the atmosphere and may affect atmospheric structures and hence radar backscatter [e.g., *Chapman and Browning*, 1997; *Chilson et al.*, 1997]. Advances in computer technology in the recent years allowed high-resolution direct numerical simulation (DNS) of the KHI [e.g., *Werne and Fritts*, 2000a, b]. The results of the simulation have been applied to explain observed mesospheric structures [e.g., *Gibson-Wilde et al.*, 2000; *Werne and Fritts*, 2000a, b]. DNS will offer us a glimpse of the instability with a time and space resolution that is not achievable for radar and *in situ* measurements. Another reason for our interest in the simulation is that KHI is the basis of one possible explanation of aspect sensitivity [*Bolgiano*, 1968]. These factors, plus the potential application of DNS to confirm the interpretation of the observed lower atmosphere temperature structures, motivate us to include DNS in this thesis. We want to understand the structures created by KHI and how they compare with observations; the more we understand the temperature structures associated with aspect sensitivity, the closer we will be at explaining the mechanisms causing aspect-sensitive echoes. Therefore, in this chapter, we review theories and computer simulations of KHI and relate them to radar backscatter.

2.1 Generalities of Aspect Sensitivity

Most aspect sensitivity measurements were made using the Doppler beam swinging (DBS) technique, where the antenna is pointed at different directions and the measured backscatter is then analyzed. Spaced antenna (SA) techniques, where at least three

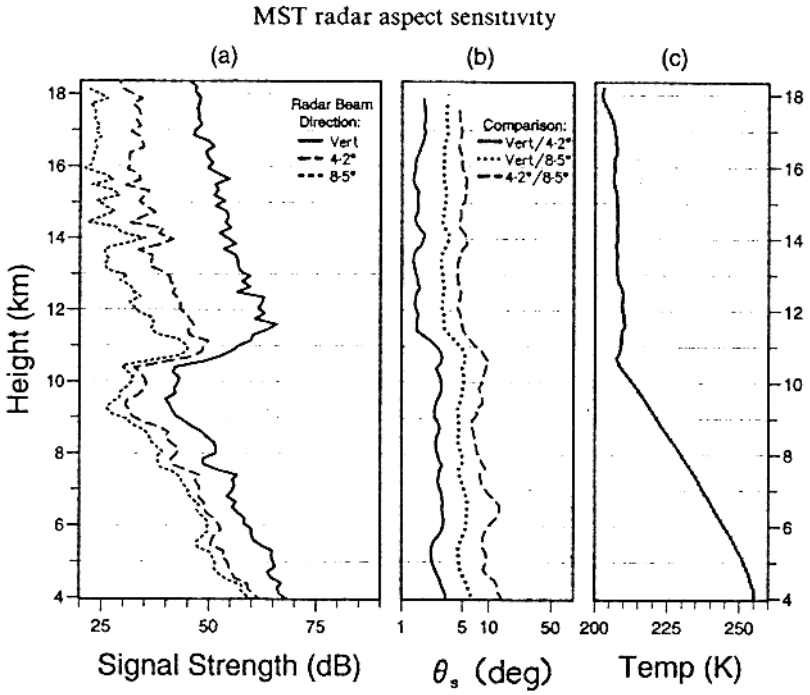

Figure 2.1: Height profile of (a) signal strength for different beam directions, (b) θ_S values derived from the corresponding ratios of signal strength, and (c) temperature profile from a radiosonde measurement, near 0600 GMT on 13 January 1993 at Aberystwyth (52.4°N, 4.1°W) at the University of Wales, UK [after *Hooper and Thomas*, 1995].

non-collinear, vertically directed receiving antennas are used, have also been applied for aspect sensitivity studies. Although the radar experiment discussed in this thesis is based on the DBS technique, we briefly discuss the SA technique as it is used for atmospheric studies and hence is relevant in this review chapter. In this discussion, we first examine the DBS technique and slowly transition to the SA techniques.

2.1.1 Echo Characteristics

Aspect sensitivity in radar experiments refers to the preferential scatter of radio signals from overhead rather than from off-vertical angles. We show an example of this in Figure 2.1. The history of observations of aspect-sensitive scatterers in the atmosphere is a very old and continuing one. Aspect sensitivity was discovered in the late 1970s. Observations at VHF by *Gage and Green* [1978] and *Röttger and Liu*

[1978] showed strong enhancements of radar signal return strength in the vertical direction relative to that at off-vertical zenith angles. It is often (but not always) found that the signal received when the center of radar beam points directly overhead exceeds that received when an off-vertical beam is used. This characteristic is evident throughout the lower and middle atmosphere at VHF (Very High Frequencies, 30-300 MHz) in the stratosphere and troposphere, and at VHF, HF (High Frequencies, < 3 MHz) and MF (Medium Frequencies, 3-30 MHz) in the mesosphere. Aspect sensitivity is extremely variable with height and time, especially in the troposphere, which is usually less aspect-sensitive than the stratosphere [*Röttger*, 1980a; *Tsuda et al.*, 1986; *Hooper and Thomas*, 1998].

VHF radar observations indicate enhanced radar return signal strength at vertical incidence to be greater for stable regions in the lower stratosphere, which suggests partial reflections from stable refractivity structures rather than backscatter from regions of turbulence [e.g., *Röttger and Liu*, 1978]. These stable refractivity structures are coherent over a reasonable fraction of the first Fresnel zone of the radar in the horizontal direction. *Green and Gage* [1980] hypothesized that the vertical echo power is proportional to the squared vertical gradient of potential refractive index M^2 given by *Ottersten* [1969a] and therefore to N^4 (with N being the Brunt-Väisälä frequency) assuming humidity is negligible. This is valid in the upper troposphere and in the stratosphere. As N^2, due to its dependence on the squared vertical potential temperature gradient, is a measure of atmospheric stability, M^2 is also. Experimental investigations confirmed that the parameter M^2 (or N^4 in the stratosphere) deduced from *in situ* measurements (of temperature, humidity, and pressure) reproduced the background scattered power received at vertical incidence, indicating a strong correlation between the static stability of the medium and the vertical echo power [e.g., *Green and Gage*, 1980; *Tsuda et al.*, 1988; *Dalaudier et al.*, 1989; *Chu et al*., 1990]. However, we will explicitly show, in a future chapter, that radar backscatter

originates both from positive and negative temperature gradients; this is not explicitly shown in the relationship between M^2 and backscattered power.

Variations on measurements of power as a function of angle were also employed to further investigate this phenomenon [*Röttger and Vincent*, 1978; *Woodman and Chu*, 1989; *Hocking et al.*, 1990]. Some studies paid particular attention to the backscattered power as a function of the beam tilt angle. For example, *Tsuda et al.* [1986], using the MU radar (46.5 MHz) pointing in 16 different directions, showed aspect sensitivity up to 10° from the vertical direction. *Hocking et al.* [1990], using the same instrument, confirmed this observation and reported that isotropic scatter is almost detected at about 10 degrees off-vertical. *Chu et al.* [1990] presented results using the broad beam method introduced by *Woodman and Chu* [1989] in order to measure aspect sensitivity from the Doppler spectrum. Their method is based on the fact that the echo spectrum from a scattering layer is determined by the superposition of the echoes from each zenith angle, each with its own Doppler shift corresponding to the projection of the mean velocity to the line of sight and with a magnitude weighted by the aspect sensitivity function $A(\theta)$. The spectrum, $S(\omega)$, is given by

$$S(\omega) \propto \int \delta(\omega - 2\mathrm{k} \bullet \mathrm{u})\, A(\alpha,\Phi)\, B(\alpha,\Phi)\, r^2 \cos\alpha \, d\alpha \, d\Phi , \qquad (2.1)$$

where **k** is the Bragg wave vector (twice the radar wave number for backscattering) while r, $(\pi/2 - \alpha)$, and Φ are spherical coordinates with their axis aligned in the direction of **u**. $B(\alpha,\Phi)$ is the antenna beam width. With this definition,

$$A(\omega/2ku) \approx S(\omega)/B(\omega/2ku). \qquad (2.2)$$

In other words, the aspect sensitivity function, at $\theta = (\omega/ku)$, is defined as the quotient between the measured Doppler spectrum and the antenna beam pattern. These authors showed that the radar detected isotropic scattering at angles greater than 4° to 10°, depending on altitude. Figure 2.2 shows an example of the echo's zenith angle dependence.

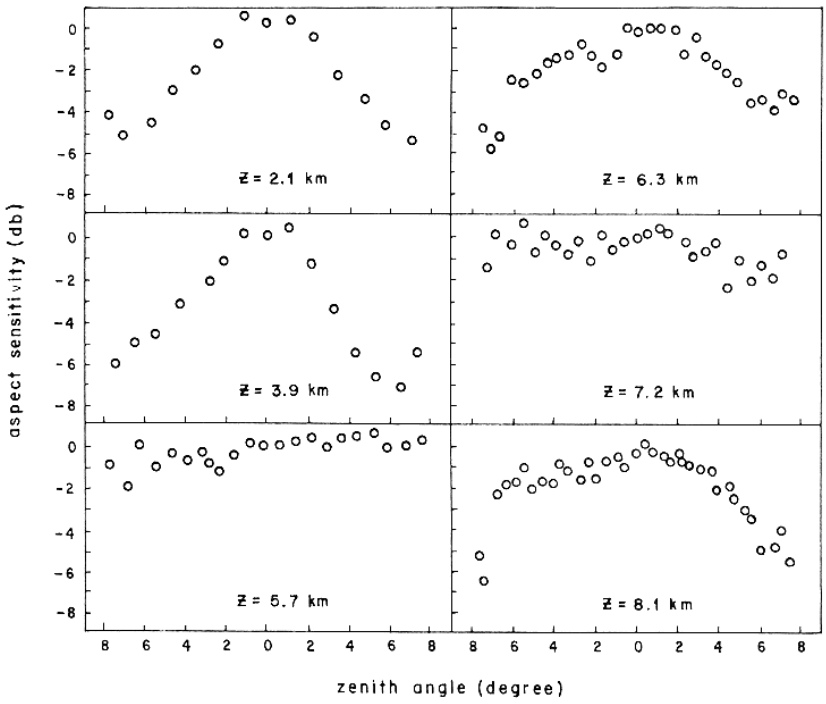

Figure 2.2: Measured aspect sensitivity with the Chung-Li VHF radar for selected heights [after *Woodman and Chu*, 1989].

Subsequent studies attempted to quantify the degree of backscatter by representing the fall-off as a function of angle by some mathematical function [e.g., *Vincent and Belrose*, 1978; *Waterman et al.*, 1985]. The most common parameterization used to represent the power as a function of angle by a form proportional to $\exp(-[\sin\theta/\sin\theta_S]^2)$ (or $\exp(-[\theta/\theta_S]^2)$ for small θ_S and θ) where θ_S has been called the aspect-sensitivity parameter. Figures 2.1 and 2.3 show examples of θ_S as determined from the measured aspect sensitivity. The above references are not a complete set, but are adequate to establish the main features of aspect sensitivity studies; a more complete bibliography can be found in *Lesicar et al.* [1994] and *Hooper and Thomas* [1995, 1998].

Papers dealing with radar wavelength dependence of radar backscatter showed that aspect sensitivity is not reported at 23 cm wavelength (corresponding to 1290 MHz) [*Balsley and Peterson*, 1981]. *Sato and Woodman* [1982] made similar measurements

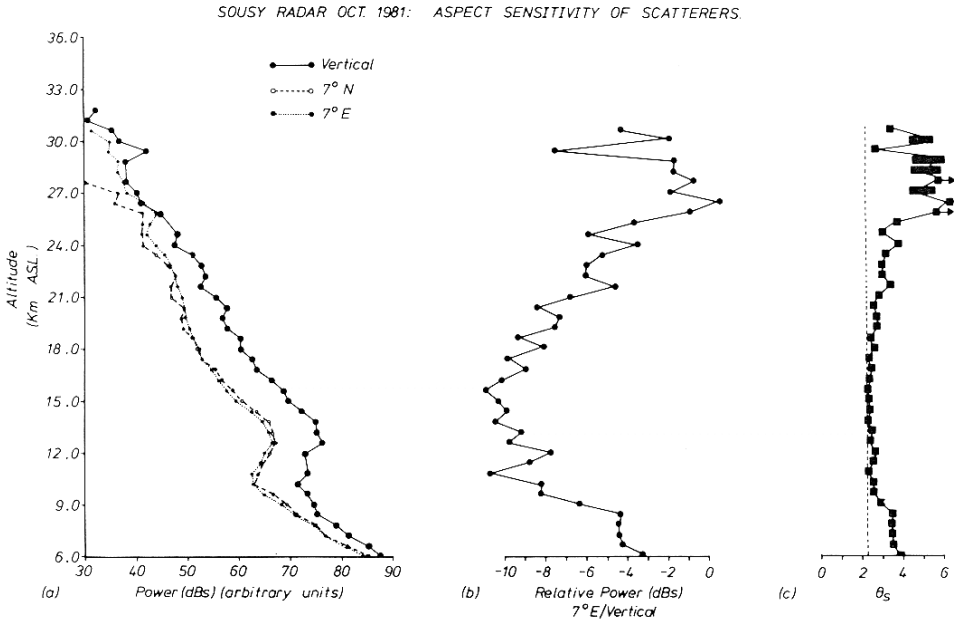

Figure 2.3: Aspect sensitivity measurements made by the SOUSY VHF radar located in the German Harz Mountains. (a) Plots of 25 h mean powers as a function of altitude for the three beams. Noise has been subtracted. (b) Ratio of powers on the 7°E beam and the vertical beam. (c) Assuming that the scatterers had backscatter diagrams of the form $\exp(-[\sin\theta/\sin\theta_S]^2)$, which is approximately equal to $\exp([\theta/\theta_S]^2)$ for small angles, this plot gives the values of θ_S as a function of height [after *Hocking et al.*, 1986a, b].

at 430 MHz and 2380 MHz, concluding that the backscatter originated from stratified turbulence. *Woodman* [1980] has made similar measurements at UHF and the likes of *Hardy et al.* [1966] made measurements in microwave frequencies. Although the measurements do not reveal aspect sensitivity, they do show stratified structures of enhanced returns with vertical widths and separations consistent with layers of turbulence. These layers of turbulence conform to the predictions made by balloon-borne or aircraft-borne *in situ* measurements [e.g., *Metlcalf and Atlas*, 1973; *Lilly and Lester*, 1974; *Crane*, 1980; *Barat*, 1982; *Barat and Bertin*, 1984; *Cot and Barat*, 1986].

Some aspect-sensitive backscatter exhibits a long lifetime. *Hocking and Röttger* [1983] observed temporary persistence of some strong echoes in the vertical direction. Using the 150-m range resolution of the SOUSY radar, these authors showed echoes

persisting at the same height for some tens of minutes and more (longer than 50 minutes for one example). *Röttger* [1980b] also observed echoes produced by layers located around the tropopause with a lifetime longer than one day. *Sato et al.* [1985] observed with the MU radar scattering layers in the stratosphere with a thickness smaller than the 150 m radar range resolution; these radar scattering layers, both in winter and summer, has a lifetime of several hours. *Larsen and Cornish* [1989] observed at the Arecibo radio observatory scattering layers that persisted for days. A long lifetime can be interpreted as the structure having a large horizontal extent.

Recent studies focused on the subtle variations of the zenith and azimuth dependence of the VHF radar echo power in the troposphere and lower stratosphere. Tilted echoing layers have been observed. They can produce the highest reflectivity at off-zenith directions and can lead to systematic wind estimation errors on short-term temporal average data [e.g., *Larsen and Röttger*, 1991; *Palmer et al.*, 1991] and long-term averages over months or years [*Muschinski*, 1996]. These tilts can be due to the surrounding turbulence [*Röttger*, 1980a] or due to vertical displacements produced by gravity waves [*Tsuda et al.*, 1997; *Worthington and Thomas*, 1996, 1997; *Worthington et al.*, 1999]. Tilts smaller than a few degrees were observed on different occasions by using the spatial domain interferometry (SDI) technique [e.g., *Röttger and Ierkic*, 1985; *Röttger et al.*, 1990]. *Worthington and Thomas* [1997] recently reported cases with larger tilt angles (~10°); the onset of a Kelvin-Helmholtz instability (KHI) was invoked to explain the observation. *Worthington* [1999] showed how mountain waves would tilt aspect-sensitive scattering layers. In a future section, we will review in some detail the investigation of aspect sensitivity using the SDI technique. At this point, we simply want to acknowledge that the SDI technique is one way to measure the "tilting" of a scattering layer.

The frequency domain interferometry (FDI) technique has been developed for probing the tilt of thin-layered structures of the atmosphere. The FDI technique has

been developed for probing thin, layered structures of the atmosphere. The position and thickness of a single layer embedded within the scattering volume can be deduced from the complex normalized cross-correlation, i.e., coherence, of received signals at two closely spaced frequencies. FDI allows a more accurate position and thickness estimation of a scattering layer [*Kilburn et al.*, 1995a, b]. The theory of this technique was discussed by many authors [e.g., *Chen et al.*, 1997, and references therein]. However, the FDI technique only permits one to detect one apparent layer (an FDI layer) in the illuminated radar volume which does not necessarily correspond to a single-layered atmospheric structure. The two sampled return signals at two different frequencies also contain an inherent ambiguity, which is discussed in *Luce et al.* [1999] and references therein. In addition, this technique also requires prior knowledge of the layer structure, which is currently difficult, if not impossible to obtain.

Recently, *Luce et al.* [2000a] studied the effects of the limited horizontal extent of a single layer on the thickness and position deduced from the dual frequency domain interferometry (FDI) technique. They also analyzed the FDI coherence function for a tilted scattering layer [*Luce et al.*, 2000b]. The difference of one order of magnitude between the thickness of the FDI layer and the thickness of the very thin layers responsible for the echoes in vertical incidence and observed by balloons indicated that the FDI layers have still to be interpreted [*Luce et al.*, 1999]. Regardless, *Luce et al.*, [1999, 2000a, b] concluded that only high-resolution *in situ* measurements can resolve ambiguities inherent in the FDI technique.

2.1.2 Aspect-Sensitivity Measurement via the Spatial Interferometry Technique

In the previous paragraphs, we discussed the investigation of aspect sensitivity in the lower atmosphere using the Doppler-beam swinging (DBS) technique. We switch gears briefly to discuss the spatial interferometry (SI) technique which can be

implemented on a VHF radar system and is an alternate way of investigating aspect-sensitive layers [e.g., *Larsen and Röttger*, 1991; *Chau and Balsley*, 1998a, b]. The SI technique was first used to determine the position of extremely localized scatterers in the ionosphere [*Woodman*, 1971]. By using two spatially separated arrays of the Jicamarca Radio Observatory (JRO), near Lima, Peru, Woodman was able to measure the inclination of the geomagnetic field using plasma instabilities in the *F*-region which are hugely aspect-sensitive. Subsequent experiments illustrated the usefulness of the SI technique for observations of the lower atmosphere [e.g., *Röttger and Vincent*, 1973; *Vincent and Röttger*, 1980; *Chau and Balsley*, 1998a, b; *Chau et al.*, 2000]. Basically, the SI technique makes use of the phase differences between signals from receiving arrays separated on the ground. The phase difference is dependent on two known quantities, radar wavelength and sensor spacing, and the angle of arrival (AOA), which is the unknown parameter of interest. The AOA can be thought of as the angle corresponding to the mean of the echo power distribution within the transmit beam of the radar; therefore, AOA provides the actual pointing direction of the radar beam.

Aspect-sensitive scatterers cause the echo power distribution at VHF wavelengths to be irregular across the sky. This has been thought to be a major factor in causing a distinct AOA; isotropic scatter would produce a uniform echo power distribution and this is an ill-defined AOA. AOA would be altered if there were tilted aspect-sensitive scatterers, and tilting by gravity waves has been reported by *Gage et al.* [1981], *Röttger et al.* [1990], and *Palmer et al.* [1993]. Tilt angles of 1-2° have been reported using this method [*Röttger et al*., 1990; *Larsen and Röttger*, 1991; *Palmer et al.*, 1991] and these will introduce an error into wind measurements in the vertical direction. *Palmer et al.* [1998] recently tested SI-derived AOA estimates against direct Doppler beam-swinging (DBS) measurements of the echo power distribution. Using the Japanese middle and upper atmosphere (MU) radar with an unprecedented

number of beam directions, they showed that SI could be used to measure the tilt of the echo power distribution. *Chau and Balsley* [1998a, b] and *Chau et al.* [2000] measured the aspect sensitivity of the first few kilometers of the atmosphere above ground at JRO. We remind the reader that the focus of the thesis is not on radar techniques although a brief discussion on technique is relevant for this review chapter.

2.2 Backscatter From Clear Air Turbulence (CAT)

Regardless of the types of structures that play a role causing aspect sensitivity, atmospheric turbulence will be responsible for the measured radar backscatter. Turbulence is an important aspect of atmospheric phenomena. This is especially important in the diffusion of pollutants and contaminants in the atmosphere over both large and small scales. It also has impact on aircraft flight safety; occurrences of strong turbulence at upper levels of the troposphere and the lower stratosphere can cause discomfort for civil aircraft passengers, and in some cases, can have more catastrophic effects. In addition, as we will discuss later, turbulence has also been invoked to explain aspect-sensitive echoes. An important objective in the radar study of the lower atmosphere is to understand the role of turbulence in the vertical transport of aerosols and atmospheric constituents [e.g., *Knapp et al.*, 1998]. Identification and measurement of turbulence are thus important goals of modern atmospheric studies.

Backscatter from small-scale turbulence is known to be an important contribution to radar returns from the clear air. The theory of radar backscatter from isotropic turbulence were developed first by *Booker and Gordon* [1950] and improved by *Tatarski* [1961] and *Ottersten* [1969a, b]. Early observations by *Kropfli et al.* [1968] indicated that the characteristics of the backscattered signal at VHF/UHF for zenith angles greater than 10° were consistent with isotropic scattering at the Bragg scale of the radar. Turbulent backscatter is generally accepted to explain the echo power at

oblique incidence and is combined with the partial reflection mechanisms near the vertical direction.

Turbulence has been measured in horizontal layers in the troposphere and in the lower stratosphere by instrumented aircraft [*Reiter and Burns*, 1966; *Hicks et al.*, 1967; *Browning et al.*, 1970; *Hardy et al.*, 1973; *Metcalf and Atlas*, 1973; *Lilly and Lester*, 1974; *Crane*, 1980] and balloon-borne probes [*Bufton*, 1973; *Cadet*, 1977; *Barat*, 1982; *Barat and Bertin*, 1984; *Cot and Barat*, 1986]. The vertical extent of these layers is reported to be typically between 30 m and 300 m. The layers are separated by quiet regions with thickness ranging from hundreds of meters to well over a kilometer. Clear air radar observations at UHF [e.g., *Woodman*, 1980; *Sato and Woodman*, 1982] and microwave frequencies (wavelength ~10 cm) [e.g., *Hardy et al.*, 1966; *Lane*, 1969] have also shown stratified structures of enhanced returns with vertical widths and separations consistent with those for layers of turbulence referred to above. Aspect sensitivity was not observed in these layers at UHF and microwave frequencies. Several *in situ* observations have confirmed that layers of radar returns in these frequency ranges are associated with layers of turbulence [e.g., *Browning et al.*, 1973; *Hardy et al.*, 1973; *Metcalf and Atlas*, 1973; *Robinson and Konrad*, 1974]. However, turbulence does play a role in an explaining the cause of aspect sensitivity at MF and VHF.

2.3 Interpretations of Aspect Sensitivity

Few attempts were made prior to 1984 to relate aspect-sensitive radar backscatter and parameterizations to quantities like the degree of anisotropy of the scatterers. In fact, some earlier experimental reports simply classified the scatterers as “specular” and “isotropic” [e.g., *Gage and Green*, 1978; *Röttger and Liu*, 1978; *Fukao et al.*, 1979; *Hocking*, 1979]. The initial theoretical attempts to explain aspect sensitivity included ones by *Briggs and Vincent* [1973] and *Vincent* [1973]. Their work was followed by

Doviak and Zrnic [1984] and *Hocking* [1987, 1989]. Experimental studies have been carried out which utilize these theoretical developments [e.g., *Reid*, 1990], including extensive multi-station climatologies reported by *Lesicar and Hocking* [1992] and *Lesicar et al.* [1994]. *Sato et al.* [1985] looked at seasonal variations of aspect sensitivity with the MU radar in Japan.

The aspect sensitivity is due to refractive index structures with much larger coherence length in the horizontal dimension than in the vertical one, but views differ about the nature and the origin of these structures. Whilst we can easily determine the degree of anisotropy, the interpretations of aspect sensitivity are still debated since it is difficult to observe the local structure of refractive index fluctuation in three dimensions with sufficient resolution. One-dimensional *in situ* measurements are not sufficient if the refractive index fluctuation field were anisotropic. Some propose anisotropic turbulence to be the cause of aspect sensitivity [e.g., *Crane*, 1980; *Gage and Balsley*, 1980; *Doviak and Zrnic*, 1984; *Woodman and Chu*, 1989; *Dalaudier et al.*, 1989]. To others, aspect sensitivity is generated by a mechanism with anisotropy much more pronounced than turbulence can produce alone [e.g., *Gage and Green*, 1978; *Röttger and Liu*, 1978]. The second interpretation assumes the presence of a single or a few horizontal layers in the radar range gate. Fresnel scattering, i.e., coherent scattering: reflections from many thin layers distributed randomly in the vertical direction [e.g., *Gage et al.*, 1981; *Sheen et al.*, 1985], and diffuse (or quasi-specular) reflection from thin layers corrugated by turbulence [*Röttger*, 1980a] were also proposed to explain the overhead enhancement and can constitute extensions of the partial reflection mechanism. In this section, we examine closely these two schools of thought.

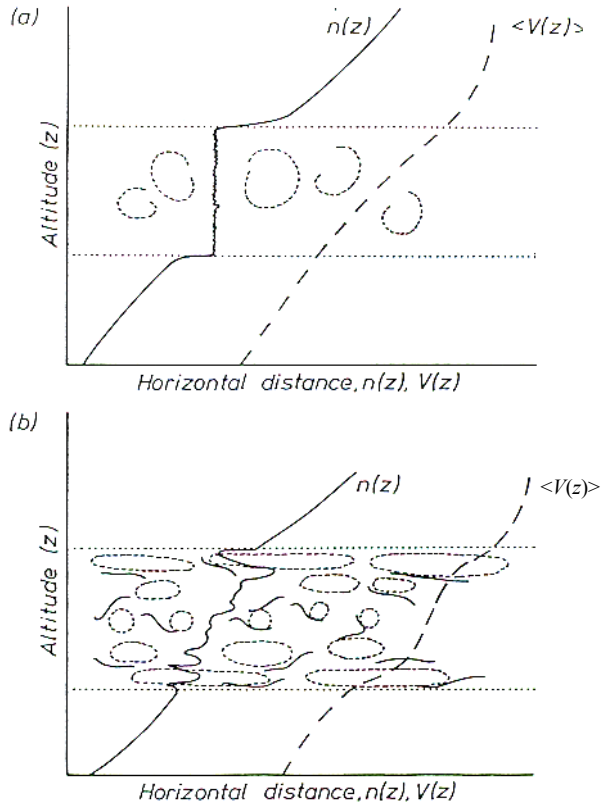

Figure 2.4: (a) A model proposed by *Bolgiano* [1968] to explain partial radar reflections in the atmosphere. (b) A model proposed by *Hocking et al.* [1984], *Hocking* [1989], and *Woodman and Chu* [1989]. The dashed lines represent the existing turbulence while the solid lines near the turbulence are the scattering surfaces [after *Lesicar and Hocking*, 1992].

2.3.1 Anisotropic Turbulence

The theory of turbulence scattering was applied to tropospheric radio propagation by *Booker and Gordon* [1950] and extended to backscatter from clear air by *Ottersten* [1962a, b]. If statistical properties of the irregularities in radio refractive index, i.e., their correlation distances, are dependent on direction, the scatter will be anisotropic, causing the observed aspect sensitivity.

Bolgiano [1968] further developed this idea and proposed a model where turbulence within a layer was strong enough to produce, by mixing, a nearly constant potential refractive index across it, resulting in sharp refractive index edges at the top and bottom of the layer. See Figure 2.4a. *Gage and Balsley* [1980] adopted a model

for forward scatter radio propagation in anisotropic turbulence to formulate a model for backscatter which showed a fairly uniform change in backscatter within about 30º off the vertical, depending on the ratio of the correlation distance in the vertical and horizontal direction. *Hocking et al.* [1984], *Hocking* [1985, 1989], *Lesicar and Hocking* [1992], and, independently, *Woodman and Chu* [1989] proposed a model where thin anisotropic turbulence exists at the edges of a scattering layer with more isotropic turbulence existing within the layer. Figure 2.4b illustrates such a model, where the proposed scatter near the edges of a confined layer of turbulence is more anisotropic than the center. The thin anisotropic turbulence causes radar partial reflections for a vertically pointing beam, while the turbulence contained within the layer produces radar scatter for oblique pointing beams. Such a model is physically likely because turbulent layers are often more stable near their edges [*Peltier et al.*, 1978; *Klaassen and Peltier*, 1985]. Evidence for the possible co-existence of both types of scatterers has recently been found [*Hocking*, 1987; *Czechowsky et al.*, 1988]. An important thing to note is that this scattering model mimics the structures created by Kelvin-Helmholtz instability; we will focus on this point in a future discussion. *Waterman et al.* [1985] showed that the tropospheric echoes sometimes showed aspect sensitivity consistent with this anisotropic turbulence model.

Not all of the radar community accepted the anisotropy turbulence interpretation. For instance, *Gage et al.* [1981] argued that this interpretation does not seem compatible with the high stability conditions of the stratosphere which are observed with strong vertical echoes. *Röttger* [1980a] showed that, via the temporal correlation of the vertical signals, it was unlikely that the scattering mechanisms would be attributed to turbulence. Others claim that the variation in power as a function of zenith angle is too rapid to be explained by turbulence alone, and they cite other evidence such as very slow fading times to support their view that the scatter occurs not from irregularities generated by anisotropic turbulence, but rather from some sort

of stratified step in refractive index [e.g., *Röttger*, 1980a, b; *Hooper and Thomas*, 1995, 1998]. This is one of the issues that we will address in this thesis.

2.3.2 Partial Reflection

The partial (or Fresnel) reflection theory assumes the existence of step-like structures or sharp refractive index gradients from thin layers with large horizontal extent, i.e., comparable to or greater than the Fresnel length. Due to horizontal stratification, partial reflection would dominate the radar scattering in vertical direction and explain the strong echoes in this direction relative to oblique directions. This mechanism was put forward to interpret transhorizon bistatic links (at gazing angles) in the lower troposphere by *Saxton et al.* [1964] and *du Castel et al.* [1966] and was supported by *in situ* measurements of refractive index sheets using a microwave refractometer. From different analyses of these measurements, *Misme et al.* [1958] proposed the presence of atmospheric sheets (at least for the first few kilometers above ground) with horizontal dimensions of several kilometers and thickness of several meters. High-resolution balloon observations made by *Dalaudier et al.* [1994] suggested that the vertical extent of these structures was typically a few meters. In addition to Fresnel reflection from an isolated horizontal layer, *Gage and Balsley* [1980] recognized the possibility that the radar returns from one range gate may represent the incoherent sum of partial reflections from several such structures, which are distributed randomly in altitude all within the radar range gate. This is known as Fresnel scattering.

Luce et al. [1995], in analyzing the RASCIBA 90 campaign data, considered a model of flat and very extended sheets to estimate quantitatively the possible contribution of sharp temperature gradients to the VHF radar backscatter power. They showed that partial reflection from atmospheric sheets is an important and generally dominant process in the vertical direction. They found the observed and predicted

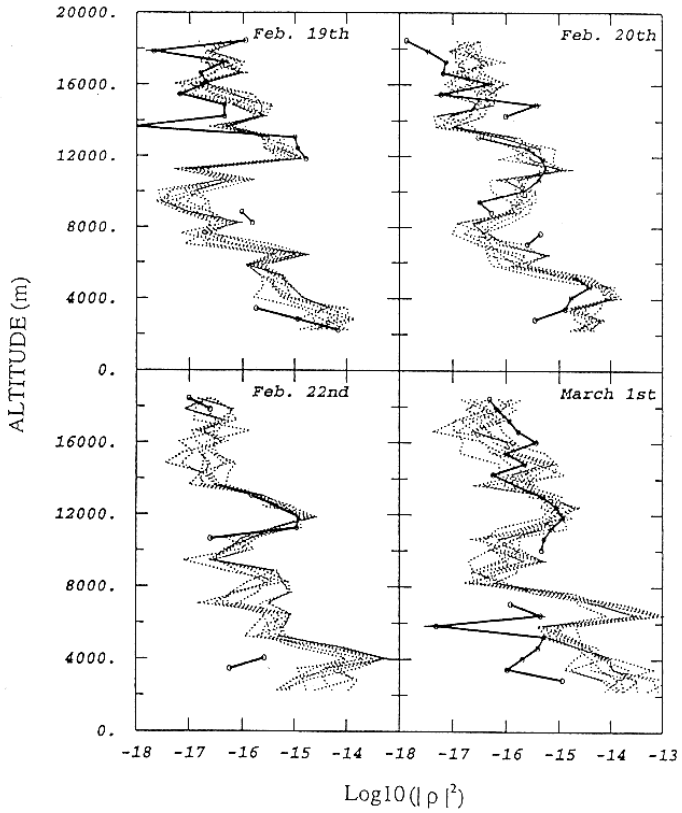

Figure 2.5: 45 MHz PROUST ST radar power reflection coefficient profiles (dotted lines) and the estimated power reflection coefficient computed from temperature sheets (thick solid lines) [after *Luce et al.*, 1995].

backscatter to be in good agreement in shape and in level, indicating that partial reflection from atmospheric sheets is an important and generally dominates the process at vertical incidence. We show their result in Figure 2.5. However, we do notice limitations in their calculation, as the scattering predictions can be only made at certain altitude ranges. In addition, agreement between the prediction and measurement is poor for $z < 8$ km for February 22 and March 1. *Hooper and Thomas* [1995, 1998] examined the relative contributions of isotropic scatter, anisotropic scatter, and Fresnel reflection or scatter to the signal backscattered in the vertical direction via a multiple-beam VHF radar observations of the troposphere and lower stratosphere at Aberystwyth (52.4°N, 4.1°W) at the University of Wales, Great Britain. The goal of the experiment was to examine the relative contribution of

isotropic scatter, anisotropic scatter, and Fresnel reflection and scatter to the signal backscattered in the vertical direction. By examining θ_S, the aspect sensitivity parameter, they discovered that Fresnel scattering is the dominant backscatter mechanism in the vertical direction. In this partial reflection model, turbulence was used to explain the echoes in the off-vertical directions.

However, *Woodman and Chu* [1989] argued that the partial reflection mechanisms must be rather exceptional at VHF because very thin layers of the order of a few meters are needed. They claim that such structures are "impossible to accept" because temperature increases (of the order of 0.5º) cannot be reached without being dynamically unstable and then without being destroyed by turbulent diffusion before their complete formation. They claim also that, given a partial reflection mechanism, the angular dependence around the vertical direction would be sharp, which is not observed by experiments. In fact, while anisotropic turbulence seems to be a more appropriate interpretation of the observed angular dependence, diffuse reflection occurring from a rough surface can also reduce the specular nature. This interpretation can be considered to be consistent with *Misme et al.*'s [1958] or *du Castel*'s [1966] sheet distortion observations in the lower troposphere. However, in this discussion, a satisfying method of identifying Fresnel scatter from anisotropic turbulence was not provided.

The wavelength dependency of the radar backscatter predicted by both the anisotropic turbulence and partial reflection interpretation is strongly dependent on the assumed model. *Dalaudier et al.* [1989] investigated an anisotropic model of temperature fluctuations based on balloon observations. The wavelength dependence predicted by models based on partial reflection is strongly dependent on the shape of the reflecting structures assumed by the models [e.g., *Green et al.*, 1979; *Woodman and Chu*, 1989]. As a general rule, a smoother structure leads to a stronger wavelength dependence.

Although these two main mechanisms, scattering from anisotropic turbulence and partial reflection from stable layers, are usually introduced independently, a more general approach has been adopted by *Doviak and Zrnic* [1984]. They account for the Fresnel scatter and anisotropic and isotropic turbulence scatter in deriving an expression for the backscatter power as a function of zenith angle. From the Born approximation for the scattered field and including the effect of the curvature of the wave front by expanding the phase term at the second order, they obtained a general formula involving the three-dimensional (3-D) (anisotropic) spectrum. They showed that this formula is identical to the partial reflection one in the case of an infinite horizontal anisotropy. On the other hand, some investigators have proposed a combination of these two mechanisms. *Hocking et al.* [1990] suggested a combination of anisotropic turbulence confined at the edges of turbulent layers and specular reflectors. As an alternate explanation for aspect sensitivity, *Hocking et al.* [1991] proposed viscosity and thermal conduction waves as the origin of such reflectors. We discuss this in Chapter 5.

2.3.3 Anisotropic Turbulence or Partial Reflectors?

The theories developed to explain aspect sensitivity contain two main components: anisotropic turbulence and partial reflectors, i.e., Fresnel reflection and Fresnel scatter. It is difficult to distinguish from the radar data the contributions of partial reflectors and anisotropic and isotropic turbulence scatter. Conclusions about the dominant type of scatter are usually based on qualitative arguments and tend to be a bit subjective. This difficulty has implications for studies directed toward turbulence intensities, Doppler wind measurements, and the nature of stable or turbulent layers.

Hocking and Hamza [1997] attacked this problem by examining the degree of anisotropy which can be reasonably expected because of turbulence. By examining how the background atmosphere will act to disturb an initially isotropic turbulent

eddy, they developed a quantitative relationship between the degree of anisotropy of turbulence and prevailing atmospheric conditions. This relationship is useful in determining whether any particular observations of "specularity" really can ascribed to anisotropic atmospheric turbulence, or whether a "specular reflection" is in effect. The relationship is valid at scales within the inertial range of turbulence, where normal Kolmogorov theory predicts that, in the absence of external distorting effects, the scales should normally tend towards isotropy [e.g., *Bradshaw*, 1975], irrespective of any initial anisotropy at the generating scales. Although this theory, due to its assumptions, cannot rigorously deny the participation of anisotropic turbulence or partial reflection in aspect-sensitive scatters, it does indicates the dominant scattering mechanism. This is a point that we will discuss in detail in Chapter 5.

Hocking and Hamza [1997] noted that their theory might have deficiencies at the largest scales if these larger scales are produced anisotropically in the first place. However, since we are looking at radar backscatter, and such backscatter usually comes from scales within the inertial range, the theory is perfectly adequate.

An alternative approach, and perhaps a more rigorous and insightful one, to ascertain more precisely the structures that cause radar backscatter is to deploy more instruments. For the lower atmosphere, balloon-borne *in situ* probes can provide high-resolution measurements of quantities, such as temperature and turbulence intensity, at a height resolution of tens of meters: at least an order of magnitude improvement or more when compared to the typical radar height resolution. This motivated observation of the atmosphere using balloon-borne *in situ* probes in concert with radar observations [e.g., *Dalaudier et al.*, 1994; *Luce et al.*, 1995; *Hooper and Thomas*, 1998].

2.4 Aspect Sensitivity Investigation via Multiple Instruments

The initial observation of aspect sensitivity relied on a VHF radar with a range resolution of hundreds of meters. The coarse height resolution of the radar measurements contributed to the uncertainty in determining the types of backscattering mechanism that led to aspect sensitivity. This controversy in the radar community may be ameliorated by *in situ* observations, which, with height resolution <100 m, may identify and describe more accurately the atmosphere structures in the vertical and perhaps the horizontal extent. Additional insight will evolve from the analysis of the *in situ* data in conjunction with radar observations. In this section, we review some results from the past multiple-instrument measurement of the atmosphere.

The relationship between the radar echoes and local atmospheric structures has been studied via balloon-borne *in situ* measurements. *Dalaudier et al.* [1994] found very strong temperature gradients that seem to exist within thin layers, i.e., sheets, in the lower atmosphere. The presence of such sheets in the temperature field of the free atmosphere was frequently hypothesized in order to account for the aspect sensitivity of the VHF radar measurements. Using high-resolution temperature sensors, they found that these sheets exist in groups within regions of high static stability. Furthermore, they concluded, via examining the temperature measured by two pairs of sensors spaced one meter apart, that these temperature sheets are not horizontally flat. They estimated the possible reflection caused by the temperature sheets and compared with the simultaneous reflectivity profiles measured by a radar and found good agreement. *Luce et al.* [1995] continued this type of multiple-instrument investigation in the RASCIBA 90, as we have previously discussed. The agreement between the predicted and measured radar backscatter is good at certain altitude ranges and spotty

at others; see Figure 2.5. Despite some inadequacies in the model, this does give credence in the role that Fresnel scatter plays in radar backscatter.

In a more recent observation, *Hooper and Thomas* [1998], looking at the VHF radar (multiple beams emitted) and radiosonde observations of the troposphere and lower stratosphere at Aberystwyth (52.4°N, 4.1°W), analyzed the radar backscatter in conjunction with *in situ* measurements of the Brunt-Väisälä frequency (*N*) and the gradient Richardson number (*Ri*). They discovered that Fresnel scatter contributions could not be ignored in radar returns even at large zenith angles. In their analysis, regions of intense turbulence can be identified by a combination of an absence of aspect sensitivity of radar returns, enhancement of vertical beam spectral width, which has been corrected for the effect of beam broadening, and values of *Ri* close to or less than 1/4. This method has highlighted the presence of layers of intense turbulence which follow descending phase fronts of long period gravity waves in the lower stratosphere.

2.4.1 Scattering Calculation

Not only do *in situ* atmospheric measurements reveal atmospheric structures unresolved by a radar, it also permits us to predict radar backscatter. Insight into the scattering process is revealed when one compares the predicted radar backscatter, computed from the *in situ* profiles, to the experimental measurement. In previous analyses, authors have developed a variety of models to represent the refractive index irregularities. The models include parabolic, sinusoidal, hyperbolic, and step function profiles [*Wait*, 1962]. These models are characterized by sharp edges at the boundaries of the layer as the profile transitions from the functional shape to a constant refractive index value. Although these techniques have proven successful for comparing *in situ* measurements to HF observations [*Hocking and Vincent*, 1982], they overestimate the scattered power at VHF frequencies [e.g., *Hoppe et al.*, 1992].

Friis et al. [1957] showed that smoothing the sharp boundaries on a linear, i.e., constant gradient, layer can greatly reduce the value of the reflection coefficient. *Woodman and Chu* [1989] expanded this result to prove that the reflection coefficient depends not only on the irregularity's amplitude and scale length, but also on the specification of the smoothness and continuity of the functional shape used to model the profiles and its derivatives. They chose a Gaussian function to model the irregularity profile, since diffusion is the main mechanism for dissipation of these structures and the Gaussian function is the Green's function of the diffusion equation. Other smooth functional shapes have been used for modeling irregularities at VHF frequencies. For example, there is the half-Gaussian [*Balsley and Farley*, 1975], the hyperbolic tangent [*Haug et al.*, 1997], and the first derivative of a Gaussian [*Hocking*, 1987].

Any of these functions can serve adequately to model the refractive index profile. The problem becomes complicated in a scattering calculation when we consider an *in situ* measurement containing many refractive index irregularities, some of which may contain discontinuities. We need to use a scattering model whose functional shape is able to characterize these irregularities. *Alcala et al.* [2000] showed that the wavelet transform, due to its inherent property of time (space) and frequency (wave number) localization, is a powerful technique capable of producing a unique and invertible representation of the data localized in both physical space and scale space. Although many functions satisfy the criteria of a wavelet basis function, the first derivative of a Gaussian was chosen, as it is a smooth function such that a close form reflection coefficient can be computed. *Alcala and Kelley* [2000] use this model to analyze an *in situ* measurement of electron density to calculate the scattering cross section for comparison with the simultaneous VHF radar observation during a mesosphere scattering event.

2.5 Observations of Kelvin-Helmholtz Instability

We are interested in the effect(s) of Kelvin-Helmholtz Instability (KHI) on atmospheric structures and dynamics as revealed by radar backscatter, particularly when there exists a scattering model based in essence on the structures created by a KHI; see Figure 2.4. This motivates us to spend some time in this chapter reviewing the theories and previous observations of KHI.

KHI has been the subject of numerous observational and theoretical studies over many years because of its role in a wide range of atmospheric and oceanic processes. In the atmosphere, KHIs can achieve large amplitudes and kinetic energies. The resultant effects are the excitation of other wave motions, the local transport of heat, momentum, energy, and constituents, the generation of turbulence and diffusion, and the excitation of other scale motions, among others [e.g., *Woodman and Rastogi*, 1984; *Fritts and Rastogi*, 1985]. Kelvin-Helmholtz billows have been shown to be an important cause of clear-air turbulence, so that at any altitude, a strong KHI could constitute an aviation hazard. This would be most relevant if the billow occurred at low altitudes during aircraft take-off and landing when the localized effects of the billows could lead to substantial underestimation of the wind shear, even at airports where wind-profilers are in use [e.g., *Thorpe*, 1987; *Fritts et al.,* 1996; *Muschinski*, 1996]. Lastly, estimates of energy dissipated by billows at high levels in the troposphere indicate that they could have a significant impact on larger-scale dynamics.

Over the last two decades, mesosphere-stratosphere-troposphere (MST) radars have been used extensively to study large and small-scale dynamic processes in the atmosphere. Owing to their good temporal and spatial resolution, these radars are applied to the study of small-scale processes like KHI and turbulence at scales equal to half of the radar wavelength. Although KHIs or stratified shear flow instabilities induce vertical mixing only on small dynamical scales, their effects could be far

reaching [*Scinocca*, 1995]. These instabilities also play an important role during the generation and termination of inertial gravity waves (IGWs) in the middle and upper atmosphere [*Chimonas and Grant*, 1984a, b; *Lindzen*, 1981]. On the basis of laboratory observations and numerical simulations of the process of vortex pairing [e.g., *Browand and Winant*, 1973; *Patnaik et al.*, 1976], *Davis and Peltier* [1979] and *Klostermeyer and Rüster* [1980a] suggested that this process might enable KHI to excite propagating gravity waves in the adjacent stably stratified fluid. This has been confirmed by *Fritts* [1984] and *Chimonas and Grant* [1984a, b]. Thus, while the KHI itself is constrained to occur only in a very localized vertical domain, it may nevertheless produce effects at large distances away from the source shear.

We are interested in the way KHI influence the vertical structure of the atmosphere, and hence the radar backscatter. We motivate this interest by first providing some overview on the observation and theoretical studies of KHIs. A detailed discussion is outside the scope of this thesis. *Chapman and Browning* [1997], *Fritts and Rastogi* [1985] and the references therein provide a comprehensive discussion on the theory and observation of KHI. This section ends with a discussion of how KHI may shed light on the cause of aspect sensitivity.

2.5.1 Observations

Ground based weather and FM-CW radars have been used to observe KHIs in boundary layer [e.g., *Gossard et al.*, 1971; *Eaton et al.*, 1995; *Chilson et al.*, 1997]. Instrumented aircrafts are also used [e.g., *Nielson*, 1992]. KHIs in the troposphere are commonly revealed by billow-cloud formation [e.g., *Ludlam*, 1967; *Bader et al.*, 1995]. In the stratosphere, KHIs have been observed by early UHF radars [e.g., *Dutton and Panofsky*, 1970; *Browning*, 1971; *Browning et al.*, 1972], instrumented aircraft [e.g., *Axford*, 1970, 1973; *Pfister et al.*, 1986] and patterns in cirrus clouds [e.g., *Young*, 1971], generally in regions of high wind shear. KHI is often observed in

concert with strong wind shears under conditions such as a coastal front inversions [*Nielson*, 1992] and jet streams [*Klostermeyer and Rüster*, 1980a; *Rüster and Klostermeyer*, 1983; *Van Zandt et al.*, 1979]. Figure 2.6 shows an example of KHI observation made with an FM-CW radar. The characteristic cat-eye signatures associated with KHIs are seen. Figure 2.7 presents a recent KHI observation in the lower troposphere on 6 September 1995 when a warm front approached the 3 GHz Chilbolton radar in England. The figure is a vertical cross-section orientated west-east parallel to the surface front. The displayed Doppler velocity is effectively equal to the west-east component of the wind. The disturbance has a wavelength of around 4 km.

KHIs are detected in the lower shear regions of the jet stream at the mid-latitudes with off-zenith radar beams. Recently, *Chilson et al.* [1997] have observed the KH billows in an upper level jet stream using VHF frequency-domain interferometry (FDI) and they have described the various billow parameters. *Van Zandt et al.* [1979] and *Klostermeyer and Rüster* [1980a, b; 1981] observed enhanced turbulence intensity at a 3 m scale in the return periodic echo power during the occurrence of KHI. The mobile SOUSY VHF radar was operated in the summer of 1987 during the MAC/SINE campaign in northern Norway to study the polar mesosphere summer echoes (PMSE). They observed periodic structures that they argue to have been generated by Kelvin-Helmholtz mechanism [*Czechowksy and Rüster*, 1997]. We show *Czechowksy and Rüster*'s observation in Figure 2.8. The power echo is attributed to secondary instabilities that were supposed to be generated by the primary KHI [*Klostermeyer and Rüster*, 1980a]. Recent advances in the numerical computation of KHI are found in *Werne and Fritts* [1999, 2000a, b], *Muschinski et al.* [1999], and references therein.

Two mechanisms have been suggested in the past to account for the strong power bursts in the VHF radar observations of KHI. One ascribes them to static instabilities produced by KHI-produced super adiabatic lapse rates, and the other ascribes them to

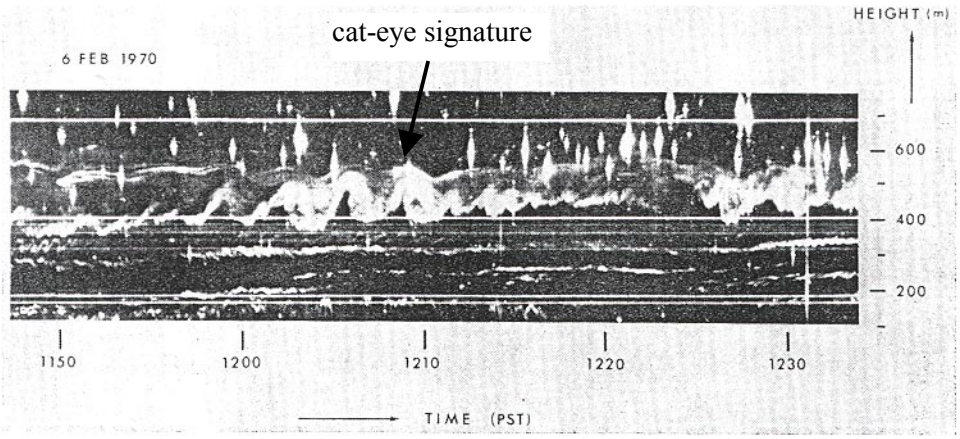

Figure 2.6: Kelvin-Helmholtz instability (KHI) imbedded in a layered atmosphere. Discrete echoes saturating the receiver are probably insects [after *Gossard et al.*, 1971].

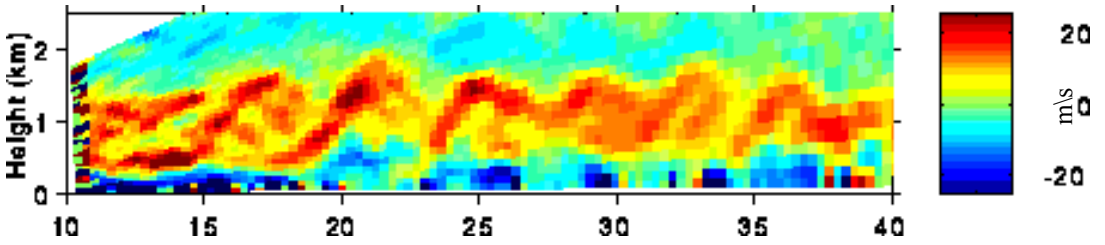

Figure 2.7: KHI observed on 6 September 1995 near the Chilbolton radar in Great Britain. The plot illustrates the distribution of vertical shear of the horizontal wind. Characteristic billow structures are observed [After *Chapman and Browning*, 1997].

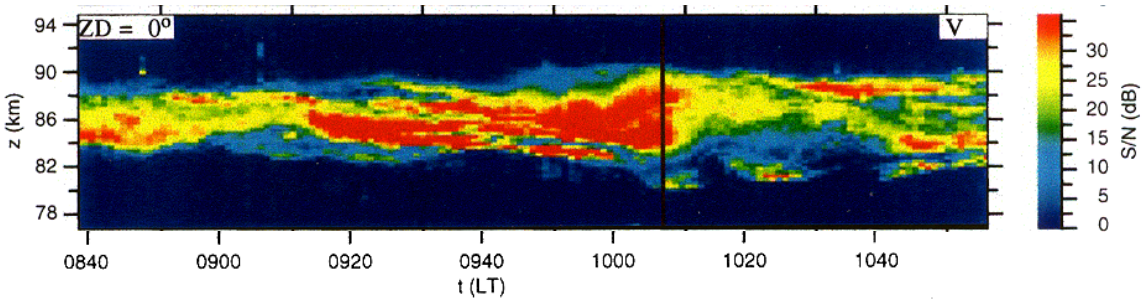

Figure 2.8: Height-time plots of the echo intensity observed on 14 July 1987 via the VHF SOUSY radar during the MAC/SINE campaign near Norway [After *Czechowksy and Rüster*, 1997].

the secondary dynamic or convective instabilities generated by the primary KHI [*James and Browning*, 1981; *Rüster and Klostermeyer*, 1983]. A good correlation between the power bursts and the vertical velocity fluctuations is also observed as the instability develops, revealing the characteristic cat-eye signatures that are seen in Figures 2.6, 2.7, and 2.8. This indicates that the power variation may be due to turbulence and secondary instabilities generated by the KHI.

KHIs have been observed using more complicated radar techniques. Recent measurements using spaced antennas have reported that, in thin regions of high wind shear, the radar backscatter is most aspect-sensitive transverse to the wind [e.g., *Brown et al.*, 1996]. This is interpreted as evidence for "fine rolls," or the cat-eye signatures, within the shear layer, consistent with the KHI in layers of high wind shear. *Chilson et al.* [1997] reported high-resolution observations of upper tropospheric Kelvin-Helmholtz billows using VHF frequency domain interferometry (FDI). The measurements were made using the sounding system (SOUSY) VHF radar located in the German Harz Mountains operating at frequencies of 53.26 and 53.75 MHz. Through the application of the FDI technique, it has been possible to track the altitude of thin scattering layers with an accuracy of a few tens of meters and a temporal resolution of 13 s. They also found examples of KHI in regions coinciding with large values of wind shear.

Turbulence layers, which are sometimes aspect-sensitive, in the stratosphere as described by *Sato and Woodman* [1982], *Tsuda et al.* [1986], and *Kilburn et al.* [1995], are closely related to the wind shear and attributed to KHI breaking. *Klostermeyer and Rüster* [1981] interpret variations of VHF echo power in a $\theta = 12.5°$ radar beam, with a period of a few minutes and amplitude up to 20 dB, to be caused by tilted specular layers or enhanced turbulence linked to KHI. *Röttger and Schmidt* [1979] used a VHF radar to detect the fine turbulence structure of KHI in echo-power measurements near a height of 4.5 km.

One limitation to remote sensing measurements of KHI is the coarse height resolution (100s of meters at VHF and 10s of meters at UHF) of the radar measurements. Although *in situ* probes can make higher resolution measurements of atmospheric parameters during a KHI event, such measurements were more often than not made by accident, as there has yet to be an experiment implemented with the goal of making *in situ* measurements of a KHI. The ambiguities in the KHI investigation have encouraged the use of computer simulations to study the instability. Computer simulation may be the only approach to investigate quantitatively the generation, evolution, and decay of KHI and its turbulence generation and its effect on atmospheric constituent transport as well as the prediction of radar backscatter, despite the fact that a simulation cannot model the full complexity of the atmosphere [e.g., *Fritts et al.*, 1996; *Gibson-Wilde et al.*, 2000]. *Muschinski et al.* [1999] applied numerical simulations of turbulence to the investigation of radar backscatter. They used a large eddy simulation (LES) to simulate UHF wind profile measurements. The LES technique provides three-dimensional simulated atmospheric variables. In a similar manner, *Gibson-Wilde et al.* [2000] applied direct numerical simulation (DNS) of KHI to predict Doppler VHF radar observations of the turbulent region. The backscattered power, radar spectral width, and radial velocity are then simulated via the direct calculation of the Doppler spectral moments from the reflectivity distribution and simulated velocities. This latter study is an important concept of this thesis.

2.5.2 KHI Generation and Evolution

VHF radar observations of KHI events have been quantitatively explained in the past with the help of model computations such as the one by *Van Zandt et al.* [1979] and others by *Klostermeyer and Rüster* [1980a, b; 1981a]. In addition, a number of laboratory experiments and theoretical studies have also addressed the evolution,

growth, and billow structures of the KHI [e.g., *Fritts and Rastogi*, 1985; *Werne and Fritts*, 1999, 2000a, b]. The growth rate and the billow structure are found to depend strongly on the gradient Richardson number (*Ri*), an instability parameter, of the shear flow. In previous studies reported from VHF radars, it has been found that the occurrence of KHI often takes place in the upper troposphere associated with the meteorological jet streams [*Klostermeyer and Rüster*, 1980a, b, 1981; *Rüster and Klostermeyer*, 1983] or at the mesospheric height [*Van Zandt et al.*, 1979].

It is insightful to examine the evolution of KHI. It is well understood that KHI begins as a small amplitude perturbation in an unstable shear, i.e., when the gradient Richardson number (Ri) < 1/4, and grows rapidly by extracting kinetic energy from the shear flow. The shear maximum occurs at the statically unstable layer sandwiched between two layers of high static stability. This provides a suitable condition for stratified shear instability to set in. On occasions, secondary KHI may develop on these strong gradients [*Woods*, 1969; *Thorpe*, 1973b], but these regions are themselves engulfed as the turbulence expands horizontally. The occurrence of horizontally localized regions of the instability, and hence large amplitude KH billows, may be the source of the low frequency oscillations seen in scattering layers.

The instability is initiated in the outermost statically unstable layer within the KH billow. The successive breakdown of statically unstable layers takes place close to the core of the billow and move outwards. It is this breakdown that mixes and transfers atmospheric mass and momentum [*Scinocca*, 1995]. The turbulence generation immediately follows the breakdown of statically unstable layers. Once initiated, the turbulence rapidly expands throughout the billows, causing regions of relatively large gradients between adjacent billows. As the amplitude of the motion increases, individual wave crests break, forming turbulent cores, which concentrate the vorticity of the initial shear layer and form the well-known cat's-eye pattern. *Hardy et al.* [1973] suggest that the most intense turbulence accompanies this phase of the

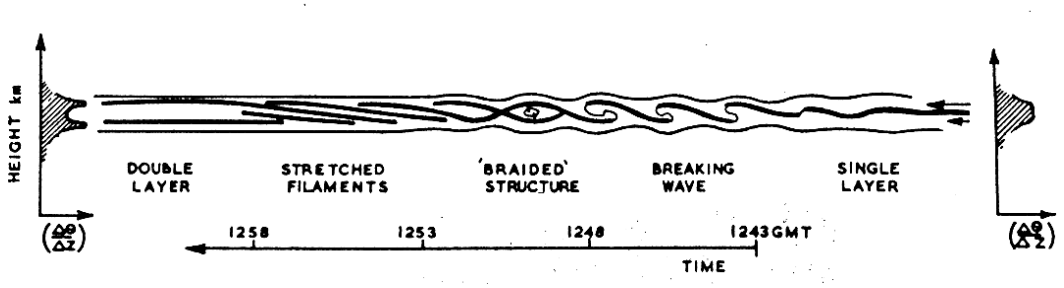

Figure 2.9: Schematic of the zones of high reflectivity associated with various stages of KH development. Evolution proceeds from right to left [after *Brown and Watkin*, 1970].

evolution. Because of the strong turbulence within the KH billows, air is rapidly mixed, causing large gradients of temperature and density (and hence radar refractivity) to occur around and between adjacent billows.

As the turbulent energy decays, these billows become nearly horizontal stratified layers where the center of the layer is marked by homogeneity while the edges are indicated by sharp gradients [e.g., *Werne and Fritts*, 1999; *Gibson-Wilde et al.*, 2000]. The double-peaked structure observed by the radar may be due to the reflection from the two turbulent layers. *Browning and Watkins* [1970] observed the stratification split into two long-lived layers downwind of the billows whereas the split shear was short-lived in the case observed in the boundary layer by *Chapman and Browning* [1997]. Some of the layered turbulent structures in the lower atmosphere may be the remnant of a KHI. However, there is inadequate information to make a confirmation. Turbulence will act on the sharp gradients at the edges, smoothing them and eventually integrating the homogeneous stratified layer into the background atmosphere. Figure 2.9 presents an illustration of the development of KHI [*Browning and Watkins*, 1970].

While many observations of Kelvin-Helmholtz billows were made using radars, few shed light on the evolution of billows or the effect they have on their environment. Although we can see the vertical structure of large amplitude KH billows via a VHF

radar, the height resolution on the order of 100 m and time resolution on the order of minutes are often too crude to resolve the structure of individual layers or KHI. On the other hand, frequency-modulated continuous-frequency (FM-CW) radars, which have excellent range and time resolution, have been employed to obtain observations of KHI [e.g., *Eaton et al.*, 1995]. Here the limitation is that they are only capable of making observations in the planetary boundary layer. A combination between observation and numerical simulation may be the best way for us to understand the complexity of KHI.

2.5.3 Relevance to This Thesis

It may appear that KHI is not directly relevant to our investigation of aspect sensitivity. We want to examine the validity of KHI as an explanation of atmospheric backscatter, as was first presented by *Bolgiano* [1968], seen in Figure 2.4. Our interest focuses on the KHI at its late stage of the evolution, where stratification transforms the billow structures into a layer of turbulence bounded by large temperature gradients. Both the turbulence and the temperature gradients that bound it would cause changes in refractive index that would be responsible for radar backscatter. In contrast to *in situ* probes, a radar, due to its coarse height resolution, cannot resolve these temperature gradients and possibly the instability itself. The multiple-instrument observational dataset discussed in this thesis therefore is ideal in our determination of the effects of KHI on aspect sensitivity.

2.6 Conclusion

The lower atmosphere has been an area of interest ever since the early days of radar development. Aspect sensitivity, i.e., the zenith angle dependence of the radar backscatter, is one of the lower atmospheric curiosities that has been investigated since the late 1970s. Despite detailed investigation using a VHF radar, via the DBS and/or

the SA technique, and sometimes in concert with *in situ* instruments, an explanation of aspect sensitivity has not been adequately resolved.

A scattering model introduced by *Bolgiano* [1968] motivated us to examine the theory and present understanding of Kelvin-Helmholtz instability (KHI). The instability, during the late stages of its development, creates temperature structures which may provide some insights into the cause of aspect sensitivity, as we will show in this thesis.

We strive forth in our march towards a better understanding of aspect sensitivity in the following chapters. Our discussion begins with an analysis of a high-resolution *in situ* measurement of the lower atmosphere that took place at Wichita, KS, followed by a discussion and analysis of an aspect sensitivity investigation at the Jicamarca Radio Observatory (JRO) near Lima, Peru. The experiment at JRO deployed a VHF radar and a series of *in situ* temperature and turbulence measurements made possible by balloon-borne instruments. We use direct numerical simulation (DNS) of KHI to unite these disparate datasets to extract insights into the cause of aspect-sensitive radar backscatter.

Chapter 3

High-Resolution Temperature Sounding of the Lower Atmosphere

Radio waves are scattered in the lower atmosphere by variations in pressure, temperature, and humidity that produce variations in the refractive index [e.g., *Booker and Gordon*, 1950; *Bean and Dutton*, 1968; *Balsley and Gage*, 1980; *Balsley*, 1981]. It has been observed that, at MF/HF/VHF frequencies, this backscatter is aspect-sensitive; in other words, the ratio of the backscatter power in the vertical direction versus that in off-vertical direction is greater than unity [e.g., *Hooper and Thomas*, 1995, 1998; *Tsuda et al.*, 1997]. It is generally thought that there are three scattering mechanisms that create aspect sensitivity: Fresnel reflection, Fresnel scatter, and anisotropic turbulence. Fresnel reflection, also termed partial specular reflection, is caused by vertical gradients of refractive index that are long-lived and have horizontal dimensions comparable to the first Fresnel zone. Scatterers with horizontal dimensions on the order of $r\theta$, where r is the range and θ is the radar half-power half-width (HPHW), i.e., less than the first Fresnel zone, or multiple Fresnel reflectors in a given range gate are known as Fresnel scatterers [e.g., *Hooper and Thomas*, 1998].

On the other hand, turbulent structures with the scale size equal to one-half of the transmitted wavelength can also create echoes observable by high-power radar systems such as the Arecibo Observatory (AO) and the Jicamarca Radio Observatory (JRO).

The Air Force Research Laboratory (AFRL) and the Naval Post-graduate School (NPG) have made a push towards high-resolution measurements of atmospheric temperature structures and turbulence for the purpose of characterizing the changes in atmospheric refractive index and their effects on a laser beam [*Beland*, Private communications]. A high-resolution *in situ* measurement of lower atmospheric temperature was made at Wichita, KS (37.8°N, 97.2°W), on 5 March 1995. We believe that our understanding of the structures associated with aspect-sensitive backscatter begins with an examination of the temperature structures in the atmosphere as revealed by high-resolution temperature measurements of the atmosphere. The goal of this chapter is to examine the structures in the atmosphere, and then, in future chapters, apply our results to the understanding of aspect sensitivity.

We organize our discussion as follows: We first describe the *in situ* instruments and then present the measured temperature data. Our attention is focused on the sharp temperature gradients at the edges of the observed potential temperature steps. The potential temperature (θ), the Brunt-Väisälä frequency (N), and the gradient Richardson number (Ri) reveal the atmospheric stability or a lack thereof associated with potential temperature steps. A Fourier analysis is then performed on the dataset.

We believe that the data is composed of three components, localized, anisotropic structures, turbulence, and instrument noise. We demonstrate this using wavelets. Since the wavelet transform can isolate features that are highly localized and have very high spatial frequency components, wavelet analysis, as oppose to Fourier analysis, is a more suitable analysis tool for data that exhibit localized structures. We

develop a wavelet-based algorithm to isolate the organized component of the signal and, after subtraction, the residual signal is investigated for evidence of quasi-homogeneous turbulence. We also compute the turbulence parameter C_n^2 from the Fourier power spectrum of the residual signal and compare it with C_n^2 computed from the higher order structure function.

3.1 Experimental Set-Up

In this section, we briefly discuss the balloon-borne instruments deployed at Wichita, KS, as well as the background climate condition.

3.1.1 Flight Conditions

The balloon launch occurred at 0100 LT on 5 March 1995 over Wichita, KS, during the declining phase of a mild winter snowstorm. The sky was 100% overcast with light, dry snow up through the cloud top at the 1.3 km boundary layer inversion. The snow declined throughout the night and stopped by 0300 LT with clear conditions developing around sunrise. The surface temperature at launch was 0 C. Because of the light snow, there was some concern that ice could form on the probes, degrading the operation or breaking the probes. This did not occur because of the very dry snow condition and the cold temperature. Surface winds were light, approximately 1 m/s or less. The tropopause occurred at 10 km with relatively strong winds from the southwest at 30 m/s at 10 km and 12 km.

3.1.2 Instrumentation

The balloon payload consisted of two thermal turbulence sensors utilized in conjunction with a commercial VIZ 9000 microsonde system. The first was an uncoated 100 μm bead thermistor with 18 μm wire leads that had a temperature response time of 30 ms near the surface; this response time increased to 90 ms in the

stratosphere as the air density declined. The thermistor sampled every 1.25 s with an analog to digital converter resolution of 15-16 bits which gives a temperature resolution of between 0.005-0.01 K. This relatively low speed sensor on the radiosonde provided absolute reference temperatures for the high-speed thermal turbulence sensor and larger scale (> 5 m) thermal turbulence data.

The high-speed thermal turbulence sensor was developed during 1994-95 at the US Naval Post-graduate School (NPS) for the U.S. Air Force (USAF) airborne laser (ABL) program. It utilized a differential thermocouple pair with different thermal time constants DC-coupled through an instrumentation amplifier and a 500 Hz analog bandpass filter. These fed a 12-bit A-D converter operating at 310 samples per second. The digital serial bit stream fed a frequency shift keying (FSK) modulator that created a 130-150 kHz, amplitude modulated, subcarrier on the 403 MHz balloon telemetry signal.

The primary sensor in the thermocouple pair was a 12 μm thermocouple with a measured time constant of 5 ms at launch that increased to 15 ms in the stratosphere. The second thermocouple was constructed of a #24 gauge wire having a time constant of 10 seconds that increased to 30 seconds. The differential connection of the two thermocouples removed the common mean temperature, while still responding to the turbulent thermal fluctuations. The differential operation of the high-speed temperature sensor suppressed the large-scale fluctuations that were handled by the independent bead thermistor. Therefore, this thermocouple pair was able to measure a one-dimensional atmospheric temperature fluctuation at a height resolution of ~5.0 cm. As we will discuss in a future section, this was not the prototypical setup of a turbulence sensor, which was composed of two temperature probes, separated horizontally by 1 m.

Measurements of optical turbulence in the free atmosphere and stratosphere required a temperature resolution of 0.001-0.01 K. The 80 K temperature changed

from launch to the tropopause with a 0.001 K temperature resolution imposes a 17 bit dynamic range on the system. This large temperature dynamic range was handled by removing the large-scale fluctuation using the thermocouple and then sampling the data at 310 Hz.

Wind speed was measured with a height resolution of 130 m via a LORAN (Long Range Navigation) system.

3.2 Observations

The low-resolution temperature data are presented in the left hand panel of Figure 3.1. The lapse rate in the troposphere is 7.4 K/km; this is slightly less than the adiabatic lapse rate, indicating a statically stable condition in which, if an air parcel were displaced in the vertical direction, it will fall back towards its equilibrium position. (A note on the lapse rate. Following meteorological convention, we define the lapse rate as the negative of the temperature gradient.) The lapse rate is 0.53 K/km in the stratosphere indicating greater stability. The tropopause is located at ~10 km. Even in the low-resolution data, considerable structure is evident in the temperature profile, a result upheld by the high-resolution measurement of the temperature fluctuations shown in the right hand panel. Asymmetric structures, which are characterized by a sudden increase in temperature followed by a gradual decrease, exist in the data stream. We discuss these organized structures in a later section. These structures appear roughly every kilometer in the troposphere; similar structures are somewhat less obvious in the stratosphere but exist there as well. The positive temperature gradients are quite steep. They are as steep as 40 K/km in the stratosphere; the steepest gradient in the troposphere is roughly 1/3 of that value. On the other hand, the negative gradients are shallower, seldom dropping to less than –10 K/km. If

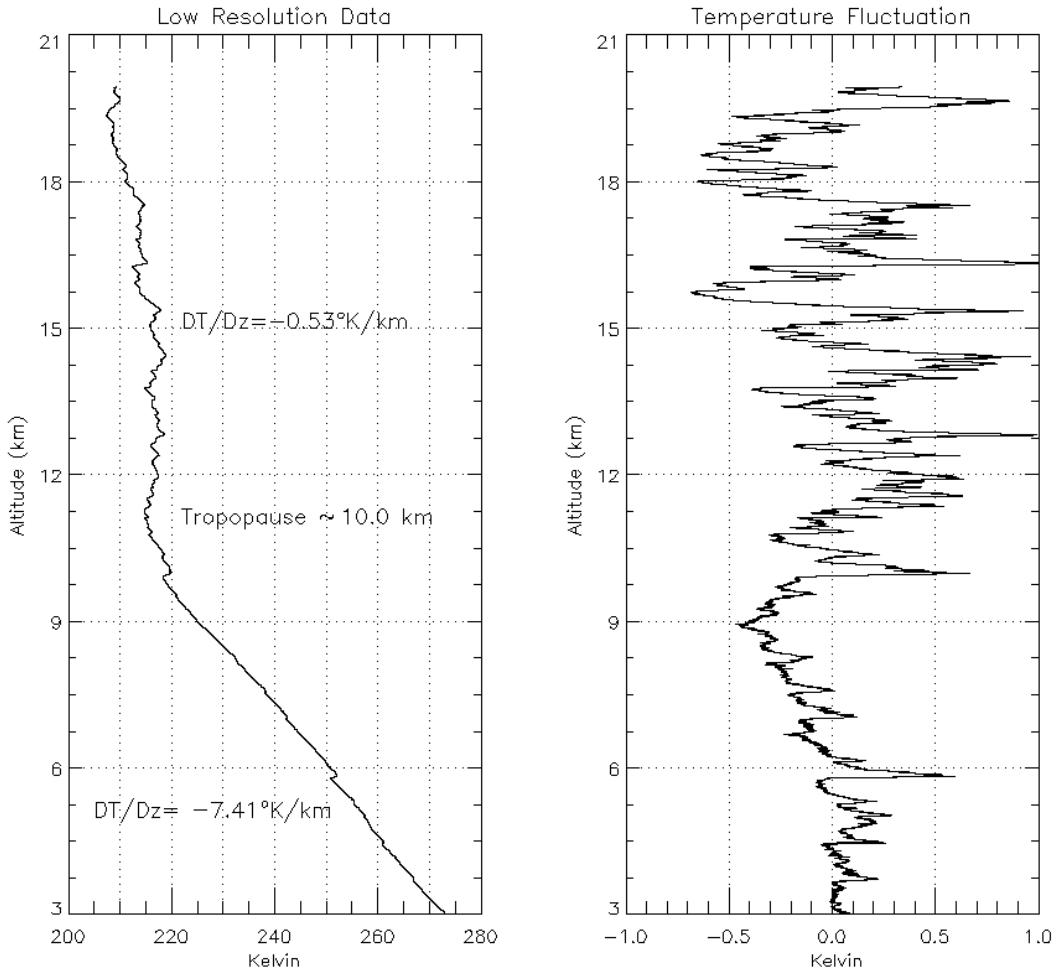

Figure 3.1: *Left panel*: Low-resolution temperature data as measured by a radiosonde over the skies of Wichita, KS, on 5 March 1995. Tropopause is at ~10 km. *Right panel*: High-resolution temperature fluctuation measured by the thermal turbulence sensor. Asymmetrical structures, which are characterized by a sudden increase in temperature followed by a gradual decrease, are prevalent in the dataset. Close-ups of these structures are seen in Figure 3.4.

isotropic turbulence does exist in our dataset, and we do later show that it may, it is overshadowed to the eye by anisotropic, large-scale structures.

In Figure 3.2 we plot the potential temperature (θ) along with its derivative. The potential temperature is defined in terms of temperature (T), pressure (p), the universal gas constant (R), the dry air specific heat at constant pressure, and a reference pressure (p_s), as

$$\theta = T\left(p_s / p\right)^{R/c_p} . \tag{3.1}$$

By definition, θ is the temperature that a parcel at pressure p would have if it were moved adiabatically to the reference pressure p_s, which we take to be 1000 mb. Potential temperature is used to measure temperature changes, since it does not change in an adiabatic move from one pressure to another and hence may be considered a property of the fluid. In the data, we see numerous examples of near-vertical potential temperature steps, i.e., regions of the potential temperature profile where the vertical potential temperature gradient approaches zero. The asymmetric structures with steep temperature gradients, as observed in Figure 3.1, are collocated with the edges of the potential temperature steps. We examine this in a later section. For this particular balloon sounding, potential temperature steps are on the order of 0.1-1.0 km thick in both the troposphere and the stratosphere.

The potential temperature gradient ($\Delta\theta/\Delta z$), plotted in the right-hand panel of Figure 3.2, is another indication of atmospheric stability. The atmosphere is statically stable when $\Delta\theta/\Delta z > 0$. In the regions where $\Delta\theta/\Delta z \approx 0$, the atmosphere is neutrally stable, indicating an adiabatically mixed atmosphere. An unstable situation is indicated by $\Delta\theta/\Delta z < 0$; this would be created when a parcel of heavier air overlies lighter air [e.g., *Holton*, 1992]. The average value of $\Delta\theta/\Delta z$ is 2.54 K/km in the troposphere and 16.35 K/km in the stratosphere. The higher $\Delta\theta/\Delta z$ in the stratosphere corresponds to the higher stability of the region. The tropopause forms the boundary between the slightly stable troposphere below and the very stable stratosphere above.

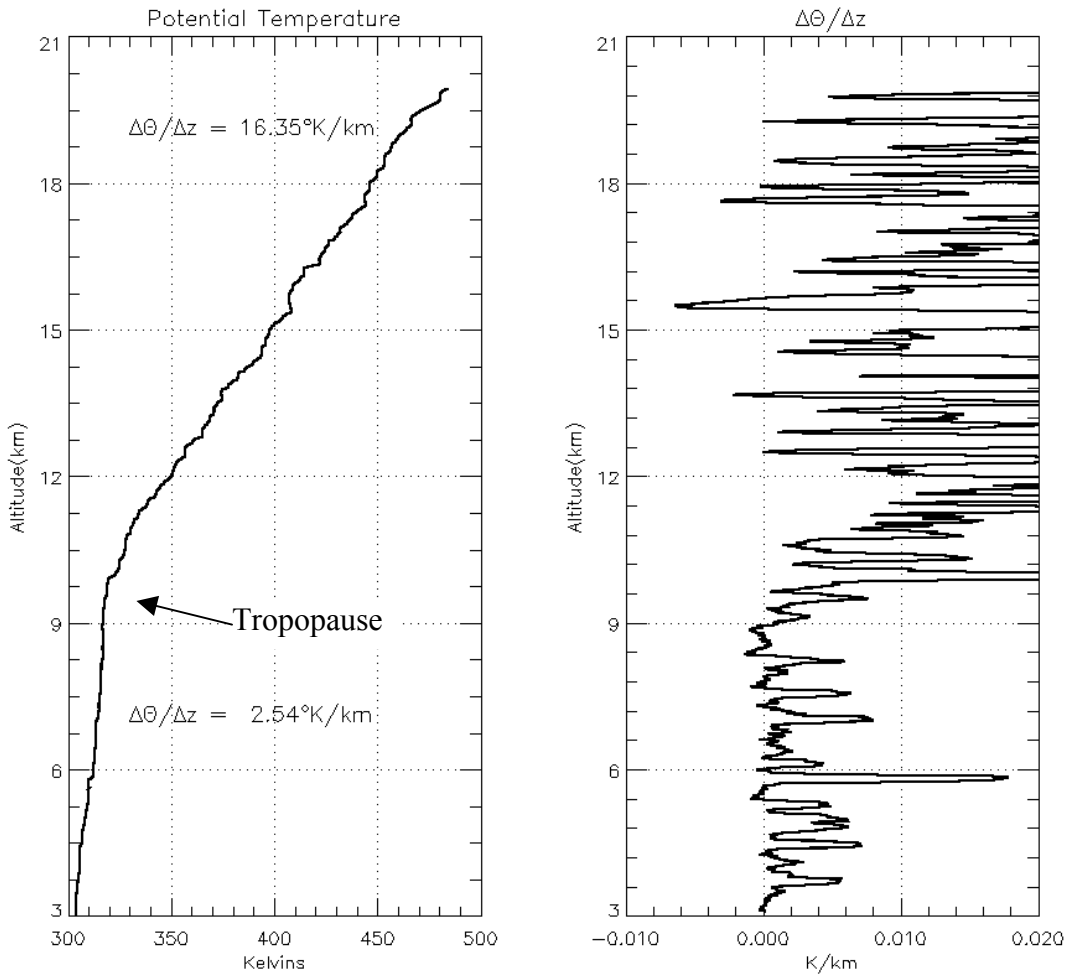

Figure 3.2: *Left panel*: Potential temperature derived from the radiosonde temperature measurement. The tropopause is at ~10 km. *Right panel*: dθ/dz.

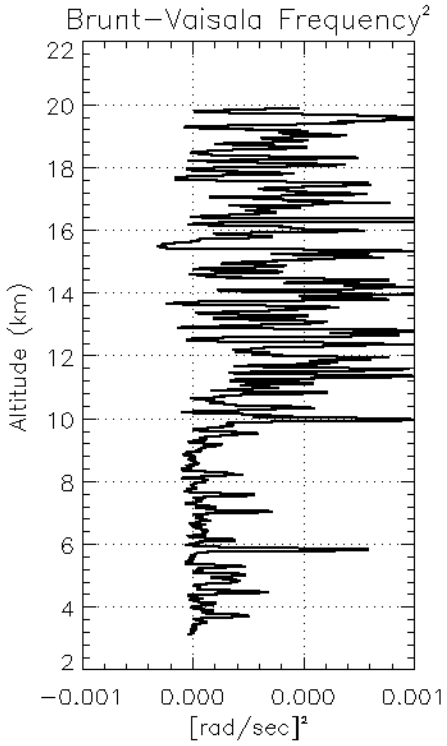

Figure 3.3: Square of the Brunt-Väisälä frequency (N^2).

Regions of lower than average $\Delta\theta/\Delta z$ actually correspond to negative gradients in the actual temperature. Regions with near constant $\Delta\theta/\Delta z$ as a function of height are seen, indicating that some process has mixed the regions of atmosphere adiabatically.

Atmospheric stability is made clear in Figure 3.3 in which we plot the square of the Brunt-Väisälä frequency

$$N^2 = \frac{g}{\theta}\frac{d\theta}{dz}. \tag{3.2}$$

This is another way of looking at the hydrostatic stability of the atmosphere. N^2 is a measure of the frequency of oscillation for a vertically displaced parcel of air. This oscillation is the result of the buoyancy force restoring the vertically displaced parcel back to its original location. If this parcel were in a highly stratified layer of atmosphere, the stratification would limit the vertical displacement of the parcel and

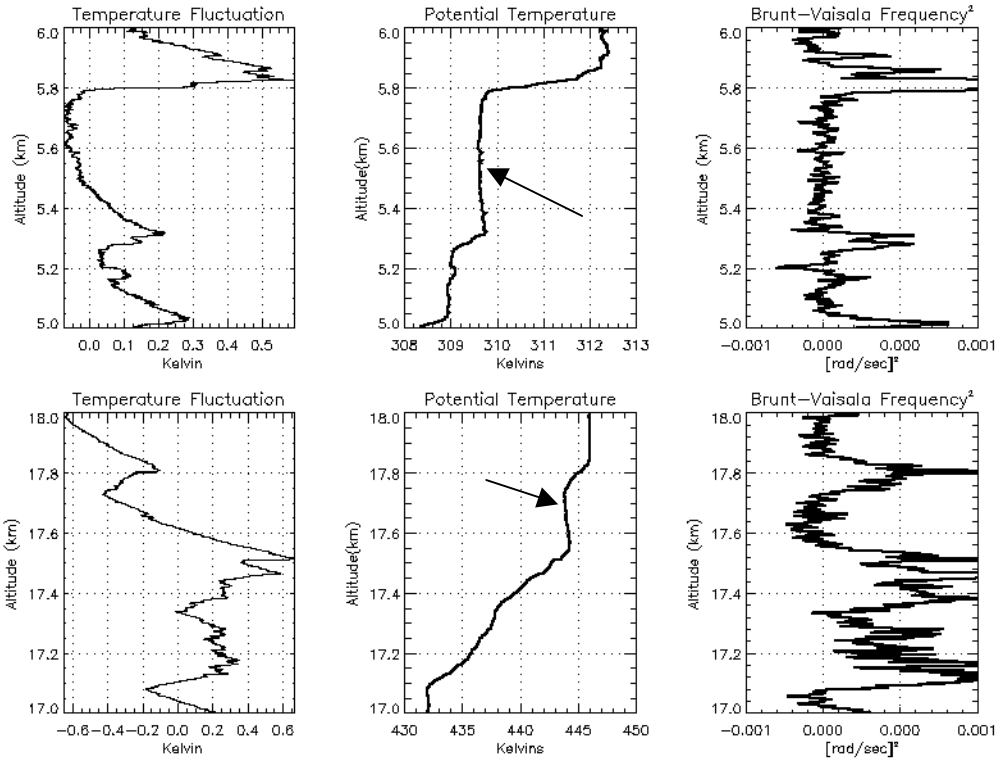

Figure 3.4: Asymmetric temperature structures and their relationship with potential temperature and Brunt-Väisälä frequency. Top row is an example in the troposphere portion of the data. Bottom row is an example from the stratosphere.

increase the oscillation frequency. In other words, large positive values of N^2 imply a stably stratified atmosphere while negative stability yields $N^2 < 0$. The average N^2 in the stratosphere is 8.5×10^{-4} [rad/sec]^2 and is 1.25×10^{-4} [rad/sec]^2 in the upper troposphere, which translates to Brunt-Väisälä periods of 3.6 min and 9.4 min, respectively. This again indicates the strong stability of the stratosphere and the marginal stability of the upper troposphere. N^2 is near zero in the center of the temperature steps and peaks near the edges.

For a closer look at the asymmetrical structures seen in Figure 3.1 and to see how they tie in with θ and N^2, we have selected two of these asymmetrical structures and magnified them in Figure 3.4. The top row shows an example in the troposphere. The saw tooth shaped temperature fluctuations are near the edges of the potential temperature steps. N^2 hovers around zero near the center of the step, implying a

marginally stable condition where the air is very well mixed. We see a similar behavior in the stratosphere, as seen in the plots in the lower row of Figure 3.4.

We plot in Figure 3.5 the wind condition for this particular radiosonde sounding. The wind was basically westward and steadily increased in speed up to the tropopause, remains steady near 25 m/s up to 15 km, and then decreased quickly with height. We can use this wind information in combination with the Brunt-Väisälä frequency to compute the gradient Richardson number (*Ri*)

$$Ri = \frac{N^2}{(dU/dz)^2}, \tag{3.3}$$

which is a measure of shear instability [e.g., *Fritts and Rastogi*, 1985; *Bertin et al.*, 1997]. Physically, it simply says that large wind shears cause turbulence. Mathematically, it measures the ratio of the stabilization effect of the stratification, as signified by N^2, to the destabilization effect of the wind shear. Stability is indicated by $Ri > 0.25$. $0 < Ri < 0.25$ indicates dynamic instability while $0 < Ri$ is hydrostatically unstable. We plot *Ri* in Figure 3.6. However, the height resolution of the wind measurement is much more coarse than that for the temperature measurement. Hence, this calculation cannot give us a good indication of where shear instabilities occur. Nonetheless, on some occasions, it is clear that *Ri* is small in the regions where N^2 is near zero and/or the vertical shear is large and certainly would yield $Ri < 0.25$.

3.3 Data Analysis

We turn to mathematical transforms in the hopes of understanding the atmospheric structures revealed by the *in situ* measurements. Our goal is to understand the anisotropic structures, as seen in the right panel of Figure 3.1 with close-ups seen in Figure 3.4, not only to understand the vertical structures of the atmosphere but also their relationship to aspect sensitivity. The popular Fourier analysis is applied to the high-resolution temperature data. We also apply wavelet analysis to our data stream.

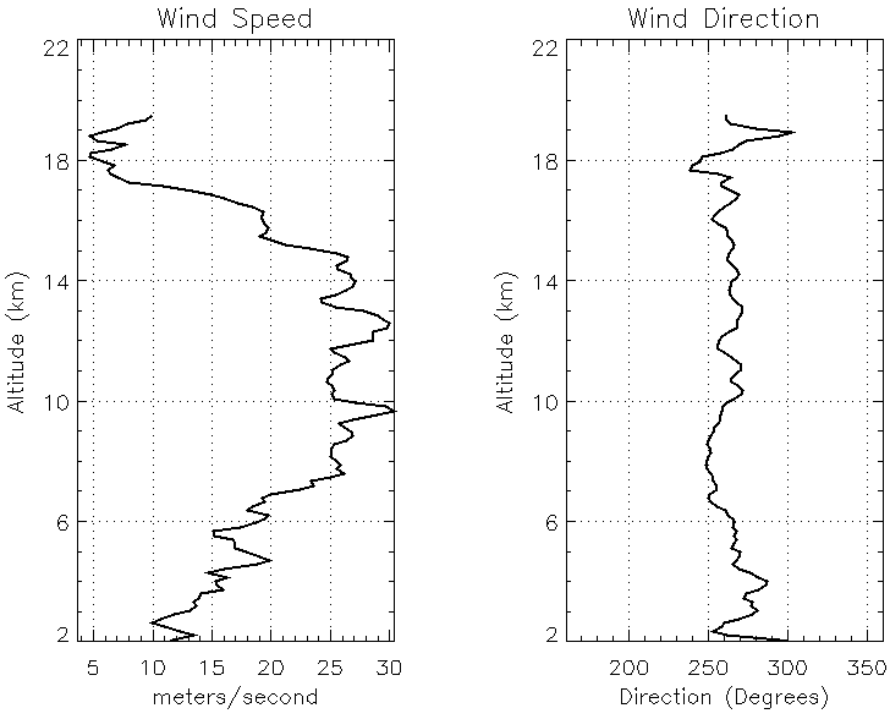

Figure 3.5: Wind profile measured on 5 March 1995. We see a westward wind with increasing velocity up to 10 km. Velocity plateaus between 10 km and 15 km and then decreases with height.

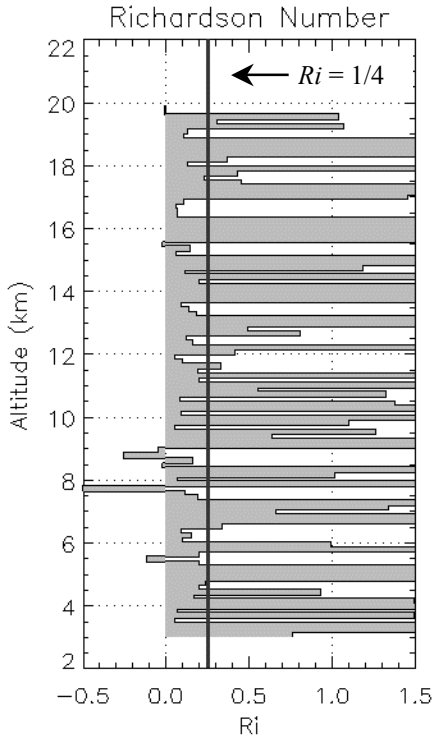

Figure 3.6: Gradient Richardson number (*Ri*). Dark line indicates *Ri* = 1/4, the boundary of stability.

There has been a great interest in using the recently developed wavelet transform technique for data analysis, [e.g., *Farge et al.*, 1999; *Alcala et al.*, 2001, and references therein]. The wavelet transform is able to localize features in space and wave number in an optimal manner and can be used to analyze asymmetrical structures. Therefore, it is reasonable to apply wavelet analysis to the temperature structures seen in Figures 3.1 and 3.4. Furthermore, we use the property of wavelets to parse the data into its components: coherent temperature structure, turbulence, and instrument noise.

Before we begin our data analysis, however, we realize that the troposphere and the stratosphere can be treated as two fluids, the latter being more dynamically stable. This motivates us to separate the dataset into the stratosphere and the troposphere segments before we proceed with the mathematical analysis.

3.3.1 Fourier Analysis

We have Fourier transformed the high-resolution temperature data and computed the power spectral density (PSD). We display the result in Figure 3.7. We have defined the wave number as $1/\lambda$. A least-squares fit to a power-law was performed over the range $10^{-2} < 1/\lambda < 10^{1/2}$ of each spectrum, the results of which are illustrated in the figure as the dashed line. The tropospheric and stratospheric sections display a –1.91 and –2.27 power law, respectively, for the range. Both are considerably steeper than the -5/3-power law expected for isotropic turbulence in the inertial subrange [e.g., *Ottersten*, 1969a, b]. We see two dominant components in both spectra at $\lambda = 2.5$ km and $\lambda = 1$ km, i.e., $1/\lambda = 4\times10^{-3}$ km^{-1} and $1/\lambda = 10^{-3}$ km^{-1}, respectively. The component at $\lambda = 2.5$ km is a factor of two larger in magnitude in the stratosphere than the troposphere. A noise floor does not appear in either PSDs. This is a bit unusual but it is quite possible for a signal to be greater than noise at all frequencies sampled.

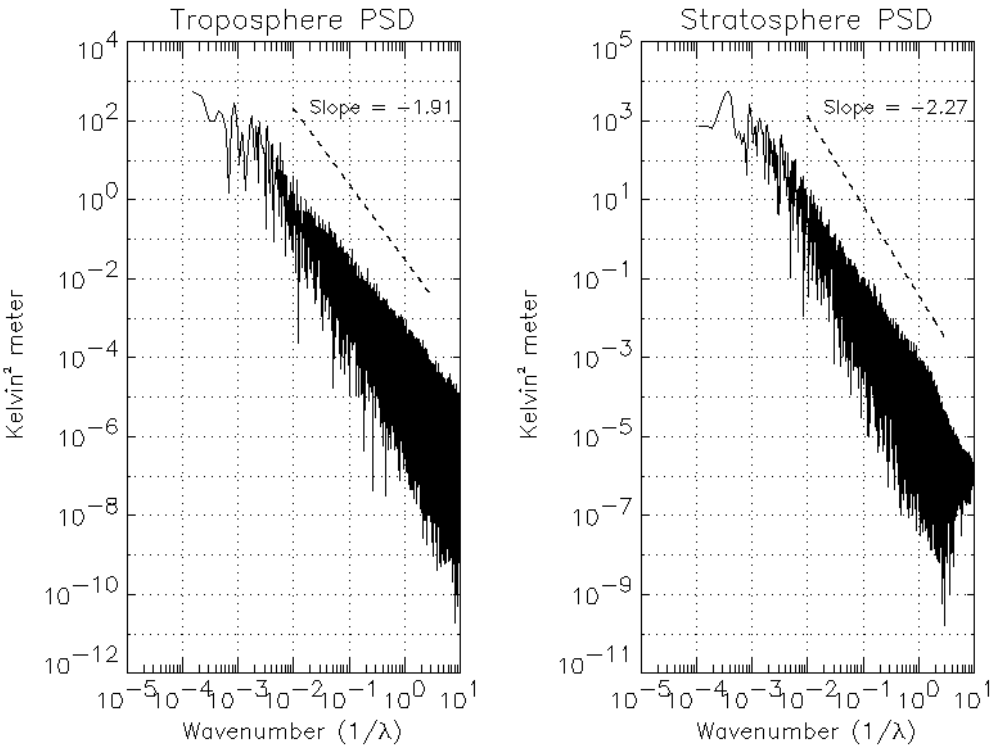

Figure 3.7: Fourier power spectrum of the tropospheric (left panel) and stratospheric (right panel) component of the data. We have performed a squares fit to a power-law to certain parts of the data. Both display power law spectra for the range $10^{-2} < 1/\lambda < 0.5$ with indices –1.91 and –2.27, respectively.

We believe that the result of the Fourier analysis is dominated by large-scale, localized anisotropic structures, possibly with small-scale, isotropic turbulence and instrument noise superimposed. These anisotropic structures, we believe, caused the temperature spectrum to follow a steeper power law than the Kolmogorov -5/3 law for isotropic turbulence. There is still the possibility that isotropic turbulence is present, which would be revealed by a –5/3 power law in the PSD of a one-dimensional temperature measurement, but it is too weak to be revealed by Fourier analysis. Hence, if we are able to isolate the localized components of our data, we may be able to separate them and search for the imbedded isotropic turbulence in the data stream, thereby making it possible for us to estimate independently the radar backscatter from the localized temperature gradients, which we call edges, and the turbulent component

of the temperature profile. In addition, this would give credence to the two main sources of radar backscatter in the neutral atmosphere: coherent structures and turbulence. To do this, we turn to wavelets.

3.3.2 Wavelet Analysis

The wavelet transform is an integral transform localized in both space (or time) and frequency. It differs from the Fourier transform in that instead of mapping the function of interest from space (or time) to wave number (frequency), the wavelet transform maps the function from space (or time) to space (or time) and scale; 1/scale is analogous to frequency in Fourier analysis. In short, the wavelet transform divides the signal into different scale components and then studies each with a resolution to match its scale [*Daubechies*, 1992]. The wavelet transform thereby achieves the ability to locate and analyze short-lived, transient events such as the anisotropic structure in our atmosphere temperature measurement.

Sine and cosine functions, the basis for the Fourier transform, allow us to perform time-frequency analysis on a dataset, such as seen in Figure 3.7. But each component must have the same amplitude over the entire data segment. It is the choice of basis function used that gives the wavelet transform its simultaneous time (space) and frequency (wave number) localization. We construct the basis functions by scaling and translating a reference function: a wavelet ($\psi(x)$) defined as [*Foufoula-Georgiou and Kumar*, 1994; *Antoine*, 1999]

$$\psi_{\lambda,b}(x) = \frac{1}{\sqrt{\lambda}}\psi\left(\frac{x-b}{\lambda}\right). \tag{3.4}$$

The scale parameter λ dilates (or compresses) the wavelet while b translates the wavelet. The wavelet transform of a function $f(x)$ is essentially the convolution of the wavelet with $f(x)$. For purposes shown later, the first derivative of a Gaussian, also known as the Canny edge detector, is our choice for a wavelet basis. It is defined as

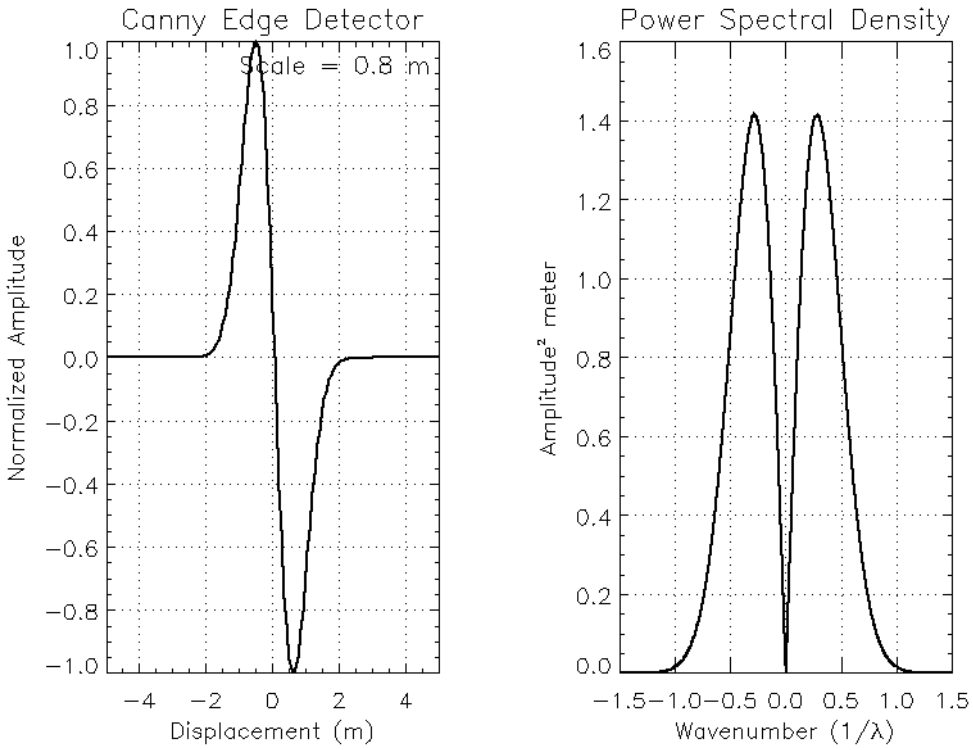

Figure 3.8: Time series of the Canny edge detector and its Fourier power spectrum.

$$\psi(x) = \frac{-1}{\sqrt{\Gamma\left(\frac{3}{2}\right)}} x e^{-x^2/2} \ . \tag{3.5}$$

Many functions can be used as the wavelet basis for wavelet transform, as long as the function satisfies the criteria which define the wavelet basis. We choose the first derivative of a Gaussian because it and its derivative are smooth, indicating that a close form radar backscatter solution can be computed. We discuss this in Chapter 8. This will be important when we use our wavelet technique in radar backscatter prediction. The gamma function appears for normalization purposes [*Torrence and Compo*, 1998]. We illustrate in Figure 3.8 the behavior of the Canny edge detector in both the time and frequency domain. In formal mathematical terms, the wavelet transform of a function $f(x)$ is defined as the integral transform

$$Wf(\lambda, x) = \int_{-\infty}^{\infty} f(u)\psi^*_{\lambda,x}(u)du \ , \ \lambda > 0, \tag{3.6}$$

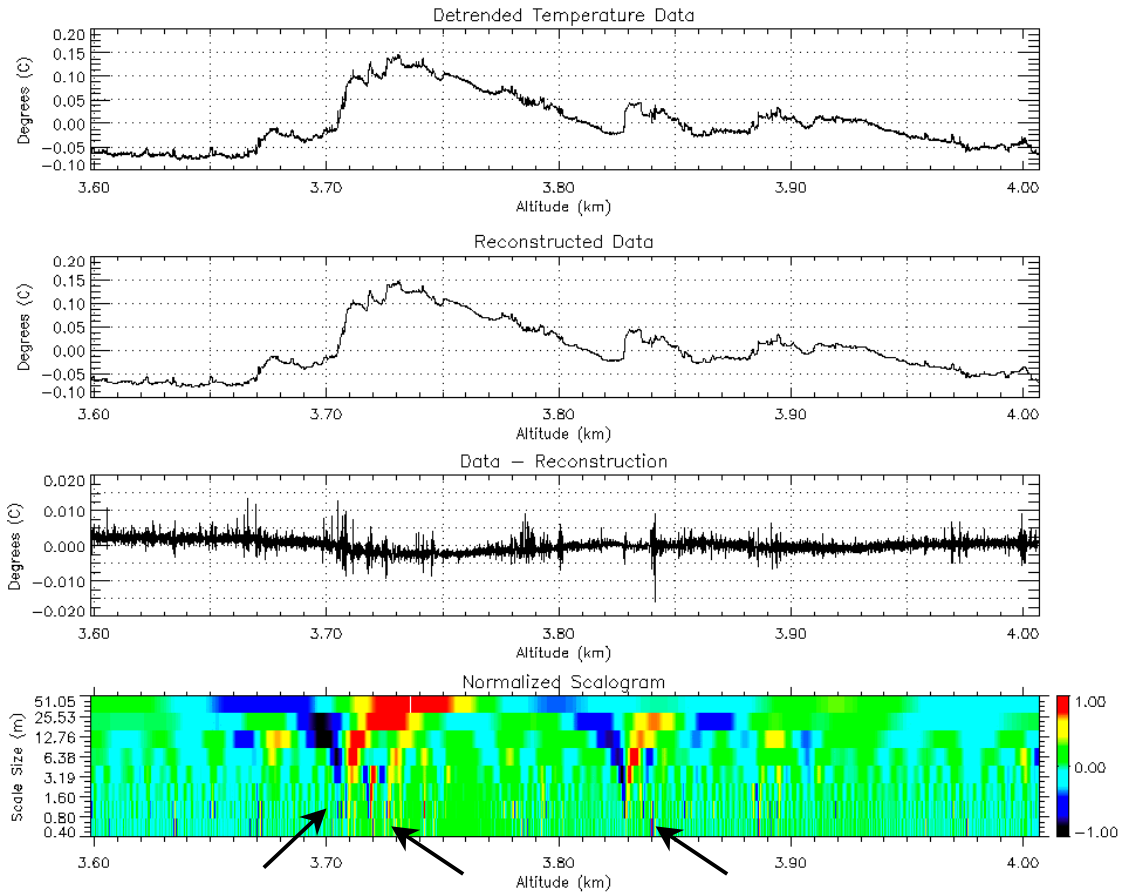

Figure 3.9: Result of our wavelet analysis performed on a piece of data from the troposphere. Our wavelet analysis involves not only wavelet transforming the dataset and computing a scalogram, but also the wavelet-based edge-tracking algorithm, which isolates the coherent structures in the data from noise and/or turbulence. We show the detrended original data on the top panel and the reconstructed data on the second panel. The residual signal, i.e., the difference between the original data and the reconstituted data, is on the third panel. We plot the scalogram of the data on the fourth panel. The magnitude of the wavelet coefficient has been normalized to unity while preserving the sign. Arrows indicate the scalogram structure of a temperature gradient, which is a coherent structure.

where $\psi^{*}_{\lambda,x}(u)$ is the complex conjugate of $\psi_{\lambda,x}(u)$. $Wf(\lambda, x)$ is the wavelet coefficient at scale λ and location x. As we increase the scale λ, we dilate the wavelet so that the wavelet focuses in on the long-term behavior of $f(t)$ and vice versa [e.g., *Torrence and Compo*, 1998; *Antoine*, 1999]. This property allows us to study the structures of the signal across the different scales.

To demonstrate the ability of the wavelet transform, we wavelet transform a section of the temperature data and show the result in Figure 3.9. The bottom panel of the figure shows the normalized wavelet scalogram of a detrended temperature dataset for the altitudes 3.6 km < z < 4.0 km. The normalized scalogram, i.e., the normalized wavelet coefficient at each λ, shows us the partitioning of energy of the signal between the various scale sizes. It allows us to track visually features in the data from large to small scales. The scalogram also preserves the sign of the amplitude because of the asymmetry of the wavelet. By comparing the scalogram with the original data, positive wavelet coefficients, denoted by red, describe a negative gradient in the density profile.

We can identify several different types of features in the temperature data from the scalogram. The main feature is the strong gradient just above 3.7 km seen prominently in the top panel of Figure 3.9. The strong upward gradient, or edge, is part of a saw-tooth shaped anisotropic temperature structure. The gradient contains structures in the large scale on the order of tens of meters down to scales comparable to the VHF Bragg wavelength as revealed in the normalized scalogram. These strong features are well defined, i.e., coherent, over multiple scale sizes. Only large-scale structures are detected from the downward-sloped portion of the temperature structure. We suspect that the small-scale components contained in these coherent structures are responsible for the Fresnel reflection component of the radar backscatter. The application of this result on radar backscatter and aspect sensitivity will be explained in a future section. In addition, numerous weaker structures exist between the stronger features, particularly at small-scale sizes. They typically only have structures at scales smaller than a few meters. They also tend to be homogeneously distributed throughout the data, suggesting the presence of a non-local phenomenon such as instrument noise or atmospheric turbulence. We discuss the reconstructed data, as plotted in the second panel, in a future section.

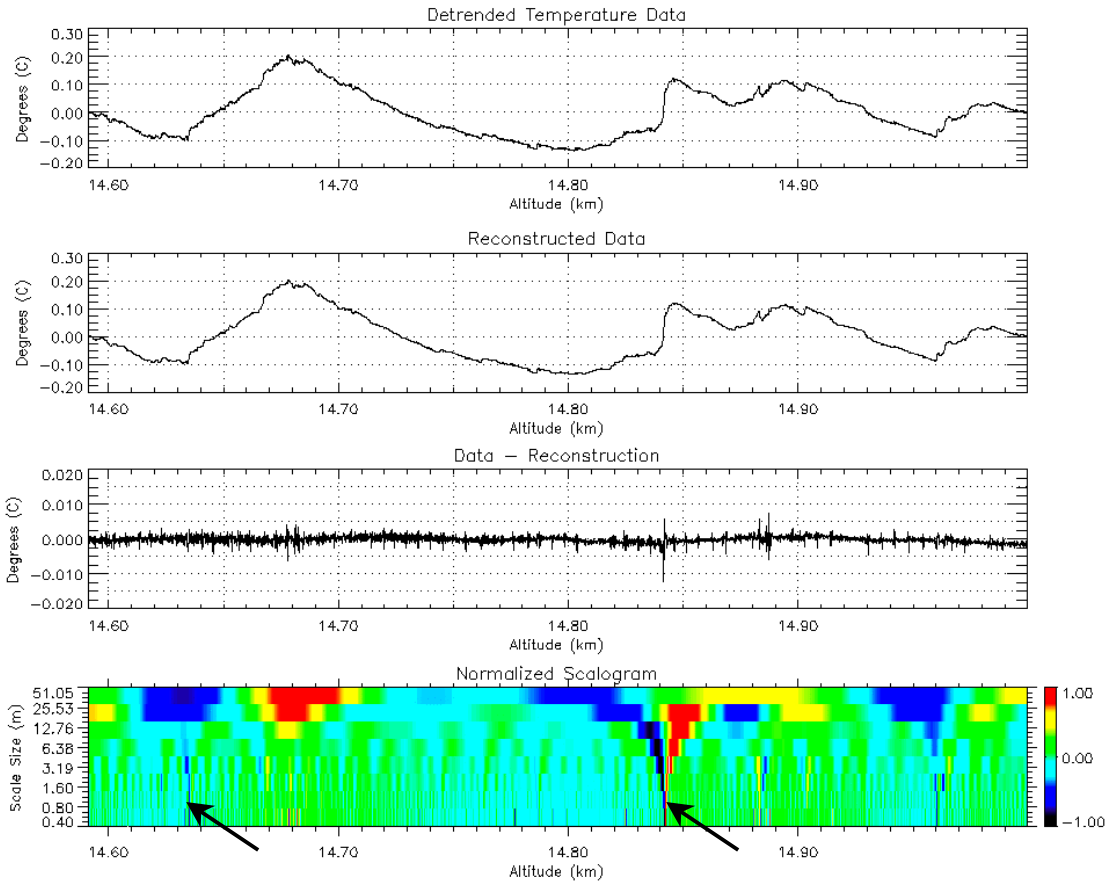

Figure 3.10: Our wavelet analysis performed on a sample stratospheric component of the data. The format follows Figure 3.9. Arrows indicate the scalogram structure of a temperature gradient, which is a coherent structure.

Figure 3.10 contains the result of the wavelet analysis as it is applied on a stratospheric portion of the temperature data. The results are similar to that seen in Figure 3.9. Specifically, the data contains a fuzz background, as indicated by the residual signal seen in the third panel of Figure 3.10. Both this and the coherent features contain structures at the Bragg scale for a radar; for 50 MHz, the Bragg scale = $\lambda/2$ = 3 m.

3.3.3 Edge Tracking

We want to extract information about the edges and turbulence in the data. We assume that turbulence and localized edges together make up the signal. Specifically,

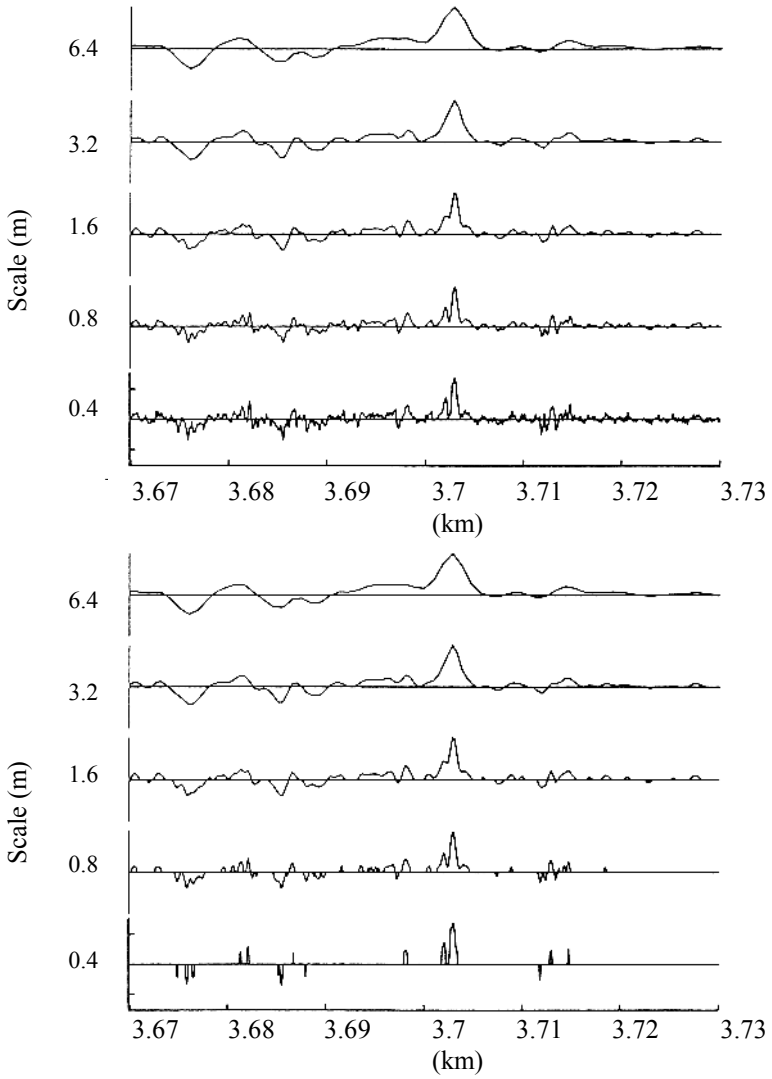

Figure 3.11: Wavelet coefficients computed for the five smallest scales both before (top panel) and after (bottom panel) use of edge tracking algorithm of the temperature gradient near 3.7 km in Figure 3.9.

edges are the localized features while the fluctuations caused by both turbulence and noise have homogeneous properties over the range of the data considered because of the statistical nature of these processes. If we can isolate the edges in the data, we will be able to extract information about the noise and/or turbulence. Furthermore, this paves the way of radar backscatter prediction. Therefore, we need to derive a method to partition the signal based on the properties of these three processes. This idea of edge tracking, originally proposed by *Witkin* [1983], has been refined by *Mallat and*

Hwang [1992] for removing noise-like interference from the signal. Our edge detection methodology follows that in *Mallat and Hwang* [1992] and *Alcala* [1998]. The temperature gradient at 3.7 km is a clear example of an edge component. In contrast, turbulent mixing is a statistical process where different eddies appear and disappear randomly over some volume. Turbulence has homogeneous properties over the range of the data considered. We extract the information about the edges and turbulence/noise in the data by isolating the edge components in the signal relying on the fact that edge components are coherent structures with localized structures persisting over multiple scale sizes.

In other words, we can isolate the edges by requiring that the wavelet coefficients must track down from the larger scales to smaller scales, with twice the sampling period (or the height resolution for our application) as the limit. We demonstrate this in Figure 3.11. As we descend to smaller scales in the lower panel, we can see how these peaks are retained by the analysis. Our partitioning method, referred to from now as the edge-tracking technique, relies heavily on this fact. Using this method, we will be able to separate the coherent component of the dataset from the turbulence/noise component. After selecting the wavelet coefficients corresponding to the edges within the data using our partitioning technique, we then use them to reconstruct the density profile for this component. This method of signal processing forms the basis for several data compression and noise suppression algorithms [e.g., *Mallat and Zhong*, 1992; *Saito*, 1994; *Antoine*, 1999]. In addition, *Hagelberg and Gamage* [1994] use a similar technique to detect coherent structures in velocity and temperature measurements in the atmospheric boundary layer during turbulent events. *Alcala et al.* [2001] and *Alcala and Kelley* [2001] use this technique to remove the instrument noise from an *in situ* electron density measurement during a PMSE event.

As an example, we apply this edge-tracking algorithm, based on the principles described above and *Alcala et al.* [2001], to the tropospheric section of data. We

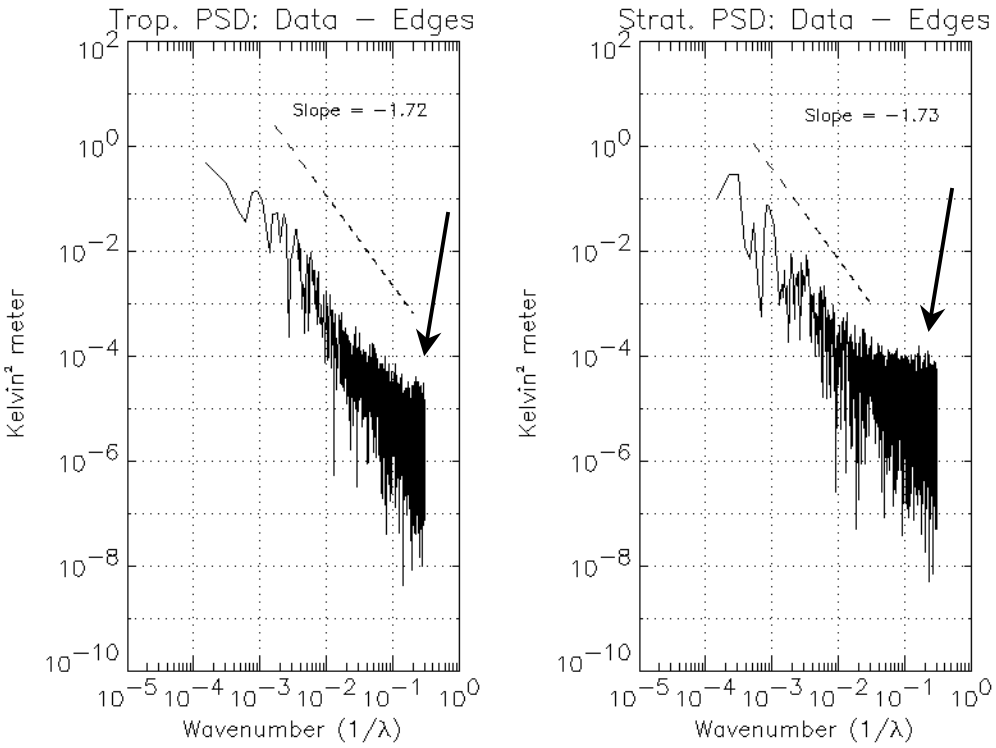

Figure 3.12: Fourier power spectra of the tropospheric and stratospheric components of the residual signal removed from the original data by the way of the edge-tracking algorithm. Both power spectra behave according to the –5/3-power law of the Kolmogorov's isotropic turbulence theory. Arrows indicate the noise floor.

examine the result in Figure 3.9. We plot the original data on the top panel and the reconstructed data via the wavelet coefficients of the edge components of the data in the second panel. This is the coherent portion of the data. We obtain the contribution of the turbulence and noise by subtracting the reconstructed data from the original data. As the figure illustrates, the edge-tracking algorithm is able to remove all but the fuzz-like component from the data; we call this the residual component of the data. We suspect that turbulence is the cause for this signal. We show later that indeed this seems to be the case and support this claim via a turbulence parameter calculation which we will discuss in a future section. This result again supports the claim of a turbulent atmosphere. Figure 3.10 shows the result of the edge-tracking algorithm

applied on a stratosphere portion of the data. Again, the result is similar to that seen in Figure 3.9.

Satisfied with the wavelet analysis results thus far, we proceed to apply the edge-tracking algorithm to the entire tropospheric and the stratospheric segments of the data and plot the PSD of the turbulence residuals from the two segments in Figure 3.12. Both spectra follow a power law near the –5/3 power law predicted by Kolmogorov's theory for isotropic turbulence. This confirms that the residual signal seen in Figures 3.9 and 3.10 is indeed caused by turbulence. This result is evidence for a background turbulent atmosphere. Further evidence for the existence of a turbulent component is provided below where we compare C_n^2 calculated from the Fourier power spectral density of the turbulence residual and higher order structure functions. It is interesting to see a noise floor appearing in the power spectral density at a level of 10^{-5} K^2/m^{-1} at inverse scales as low as 0.01 m^{-1}. This noise floor was not visible in the original signal until nearly 10 m^{-1}.

3.4 Turbulence Measurement

The refractive index structure function coefficient (C_n^2) is a parameter indicating the intensity of atmospheric turbulence; the higher the value, the more intense the turbulence. Over the past two decades, balloon-borne microthermal probes have measured atmospheric C_n^2 values. Typical *in situ* measurement method involves launching meteorological balloons ascending from ground level up to approximately 25-30 km [e.g., *Bufton et al.*, 1972; *Coulman et al.*, 1995; *Walters*, 1995]. One computes C_n^2 from the temperature differences measured by fluctuations in the resistance of two fine-wire platinum or tungsten probes separated horizontally by exactly one meter. This technique follows that described by *Bufton et al.* [1972], *Coulman et al.* [1988, 1995], *Brown et al.* [1989], *Walters* [1995], and *Hocking and Mu* [1997].

The theoretical basis of such a measurement originates from the Kolmogorov structure function. An *n*th order structure function is defined as the mean of the *n*th power of the difference of the values of a variable at a distance *r* apart [e.g., *Panofsky*, 1968]. More specifically, the conventional structure function D_X^n is of the form

$$D_X^n(\boldsymbol{r}_1, \boldsymbol{r}_2) = \langle [X(\boldsymbol{r}_1) - X(\boldsymbol{r}_2)]^n \rangle, \tag{3.7}$$

where X is an atmospheric scalar parameter such as the temperature or index of refraction, $\boldsymbol{r}_1$ and $\boldsymbol{r}_2$ are position vectors of two points in space, and $\langle\rangle$ implies an ensemble average.

For isotropic, homogeneous turbulence in the inertial subrange, *Obukhov* [1949] and *Hall* [1981] showed that, via dimensional analysis, (3.7) simplifies to

$$D_X^n(|\boldsymbol{r}_2 - \boldsymbol{r}_1|) = C_X^n r^m, \tag{3.8}$$

where

$$r = |\boldsymbol{r}_2 - \boldsymbol{r}_1| \tag{3.9}$$

and $0 < m \leq 2$. The structure parameter coefficient C_X^n is a proportionality constant. The second order ($n = 2$) Kolmogorov structure function has been used for turbulence study. Over sufficiently small regions, on the order of millimeters to meters in size, for which the turbulence is locally homogeneous and isotropic, the atmosphere can have such a Kolmogorov structure function dependence with $m = 2/3$. Appendix A presents a detailed discussion connecting the 2/3-power law of the structure function to the -5/3-power law of the Fourier representation of inertial subrange turbulence. The turbulence sensor examines the temperature, a scalar parameter, via $D_T(r)$ by measuring the root-mean-square (RMS) temperature difference between two thermometers horizontally separated by 1 m; in other words, $r = 1$. This is chosen for mathematical convenience, as scales between 1 m and 10 m are within the inertial subrange for z < 40 km [*Hocking*, 1985]. Within these constraints, a passive additive such as the atmospheric temperature has a structure function parameter becomes [*Tatarski*, 1961; *Doviak and Zrnic*, 1984]

$$C_T^2 = \frac{\left\langle [T(\mathrm{r}_2) - T(\mathrm{r}_1)]^2 \right\rangle}{r^{2/3}}. \tag{3.10}$$

We relate C_T^2 to C_n^2, the refractive index structure function parameter via the pressure and temperature measurement with the standard formula [e.g., *Coulman et al.*, 1995]

$$C_n^2 = \left(7.9 \times 10^{-5} \frac{P}{T^2} \Gamma \right)^2 C_T^2 \ [\mathrm{m}^{-2/3}], \tag{3.11}$$

where pressure (P) is measured in millibars and temperature (T) is in Kelvins [e.g., *Walters and Kunkel*, 1981; *Coulman et al.*, 1988, 1995; *Hocking and Mu*, 1997]. Humidity affects the relationship between C_T^2 and C_n^2 via Γ, which is unity for dry air. In this *in situ* measurement, humidity was not measured. Hence, we will assume that humidity is negligible (< 1%) and we take $\Gamma = 1$. The numerical coefficient 7.9×10^{-5} comes from the expression of the refractive index of air which slowly varies over the infrared (IR) through the ultraviolet (UV). The numerical values range from 8.29×10^{-5} in the UV (0.3 μm) to 7.75×10^{-5} in the IR at 10 μms. In the middle of the visible at 0.5 μms, the value is 7.9×10^{-5} which is what is commonly used [*Beland*, private communications].

In short, an *in situ* instrument, composed of two temperature probes separated by 1 m, is able to measure C_T^2 directly from the atmosphere. In the Wichita experiment, we used a different turbulence probe. With (3.11), we can convert C_T^2 to C_n^2, where the latter is the relevant parameter in the radar community as one can use it to compute the isotropic turbulence backscatter from the atmosphere.

There are other ways to compute C_n^2, both directly and indirectly, from atmospheric temperature measurements. Using two temperature probes to measure C_T^2 is expensive. As we will show later, one can compute C_T^2, and hence C_n^2, from a high order structure function, as defined by a higher order difference based on a one-dimensional vertical temperature measurement. This is a more esoteric method that has been verified experimentally by *Walters* [1995]. One can also compute C_T^2, and

hence C_n^2, from the Fourier spectrum of a turbulence-affected passive scalar, e.g., potential temperature. In other words, in this second method, we calculate C_n^2 from the Fourier power spectral density of a one-dimensional potential temperature measurement. In the past, this has been inaccurate as it was impossible to isolate the turbulent component of an atmospheric temperature sounding while the coherent portion of the data would over-estimate C_T^2, and hence C_n^2. We will show that we can avoid this as the edge-tracking algorithm can isolate the turbulent component of the temperature dataset. The relationship between C_n^2 and the Fourier spectrum of a turbulent scalar parameter was developed in the late 1960s [e.g., *Ottersten*, 1969a, b]; using wavelet analysis as part of this process is new.

We have two motivations for calculating C_n^2 via these two alternate methods. By comparing the two results, we verify the ability of the edge-tracking algorithm to parse the data into the edge, i.e., coherent, and turbulent components. In addition, as we will illustrate in a future chapter, from a radar application stand point, we will use C_n^2 to calculate a theoretical turbulence backscatter that a radar may experience given the atmospheric condition as specified by this temperature sounding and relate this prediction to radar observations of aspect sensitivity. Comparing this predicted backscatter to the measured radar backscatter will help us assess the role turbulence plays in the cause of aspect sensitivity.

3.4.1 Calculating C_T^2 Using Higher Order Structure Function

As was briefly discussed in the introductory paragraphs to section 3.4, the common approach of direct measurement of C_T^2 based on (3.10) is to use two temperature probes positioned horizontally one-meter apart. C_T^2 is square of the root mean square (RMS) average of the difference between these two probes which are typically attached to a radiosonde so that C_T^2 will be measured in conjunction with atmospheric thermodynamic parameters. In other words, we construct a C_T^2 profile from two

vertical temperature profiles, separated horizontally by 1 m. As this balloon-borne instrument is not recoverable, this is an expensive method, particularly when the cost of such turbulence sensor is ~$1000 [*Beland*, private communications]. We would reduce the expense if only one probe were used to measure C_T^2.

Would it not be easier to take one vertical temperature profile and compute C_T^2 based on (3.10) from the square of the difference of two temperature samples, separated by 1 m in the vertical direction? However, this method violates the isotropic turbulence assumption. Examining the temperature difference of a vertical temperature profile subtly introduces into the calculation contributions from the large-scale structures, such as the saw-tooth structures seen in Figures 3.1 and 3.4, which would overestimate the actual C_T^2. A similar phenomenon is also seen in the Fourier analysis of our temperature dataset before and after the application of the edge-tracking algorithm. An examination of Figures 3.7 and 3.12 indicates that the Fourier spectrum is dominated by the saw-tooth structures in the temperature data; the saw-tooth structures overshadow the contribution from turbulence to the Fourier power spectral density.

The contamination of C_T^2 by large-scale structures is avoided when one implements the measurement using two temperature probes, separated horizontally by 1 m. This is commonly done in current atmospheric turbulence measurements [e.g., *Balsley et al.*, 1994; *Hocking and Mu*, 1997]. However, there are other ways to measure C_T^2 using one vertical temperature profile originating from one probe. One way is to use temperature data with very high vertical resolution so that we can ignore the higher order trends. Another approach is to use some form of moving average or other trend removal techniques. Both of these alternatives are arbitrary, and they are difficult to achieve in practice. We examine two other alternatives.

Yaglom [1987] introduced a generalized structure function for a *p*th-order stationary random process that incorporate *p*th-order differences. According to

Yaglom, a *p*th order difference removes the inherently lower $p - 1$ polynomial components of the data. Rather than resorting to arbitrary, trend-removal techniques, the higher-order structure function removes trends, which is, in our case, temperature steps, in a robust manner. The combination of a single probe with the *p*th order difference provides results that are equivalent to those collected with conventional, horizontal differential temperature probes [*Walters*, 1995]. We want to compute C_T^2, and hence C_n^2, from the one-dimensional, high-resolution temperature profile (right panel, Figure 3.1) via the *p*th-order difference approach. In a later section, we will show that C_T^2 can be computed from the residual signal extracted from the measured temperature from via the wavelet-based edge-tracking algorithm. The *p*th-order difference approach is perhaps an easier approach, as the calculations involved in this can be easily implemented.

A *p*th order, self-similar, stationary random process $X(r)$ has a *p*th order difference expressed as

$$\Delta_r^p X(\rho) = \sum_{k=0}^{p} (-1)^k \binom{p}{k} X(\rho - kr). \tag{3.12}$$

Following *Yaglom* [1987] and *Walters* [1995], the mean square of (3.12) gives the *p*th order structure function

$$\left\langle \left| \Delta_r^p X(\rho) \right|^2 \right\rangle = D^{(p)}(r). \tag{3.13}$$

$D^{(p)}(r)$ is an *p*th order structure function having the form

$$D^{(p)}(r) = C^{(p)} |r|^m, \tag{3.14}$$

where r is as defined in (3.9) and $C^{(p)}$ is the *p*th-order structure parameter. Equation (3.14) is analogous to the conventional Kolmogorov structure function, as defined by (3.8) and (3.10).

When (3.12) is applied to a one-dimensional temperature profile, *Walters* [1995] shows that one can relate $C^{(p)}$ to C_T^2 by

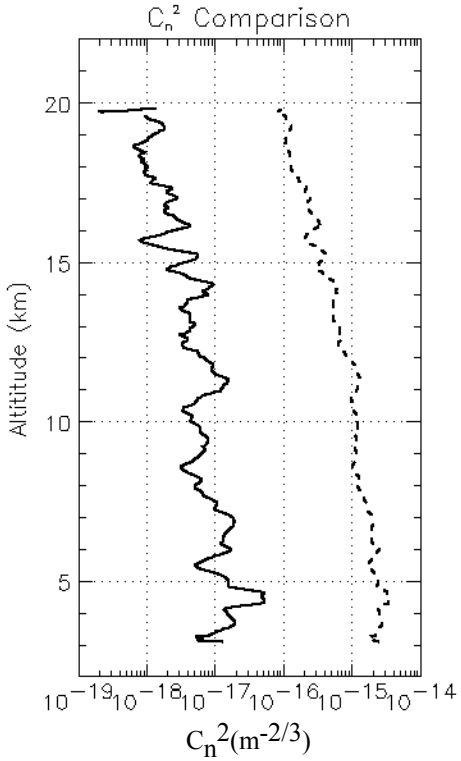

Figure 3.13: C_n^2 computed from a one-dimensional vertical temperature profile. *Dashed line*: C_n^2 calculated from the second order structure function of a vertical temperature profile. *Solid line*: C_n^2 from the second order temperature difference via (3.12) and (3.15).

$$C^{(p)} = C_T^2 \sum_{j=0}^{p-1} \binom{2p}{j} (-1)^{p+1} (p-j)^m . \tag{3.15}$$

The structure parameter ($C^{(p)}$) for the first order difference is equal to C_T^2 while for higher order differences, $C^{(p)}$ is directly proportional to C_T^2. In other words, for atmospheric vertical temperature data, we can use (3.12) to remove the large scale, inhomogeneous components of the temperature data and then compute C_T^2 via (3.15). Finally, we use (3.11) to compute C_n^2. The resolution of the computed C_n^2 will be comparable to the height resolution of the temperature measurement.

The solid line that appears in Figure 3.13 is C_n^2 computed using the 2nd order difference, i.e., p = 2. This calculation is carried out over the entire dataset while setting r = 1; we average the result over 5 m before plotting. As a check of the effectiveness of the way contributions from large scale structures are removed from

the 2nd order difference, we compute C_n^2 via the square of the difference of two temperature samples, separated by 1 m in the vertical direction. This result, plotted as the dashed line in Figure 3.13, overestimates the real C_n^2 (solid line) by two orders of magnitude. For completeness, we examine C_n^2 computed via higher order difference ($p > 2$); the result is indistinguishable from the result computed from the second order vertical temperature difference ($p = 2$). This again testifies to the way the higher order structure function isolated the edge component of the temperature data. Based on the published experimentally measured values of C_n^2, [e.g., *Coulman et al.*, 1988, 1995; *Hocking and Mu*, 1997], the typical values of C_n^2 range from a lower limit of $\sim 10^{-19}$ $m^{-2/3}$ to an upper limit of $\sim 10^{-14}$ $m^{-2/3}$. The C_n^2 values calculated here are near the lower bound. This does not surprise us, as the lapse rate in the troposphere and stratosphere indicates stability.

3.4.2 Calculation of C_n^2 via the Fourier Power Spectrum

For isotropic turbulence in the inertial subrange, we can relate C_n^2 to the one-dimensional spectrum of the passive scalar via

$$S_n(k) \approx \frac{1}{4} C_n^2 k^{-5/3}, \tag{3.16}$$

where S_n is the one-dimensional Fourier spectrum of the refractive index as measured by a sensor moving through the medium and k is the radian wave number corresponding to the spatial wavelength $k = 2\pi\lambda^{-1}$ [*Ottersten*, 1968]. It is insightful to understand the steps that led to (3.16). We present two different derivations of (3.16) in the turbulence primer that appears in Appendix A of this thesis.

Recall that we used the wavelet-based edge-tracking algorithm to isolate the coherent portion of the temperature, and subtracting this from the original data yielded a fuzz-like component, i.e., the residual data. Since Fourier analysis indicates the residual data as isotropic turbulence, we can compute C_n^2 from the power spectral

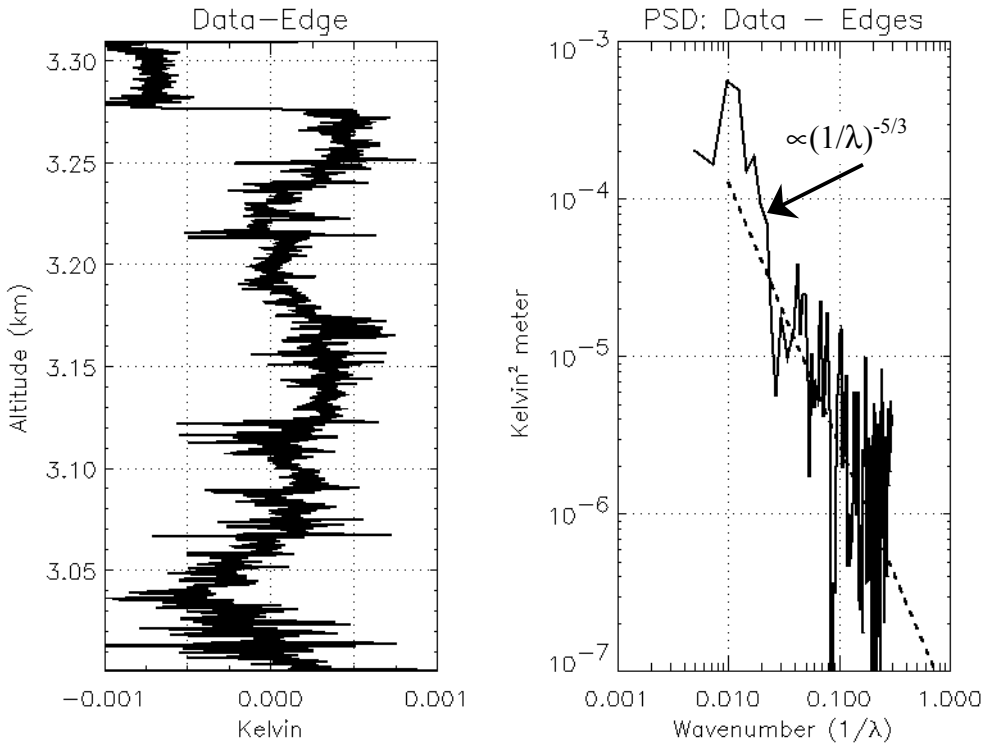

Figure 3.14: An illustration of how we compute C_n^2 from the power spectrum of the residual signal. *Left panel*: A sample of the residual signal. *Right panel*: Fourier power spectrum of the residual signal. Dashed line follows a -5/3-power law.

density of the residual data via (3.16). Comparing this C_n^2 with its counterpart computed via the higher order structure function will validate the residual to be isotropic turbulence.

We compute a C_n^2 profile from the one-dimensional profile of the residual data by first parsing the data into segments 300 m in length. This in essence allows us to compute a value of C_n^2 via (3.16) every 300 m, a height resolution comparable to a typical VHF radar. We then calculate the Fourier spectrum, i.e., $S_n(k)$, of this data segment, least square fit a –5/3 power law to the spectrum, and evaluate the fit at $k = 2\pi/\lambda$, where $\lambda = 50$ m which is in the inertial subrange for this altitude range and is such that $S_n(k)$ is well above the noise level [*Hocking*, 1985]. We show an example of this in Figure 3.14. The dashed-line follows a -5/3-power law.

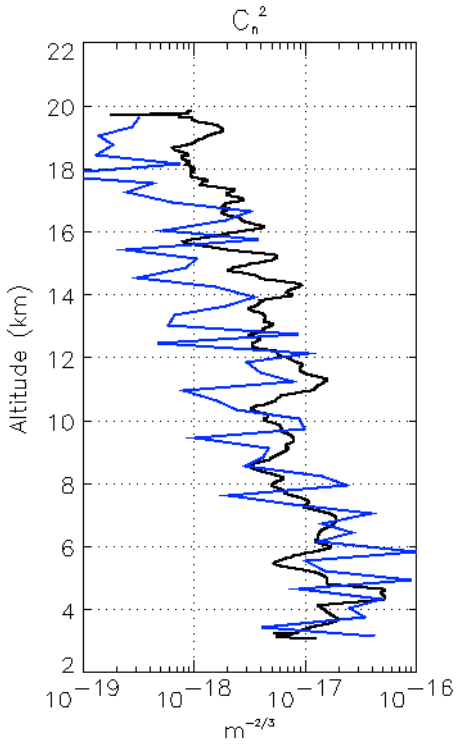

Figure 3.15: C_n^2 calculated from two different approaches. Black line: C_n^2 calculated from the higher order temperature difference. Blue line: C_n^2 determined from the Fourier spectrum of the residual signal. Two results agree very well, particularly in the tropospheric region of the atmosphere.

C_n^2 computed from the turbulence spectrum is plotted in Figure 3.15 as the blue line. We have reproduced the result of C_n^2 computed from the higher order difference. The two profiles have fairly good agreement in the troposphere. In the stratosphere, C_n^2 derived from our residual data is lower than the one given by Walters' method. Nevertheless, this is another indication of the effectiveness of the edge-tracking algorithm. Furthermore, as the PSD of the residual signal in Figure 3.12 is about four orders of magnitude smaller than the original PSD in Figure 3.7, we realize that had we used the original PSD in (3.16) to computed C_n^2, we would have over-estimated C_n^2 by about four orders of magnitude.

3.5 Anisotropic Temperature Structures

We turn our attention back to the anisotropic structures observed in Figure 3.1. These seemingly organized temperature structures are observed as a slow, nearly linear increase of temperature with height, followed by an abrupt sharp decrease in temperature to the ambient level before the relative slow increase begins. Temperature fluctuations, which exhibit a characteristic structure (often termed ramps, triangular, or saw-tooth patterns after their obvious geometrical signatures), have been observed in atmospheric turbulent shear flows, the ramps being effectively the signature of the large-scale structures of the flow [e.g., *Taylor*, 1958; *Antonia and Atkinson*, 1976; *Antonia et al.*, 1977; *Van Atta*, 1977]. The distinctive saw-tooth feature is a result of large temperature jumps across sharp shear zones at the outer boundary of large scale eddies. They also indicate that one important consequence of the ramp characteristic is the possible resulting anisotropy of small-scale scalar fluctuations [*Antonia et al.*, 1977]. *Kaimal and Businger* [1970] identified the ramp structure in the atmospheric boundary layer with individual convecting thermal plumes being sheared by the mean velocity gradient. On the other hand, the atmospheric temperature ramps may be interpreted as the signature of an organized large-scale motion rather than a necessary consequence of the presence of buoyant plumes [*Antonia et al.*, 1977]. In a boundary layer over a heated surface, the ramp structure has the form of a relatively slow increase in temperature followed by an abrupt decrease back to the level of the external stream. Regardless of where these triangular temperature structures occur or what causes them, they are important in the propagation of optical and electrical-magnetic radiation through the atmosphere. The temperature ramps, as it will scatter electromagnetic radiation, will account for a significant fraction of signal degradation [*Antonia et al.*, 1977].

Temperature signals with such a ramp signature were first reported for the atmospheric boundary layer by *Taylor* [1958]. He described the structures (for un-

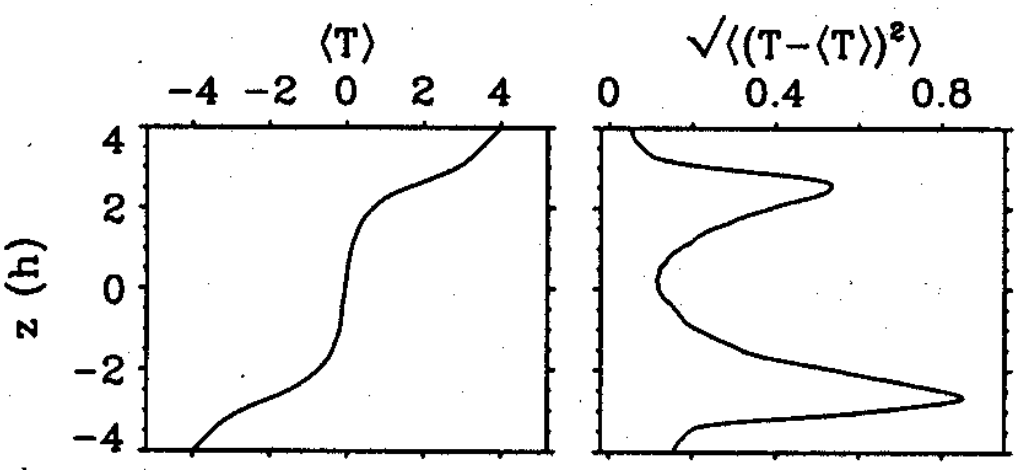

Figure 3.16: Mean and RMS vertical temperature profile computed from a simulated Kelvin-Helmholtz billow [after *Werne and Fritts*, 1999].

stable buoyancy conditions) as "asymmetrical triangular waves of temperature [gradual rise (with time) followed by a sudden drop] which frequently attain several degrees Celsius in magnitude with duration mostly about 10-20 seconds." *Kaimal and Businger* [1970] identified the ramp structure in the atmospheric boundary layer and *Frisch and Businger* [1973] inferred the statistical distribution of the plume geometry from atmospheric temperature signals. *Bean et al.* [1972] observed similar structures over the ocean.

Such anisotropic ramp structures have been reported earlier in the stratosphere and troposphere based on balloon-borne *in situ* measurements [*Barat*, 1982; *Barat and Bertin*, 1984; *Dauladier et al.*, 1994]. In this context, the terms *layers* and *sheets* have been used to describe the temperature structure. *Bertin et al.* [1997] studied stratosphere sheet structures with high-resolution temperature probes and made wind shear measurements and showed that a low gradient Richardson number (*Ri*) indeed occurs in the regions of small negative potential temperature gradients, as we conjecture above.

We believe that the sharp temperature gradients of the ramp structures, which occur at the edges of well-mixed turbulent layers as indicated by the potential temperature steps, contribute to VHF radar backscatter, and perhaps result in aspect sensitivity. Furthermore, there is a close resemblance between the measured temperature steps with the vertical profile of a late-term Kelvin-Helmholtz instability (KHI). As we saw in Chapter 2, during the end of the KHI evolution, the instability evolves into a well-mixed adiabatic layer marked by sharp boundaries. We show in Figure 3.16 the vertical temperature and variance (which is comparable to C_T^2) profile of a late term KHI, as simulated by *Werne and Fritts* [1999]. The comparison between the simulation in Figure 3.16 and the experimental data in Figures 3.1 and 3.4 is remarkable and is discussed in more detail below.

3.6 Conclusion

This chapter is the first step in our journey towards a better understanding of the mechanisms that case aspect sensitivity. We present a high-resolution temperature sounding that took place on 5 March 1995 at Wichita, KS that revealed anisotropic, triangular temperature structures. Understanding these temperature structures, we believe, will move us a step closer to solving the puzzle of the cause(s) of aspect sensitivity.

Wavelet transform is a promising tool for the study of anisotropic coherent structures in the atmosphere. In this chapter, we presented a wavelet-based edge-tracking algorithm which successfully extracted the coherent structures from an *in situ* temperature measurement. In addition, once the coherent structures are removed, the residual signal, via Fourier analysis, well represents the turbulent component of the atmospheric structure as a –5/3 power law is revealed. This is a good indication that the atmosphere is composed of coherent structures and background turbulence. C_n^2 computed from the Fourier PSD of the residual signal compares well with the C_n^2

computed from the higher order difference. We will revisit this result, as C_n^2 computed from the *in situ* temperature measurements will help us assess the role of turbulence in the cause of aspect-sensitive echoes.

We believe that the steep temperature gradients (>10 K/km) that occur at the edges of the potential temperature steps are responsible for strong radar backscatter in the vertical direction. Our suspicion is verified by the wavelet analysis of the temperature structure. In addition, the strong temperature gradients contain structures at scales comparable to the Bragg scale length where the most efficient radar backscatter occurs.

The observed potential temperature steps mimic the structures created in a dynamic instability known as the Kelvin-Helmholtz instability (KHI). A comparison between our observations and the structures created by a computer simulation confirms our suspicion. This is fortunate, as the computer simulation will confirm our interpretation of the observed temperature structure. This topic deserves a close examination; we do this in Chapter 7.

In the next few chapters, we will incorporate what we have learned about the potential temperature steps and apply it to the results of an aspect sensitivity experiment that took place in Peru where both a VHF radar and balloon-borne probes were used to probe the atmosphere. We are particularly interested in the similarities and differences in the temperature structures measured at Peru and Wichita. It is also our goal to compare the measured radar backscatter with the prediction computed from the *in situ* temperature measurements based on the properties of the wavelet transform. We will also examine in detail the similarities between the measured temperature structures and the structures created by a KHI.

Chapter 4

Observations of Aspect Sensitivity at the Jicamarca Radio Observatory

We established in previous chapters that the atmosphere is aspect-sensitive. This trait is common to most regions of the atmosphere, from the troposphere to the mesosphere, and is observed by radars operating through the HF, MF, and VHF bands [e.g., *Röttger and Vincent*, 1978; *Hocking*, 1989; *Lesicar and Hocking*, 1992]. There is a great deal of debate as to the origin and shape of the structure(s) that partially reflects signals from near-vertically pointing radars. The fundamental question that we wish to address is this: what is the cause of the aspect-sensitive echoes? Advances in the understanding of the scattering mechanisms, we feel, may come from a combination of *in situ* and remote-sensing techniques, especially those made simultaneously during joint campaigns. In one joint campaign called MIST (Multi-Instrument Stratosphere Troposphere) involving the Air Force Research Laboratory (AFRL), Cornell University, and the Instituto Geofísico del Perú (IGP) and carried out at the Jicamarca Radio Observatory (JRO) during 7-14 September 1998, we probed

the lower atmosphere with radiosondes and turbulence sensors carried aloft via balloons and with a powerful 50 MHz VHF radar.

This is the first of three chapters that are devoted to the presentation of the MIST campaign dataset and analysis results. The two specific goals of this chapter are: 1) to familiarize the reader with the instruments deployed during the MIST campaign and 2) to present some representative radar and *in situ* measurements of the atmosphere. This paves the way to our discussion in the following two chapters. In Chapter 5, we will analyze the radar data in concert with the *in situ* temperature and turbulence measurements in the hopes of determining the characteristics of the radar scattering mechanisms. This is followed by a discussion of radar and *in situ* measurements of atmospheric turbulence intensity in Chapter 6.

We organize the discussion as follows. We first introduce to the reader the goal of the MIST campaign. This is followed by a detailed discussion of the configuration of the Jicamarca VHF radar and the balloon-borne *in situ* instruments. A section is devoted to the representative radar and *in situ* data taken during the MIST campaign. We draw the reader's attention to the aspect-sensitive radar backscatter and the associated *in situ* measured temperature structures. This chapter ends with a presentation of some unique observations where additional atmospheric dynamics are revealed.

4.1 Campaign Description

The MIST campaign was conducted at the Jicamarca 50 MHz VHF radar site (11.95ºS, 76.87ºW) near Lima, Peru, on 7-14 September 1998. The main goal of the experiment is to investigate the cause of the radar backscatter through direct measurement and remote sensing of the atmosphere. The Air Force Research Laboratory (AFRL), Cornell University, and Instituto Geofísico del Perú (IGP) participated in the MIST campaign. The VHF radar provided continuous coverage of

the lower atmosphere from dusk to near midnight daily. On average, two balloons carrying a thermosonde system, i.e., a radiosonde mated with a turbulence sensor, were launched each night to provide *in situ* measurements of atmospheric thermodynamic parameters and atmospheric turbulence intensity.

4.1.1 Radar System

The Jicamarca VHF radar operates at ~50 MHz and is a 288 m by 288 m array antenna. The array is composed of 64 modules; each module consists of a 12 by 12 array of cross-polarized half wave dipoles. During the course of the campaign, three separate radar experiments were performed, two of which involved multi-beam emissions from the radar while the other used only the vertical beam. Table 4.1 summarizes this information. We comment on the quality of the data and the transmitted power in Table 4.2. For the multi-beam experiments, e.g., Experiments 01 and 03, the radar was programmed to emit three beams: one pointing nearly vertically, one tilted 2.5º off-vertical pointing to the north, and another tilted at the same angle to the west. Figure 4.1 depicts the antenna configuration. The inter-pulse period (IPP), the time interval between transmitted pulses, in Experiment 03 was increased to 625 μs to prevent the signal from the developing Equatorial Spread F (ESF) from contaminating the neutral atmospheric signal. Incoherent integration was implemented to the raw data such that resultant time resolution between each spectrum is 2 minutes. Due to radar recovery problems and radar receiver malfunctions, data taken on 13 September 1988 will be omitted from our discussion.

The vertical beam was generated with the whole antenna in one linear polarization so that the two-way full width of the beam at *1/e* power is ~1º. We generate each oblique beam with two diagonal quarters of the orthogonal polarization. This configuration changes the beam shape from circular to elliptical with a minor axis of ~1º in the direction of the tilting and ~1.5º in the orthogonal direction. This is not

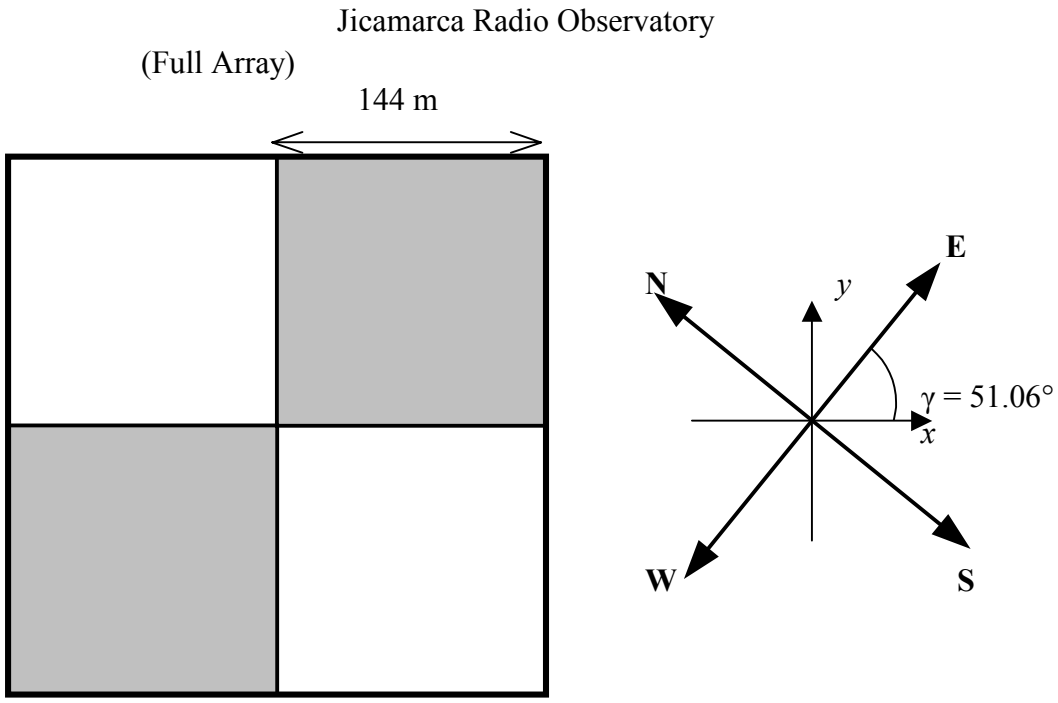

Figure 4.1: Antenna setup for the lower atmosphere experiment at JRO. Notice that neither antenna axis is aligned with the geographical coordinates. The vertical beam was generated with the whole antenna in one linear polarization so that the two-way full width of the beam at half power is ~1º. We generate each oblique beam with two diagonal quarters of the orthogonal polarization. The gray-colored diagonals generated the west beam while the white colored diagonals generated the north beam. This configuration changes the beam shape from circular to elliptical with a minor axis of ~1º in the direction of the tilting and ~1.5º in the orthogonal direction.

Table 4.1: Radar Experiment Information. This table details the characteristics of the three radar experiments carried out at Jicamarca on 7-14 September 1998. Under the column "Beams", WNV means that three beams were emitted: one off-vertical to the west, and one to the north, and one vertical. V implies that only a vertical beam was generated. IPP is the inter-pulse period.

Exp.	Beams	Height res. (m)	IPP (μs)	N. Coh. Int.
01	WNV	300	625	150
02	V	150	625	150
03	WNV	300	2500	30

Table 4.2: Transmitted Power and Data Quality.

Date (Julian Day)	Exp.	Transmitted Power	Observations
09/07/98 (250)	01	100kW, 5% duty cycle	V pointing 0.3º off-vertical (SE).
09/08/98 (251)	01	100kW, 5% duty cycle	V pointing 0.3º off-vertical (SE).
09/09/98 (252)	01	100kW, 5% duty cycle	V pointing vertical.
09/10/98 (253)	02	100kW, 5% duty cycle	
09/11/98 (254)	01	1MW, 5% duty cycle	
09/11/98 (254)	03	1MW, 5% duty cycle	
09/12/98 (255)	02	1MW, 5% duty cycle	
09/13/98 (256)	01	100kW, 5% duty cycle	Only V is good; problems with two receivers.
09/13/98 (256)	03	100kW, 5% duty cycle	Only V is good; problems with two receivers.
09/14/98 (257)	01	100kW, 5% duty cycle	

Table 4.3: Balloon Flight Log.

Date (Julian Day)	Launch Time (LT)
09/07/98 (250)	1830
	2012
09/08/98 (251)	1830
	2005
	2143
09/09/98 (252)	1840
	2016
	2152
09/10/98 (253)	1830
	2007
	2144
09/13/98 (256)	1933
	2177
09/14/98 (257)	1820
	2002

affected by the near-field effect. We will examine this in some detail in Appendix B. Since the neutral atmosphere echoes are polarization independent, there is no cross-talk among the signals and the measurements are independent. The oblique beams are emitted with half of the transmitted power of the vertical beam, i.e., one transmitter module for the vertical beam, the other for both oblique beams.

4.1.2 Balloon-borne Instrumentation

Table 4.3 summarizes the launch time of the balloons during the MIST campaign. The *in situ* instrument package consists of two parts, both of which are mounted below a meteorological balloon. One part is a standard Vaisala, Inc.'s RS-80-15 GPS radiosonde, which makes excellent height-resolution measurements of the standard thermodynamic parameters (pressure, temperature, and humidity) and the horizontal

wind velocity (wind speed and direction). The meteorological data are recorded every 1.4 seconds, which gives about a 7 m height resolution. The resolution of the temperature sensor on the radiosonde is a function of the sensor's time constant which varies with air temperature and density and hence altitude. In the vicinity of 20 km, the time constant is approximately 10 s, i.e., 50 m, and increases with altitude. This affects the accuracies in the pressure sensor used to derive altitude.

The wind data are recorded every 2 seconds, which gives about a 15 m height resolution. Wind is derived from the Doppler shift of the global positioning system (GPS) signal emitted from the GPS beacon on the radiosonde. The GPS system enables precise measurement of the gondola's pendulum motion. Digital filtering is used to remove the complex pendulum motion and extract the atmospheric winds. The data is carried on the 403 MHz telemetry signal of the radiosonde. A meteorological balloon is used to lift the instrument package with an ascent rate of about 5 m/s.

The thermosonde, i.e., the turbulence sensor, measures the root-mean square (RMS) temperature difference between two unheated fine wire tungsten probes (3.5 μm diameter) separated horizontally by one meter. This measurement is based on the second order structure function, a theoretical principle that we discuss in Chapter 3 and Appendix A. These two fast response probes (~10 ms response time) are designed to sense temperature differences as small as 0.005 K. These two probes are essentially two resistors in a Wheatstone bridge driven by a 3 kHz oscillating current of 100 μAmp. The change in probe resistance modulates the 3 kHz carrier. The alternating current (AC) is used to accommodate low signal-to-noise problems. All amplification is performed within the AC portion of the circuit. The signal is then stripped from the carrier using synchronous detection. It is an analogue instrument that performs RMS averaging of the temperature difference. The output of the RMS chip is sampled and transmitted every 1.4 seconds by the radiosonde. The RMS average is computed with

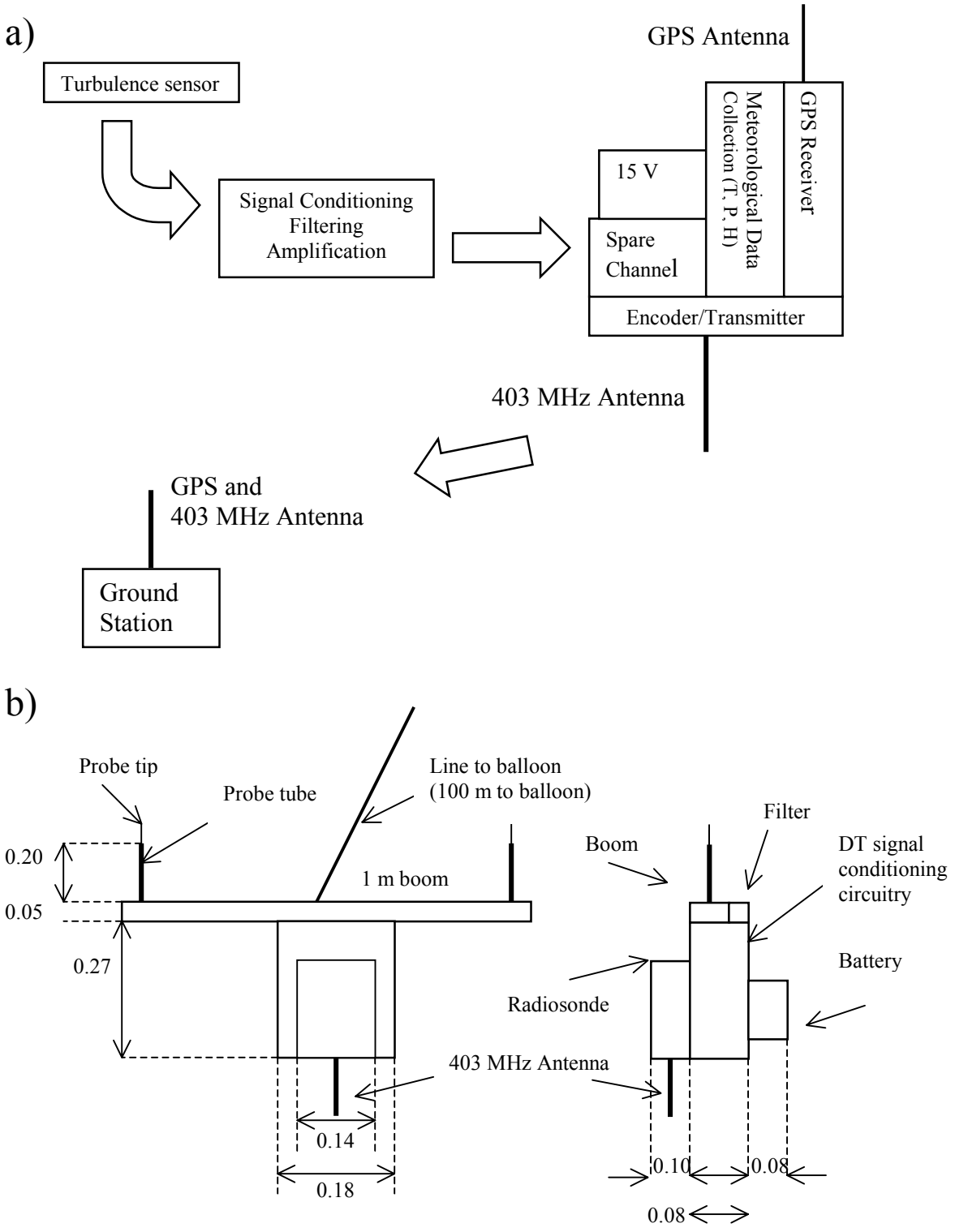

Figure 4.2: *In situ* probe package. a) Functional schematic of the thermosonde integrated with a radiosonde. b) Dimensional schematic of the thermosonde integrated with a radiosonde. Dimensions are in meters.

a 3.75 sec time constant; with a ~5 m/s ascent rate, this means an average over ~10 m. Finally, the noise floor of the thermosonde corresponds to a RMS temperature difference of 0.002°. The thermosonde system was suspended about 100 m below the balloon to ensure that the turbulent wake from the balloon did not affect the measurements. We present in Figure 4.2 the dimensions and functional schematics of the *in situ* instrument package.

4.2 Data Presentation

Considering the volume of data collected during the MIST campaign, it is neither practical nor educational for us to display all the data. We therefore present a representative example of the atmosphere characteristics at JRO as seen by the *in situ* instruments. We will examine in detail the radar backscatter characteristics seen in a typical evening. Later in the chapter, we will focus on some of the unique scattering events observed during this campaign.

In the data presentation, we first present the balloon-borne data so that the reader will have a good grasp for the atmospheric structures of Peru. This will set the scene for the presentation of the radar measurements.

4.2.1 Balloon Data: 2012 LT, 7 September 1998

The left-hand panel of Figure 4.3 displays a typical example of the balloon-borne *in situ* measurement of atmospheric temperature. This dataset comes from a balloon launched at 2012 LT on 7 September. Although the balloon is launched at the radar site, we do not assume that the balloon-borne sensors and radar are necessarily measuring the same air mass above 10 km, due to the horizontal drift of the balloon. We display only the data between the altitudes of 10 km and 22 km, the range in which the radar measurements are reliable.

The mean temperature lapse rate in the troposphere is 7.90 K/km. This is less than

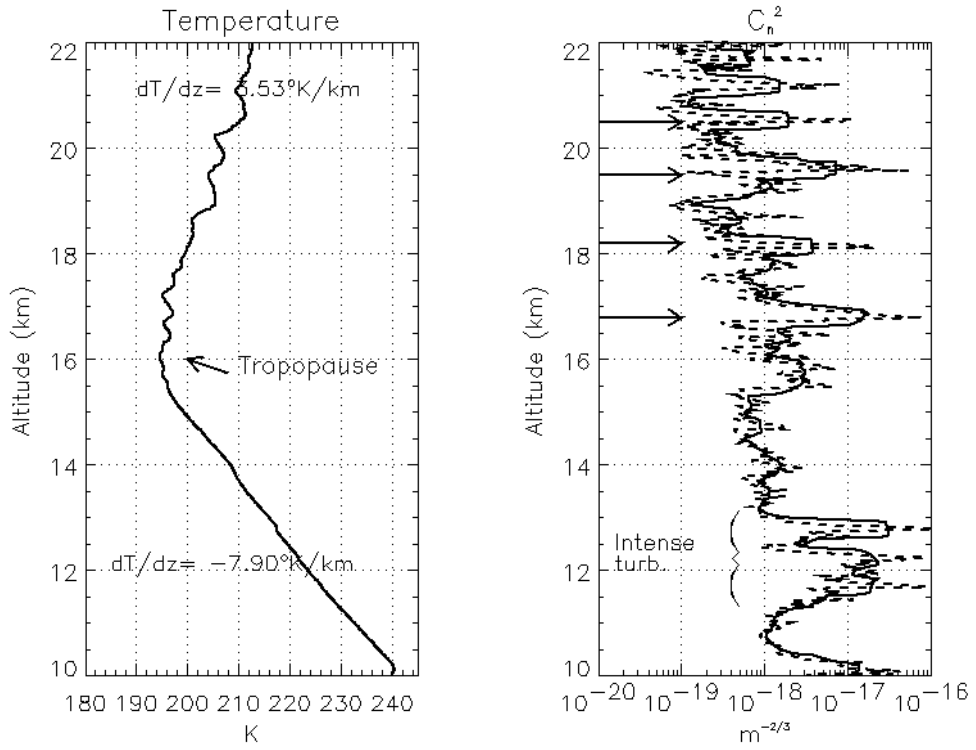

Figure 4.3: A typical example of the balloon-measured atmospheric parameters at Jicamarca Radio Observatory (JRO). This launch took place on 2012 LT, 7 September 1998. The balloon was launched at the radar site. *Left panel*: Temperature profile. Tropopause is at ~16 km. *Right panel*: C_n^2, an indicator of the turbulent intensity of the atmosphere.

the adiabatic lapse rate, indicating a statically stable troposphere. -3.53 K/km is the lapse rate in the stratosphere, slightly less than the average ~-2 K/km for the lower stratosphere [*Salby*, 1996]. The change in the lapse rate suggests that the tropopause is located at about 16 km. However, this tropopause does not distinctly separate the troposphere from the stratosphere, as it does in typical balloon soundings [e.g., *Holton*, 1992; *Walters*, 1995]. In the temperature profiles of other balloon soundings of this campaign, the tropopause appears distinctly in some of the soundings and obscurely in others. In the stratosphere, distinct ripples in the temperature profile are evident between 16 km and 18 km with an oscillation period of about 0.5 km; the period is 1 km between 18.5 km and 21 km. Similar wave-like behavior occurs in the other temperature profiles. The periodicity of the oscillations may be an indication of

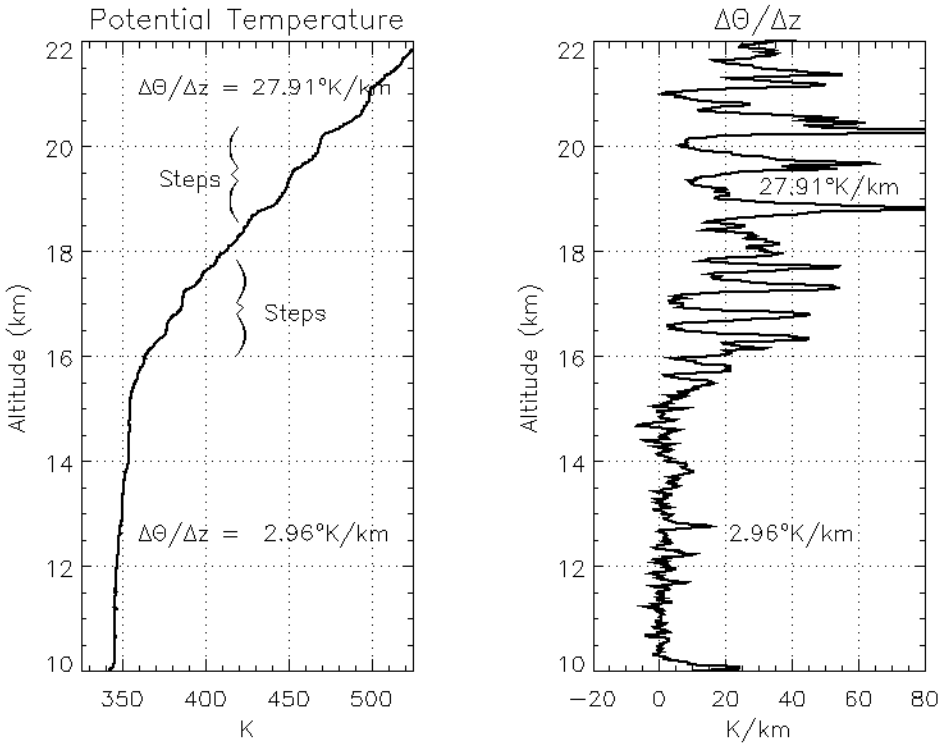

Figure 4.4: *Left panel*: Potential temperature. Potential temperature steps exist in the data especially in the stratosphere. *Right panel*: $\Delta\theta/\Delta z$. Troposphere is marginally stable, as seen with $\Delta\theta/\Delta z$ near or below zero; the stability in the stratosphere is seen via positive values of $\Delta\theta/\Delta z$.

inertial wave activity [*Larsen and Cornish*, 1989].

We plot the turbulence parameter C_n^2 computed from the measured C_T^2 in the right-hand panel of Figure 4.3. As seen in Chapter 3, C_n^2, which is proportional to and computed from the *in situ* measurement of C_T^2, provides a measurement of the atmospheric turbulence intensity. The solid line is the average C_n^2 computed via a moving boxcar filter 300 m in width; the measured C_n^2 is the dashed line. The plot shows that the balloon passed through several patches of strong mechanical mixing, perhaps turbulent in nature, as indicated by dramatic jumps in C_n^2 (by an order of magnitude or more) above the background value. A region of strong turbulence is seen below the tropopause between 11 km and 13 km. In the stratosphere, we see turbulent patches near 16.8 km, 18.2 km, 19.5 km, and 20.5 km as indicated by the

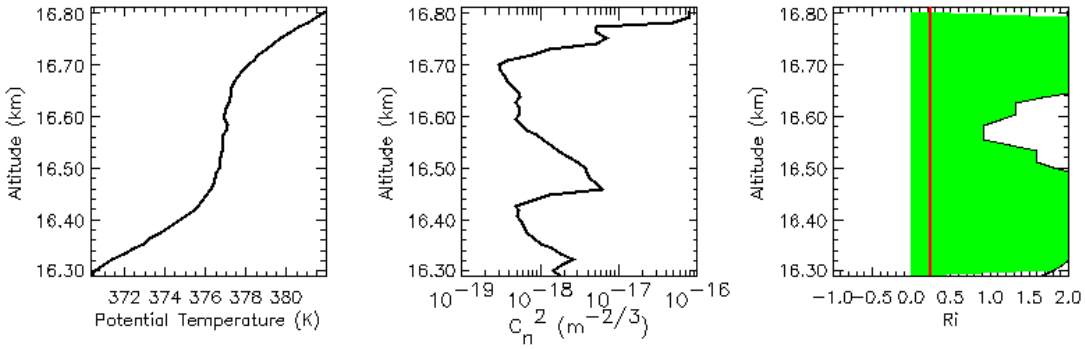

Figure 4.5: *Left panel*: An example of the temperature steps seen in the potential temperature profile in Figure 4.2. Temperature steps are about 300 m deep. *Central panel*: C_n^2, refractive index structure function coefficient. *Right panel*: Gradient Richardson number (*Ri*). $Ri = 1/4$ is the boundary of instability.

arrows. These sharp turbulent layers, indicated by jumps of C_n^2, are superimposed on trend that decreases in altitude. This decreasing trend is due to pressure and temperature dependence of C_n^2 in (3.11).

We plot the potential temperature (θ), as defined by (3.1) in Chapter 3, along with its derivative in Figure 4.4. Again, we associate a statistically stable atmosphere with $\Delta\theta/\Delta z > 0$, convective instability, a parcel of heavier air overlying lighter air, with $\Delta\theta/\Delta z < 0$, and neutral with $\Delta\theta/\Delta z \approx 0$. In the stratosphere, the average gradient is much higher than its counterpart in the troposphere, corresponding to the higher stability of the region. Very high positive $\Delta\theta/\Delta z$ can form in the stratosphere. The observed potential temperature steps correspond to regions of near zero $\Delta\theta/\Delta z$ as a function of height.

Before we leave this potential temperature discussion, we want to spend some time looking at the potential temperature steps. We have zoomed in on one temperature step centered at 16.5 km and plotted it along with the C_n^2 and the gradient Richardson number (*Ri*). We show this in Figure 4.5. Not only is the center of the temperature step adiabatic in nature, i.e., $\Delta\theta/\Delta z \approx 0$, but C_n^2 reaches a minimum as well. This indicates that some mechanism(s) acted on this parcel of air such that the contents of

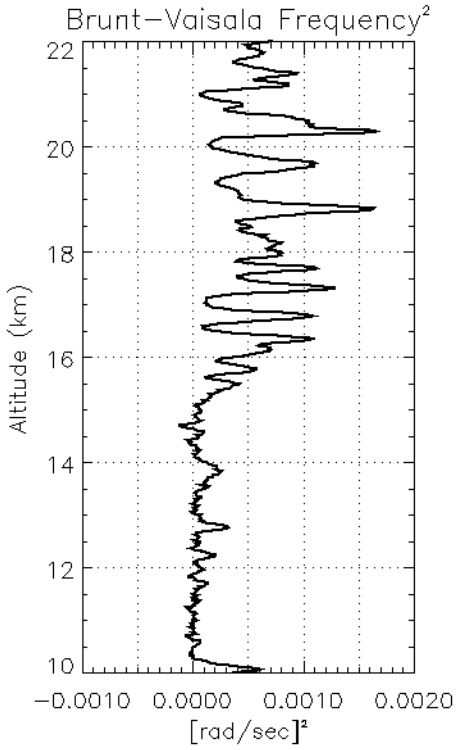

Figure 4.6: Square of the Brunt-Väisälä frequency (N^2). N^2 is another telltale sign of the stability of the atmosphere. $N^2 < 0$ indicates instability while stability implies a large, positive value of N^2. Average N^2 in the stratosphere is 6.05×10^{-4} [rad/sec]^2 and 6.88×10^{-5} [rad/sec]^2 in the troposphere.

the parcel have been homogenized and well mixed. In Chapters 7 and 8, we will discuss the significance and the relevance of *Ri* to these temperature steps. This type of temperature structure is commonly seen in the MIST campaign. In a future chapter, we will not only consider this structure in the context of a radar backscatter calculation, but also examine the mechanism(s) that is responsible for creating this structure. We introduce this now because we want to associate this type of temperature structure with the radar backscatter characteristic in this altitude range.

In Figure 4.6, we plot the square of the Brunt-Väisälä frequency, as defined by (3.2). The average N^2 in the stratosphere is 6.05 x 10^{-4} [rad/sec]^2 and is 6.88 x 10^{-5} [rad/sec]^2 in the upper troposphere, which translates to a Brunt-Väisälä period of 4.23 minutes and 12.6 minutes, respectively. This again indicates the strong stability of the

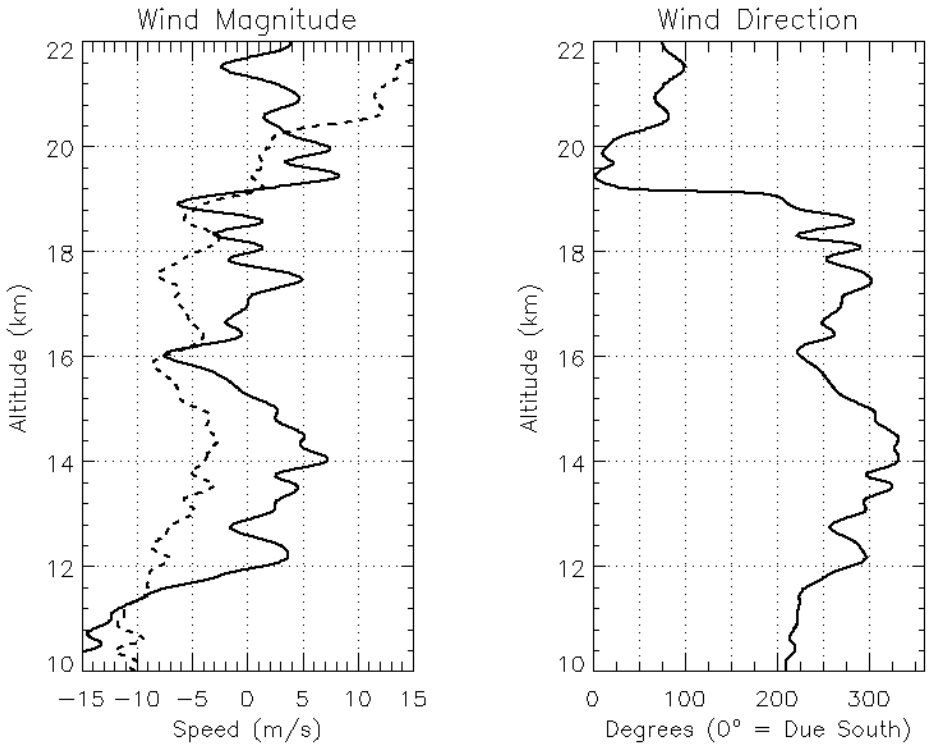

Figure 4.7: Radiosonde-measured horizontal wind at 2012 LT, 7 September 1998. The height resolution is ~15 m. *Left panel*: The horizontal wind velocity. Solid line: meridional component; dashed-line: zonal component. *Right panel*: Wind direction.

stratosphere and the marginal stability of the upper troposphere. N^2 peaks near the edges of the temperature steps, which indicate the transition from the well-mixed air in the temperature step to the background atmosphere.

We plot in Figure 4.7 the horizontal wind components in the left panel. Vertical shears are present in both wind profiles, but they are particularly intense in the meridional wind. These shears, when found in a statically stable atmosphere where (potentially) warm air lies above cold air, can play an important role in the dynamics of the atmosphere. If a strong wind shear exists across the interface, the two air masses are then in relative motion and then the interface will become dynamically unstable. The direction of the wind, as seen in the right hand panel, remains fairly constant in the easterly direction for $z < 19$ km. The wind direction changes sharply at 19 km.

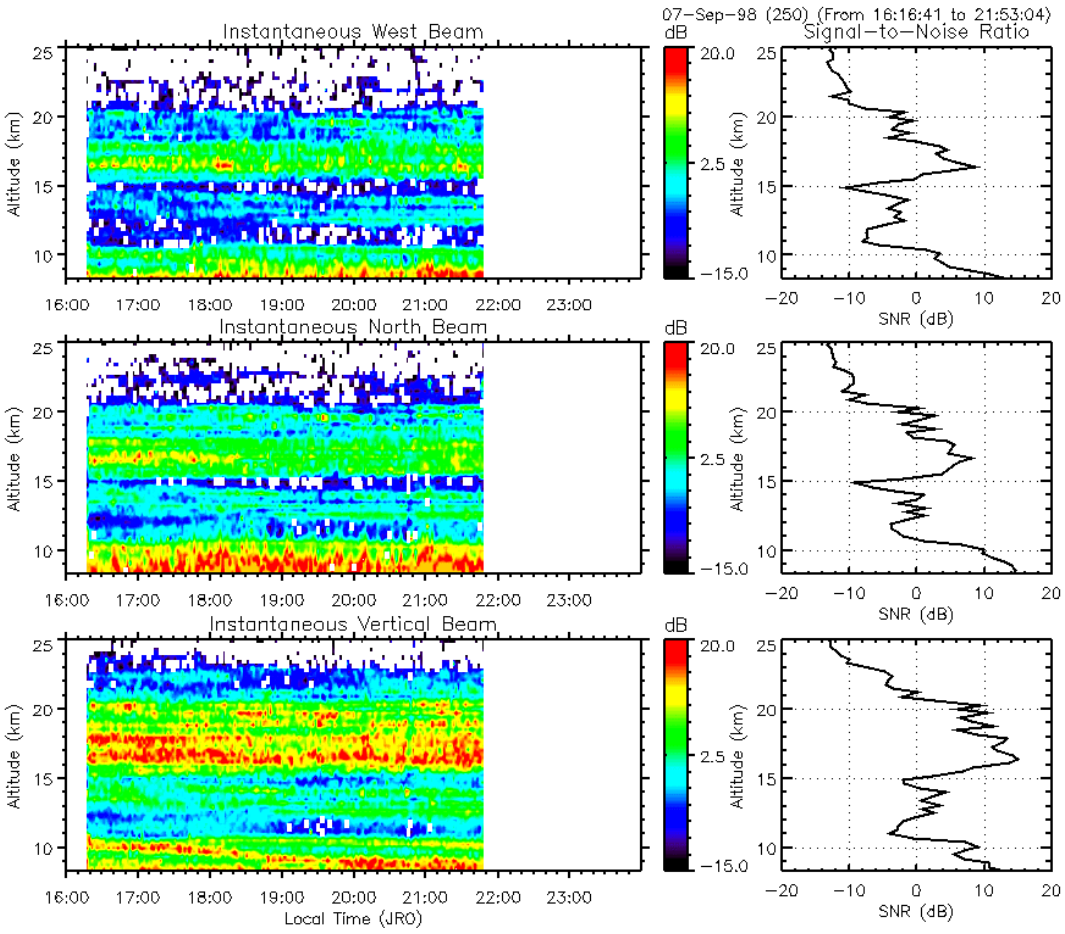

Figure 4.8: Range-time-intensity (RTI) plot of the signal measured by the Jicamarca VHF radar in its multi-beam configuration on 7 September 1998. Panels, from top to bottom, display the data for the west, north, and vertical beam. Large signal below 10 km may contain ground clutter. Signals above 22 km are mostly noise.

4.2.2 Radar Data: 7 September 1998

Given the *in situ* observations of the thermodynamic parameters and turbulence that exist in the Peruvian lower atmosphere, we are ready to examine the radar data. We will pay particular attention to aspect sensitivity and the temperature structures as seen in Figures 4.3 and 4.4.

Figure 4.8 shows the range-time-intensity (RTI) plot of the signal measured by the radar in its multi-beam configuration on 7 September 1998. We plot altitude on the vertical axis and time on the horizontal axis. The colors indicate the intensity of the radar echo, i.e., signal-to-noise ratio (SNR), in decibels, where we have defined SNR

as the difference between the atmospheric signal (in decibels) and the noise level (in decibels) of the highest range gate (at 30 km). SNRs of the vertical and the oblique beams are computed taking into account the differences in the transmitted power and the antenna area. Range gates where SNR was less than –15 dB have been omitted. The white color in the plot indicates regions where either no data were recorded or the signal is below the SNR threshold.

We can make a few general statements about the radar signals of a typical dataset. Signals seen below 10 km are sometimes contaminated by ground clutter and receiver recovery problems, as is seen particularly in the north beam signal. Only noise is detected for altitudes above ~22 km. For this reason, our analysis will focus on signals between 10-22 km. One of the most interesting features of this data is the increase in signal at the tropopause which is seen not only in the vertical direction but also in the off-vertical directions. We see layers of strong signal return for altitudes for 16 km$< z <$ 20 km. The sharp signal increase seen above 16 km is real and occurs just above the tropopause. The radar observation indicates these layers to have a long horizontal extent. We recall that the radar observes the structures that are being horizontally advected by the background wind across the radar beam. Our observing a scattering layer continuously for 5+ hours implies that the structure in the lower stratosphere has a horizontal extent of 90 km (assuming a background horizontal wind of 5 m/s, as seen in Figure 4.7).

We digress for a moment to discuss the electromagnetic radiation that is emitted from the radar. The radiation expands spherically away from the transmitting antenna. When the range is large, i.e., in the far-field region of the radar, the spherical surface of uniform power density appears. The far-field wave front is then considered planar. At shorter ranges, i.e., the near field region, the spherical wave front no longer appears flat. In addition, in the near-field, the power is proportional to $1/R$ instead of being proportional to $1/R^2$. The range where the far-field region begins is

$$R_{ff} = \frac{2D^2}{\lambda}, \tag{4.1}$$

where λ is the radar wavelength and D is the largest dimension of the transmission antenna. Since the vertical beam is generated by the full antenna array, its near-field extends to 30 km. However, at 9 km, the near-field effect changes the SNR of the vertical beam by 20 % and this change decreases as $1/R$. We demonstrate this in Appendix B. In short, for the purpose of this thesis, although near-field effects are present, they are negligible as we are interested in the data for $z > 10$ km.

The stratospheric echoes are, on the average, 8 dB larger than the upper tropospheric echoes. Also, the vertical echoes are always larger than the oblique ones, from about 3 dB in the upper troposphere to about 10-15 dB in the stratosphere; the strongest contrast is at ~16.5 km, near the tropopause. In other words, the radar backscatter is aspect-sensitive. We will analyze this aspect sensitivity result in Chapter 5. But first, for the sake of completeness, we examine the scattering features present in the RTI plot. Although some of the discussion that follows is not directly relevant to the focus of this thesis, i.e., aspect sensitivity, they do indicate the complexity of the atmospheric structures present at JRO.

We turn to the radar spectral width, computed from the Doppler spectrum, to learn more about the atmospheric dynamics associated with the aspect-sensitive backscatter. Radar spectral width provides us additional information regarding the turbulent/non-turbulent nature of the scattering mechanism. The Fourier transform of the radar signal incident on the scatterer resembles a Gaussian function of some finite half-power half-width (HPHW). If the scattering volume were composed of random fluctuations in refractive index moving randomly as caused by turbulence, the random motion manifests itself in the broadening of the HPHW of the incident Gaussian signal. In short, the spectral width is a measure of the turbulent motion in a radar

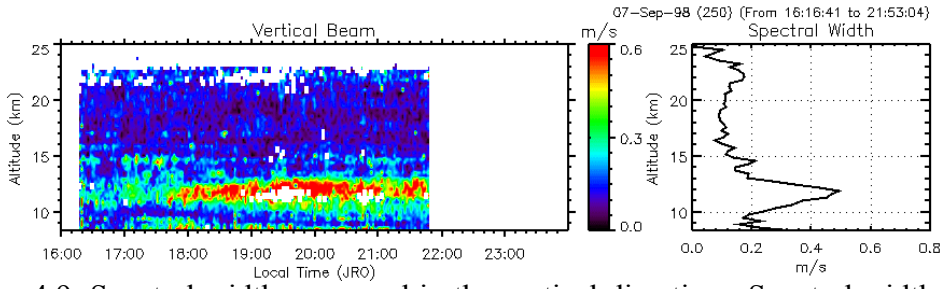

Figure 4.9: Spectral width measured in the vertical direction. Spectral width for SNR < -8 dB is omitted.

range volume. Spectral width of the backscattered signal will indicate regions of strong turbulent mixing.

We plot the spectral width as observed by the vertical beam on 7 September 1998 in Figure 4.9. Non-turbulent spectral-width broadening mechanisms are minimized, if not negligible, in the radar measurement in the vertical direction because of the smallness of the radar beam. As expected, the spectral width is large in the more turbulent troposphere as was seen in the temperature profile (see Figure 4.3). What catches the eye is the larger spectral width measured starting at 1700 LT, centered around 12 km with ~1.5 km vertical extent. This indicates a strong turbulent activity, as supported in Figures 4.3 and 4.10 by the *in situ* measurement of C_n^2; we will discuss this in a future section.

On the other hand, less intense turbulence, as indicated by a smaller spectral width (~0.1 m/s), is seen in the stratosphere, indicating a lower level of active turbulence activity. Comparing Figure 4.9 with 4.8, strong scattering layers, e.g., when SNR > 10 dB, particularly the aspect-sensitive layers in the lower stratosphere, are regions of low turbulence activity, as indicated by the small spectral width. In other words, the scatterer(s) is (are) coherent, contrary to the descending turbulent layer as observed by *Sato et al.* [1985].

4.3 Interesting Scattering Events

At this point, we briefly walk away from discussion of aspect sensitivity measurement and instead examine several interesting scattering events during the MIST Campaign. We will present these radar observations and analyze them with the complementary *in situ* data.

4.3.1 Descending Scattering Layer

Layers of persistent echoes, on the order of 1 km or so in vertical extent, are commonly seen in the troposphere and the stratosphere. The scattering layers, as seen in Figure 4.8, are oftentimes thinner than 1 km and cannot be resolved by the radar with a 300 m height resolution. By tracking the behavior in time of the scattering layer, we see evidence of some low frequency background atmosphere motion. For example, in the upper troposphere, a scattering layer appears between 13 km and 15 km and moves slowly downward by 0.5 km over the 5-hour period. This is reminiscent of the downward phase progression of an internal gravity wave; this is only speculation, as our dataset is limited [*Larsen and Cornish*, 1989; *Cho*, 1995; *Yamanaka et al.*, 1996; *Riggin et al*., 1999]. The persistent echoes are more stationary in the stratosphere. These observations are typical during the MIST campaign.

A dramatic example of a persistent descending scattering layer is seen near 11 km in Figure 4.9, where the layer is initially seen at 11 km at 1620 LT and descends steadily; at 1900 LT, it is at 10 km. This is best seen in the backscatter in the vertical direction. Unfortunately, ground clutter and receiver recovery problems have overwhelmed the atmospheric signal from the north direction at this altitude range; the signal from the west direction is still good between 1620 LT and 1800 LT and we can vividly see the descending scattering layer. This signal is about 4-5 dB less than what was observed by the vertical beam, indicating an aspect-sensitive scattering mechanism.

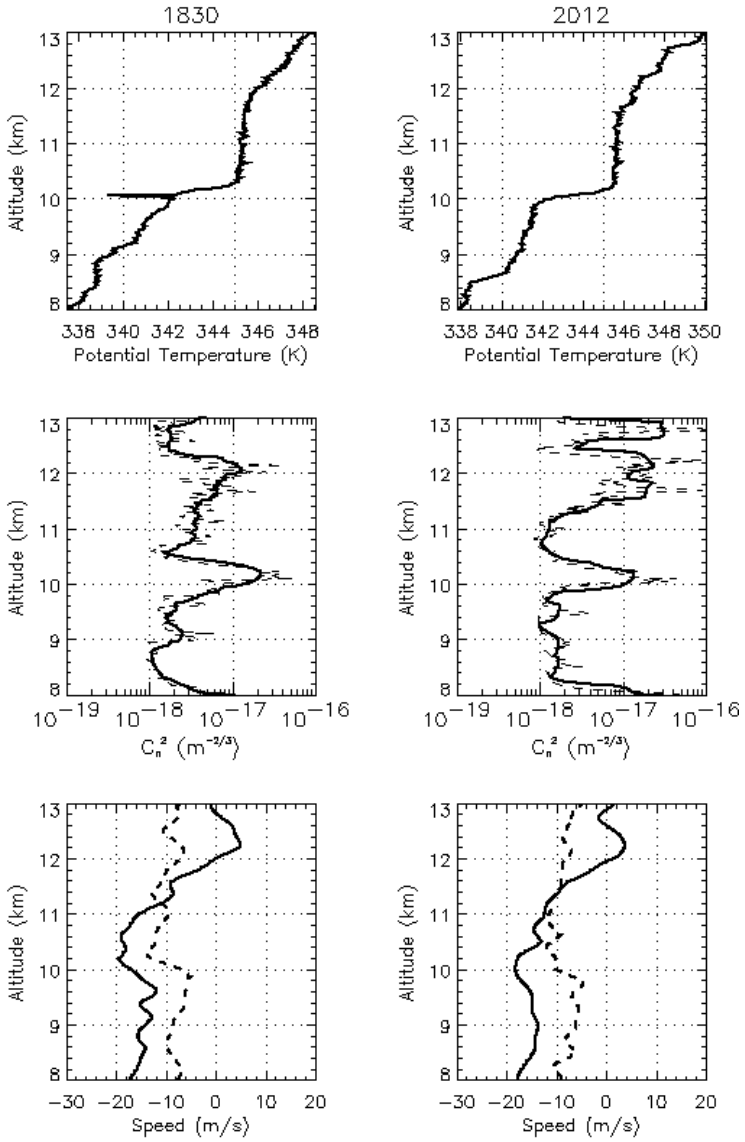

Figure 4.10: *In situ* measurements from the balloon launched 1830 LT and 2012 LT on 7 September 1998. *Top row:* Potential temperature. *Center row:* C_n^2, an indicator of the turbulent intensity of the atmosphere. *Bottom row*: Radiosonde-measured horizontal wind. Solid line: meridional component; dashed-line: zonal component.

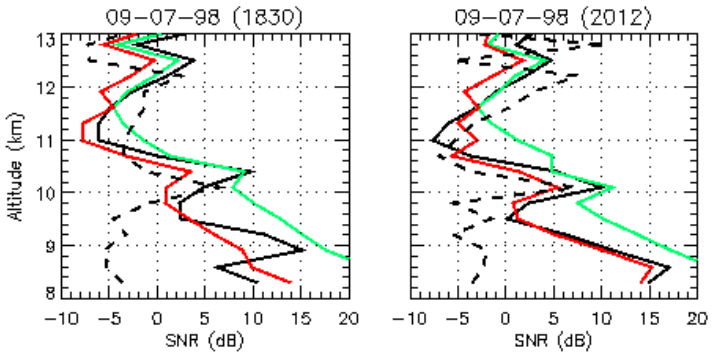

Figure 4.11: Radar backscatter measured on 7 September 1998. Green line is the SNR from the north direction; red line is SNR from the west direction; black line is the SNR from the vertical direction. The dashed line represents the predicted turbulent backscatter based on the *in situ* measured C_n^2.

Before examining the radar backscatter further, we first investigate the *in situ* measurements of this region. When interpreting the *in situ* data in the context of the radar data, we need to account for the finite ascent rate (5 m/s) of the balloon. In other words, if the balloon were launched at 1830 LT, it will reach 10 km ~30 minutes later. In Figure 4.10, we plot θ, C_n^2, and wind profiles near the scattering layer measured at 1830 LT and 2012 LT. An instrument glitch appears at 10 km in the 1830 flight. A potential temperature step appears centered at ~11 km; this mimics the potential temperature steps observed in Wichita, KS, as discussed in Chapter 3. The air in the center of the temperature step is adiabatic mixed, as indicated by $\Delta\theta/\Delta z \approx 0$ and small C_n^2; C_n^2 is large at the edges of the temperature step due to the temperature gradient. The *in situ* turbulent measurement compares well with the spectral width measurements in Figure 4.9.

As the evening progresses, a potential temperature step begins to form near 9.2 km. Again, the center of this temperature step is associated with low values of C_n^2 and $\Delta\theta/\Delta z \sim 0$, again indicating mixing of the atmosphere. C_n^2 is large near the edges of the temperature step. Again, we see that the *in situ* measurement of C_n^2 and the radar spectral width, as indicators of turbulence activity, yield similar results.

We can examine the radar backscatter coincident with the *in situ* measurement by looking at 30-minute averages of the radar data. In Figure 4.11, we plot the average SNR between 1830-1900 LT (left panel) and 2012-2042 LT (right panel). We compute the predicted turbulence scatter, plotted as the dashed line, based on C_n^2 computed from the *in situ* measured C_T^2. The details of this calculation will be addressed in Chapter 5; we introduce it now for necessity. In this observation, SNR from the vertical direction compares well with the SNR from the off-vertical directions except below 10 km where ground clutter contaminates the signal. There is a correspondence between the radar backscatter and the temperature structure. SNR increases at the edges of the temperature steps, e.g., ~9 km, 10 km, and 12 km for the 1830 LT balloon flight and ~8.5 km, 10 km, and ~12 km for the 2012 LT balloon flight. This correspondence indicates that the radar backscatter reflects the increase in C_n^2 and potential temperature gradient at the edges of the temperature steps. In addition, the mechanisms causing the radar backscatter seem to be dominated by turbulence, as indicated by a good agreement between the predicted turbulence scattering and the measured radar backscatter.

In conclusion, we have examined the downward propagating scattering layer via balloon-borne *in situ* probes and a VHF radar. Strong backscatter seems to be associated with the edges of potential temperature steps. In the radar data, we see patches of active turbulence concentrated initially at 11 km and descending to ~9 km, particularly 2000-2100 LT. Turbulence is typically responsible for mixing air constituents. Turbulence may be responsible for instigating the formation of the temperature step near 9.2 km.

4.3.2 Periodic Echoes

We plot the radar data from 8 September in Figure 4.12. The data from 8 September is similar to that from 7 September. Both indicates an aspect-sensitive atmosphere,

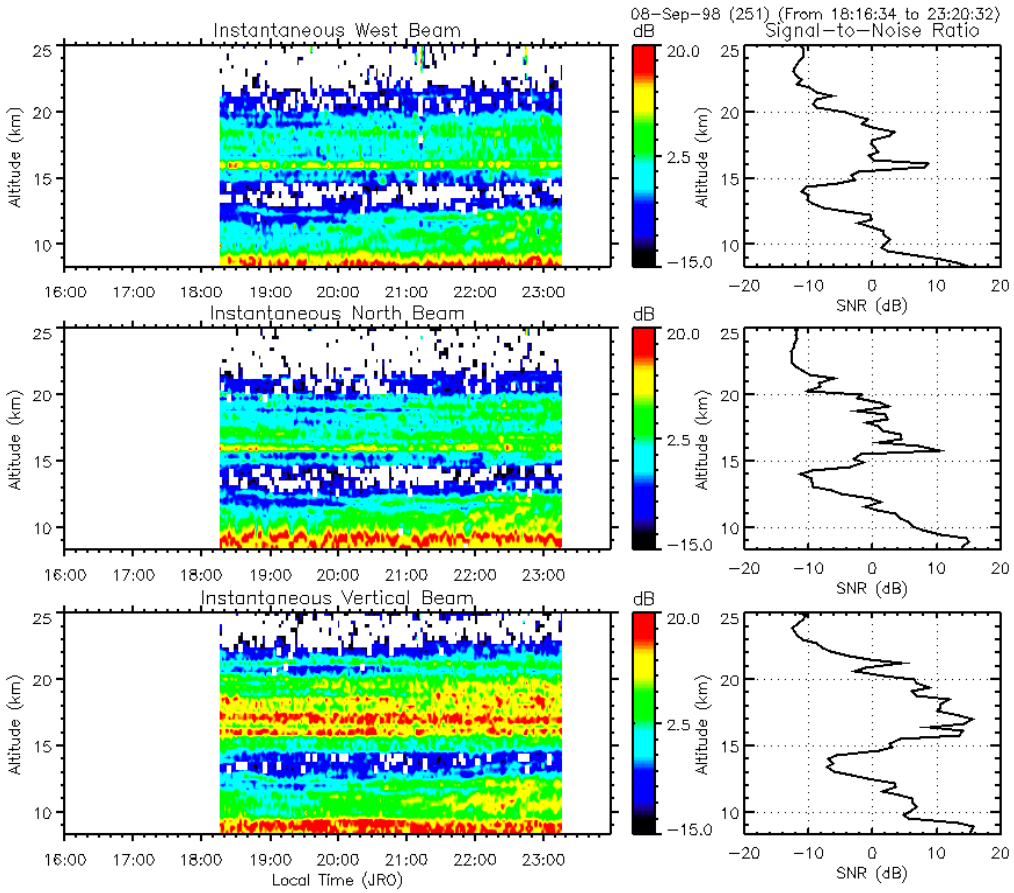

Figure 4.12: Range-time-intensity (RTI) plot of the signal measured by the Jicamarca VHF radar in its multi-beam configuration on 8 September 1998. This is plotted in the same format as Figure 4.8.

especially in the lower stratosphere. Ground clutter again contaminates the range gates below 10 km. We want to draw the reader's attention to the oscillatory structure centered at ~11 km seen starting at 2000 LT. The fact that the same structure is seen in the vertical and off-vertical direction at the same intensity indicates the isotropy of the structure. The vertical extent of this structure is increased by 1 km in a period of 2 hours. This resembles previous Kelvin-Helmholtz instability (KHI) observations (see Figures 2.6 and 2.7). We will examine this further in Chapter 5.

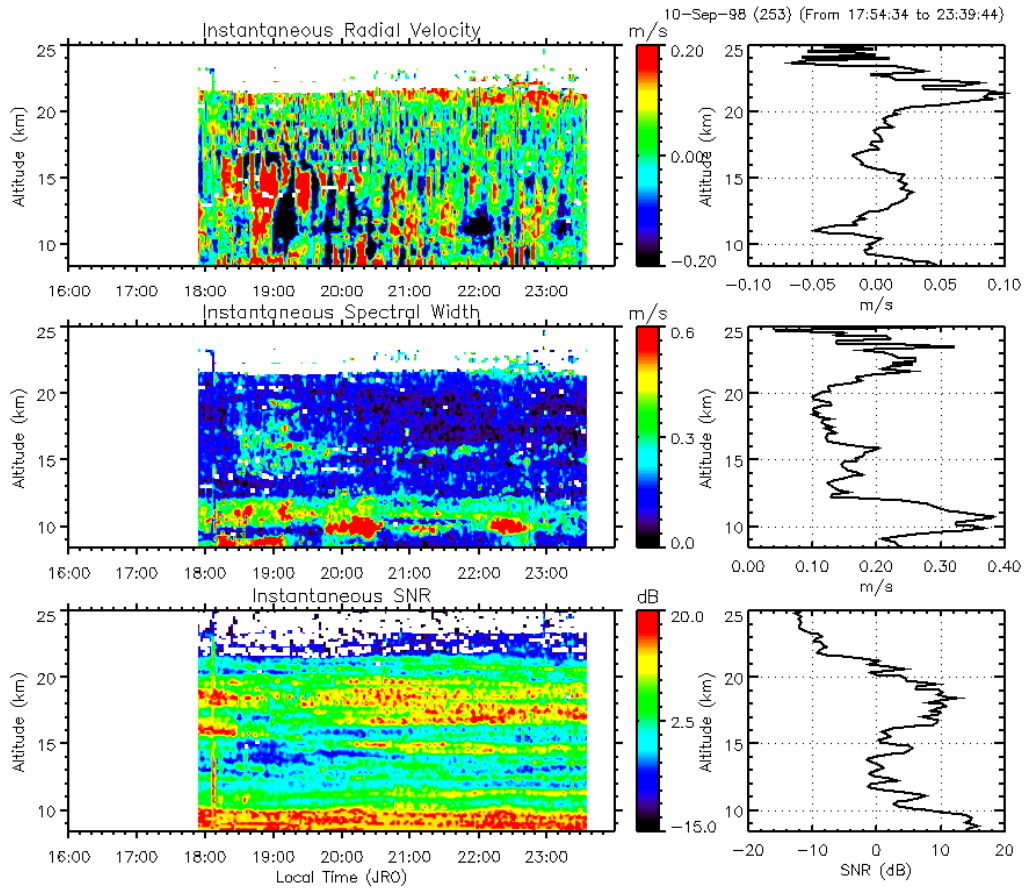

Figure 4.13: Data measured by the Jicamarca VHF radar in its single-beam configuration on 9 September 1998. The radar beam was pointed in the vertical direction. *Lower panel*: Range-time-intensity (RTI) plot. *Center panel:* Spectral width. *Top panel*: Radial velocity.

4.3.3 Missing Scattering Region

As seen in Figures 4.8 and 4.12, persistent echoes are observed in the stratosphere. We see an exception to this rule on 9 September 1998. The atmospheric dynamics can be gleaned from the SNR, radial velocity, and spectral width. We display the radar data in Figure 4.13. The average of these quantities is plotted in the right-hand columns. On this evening, a solitary vertical beam was transmitted with 150 m height resolution. With this resolution, the radar was able to resolve the scattering structures and associated atmospheric dynamics with more detail.

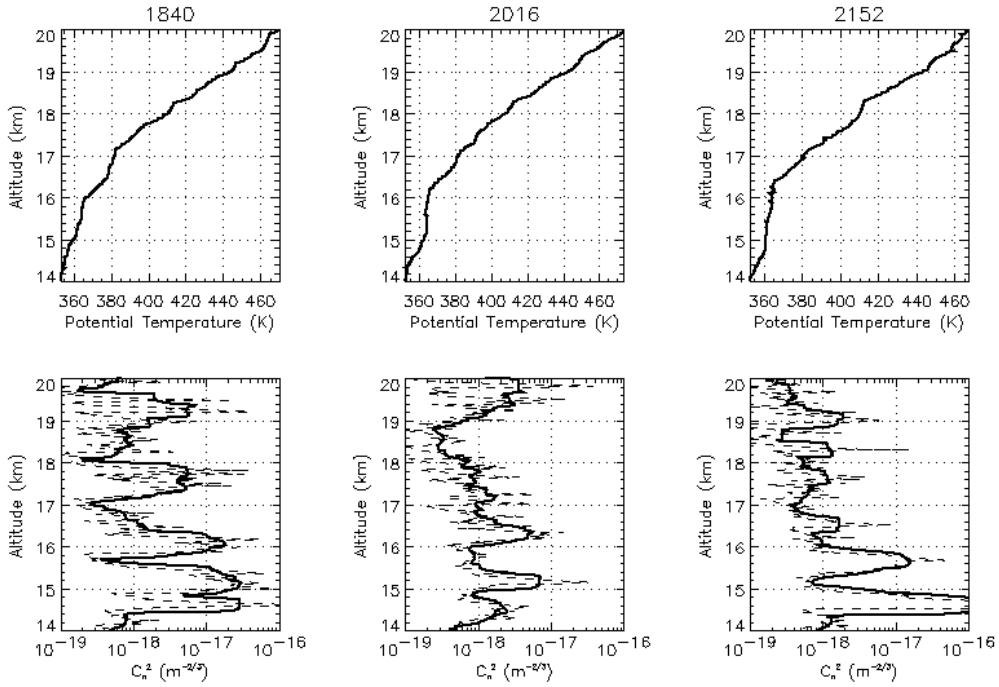

Figure 4.14: *In situ* measurements from the balloon launched 1840 LT, 2016 LT, and 2152 LT on 9 September 1998. *Top row:* Potential temperature. *Bottom row:* C_n^2. Solid line is the average C_n^2 that we have computed via a moving boxcar filter 300 m in width; the measured C_n^2 is the dashed line.

The backscatter measured this evening is similar to that observed in previous evenings. What makes this particular observation unique is not the ability to observe these scatterers with a vertical resolution of 150 m, but it is the decrease in the radar backscatter seen in the lower stratosphere between 1830 and 1930 LT. During this period, the atmospheric structure responsible for the strong radar backscatter disappears and restores itself again between 2000-2100 LT. Such an event was observed only on this evening during the MIST campaign.

We turn to the Doppler spectral width to investigate the disappearance of the backscatter. An increase in the measured spectral width, indicating the existence of turbulent mixing, is seen with the decrease in the stratospheric backscatter. On the other hand, near 1800 LT and after 2000 LT, strong stratospheric scattering is

associated with low spectral width, indicating the stability of the structure. Patches of turbulent air are seen advected through the radar beam in the upper troposphere.

More information about the radar backscatter may be gleaned from the vertical radial velocity, which gives us insight into the vertical motion of the atmosphere. Data reveal some kind of background oscillation. Strongest oscillation occurs just as the scatterers disappear, near 1830 LT. The oscillation period is 10-12 minute, which is near the local Brunt-Väisälä frequency and much larger than the oscillations in the vertical velocity associated with Kelvin-Helmholtz instabilities; *Chilson et al.* [1997] measured, via VHF frequency domain interferometry, KHI related oscillations with a local period of 90 s. In short, the disappearance of the scatterers is observed simultaneously with an increase in the spectral width and a periodic behavior of the atmospheric motion in the vertical motion.

Figure 4.14 shows the *in situ* measurement values of C_n^2 and θ during this event. Balloon-borne instruments were launched at 1840, 2016, and 2152 LT; forty minutes are needed for the balloon to reach 14 km. It is not obvious from the potential temperature measurement what is happening here. However, C_n^2, as computed from the *in situ* measured C_T^2, indicates strong mechanical stirring between 15-20 km around 1930 LT. As the evening progresses, C_n^2 decreases by a factor of two. Unfortunately, no wind data were available in this altitude range at this time.

Based on the results of our analysis, we do not believe that a wave caused the disappearance of the scattering layer; this seems instead to be a transient turbulent event. We believe that what is going on here is an instability that evolved in a wave-like behavior. The periodicity seen in the vertical radial velocity in concert with the locally strong spectral width indicates that the instability is decaying in a wave-like fashion. This process creates strong mechanical turbulence which stirs the scattering layer and decreases the backscattered power. The scattering layers appear to restore themselves when the turbulent energy is dissipated via molecular and viscosity

dissipation and perhaps other mechanisms. However, this analysis is somewhat speculative, as we lack the wind measurements determine the magnitude of the vertical shear, which is needed to ascertain the dynamic/static stability of the atmosphere.

4.4 Temperature Steps and Radar Backscatter

Comparing the SNR profile in Figure 4.8 to the location of the potential temperature steps, such as the ones isolated in Figure 4.4 and perhaps more dramatically in Figure 4.5, it seems clear that the strong backscatter layers are collocated with and perhaps related to the temperature steps in the potential profile. A comparison between Figures 4.4 and 4.9 indicates that the SNR is strong at the edges of the temperature steps. This is not surprising. According to the scattering theory developed by the likes of *Wait* [1962], radar backscatter comes from the changes of refractive index which are caused by changes in temperature. Such changes are strongest at the edges of the potential temperature steps; the gradients would contain Bragg length (= $\lambda/2$) components at VHF, thereby creating radar backscatter. This suggests that potential temperature steps play a role in causing aspect sensitivity. This also indicates that potential temperature steps have a long horizontal correlation length, as an aspect-sensitive scattering layer is observed for hours at a time. Potential temperature steps of different vertical depths are seen in other altitudes and also other balloon soundings. Figures 4.3 and 4.4 indicate strong C_n^2 events at the edges of the potential temperature steps. In Figure 4.5, next to the potential temperature and C_n^2 profiles, we also plot the gradient Richardson number (*Ri*), defined as

$$Ri = \frac{N^2}{(dU/dz)^2}, \tag{4.2}$$

where N^2 is the square of the Brunt-Väisälä frequency and dU/dz is the vertical shear of the horizontal wind (U). As discussed in Chapter 3, Ri is a measurement of stability. In this example, Ri reaches a minimum at the center of the temperature step as $N^2 \sim 0$, indicating homogeneous mixing.

Potential temperature steps and C_n^2 profiles in Figures 4.4 and 4.5 remind us of the plot in Figure 3.15, which is the vertical profile of a 3D simulation of the Kelvin-Helmholtz instability (KHI) by *Werne and Fritts* [1999]. The final state of the numerical simulation yields a nearly vertical potential temperature profile bounded by sharp positive and hence very stable gradients. The temperature fluctuations ($\sim C_T^2$) in the right hand panel peak in the stable regions and almost vanish in the center. This is a result of the smoothing of the potential temperature gradient by the turbulent mixing. At the boundaries of the layer, two strongly positive gradients exist as the temperature structure merges with the background atmosphere. The velocity variance is quasi-uniform in the layer and greater outside, while the temperature variance exhibits two maxima restricted to the boundaries, a relative minimum appearing in the central part of the layer. This structure is a consequence of the spatial evolution of the mean temperature gradient in a KHI layer, due to the turbulent mixing processes fed by the energy in the vertical shear of the horizontal wind.

The measured temperature steps in Figures 4.4, 4.5, and 4.11 look remarkably like the simulation results. The C_n^2 structure is less clear but there are definite similarities to the RMS temperature profile. For example, in Figure 4.5, *in situ* measurements of large C_n^2 at the upper edge of the topside stable temperature region near 16.55 km and is down by an order of magnitude near the center of the temperature step and shows a modest bump in the lower stable zone. Given the complexity of the atmospheric dynamics and the limited ability of a computer simulation to capture the complexity, it is perhaps remarkable that the apparent agreement between the observation and the simulation is so good. We are led to the conclusion that the late-time evolution

Kelvin-Helmholtz billows as one plausible explanation for the temperature steps in the stratosphere and the observed aspect-sensitive radar echoes in the stratosphere and sometimes in the troposphere, such as the case examined for 7 September 1998 in Figure 4.8. The relationship between the potential temperature step, aspect sensitivity, and KHI is a topic of discussion in Chapter 7.

4.5 Discussion and Conclusion

In this chapter, we presented the radar and *in situ* data collected during the MIST campaign at the Jicamarca Radio Observatory, near Lima, Peru. The goal of the experiment is, via multiple-instrument observations, to understand the mechanisms responsible for aspect sensitivity. The radar data show strong persistent aspect-sensitive scattering layers in the stratosphere. The scattering in the troposphere is less intense, by about 10 dB or so, than the lower stratosphere; persistent scattering layers are sometimes observed in the troposphere.

We examine the *in situ* measurements made by balloon-borne radiosondes and turbulence sensors. The thermodynamic parameters provided by the *in situ* probes suggest a turbulent troposphere and an extremely stable stratosphere. The claim is substantiated by the turbulence parameter, C_n^2, computed from the *in situ* measured C_T^2, which steadily decreases with altitude. We also observe sharp layers of C_n^2. *In situ* data also reveal potential temperature steps with a vertical extent on the order of 0.5-1 km. There appears to be a relationship between strong radar backscatter and the strong temperature gradients and large C_n^2 at the edges of these temperature steps.

An examination of the *in situ* data in the context of the radar data indicates that the potential temperature steps may be responsible for aspect-sensitive backscatter. We explore this theory and also analyze the MIST campaign dataset in the next two chapters. In Chapter 5, we take a look at the aspect sensitivity observed at JRO. The possible causes of this dependence are considered. We dedicate Chapter 6 to a

discussion of atmospheric turbulence. Turbulence parameter measurement techniques, as well as the results computed from radar data and *in situ* sensors, are presented.

Chapter 5

Aspect Sensitivity and Radar Backscatter

In this chapter, we continue our discussion of the MIST campaign dataset. Our focus is on aspect sensitivity, the decrease in backscattered power as a function of zenith angle, that was observed at the Jicamarca Radio Observatory (JRO), particularly in the lower stratosphere. Radar observations, complemented by *in situ* measurements of the atmospheric thermodynamic parameters and turbulence intensity, will be used to characterize the possible scattering mechanisms that lead to the observed aspect-sensitive echoes.

As noted in the discussion of the RTI plots in Figure 4.8, the backscatter power detected in the vertical direction exceeds that received from 2.5º off-vertical. The backscatter is thus aspect-sensitive throughout the 10-22 km height range. This property has been reported many times in the past VHF radar studies [e.g., *Hooper and Thomas*, 1998, and references therein]. For discussion and analysis purposes, we will define aspect sensitivity (AS) as the difference between the SNR from the vertical direction and off-vertical direction, i.e.,

$$AS = SNR(\text{vertical}) - SNR(\text{off-vertical}) \tag{5.1}$$

where the SNR is in decibels. This is a common way of describing aspect sensitivity. On the other hand, it would be ideal to examine the functional dependence between the backscattered power and the zenith angle. To this end, we assume that the scatterer has some backscatter polar diagram and then derive the aspect sensitivity parameter θ_S, which is commonly used in aspect sensitivity studies. We examine the horizontal correlation length, which is computed from AS and θ_S, to give us an estimate of the size of the scatterer seen at 50 MHz.

In this chapter, we begin our discussion by computing the aspect sensitivity as defined by (5.1) and θ_S, the aspect sensitivity parameter, which is derived from AS. *In situ* measurements of atmospheric parameters provided by the radiosonde give us information about the atmospheric stability and the temperature structures. The turbulence sensor on the balloon provides a measure of C_T^2, a turbulence parameter, which in turn allows us to calculate a theoretical backscatter due to turbulence. Taken together, the analysis results of the MIST campaign dataset allows us to come to some conclusions about the scattering mechanisms responsible for the observed aspect sensitivity and the relevant temperature structure.

In this aspect sensitivity discussion, we will lean heavily on the *in situ* measurements for insight into the scattering mechanism(s). In order to analyze the radar measurements in concert with the *in situ* measurements, we first need to consider the finite ascension rate of the balloon. For a balloon ascending at a velocity of 5 m/s, it will take the balloon 34 minutes to reach an altitude of 10 km and an additional 40 minutes to reach 22 km. Therefore, to make the best comparison between the radar and balloon measurements, we will restrict our aspect sensitivity analysis to a 40-minute segment of the radar data where the beginning of the segment corresponds to 30 minutes after the balloon launch. For example, for the balloon launched at 2012

LT on 7 September 1998 that was discussed in Chapter 4, we would examine the radar data from 2042 to 2122 LT.

5.1 Aspect Sensitivity and SNR

We begin our aspect sensitivity analysis by looking at a small segment of radar data in detail before making some general statements regarding the backscattering characteristics of the Peruvian atmosphere. We plot the average SNR from 2042 LT to 2122 LT on the left hand panel of Figure 5.1. The backscatter from the vertical direction is larger than that from both oblique directions, particularly in the stratosphere. In this plot, we also include the predicted SNR caused by isotropic turbulence. To compute this prediction, we recall that the radar wavelength is in the inertial subrange for the atmospheric turbulence in the altitude range discussed here [*Hocking*, 1985]. We therefore can predict the turbulence backscatter based on the measured turbulence intensity parameter C_n^2 via the volume reflectivity defined as,

$$\eta(\lambda) \approx 0.38 C_n^2 \lambda^{-1/3} \quad [\mathrm{m}^2/\mathrm{m}^3] \tag{5.2}$$

[e.g., *Ottersten* 1968, 1969a, b]. We briefly discuss the derivation of (5.2) from turbulence theory in Appendix A. The volume reflectivity is a measurement of reflectivity caused by a volume of scatterers with a correlation length on the order of the Bragg wavelength, i.e., one-half of the radar wavelength, in contrast to the reflection coefficient ρ, which is a measurement of the reflectivity from a slab structure. Fortunately, *Röttger and La Hoz* [1990] have compared the reflected power based on ρ to the reflected power based on η and obtained the following conversion factor,

$$\eta = \frac{4 A_e}{\Delta r \lambda^2} |\rho|^2 \tag{5.3}$$

where Δr is the range resolution of the radar, A_e is the effective antenna area, and λ is the radar wavelength. This equation tacitly assumes that the scatterers completely fill

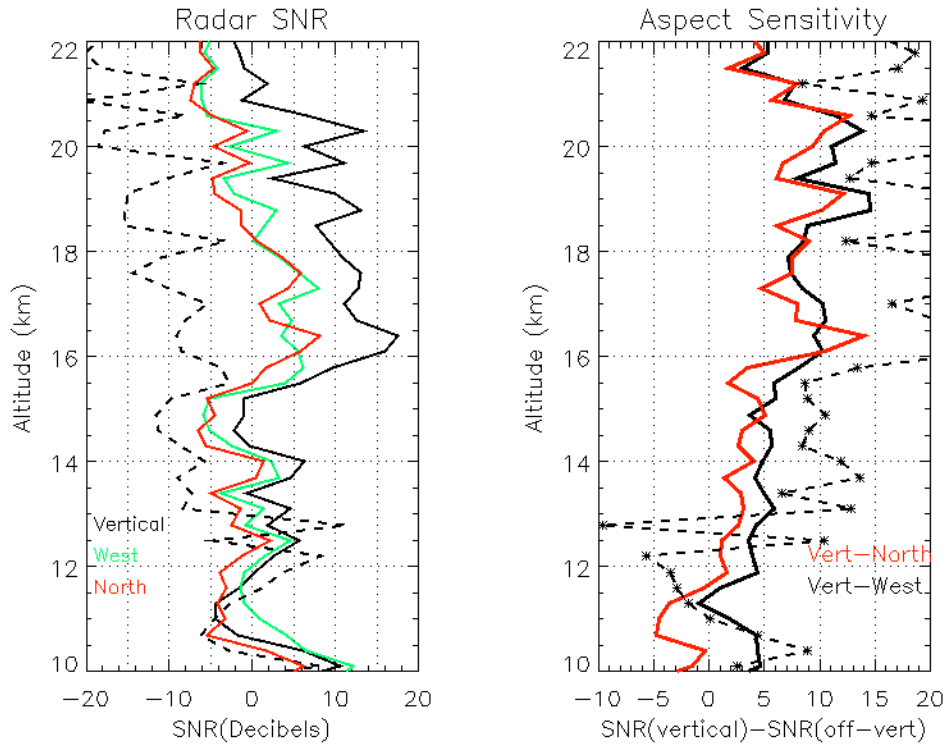

Figure 5.1: *Left panel*: Average SNR between 2042-2122 LT. Red line is the SNR from the north direction, green line is the SNR from the west direction, and black line is the SNR from the vertical direction. Dashed line is the turbulence backscatter predicted from the *in situ* measured C_n^2. *Right panel*: Aspect sensitivity as defined by (5.1). Large aspect sensitivity is seen in the stratosphere. Dash-star line is the difference between the vertical backscatter and the predicted turbulent backscatter, in decibels.

the radar range volume, which may not be valid. We use (5.3) to convert η defined by (5.2) to an effective ρ and then predict the backscatter from turbulence via

$$P_R = \frac{P_T A_e^2}{4r^2\lambda^2}|\rho|^2 \tag{5.4}$$

where P_R and P_T are, respectively, the received and transmitted powers and r is the radial distance from the antenna [*Gage and Balsley*, 1980]. The predicted turbulence backscatter signal is less than the measured backscatter at most altitudes. The exception occurs in the troposphere, where the predicted turbulent scatter is comparable to the measured radar backscatter.

The right hand panel of Figure 5.1 illustrates the aspect sensitivity as defined in (5.1). This is a more common way of comparing the relative strength of the SNR (in decibels) from the vertical direction against that from the oblique direction. Aspect sensitivity is about a few decibels in the troposphere and jumps to 10 dB in the stratosphere. Near 10 km, the apparent AS < 0 is due to the effect of the ground clutter and receiver recovery problems on the oblique beam signals. On the other hand, we find that SNR(vertical) is ~20 dB, i.e., 100 times, larger than the predicted SNR for turbulent backscatter.

We are surprised to measure an aspect sensitivity of this magnitude by simply tilting the beam 2.5º off-vertical. The signal decreases by about 4 dB-per-degree off-vertical. In previously published research, an aspect sensitivity equal to that measured here was achieved by tilting the beam 10-15° off vertical [e.g., *Tsuda et al.*, 1986, 1997; *Hooper and Thomas*, 1998]. The extreme aspect sensitivity at JRO suggests that the scattering structure has a long horizontal extent, as was discussed in section 4.2. We will examine the horizontal correlation length later in this chapter.

There is another way of analyzing aspect sensitivity. *Hocking et al.* [1986a, b; 1990] and *Hooper and Thomas* [1995] describe θ_S as a parameter that is used to quantify the degree of aspect sensitivity in the lower atmosphere and the mesosphere. We implement this type of analysis on the JRO data. We begin by assuming that the scatterers at any particular height have a backscatter polar diagram of the type

$$\exp\left(-\left[\sin\theta/\sin\theta_S\right]^2\right) \tag{5.5a}$$

(5.5a) represents the mean (normalized) backscattered power expected (after compensation for the different ranges of the scatterers at different zenith angles) as a function of tilt angle (θ) for a radar beam with small half-power half width θ_S. If θ and θ_S are small, such that $\sin\theta_S \sim \theta_S$ and $\sin\theta \sim \theta$, (5.5a) becomes

$$\exp\left(-\theta^2/\theta_S^2\right). \tag{5.5b}$$

For our discussion, we will use (5.5a). The parameter θ_S describes the degree of aspect sensitivity; it may be height dependent. θ_S for a truly specular reflector approaches 0º whereas for isotropic scatterers θ_S approaches infinity. In practice, any value in excess of about 20º can be regarded as almost isotropic. We model the radar beam in a similar fashion

$$\exp\left(-\sin\theta^2/\sin\theta_0^2\right), \tag{5.6}$$

where θ_0 is the half-power half width of the radar beam.

The backscatter polar diagram described by (5.5a) and (5.5b) would result if the scatterers were oblate spheroids with a Gaussian increase (or decrease) in refractive index from the edge towards the center [*Briggs and Vincent*, 1973; *Hocking*, 1987]. That is, for such a model the refractive index perturbation in a single scatterer would be proportional to

$$\exp\left(-x^2/L^2 - y^2/L^2 - z^2/h^2\right), \tag{5.7}$$

where x, y, and z describe a Cartesian coordinate system with z vertical, L is the *1/e* horizontal half-length of the scatterer and h is the *1/e* half-depth. Equivalently, based on *Hocking* [1987], the autocorrelation function of the refractive index fluctuations is equal to

$$\exp\left(-\zeta_x^2/2L^2 - \zeta_y^2/2L^2 - \zeta_z^2/2h^2\right), \tag{5.8}$$

where ζ_x, ζ_y, and ζ_z are horizontal correlation lengths in the x, y, and z directions, respectively. In fact, even if the scatterers were not ellipsoids, the autocorrelation function can still satisfy (5.8). Equation (5.8) does not give us insight into the nature, i.e., turbulent or specular, of the scattering process, but it does give us the horizontal correlation length. The latter is the main advantage of this procedure as it provides a parameterization which allows quantitative comparisons of the different degrees of aspect sensitivity at different radar installations and which can at least be related to a mathematical model of the refractive index fluctuations, something that has been

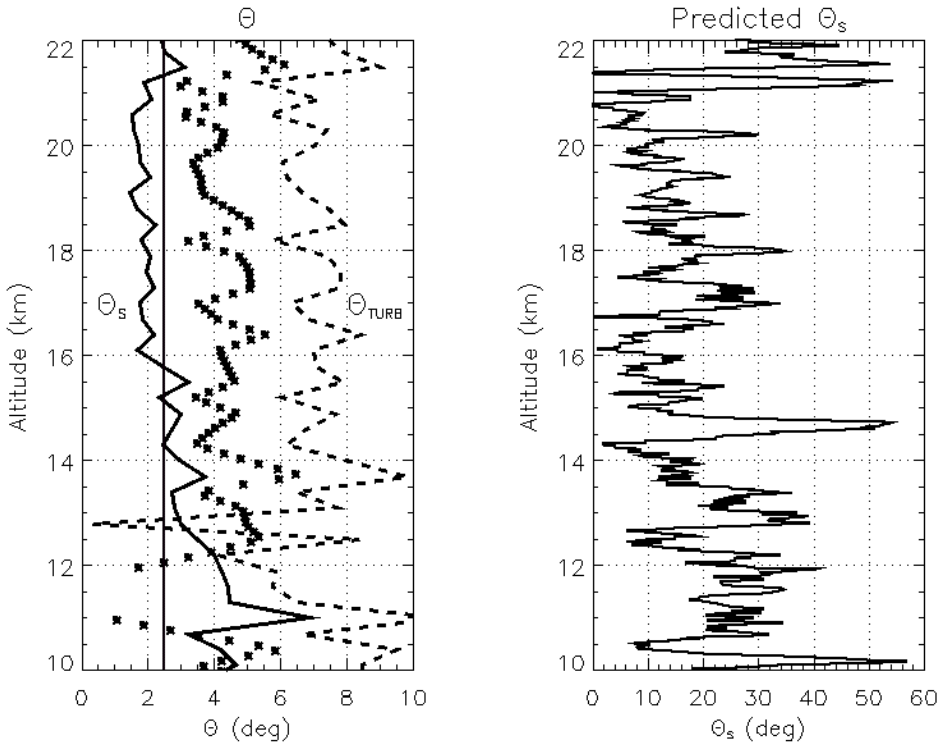

Figure 5.2: *Left panel*: Aspect sensitivity parameter (θ_S). Black solid line is the average of the θ_S calculated from the SNR(vertical) and SNR(north) and the SNR(vertical) and SNR(west); θ_S reaches a minimum of a little less than 2º in the stratosphere. Starred line is the tilt angle (θ_{TURB}) needed for the oblique beam of the JRO radar to see only turbulent scatter. Dashed line is θ_{TURB} computed based on the MU radar parameters. *Right panel*: Aspect sensitivity parameter, θ_S, as would be caused by anisotropic turbulence that the atmosphere can support based on the atmospheric parameters measured by the balloon.

lacking in some earlier qualitative comparisons [e.g., *Tsuda et al.*, 1986, and references therein].

Based on (5.6) and including (5.5a), it follows that θ_S can be determined by comparing the backscatter power, $P(\theta)$, received at two zenith angles θ_1 and θ_2:

$$\theta_S = \sin^{-1}\left[\sqrt{\frac{[\sin\theta_2]^2 - [\sin\theta_1]^2}{\ln[P(\sin\theta_1)/P(\sin\theta_2)]} - [\sin\theta_0]^2}\right]. \qquad (5.9)$$

In the left-hand panel of Figure 5.2, the solid line is the average of θ_S calculated from the measured aspect sensitivity shown in Figure 5.1. As a point of reference, we plot

the tilt angle (2.5°) of the oblique beams. θ_S decreases with altitude, reaching a minimum (maximum aspect sensitivity) of a little less than 2º around 20 km. The SOUSY radar, the MU radar, and the Aberswyth VHF radar have made measurements of θ_S in the lower atmosphere in the same altitude range [e.g., *Tsuda et al.*, 1997; *Hooper and Thomas*, 1998]. These previous measurements yielded larger values of θ_S, i.e., less aspect-sensitive, than the θ_S measured at JRO. These results provide strong evidence that the aspect-sensitive scatterer has characteristics of a Fresnel reflector and that this effect is more pronounced near the equator than at mid-latitudes.

Given the information we have about aspect sensitivity (see Figure 5.1) and θ_S (see Figure 5.2), we can use (5.9) to compute θ_{TURB}, the tilt angle at which turbulent scatter equals the Fresnel component. In other words, given the scattering mechanism described by θ_S and knowing the backscatter in the vertical direction based on the radar observations, we can use (5.9) to determine the angle off-zenith where the radar backscatter is equal to the turbulence backscatter predicted from C_n^2. We call this angle θ_{TURB}. We plot this in the left-hand panel of Figure 5.2 as the starred line. The calculation indicates that for JRO, tilting the beam more than about 4° in the stratosphere will allow turbulence to be the dominant backscattering mechanism.

We carry this analysis a step further by predicting the θ_{TURB} we would get if another radar made the same aspect-sensitive measurement under the atmospheric condition described by the *in situ* measured C_n^2 and the scattering mechanism described by θ_S. We choose the MU radar in Japan as this radar has been previously used to investigate aspect sensitivity [e.g., *Tsuda et al.*, 1997, and references therein]. The dashed line is θ_{TURB} computed for the MU radar using the average θ_S computed from the JRO data and turbulent scatter derived from C_n^2 but using the MU radar parameters. The resultant θ_{TURB} is, on average, about 7°. This is a factor of two smaller than what is typically observed at the MU radar. This calculation again supports a difference in the atmospheric conditions between Peru and Japan.

5.2 Horizontal Correlation Length

An oblate spheroid yields the backscatter diagram defined by (5.5a) and (5.5b). In this section, we want to covert θ_S into the horizontal correlation length related to the spheroid, which may provide some insight about the scatterers and aspect sensitivity. First, we will assume for mathematical conveniences that the index of refraction variations of the scatterers are elliptical in shape, as discussed in section 5.1 and described by (5.7). Based on *Hocking* [1987] and *Hocking et al.* [1989], we can describe the length-to-depth ratio of the oblate spheroid by the aspect sensitivity parameter θ_S. The relevant expression is

$$[L/h]^2 = \left(\frac{\lambda^2/h^2}{8\pi^2[\sin\theta_s]^2} + 1 \right), \tag{5.10}$$

where L is the *1/e* horizontal half-length of the scatterer, h is the *1/e* half-depth, and λ is the radar wavelength. As shown by *Briggs and Vincent* [1973], although a range of scatterers is capable of producing backscatter, the most effective are the ones with $h \approx 0.2\lambda$. Thus, there is a range of (L, h) pairs that are capable of causing the same values of θ_S. For small values of θ_S (< 10º), the equation above can be written as

$$L = 0.11\ \lambda/\sin\theta_S. \tag{5.11}$$

In other words, for small angles, θ_S gives a direct measure of the horizontal *1/e* half-length of the scatterer. This theory assumes that a Fresnel scattering mechanism is operating.

Equation (5.11) gives a measure of the horizontal correlation length of the refractive index fluctuations. Since L is the *1/e* half-width, the refractive index deviation from that of the surrounding environment falls to half of its maximum at

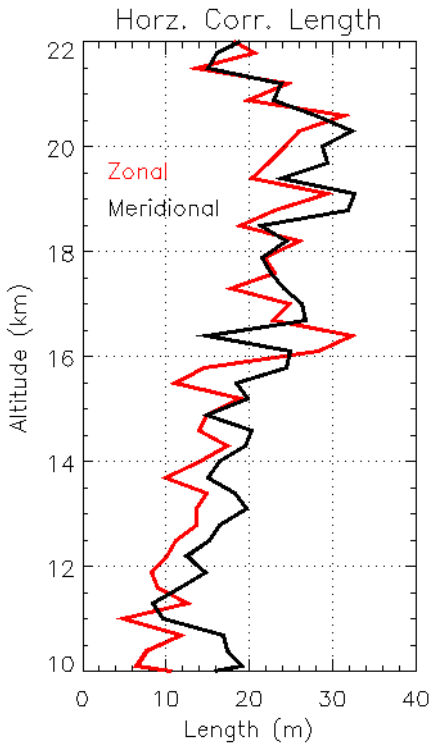

Figure 5.3: Horizontal correlation length in the zonal (red) and meridional (black) directions computed from the radar data for 2042-2122 LT on 7 September 1998. Horizontal correlation length increases from ~15 m in the troposphere to ~25 m in the stratosphere.

$L(\ln 2)^{1/2}$; $2^{1/2}$ times this gives us the width of the autocorrelation function of the scatterer. Thus, the horizontal correlation length is given by

$$\zeta = 0.13\lambda/\sin\theta_S \cong 0.13\lambda/\theta_S. \qquad (5.12)$$

Comparing (5.12) to (5.11), we note that for small θ_S, the horizontal extent and the horizontal correlation length for the scatterer are approximately equal. We plot ζ in the zonal and the meridional direction in Figure 5.3. ζ increases from ~15 m in the troposphere to ~25 m in the stratosphere. Values of ζ are about an order of magnitude less than the Fresnel radius (~200 m) at these altitudes.

It should be noted at this point that the horizontal correlation lengths deduced above may not be the same as would be determined if one were to fly a refractometer horizontally through the region because the radar measurements are sensitive to

Fourier scales of one half of the radar wavelength parallel to the radar pointing direction. A refractometer would measure fluctuations caused by the full range of vertical Fourier scales. L is therefore a measure of the length of those scattering irregularities which backscatter the radar signals, or, in other words, those scatterers with vertical extents of about one half of a radar wavelength; or more precisely, those scatterers with $h \cong 0.2\lambda$ if we adopt the description (5.7) for the shapes of the scatterers.

5.3 General Scattering Characteristic Over JRO

Thus far in this chapter, we have analyzed the aspect sensitivity observed at JRO based on one forty-minute segment of radar data. We present summary plots of the aspect sensitivity and the magnitude of the horizontal correlation length measured on 7 September 1998 as well as those computed from 40-minute averages of radar data from other days of the MIST campaign. Our goal is to provide the reader with a more general understanding of the scattering characteristics observed during the MIST campaign.

In Figure 5.4a, we examine the aspect sensitivity, as defined in equation (5.1), in the two orthogonal directions on 7 September 1998. The results in both orthogonal directions are quite similar: the average aspect sensitivity in the stratosphere is about 15 dB versus the 3-5 dB in the troposphere.

Figure 5.4b shows the meridional and zonal horizontal correlation length computed from the radar data. As indicated by the aspect sensitivity in Figure 5.4a, the horizontal correlation length in the stratosphere is larger than that in the troposphere, by a factor of two or so, in both the zonal and meridional direction. Ground clutter and receiver recovery problems prevented us from getting good measurements of the correlation length in the troposphere.

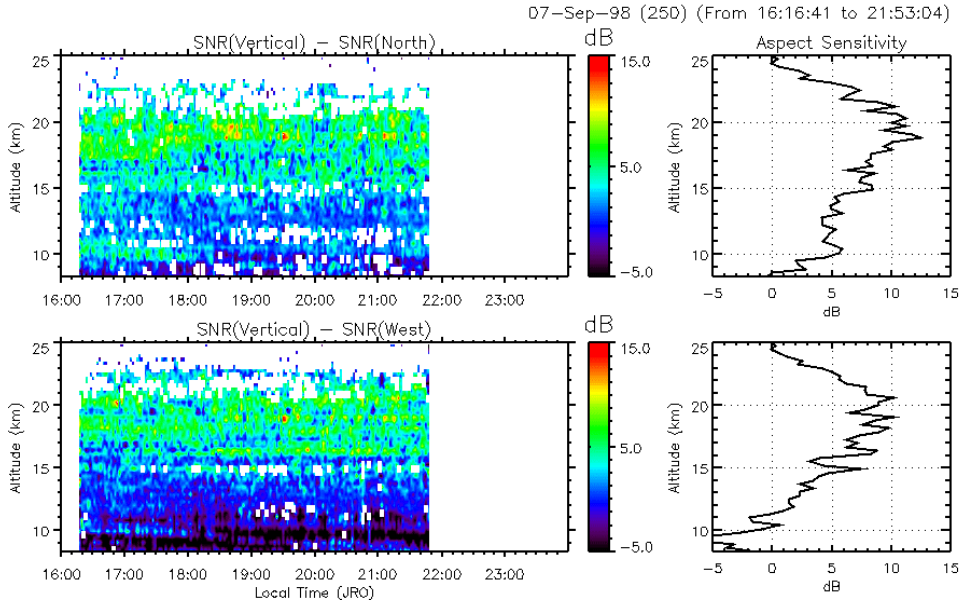

Figure 5.4a: Aspect sensitivity in the zonal and meridional direction as defined by (5.1) based on radar measurements measured on 7 September 1998.

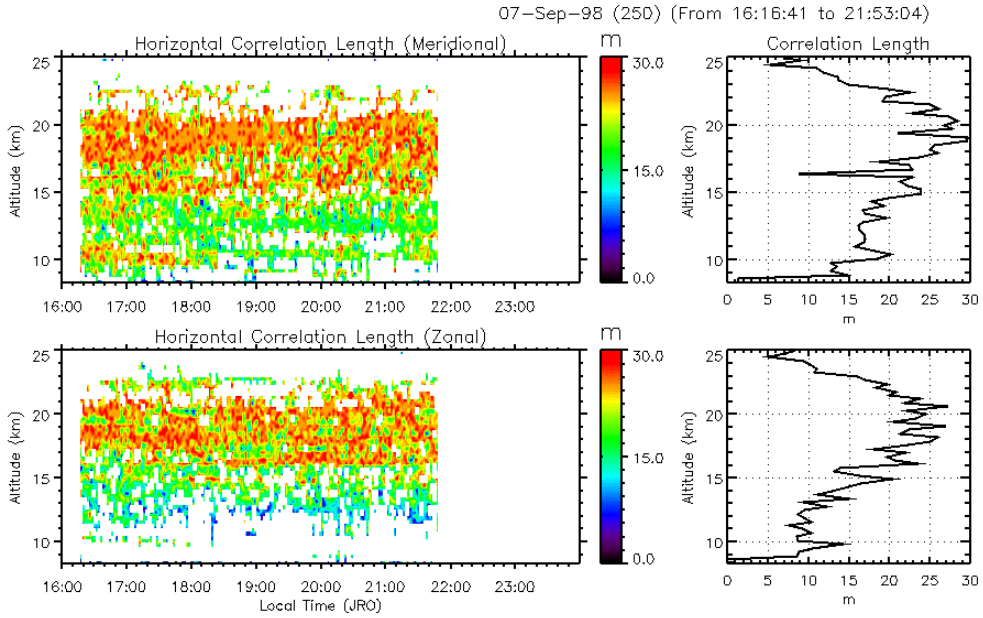

Figure 5.4b: Horizontal correlation length in the zonal and meridional direction as computed via (5.12) from the aspect sensitivity measured on 7 September 1998.

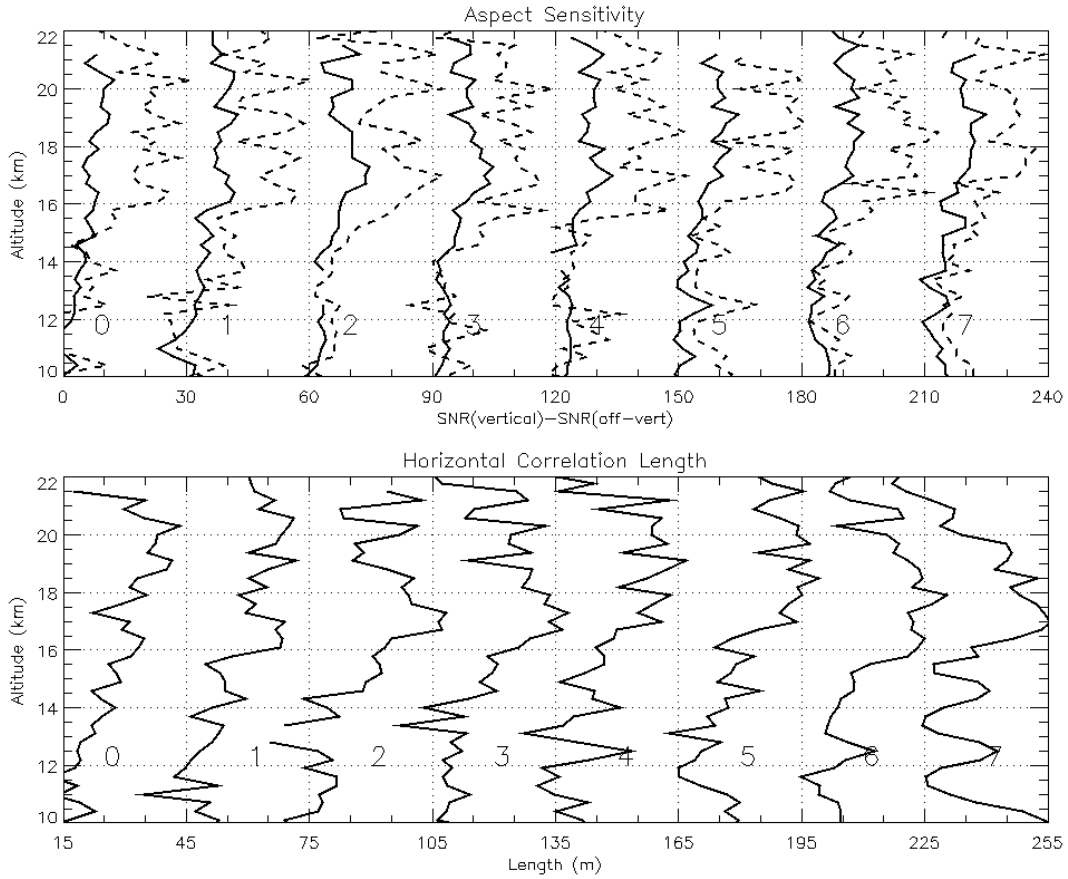

Figure 5.5: *Top panel*: Mean aspect sensitivity, as defined by (5.13), measured on 7-9 and 13 September 1998. Dashed line is the difference the SNR (in decibels) in the vertical direction and the predicted SNR as caused by turbulence. *Bottom panel*: Magnitude of the horizontal correlation length. *Key to the figure*: 0 = 09/07/98, 1900-1930; 1 = 09/07/98, 2042-2112; 2 = 09/08/98, 1900-1930; 3 = 09/08/98, 2035-2105; 4 = 09/09/98, 1910-1940, 5 = 09/09/98, 2046-2106, 6 = 09/13/98, 2000-2030, 7 = 09/13/98, 2147-2217.

In order to provide a more general understanding of the scattering characteristics in the lower atmosphere over JRO, we will present the radar data measured from 7-9 and 13 September in Figure 5.5. We have selected two 40-minute segments from each day. Each data segment corresponds to a balloon launch. The top panel of Figure 5.5 looks at the mean aspect sensitivity plotted as the solid line, which we have defined as

$$\textit{Mean AS} = \textit{SNR}(\text{vertical}) - \langle \textit{SNR}(\text{oblique}) \rangle, \qquad (5.13)$$

where $\langle \textit{SNR}(\text{oblique}) \rangle$ is an average of the SNR in the two oblique directions; we computed the $\langle \textit{SNR}(\text{oblique}) \rangle$ in linear space before converting the result to decibels.

We also include in the plot the difference between SNR(vertical) and the predicted turbulent backscatter. We have separated the plot of each data segment by 30 dB. The aspect sensitivity appears to remain fairly constant from day to day: 10 dB in the stratosphere versus 3 dB in the troposphere. Based on this result, we speculate that the atmospheric dynamics, as revealed by aspect sensitivity measurements, near the equator region differ from that at mid-latitudes and deserve more research. The bottom panel of Figure 5.5 illustrates the magnitude of the horizontal correlation length. We have separated the plot of each data segment by 20 m. Again, we see that the correlation length in the stratosphere is about 50-100% larger than that in the troposphere. Although the average aspect sensitivity and horizontal correlation length do not vary greatly from day-to-day, differences do exist. For example, for the altitude range from 16 km to 18 km, we see that the aspect sensitivity is larger for 8 September than 7 September. Regardless, this dataset does suggest that Peruvian lower atmosphere may almost always be aspect-sensitive.

5.4 Discussion and Analysis

An examination of the radar data alone, as we have in section 5.3, does not allow us to understand the structures causing the aspect-sensitive backscatter. This is mainly due to the coarse vertical resolution, typically on the order of hundreds of meters, of the radar measurement. Balloon-borne probes, launched near the radar site, have been used to overcome this shortcoming of radar measurements. Although past experiments have included balloon-borne probes launched near the radar site, seldom were the balloons launched at the radar site [e.g., *Dalaudier et al.*, 1989, 1994; *Hooper and Thomas*, 1998]. This compounds the error caused by the horizontal drift motion of the balloon where the radar and the balloon-borne instruments are observing two separate parcels of the atmosphere. In addition, past balloon flights did not carry

turbulence sensors that measured C_T^2, the turbulence parameter that can be used to compute the turbulent component of radar backscatter.

For the MIST campaign, *in situ* data from the radiosondes launched at the radar site gives us a unique opportunity to analyze the radar backscatter in the context of the atmospheric condition as revealed by *in situ* measurements. The goal of this section is to use the *in situ* measured atmospheric thermodynamic parameters and turbulence intensity and try to explain the measured radar backscatter.

5.4.1 Scattering and Stability

The vertical gradient of the potential temperature ($\Delta\theta/\Delta z$) is a measurement of atmospheric stability. Our calculations, presented in Figure 4.4, indicate an increase of atmospheric stability as a function of altitude, with the stratosphere being more stable. A comparison between Figures 4.4 and 5.1 indicates a relationship between atmospheric stability, the radar backscatter in the vertical direction, and aspect sensitivity.

A negative $\Delta\theta/\Delta z$ is indicative of a more turbulent atmosphere. As expected, $\Delta\theta/\Delta z$ is less than or near zero between 10 km and 15 km, where the aspect sensitivity is not so large. This makes physical sense; if the atmosphere is stable, it promotes the existence of stable, horizontally stratified scatterers to exist, which lead to an increase in radar backscatter.

5.4.2 Possible Scattering Mechanisms

Several pieces of evidence from the tropospheric portion of the data indicate the important role that turbulence plays in the radar backscatter in this altitude range. First, the aspect sensitivity in the upper troposphere, plotted in Figures 5.1 and 5.4a, is a few dBs. This indicates near isotropy. Furthermore, the observed SNR agrees with the expected SNR from turbulence agree up to 16 km and then begin to diverge. The

aspect sensitivity rises at 13 km as does the horizontal correlation length, as seen in Figure 5.3. Tropopause marks a transition from turbulent scatter to strikingly different scattering processes which begin to dominate beginning around 16 km; as atmospheric stability increases, the SNR in the vertical direction and the aspect sensitivity also increase.

A few models have been invoked to explain the observed aspect sensitivity. These models can be generally classified into three separate categories: Fresnel scatter, Fresnel reflection, and anisotropic turbulence. In the first case, it is hypothesized that the structures causing partial radar returns are numerous individual sheets in the beam for which the ratio of the horizontal to vertical scale is variable [*Gage and Green*, 1978; *Röttger and Liu*, 1978]. The second case proposes that the radar returns are due to extensive horizontal layers, which, under the influence of dynamic conditions, may be gently distorted [*Hocking*, 1979, 1989; *Woodman and Chu*, 1989]. One can differentiate the two scattering processes rigorously via conditions described in *Chau et al*. [2000]. In the third case, the turbulent velocity field is anisotropic, leading to a different turbulent intensity in the vertical than in the horizontal direction. In this case, the spatial Fourier transform of the change in refractive index, $\Delta n^2(\boldsymbol{r})$, at the Bragg wavelength scale is greater in the vertical than the oblique direction, leading to aspect sensitivity. Some researchers explain aspect sensitivity by drawing on all three models in which sheet-like and individual scatterers co-exist; therefore, the radar returns are aspect-sensitive but dependent on local conditions and the type of radar used [*Hocking et al.*, 1984; *Hocking*, 1989; *Woodman and Chu*, 1989]. These models envisage a thin layer of anisotropic structure (turbulent or coherent) embedded in a region of isotropic turbulence. Oblique beams, tilted typically 10-15°, would therefore only *see* isotropic turbulence whereas the vertical beam would receive scatter from both isotropic and anisotropic irregularities.

If the scatterer in the atmosphere had an infinite horizontal correlation length such that the scatterer acts like a reflector, i.e., a Fresnel reflector, isotropic turbulence will be seen when the radar beam is tilted just slightly off-vertical; this result has not been observed. Therefore, Fresnel scattering seems to be a reasonable explanation for the measured finite aspect sensitivity and correlation length. However, we cannot rule out the possibility that anisotropic turbulence is responsible for the measured aspect sensitivity. To settle this controversy, we will look at the length and height parameters of the anisotropic turbulence that can be produced under the atmospheric condition measured by the balloon sounding.

Hocking and Hamza [1997] examined the likelihood of anisotropic turbulence as the source of aspect sensitivity. They examined how wind shear will act to disturb the initially isotropic eddies, where the scales are within the inertial range of turbulence, where normal turbulence theory predicts that, in the absence of external distorting effects, the scales should normally tend towards isotropic irrespective of any initial anisotropy at the generating scales [*Bradshaw*, 1975]. *Hocking and Hamza* [1997] developed a simple expression that places limits on the degree of anisotropy that can reasonably be expected because of turbulence. The theory examines how wind shear will act to distort initially isotropic eddies. We summarize their discussion here. We assume that turbulence at the scale of interest (in our case, 3 m) is initially isotropic.

Let us first consider how an eddy diffuses. Consider a circularly shaped eddy of size h'. The mean square diameter of such an eddy will be approximately $h'^2 \sim Kt$, where t is the time since the eddy was created and K is the scale-dependent diffusion coefficient. The scale dependence arises because diffusion within an eddy which takes place because of the motions of even smaller eddies which are embedded inside it, and the net diffusion is the cumulative effect of all such smaller eddies. By dimensional considerations, $K \sim h'v$, where v is a typical velocity associated with movement within the eddy (typically considered to be comparable with the speed of rotation of a

particle towards the perimeter of the eddy) and if we let the turbulent energy dissipation ε be $\sim v^2/t \sim v^3/l$, then $K \sim h'^{4/3}\varepsilon^{1/3}$. Substitution for K in the equation $h'^2 \sim Kt$ therefore gives

$$h'^2 \sim \beta\, \varepsilon\, t^3, \tag{5.14}$$

where β is a dimensionless constant of order unity. This is a well known relation first noted by *Bachelor* [1950].

Consider now the initial diameter of the isotropic eddy, denoted by h_o. The eddy will diffuse outward as time progresses, but it will also be stretched horizontally by the wind shear. It will also gradually destroy itself during this process, and the energy it contains will cascade to smaller eddies, but we are interested in the initial period of diffusive expansion. After time t, the vertical extent (vertical scale) of the eddy will be given by h, where

$$h^2 \sim \beta\, \varepsilon\, t^3 + h_o^2. \tag{5.15}$$

Since the eddy was considered small at time $t = 0$, and we expect the degree of anisotropy to grow larger as the eddy evolves, we can neglect the small h_o term, at least to the first order, to give

$$h \sim \sqrt{\beta \varepsilon t^3}\ . \tag{5.16}$$

What happens to the eddy over a long time? Well, the eddy will rotate, and after a quarter cycle it will be aligned against the mean shear. As the eddy rotates, it will become twisted and stretched in a chaotic manner, so the process is not reversible. Once the eddy rotated half a cycle, it is conceivable that the mean wind will again try to return the eddy to its original shape, but in fact it will only succeed in twisting and deforming the shape even further. This process will be especially enhanced by the presence of larger scale eddies in the vicinity which will also impart their own shearing and tearing motions to the eddy. We depict the eddy development in Figure 5.6.

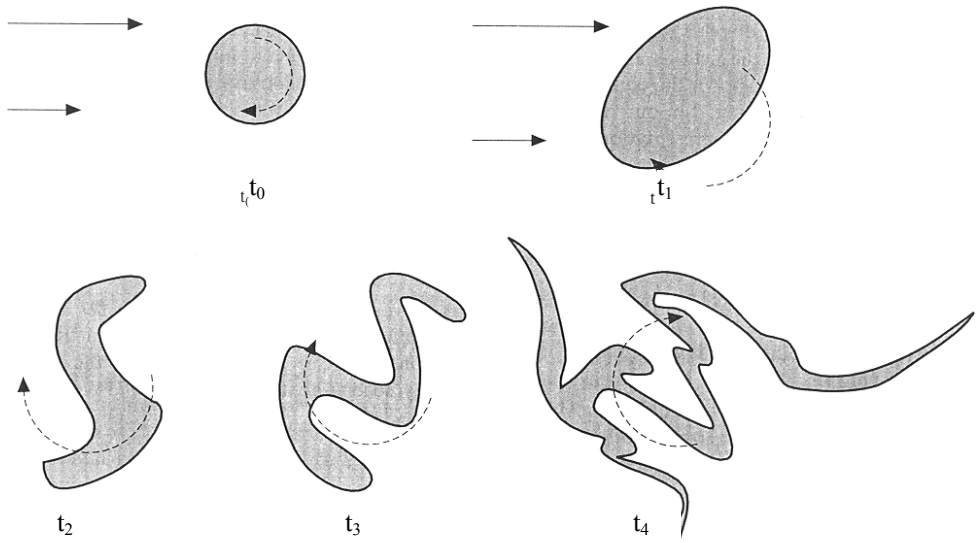

Figure 5.6: An artist's rendition of the way in which an eddy is distorted by a wind shear as time progresses. Adapted from *Hocking and Hamza* [1997].

Given this initially isotropic turbulence that is being structured and rotated and torn by the background atmosphere, we quantify the amount of horizontal stretching by $\Delta x \sim (\Delta v)t$, where Δv is the velocity difference between the top and bottom of the eddy, or $\Delta v = h\left(d\bar{u}/dz\right)$. If we consider the diffusive and wind-shear induced stretching to be additive, then we may write

$$L \sim \sqrt{\beta \varepsilon t^3} + \frac{d\bar{u}}{dz} ht \,. \tag{5.17}$$

However, we already know that $h \sim \sqrt{\beta \varepsilon t^3}$ so we may use this to substitute for t in the above equation. We are especially interested in the degree of isotropy, so let us examine the ratio L/h. The result is

$$\frac{L}{h} \sim 1 + \left|\frac{d\bar{u}}{dz}\right| h^{2/3} \beta^{-1/3} \varepsilon^{-1/3} \,. \tag{5.18}$$

Equation (5.18) shows that, for larger eddies, the degree of anisotropy is larger, a result which might be expected intuitively, since larger eddies are longer-lived and

have more time to suffer the effects of the wind shear. It can be shown that this can be recast as

$$L/h \sim 1 + 0.75 \times 2\pi\beta^{-1/3}\gamma\left|\frac{du}{dz}\right|N^{-1}, \tag{5.19}$$

where β and γ are constants of order unity, *du/dz* is the horizontal wind shear, and *N* is the Brunt-Väisälä frequency. Assuming that $h \sim 0.2\lambda$, the *in situ* measured wind and atmospheric thermodynamic parameters allow us to compute the θ_S expected from anisotropic turbulence using (5.10) based on (5.19). We have plotted this in the right hand-panel of Figure 5.2. This theory cannot, in itself, prove the existence of anisotropic turbulence. However, it does place lower limits on the values of θ_S that can be expected because of anisotropic turbulence. Thus, we can be quite sure that if we measure values of θ_S falling below this limit, we truly have a specular reflecting process at work. Indeed, comparing θ_S derived from anisotropic turbulence with the measured θ_S plotted in the left-hand panel of Figure 5.2, we see that the former is about an order of magnitude greater than the latter. This argues against a role for anisotropic turbulence in aspect-sensitive scatter. It seems that the probable cause for aspect sensitivity is horizontally stratified coherent structures whose horizontal extent is about an order of magnitude less than the Fresnel radius (the Fresnel radius for JRO is about 200 m for 10 km < *z* < 22 km), implying Fresnel scattering [*Chau et al.*, 2000]. We do not deny the possible existence of anisotropic turbulence, but we do believe that it plays a minor role in aspect-sensitive scatter. However, for this JRO dataset, while it is likely that some of the aspect sensitivity can be explained by anisotropic turbulence, considering echoes of such stable, slowly fading character and such strong aspect sensitivity, it really becomes hard to believe that the radar backscatter is due to turbulence.

Regardless of the cause of the aspect sensitivity of the scatters, another scattering phenomenon worth noting is the decrease in SNR for *z* > 22 km. This is seen in

Figures 4.8, 5.1, and 5.4. To explain similar observations, *Hocking* [1980] proposed that both turbulence and specular scatterers exist at all heights. He assumed that the scattering scale size is comparable to the inner scale of turbulence. As the altitude increases, the kinematic viscosity increases exponentially and so the depth of any specular reflecting structures increases markedly. Hence, these structures become less efficient reflectors with increasing height. The turbulent component of the backscattered signal does not fall off so rapidly; at very high heights, scatter from turbulence occurs at scales within the viscous range; this only arises at heights much higher than the heights where specular reflection becomes inefficient. For any radar, there is an upper altitude limit, above which specular reflectors become very inefficient and no reflected signal is detectable.

A close examination of Figures 4.8 and 5.1 indicates a return to near isotropy in the radar backscatter at heights above 22 km that are no doubt important for the understanding of atmospheric dynamics. For example, this might be an indicator that buoyancy waves are beginning to *saturate* even at these low heights in the atmosphere, and, if this is so, it may mean that there is a transfer of momentum from the waves to the mean flow even at 20 km [*Lindzen*, 1981]. A considerable amount of extra work is needed in order to determine just what this change in aspect ratio means for the atmosphere. Yet, this aspect ratio change cannot be ignored and will have at least some implications for the dynamics of the atmosphere. It is also worth noting that the turbulent diffusion coefficient in the atmosphere has a local minimum in the lower stratosphere. The weak level of turbulence in the lower atmosphere allows a greater degree of stability and therefore allows more anisotropic scatterers to be stable [*Chakrabarty et al.*, 1987].

5.4.3 On the Origin of Scattering Structures

The generation mechanism(s) for these Fresnel scattering layers is still a very controversial subject. Several hypotheses were investigated: *Bolgiano* [1968] explained these scatterers as a consequence of Kelvin-Helmholtz instabilities (KHI). The turbulence in a stable atmosphere is produced by the wind shears that give rise to KHI. The mixing of the turbulent layer leads then to strong gradients at the boundaries. *Van Zandt and Vincent* [1983] suggested that these structures were associated with low-frequency buoyancy waves, but *Hocking et al*. [1991] refuted this hypothesis because the equiphase planes of these waves are necessarily tilted several degrees from horizontal due to viscosity. Consequently, low-frequency buoyancy waves cannot explain the reflected echo received at vertical incidence.

One could surmise that the turbulence was spatially inhomogeneous and did not exist directly over the radar. This could permit very stable conditions immediately overhead, allowing the stratified structures to exist. Elsewhere exist small patches of turbulence which could contribute to the small amount of backscatter observed with the off-vertical beams. Turbulence scatter will not persist for hours. Nevertheless, such a model involves a rather specific and contrived set of circumstances, and it would be preferable if a more general model could be found which does not have such a degree of spatial requirements [*Hocking et al.*, 1991].

Hocking et al. [1991] proposed that damped diffusive waves, i.e., viscosity waves, could be responsible for the specular reflectors both in the stratosphere and the mesosphere. These waves would arise from partially reflected gravity waves and from gravity waves that become strongly nonlinear and then reach a critical level. They are strongly damped and they would propagate only on a vertical distance of the order of one vertical wavelength (λ_z). This wavelength is proportional to the square root of the viscosity (or thermal conduction) and to the temporal period T of the primary gravity wave. The authors showed that the equiphase plane could be almost horizontal,

justifying the vertical nature of the specular reflection. These kinds of waves would produce temperature (or density) fluctuations which, added to the mean gradient of the zone where they are created, can have the appearance of the sheets observed by our measurements. Moreover, they noted a good agreement between the vertical scales of the viscous waves and the Bragg scales of regions of highest aspect sensitivity in the stratosphere (at VHF frequencies). The values of the gravity wave period and viscosity parameters in the stratosphere can produce viscosity wave wavelengths of the order of the observed sheet thickness.

Furthermore, *Hocking et al.* [1991] concluded that a viscosity wave horizontal perturbation velocity of the order of 1 cm/s is sufficient to generate the typical values of C_n^2 at 20 km in the stratosphere. *Hocking et al.* [1991] and *Hocking* [1995] predict the backscatter in the vertical direction caused by viscosity waves. According to their theory, the peak of the reflection coefficient (R) is defined as

$$R = 6.4 \text{ x } 10^{-5} \left| \rho'_A \right|, \tag{5.20}$$

where $\left| \rho'_A \right|$ is the density fluctuation caused by the viscosity wave. This can be re-expressed by vertical and horizontal wave numbers as well at the atmospheric thermodynamic parameters

$$R = 6.4 \text{ x } 10^{-5} \rho_o \frac{N^2}{g} \frac{k}{|m|} \frac{1}{\omega} u'_A, \tag{5.21}$$

where ρ_o is the atmospheric density, N is the Brunt-Väisälä frequency, g is gravity, ω is the frequency of the viscosity wave, u'_A is the horizontal perturbation velocity, m is the vertical wave number, and k is the horizontal wave number. As we will see later, R is related via u'_A to C_n^2.

Hocking [1995] proposed that the potential temperature steps might be related to viscosity waves. In particular, the edges of the temperature step, with their high Brunt-Väisälä frequency, will strengthen the efficiency of the backscatter of viscosity waves as well as permit these waves to grow to larger amplitudes before they become

unstable. The multi-instrument campaign dataset from JRO is ideal in examining this proposal.

We test the viscosity wave theory with the temperature steps observed in Figures 4.4 and 4.5. Let us compute (5.21) for this JRO dataset. As seen in Figure 4.6, $N^2 = 2\times10^{-3}$ [rad/sec]^2 at the edges of the temperature steps. To compute R via (5.21), we will choose ρ_o = 0.1 kg/m^{-3} near 18 km, g = 9.8 m/s^2, and $|m|$ = 2π/1.5 m^{-1}, N = 2π/3600 [rad/sec], and take the horizontal wavelength to be 50 m. This gives us

$$R \approx 2.245\times10^{-8}\, u'_A . \tag{5.22}$$

Hocking and Vincent [1982] derived a relationship that relates C_n^2 to R:

$$R^2 = 0.38\lambda^{-1/3} C_n^2 \theta_{1/2}^2 L, \tag{5.23}$$

where L is the pulse length and $\theta_{1/2}$ is the two way half-power half width. In our case, λ = 6 m, L = 300 m, and $\theta_{1/2}$ = 0.5°. This yields

$$C_n^2 = 209.3\, R^2, \tag{5.24}$$

which, with (5.22) gives us

$$C_n^2 = 1.055\times10^{-13}(u'_A)^2. \tag{5.25}$$

Following *Hocking* [1995], let us say that there are five viscosity waves within the radar pulse length, then C_n^2 would be five times larger, giving us

$$C_n^2 = 5.275\times10^{-13}(u'_A)^2, \tag{5.26}$$

where we have assumed that u'_A is the amplitude of all the viscosity waves. From Figure 4.3, we notice that he typical value of C_n^2 is 10^{-17}. This gives us a value of the velocity amplitude of only $u'_A \approx 0.435$ cm/sec. We can compute the corresponding Richardson number via

$$Ri = N^2 \big/ \left(|m| u'_A\right)^2 , \tag{5.27}$$

which gives us $Ri \approx 1.09\times10^{-3}$. This is ~$10^3$ larger than the measured value; this result may not be trustworthy, as height resolution of the wind resolution is too coarse to yield an accurate indication of the wind shear. Unfortunately, this backscattering strength is still about two orders of magnitude less than the measured backscatter from

the vertical direction (see Figure 5.1). However, if $u'_A \approx 40$ cm/sec, this would give us $C_n^2 \approx 10^{-15}$, which would gives us a backscatter comparable to the measured backscatter from the vertical direction. With this result, we cannot deny that viscosity waves do not contribute to radar backscatter; yet, it seems that viscosity waves may not be the cause of backscatter. According to *Luce et al.* [1995], the viscosity wave model is inadequate because it would predict unstable temperature sheets associated with unrealistic index of refraction perturbations. However, the physical model behind viscosity waves seems interesting and it is possible that a modified version of this model can account for some of the observed temperature sheets.

We believe that the potential temperature steps, whose edges may be responsible for the measured radar backscatter, are instead caused by Kelvin-Helmholtz instability (KHI) – a dynamic instability – in the atmosphere. Our first evidence originates from the similarity between the observed temperature structure in Figures 4.4 and 4.5 with the vertical profile of the vertical profile of a 3D simulation of the KHI, seen in Figure 3.15. We examine this proposal in Chapter 7.

5.5 Conclusion

In this chapter, we have presented the radar and balloon data taken at the Jicamarca Radio Observatory (JRO). In general, the radar backscatter is aspect-sensitive in the stratosphere and less so in the troposphere. Only in the lower range gates do we detect what might be called isotropic turbulence. For $z > 13$ km, the aspect sensitivity and the horizontal correlation length ~ 25 m (roughly 10% of the Fresnel scale for the VHF radar at that height) strongly argue for a Fresnel scattering mechanism.

Regarding the controversy of Fresnel scatter versus anisotropic turbulence, our results seem clear. Our correlation lengths are much too large to be explained by anisotropic turbulence as according to the theory presented by *Hocking and Hamza* [1997]. On the other hand, the correlation lengths are too small for Fresnel reflection.

We have strong evidence that the temperature steps play a strong part in the measured radar backscatter. These temperature steps may be caused by a dynamic Kelvin-Helmholtz instability instead of viscosity waves.

We will examine the computer simulations of stratospheric dynamics to see if the final state of the dynamical evolution of shear instabilities will mimic the temperature structures and the underlying, weakly turbulent phenomena we find in this dataset. We will examine this in Chapter 7. Before doing that, we examine the turbulence parameters as measured by the *in situ* turbulence sensor and the VHF radar.

Chapter 6

Turbulence Parameter Measurement

Turbulence in the presence of gradients in the index of refraction can set up small-scale irregularities in the index of refraction which scatter radio waves. There are a number of possible turbulence generation mechanisms. Common sources of energy for turbulent fluctuations, in velocity and passive scalar, are large-scale anisotropic eddies produced from atmospheric events such as, among others, atmospheric gravity waves and wind shear produced by Kelvin-Helmholtz instabilities. Other sources are jet streams and convection during the passage of a cold front or thunderstorm. The energy then cascades continually downward to smaller-scale sizes until it is finally dissipated by viscosity. Several scale sizes then characterize the turbulence: the scale of the largest anisotropic eddies, the scale where the turbulence becomes isotropic, and the scale where the turbulence is strongly damped by molecular viscosity. The region where the turbulence can be considered isotropic and not highly damped is called the inertial subrange. Turbulence measurement theories have been developed assuming that the scale of interest is in the inertial subrange, which is valid for VHF radars and *in situ* instruments. *Hocking* [1985] summarized this fact via a plot which we have reproduced in Figure 6.1.

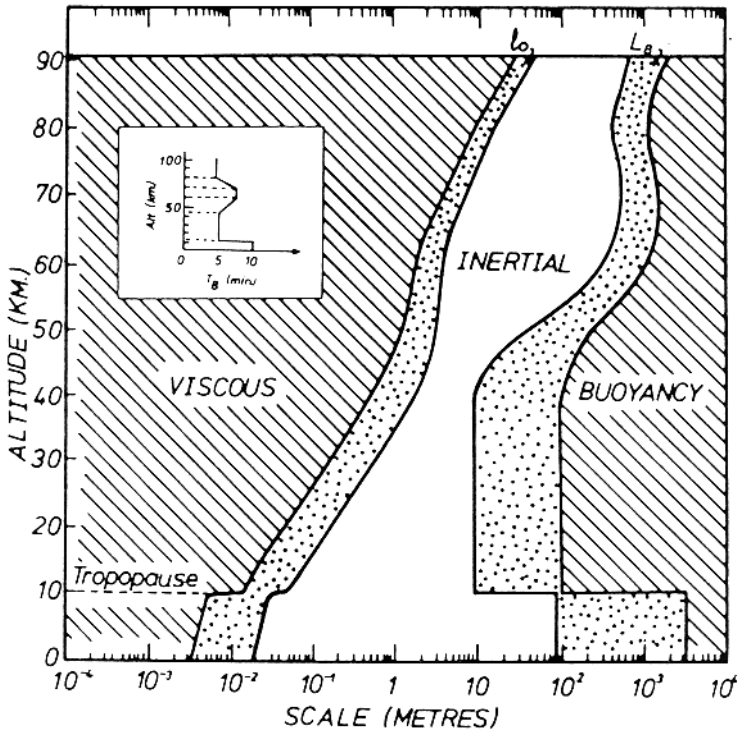

Figure 6.1: Typical inner and inertial range/buoyancy range transition scales for turbulence in the atmosphere. The inner scale is defined as $l_0 \approx 7.4\sqrt{\nu^3/\varepsilon}$ [e.g., *Hill and Clifford*, 1978]. Buoyancy scale is defined as $L_B \approx (2\pi/0.62)\varepsilon^{1/2} N^{-3/2}$ [*Weinstock*, 1978]. The profile of the assumed Brunt-Väisälä period (τ_B) is also shown in the insert. Shaded region is the transition between the inertial range and the viscous and buoyancy ranges [After *Hocking*, 1985].

To describe the morphology of turbulence, it is necessary to calculate certain parameters associated with it. Two important parameters are the refractive index structure function coefficient C_n^2, which is related to the temperature structure function coefficient (C_T^2), and the kinetic energy dissipation rate (ε). The former is a measure of the refractive index (or temperature for C_T^2) fluctuations induced by turbulence and the latter is a measure of the severity of turbulence. C_n^2 is related to C_T^2 via temperature and pressure, as seen in Chapter 3. More specifically, ε quantifies the energy deposited as heat into the atmosphere, per unit mass and per unit time.

These turbulence parameters can be measured via *in situ* probes and radars. The dataset from the MIST campaign provides us a chance to compare the radar and

balloon measurements of turbulence parameters. Such a comparison will demonstrate a radar's ability to measure accurately the atmospheric turbulence intensity and provide a consistency check for the different turbulence measurement techniques. Furthermore, this will help us understand the dynamic properties governing clear air turbulence echoes in the optically clear air of the lower atmosphere. Therefore, the goal of this chapter is to examine and compare the atmospheric turbulence intensity as revealed by the radar and *in situ* instruments.

This chapter is organized as follows. We will examine two radar-based techniques of atmospheric turbulence measurements; their limitations are also discussed. We then compare the turbulence parameters computed from the radar data and compare that to the results of the balloon measured parameters.

6.1 Measurement Methodology

Turbulence measurement techniques use aspects of how turbulence affects the local atmospheric medium. Turbulent motion causes temperature and, hence, refractive index fluctuations. *In situ* turbulence sensor measures the local temperature fluctuations which, via turbulence theory, yield information about the turbulence intensity as discussed in Chapter 3. On the other hand, there are two independent ways in which a radar can measure turbulence parameters. Both measurement methods are dependent on turbulent atmospheric motion.

At radio wavelengths, the humidity and its gradients as well as the temperature gradients contribute significantly to the refractive index. A radar measures turbulence intensity by remotely sensing the effects of refractive index fluctuations on the scatter of electromagnetic waves. There are two ways a radar can measure atmospheric turbulence intensity. The turbulence parameter C_n^2 can be derived from the radar backscatter via first the relationship between backscattered power and a beam-filling scatterer and second, the relationship between the volume reflectivity and C_n^2.

Turbulence mixes the refractivity structures in the atmosphere such that random irregularities of refractive index result. The power is scattered back from these irregularities at the Bragg scale, i.e., one half the radar wavelength; for JRO, the Bragg scale is 3 m. Therefore, the received power no longer results from reflection at a deterministic discontinuity, but from the reflection at many disordered turbulent refractivity irregularities. Assuming that these scatterers fill a volume defined by the radar beam width and pulse length, the radar equation yields the received power from volume scatter

$$P_r = \frac{P_t \cdot G \cdot \lambda^2 \cdot \Delta z}{16\pi^2 z^2} \cdot \eta, \tag{6.1}$$

where Δz is the range resolution of the radar, η is the total backscatter cross section per unit volume, and G is the gain of the radar [*Röttger and Liu*, 1978b]. Once η is known, we can compute C_n^2 via (5.2).

$$\eta(\lambda) \approx 0.38 C_n^2 \lambda^{-1/3} \ [\mathrm{m}^2/\mathrm{m}^3], \tag{5.2}$$

where λ is the radar wavelength [e.g., *Ottersten*, 1968, 1969a, b].

However, in order to be able to use radars to measure turbulence intensities, it is necessary to verify that the entire scatter is due to isotropic turbulence. Often, this is not the case, since, as we have discussed in earlier chapters, the existence of quasi-specular reflection is well known [e.g., *Gage and Green*, 1978; *Röttger and Liu*, 1978]. In the MIST campaign, the data manifested characteristics of specular reflection, as indicated by the aspect-sensitive lower stratosphere (see Figures 4.8, 5.1, and 5.4). Specular reflections can seriously modify the received signal, compared to what it would have been if the scatter were due to turbulence alone (see Figure 5.1) and therefore complicate the extraction of turbulence estimated from the signal. As turbulence calculation based on radar backscatter rests on the assumption that the entire scatter is due to isotropic and homogeneous turbulence, we want to evaluate in

this chapter the results of the violation of this assumption. In our dataset, humidity is negligible at the altitude range where the radar data are available.

We emphasize that this method gives an effective value of C_n^2 but unfortunately does not give the true structure function constant of the turbulence itself. It would if the turbulence fills the radar volume. In reality, however, turbulence occurs within horizontal layers, with depths of tens to hundreds of meters [*Woodman and Guillen*, 1974; *Van Zandt et al.*, 1978; *Crane*, 1980; *Weinstock*, 1981]. Thus, scattering within the radar volume is usually from a few thin layers. In other words, if the balloon-measured C_n^2 (hereafter referred to as C_n^2(balloon)) were an accurate measurement of the background turbulence, and given a radar-measured C_n^2 (hereafter referred to as C_n^2(radar)), we could relate the two C_n^2 by

$$C_n^2(\text{balloon}) = C_n^2(\text{radar})/F, \tag{6.2}$$

where F is the filling factor. In our calculations, we assume $F = 1$.

Another indication of turbulence intensity comes from the spectral width of the Doppler spectrum, which is a measure of how turbulent motion affects the incident radar signal [e.g., *Ottersten*, 1969a; *Van Zandt et al.*, 1978; *Hocking*, 1985]. The spectral width due solely to the random motion of the scatterers (denoted by f_{turb}) can be determined from the formula

$$f_{turb}^2 = f_e^2 - f_b^2, \tag{6.3}$$

where f_e is the experimental half-power half-width and f_b accounts for the non-turbulent processes contributing to the spectral width. Finite beam width broadening of the spectrum due to the vertical shears in the horizontal wind is an example of a non-turbulent process that will affect the radar spectral width [e.g., *Nastrom*, 1997, and references therein].

We can connect f_{turb}^2 of the Doppler spectrum to the variance of the radial (line of sight) velocity $\langle V^2 \rangle^{1/2}$, where V is the deviation from the mean radial velocity and $\langle\rangle$ indicates an ensemble average, inside the sampled volume through the relationship

$$<V^2> = (\lambda/2)^2 f_{turb}^2/(2 \ln 2). \quad (6.4)$$

To extract turbulence parameters from f_{turb}^2, we postulate that we observe the entire inertial subrange obeying the Kolmogorov –5/3-power law for the power spectrum of a passive scalar. Following the discussion by *Hocking* [1983b, 1986b], we write [*Frisch and Clifford*, 1974; *Bohne*, 1982]

$$\frac{3}{2} < V^2 > \approx \int_{k_B}^{k_v} \alpha \varepsilon^{2/3} k^{-5/3} dk \,, \quad (6.5)$$

where α (≈ 1.5) is the Kolmogorov constant, ε is the mean kinetic energy dissipation rate, $k_B \cong N/\sqrt{< V^2 >}$ is the lowest wave number of the inertial subrange (the highest wave number of the buoyancy subrange), N is the Brunt-Väisälä frequency, and k_v is the highest wave number of the inertial subrange (the inverse dimension of the minimum eddy surviving in a viscous atmosphere). Performing the integration on the right-hand of (6.5) and noting that ε is constant in the inertial subrange, we obtain

$$\varepsilon_{radar} = C <V^2> N, \quad (6.6a)$$

where

$$C = \alpha^{2/3} \left[1 - \left(k_B / k_v \right)^{2/3} \right]^{-3/2} . \quad (6.6b)$$

We define ε_{radar}, the mean rate of the energy dissipation, as a radar measurement of the rate at which the kinetic energy of the turbulent velocity fluctuations is removed by viscous damping. *Weinstock* [1981] showed that C = 0.4. The derivation of these relations, which contain some subtleties, is based on the works of *Tatarski* [1961] and [*Hocking*, 1985, 1999].

We define an effective radar measured C_n^2 based on ε_{radar} via

$$\varepsilon_{radar} = \left(1.43 C_n^2 N^2 / M^2 \right)^{3/2} \quad (6.7)$$

[*Van Zandt et al*., 1978; *Gage et al.*, 1980; *Hocking*, 1985; *Hocking and Mu*, 1997; *Hocking*, 1999]. M^2 is the square of the mean vertical gradient of the potential refractive index defined as [*Ottersten*, 1969a, b],

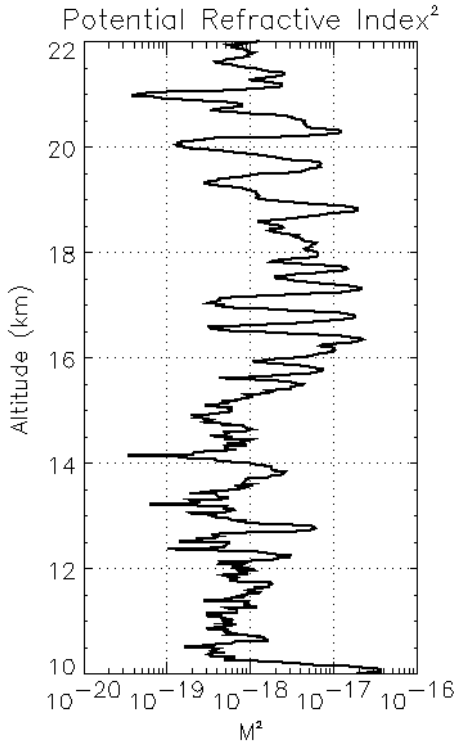

Figure 6.2: Square of the mean vertical gradient of the potential refractive index (M^2).

$$M = -77.6\times10^{-6}\ \frac{P}{T}\left(\frac{\partial \ln\theta}{\partial z}\right)\left[1+\frac{15500q}{T}\left(1-\frac{\partial \ln q/\partial z}{\partial \ln\theta/\partial z}\right)\right], \qquad (6.8)$$

where P is the pressure in millibars, T is temperature, q is the specific humidity, and θ is the potential temperature. The term in the square brackets was denoted as χ by *Van Zandt et al.* [1978]. χ tends to unity as humidity tends to zero, as it is the case for the upper troposphere and lower stratosphere. In the lower troposphere, M depends very much on the humidity gradient. On the other hand, the potential temperature term dominates M for the upper troposphere and higher.

M describes changes in the potential refractive index in terms of the potential temperature as an air parcel is displaced in the atmosphere by turbulent motion. When air parcels are displaced in the atmosphere by turbulent mixing, inhomogenieties are created because the characteristics of the displaced air parcels differ from the characteristics of their nearby environment. The pressure of the displaced parcels

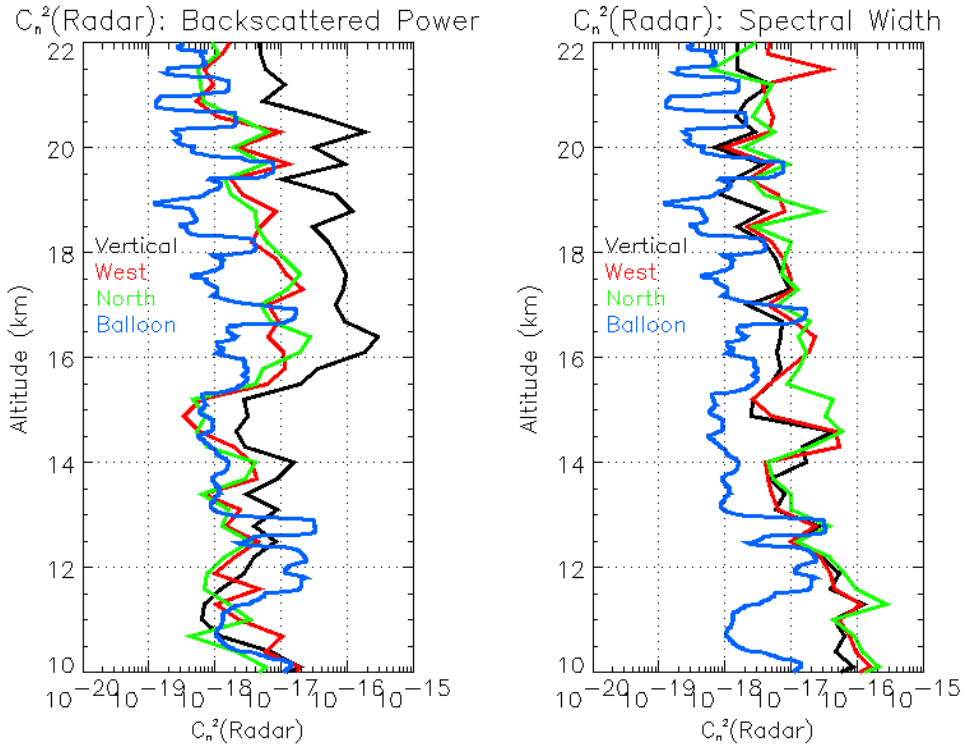

Figure 6.3: *Left panel*: C_n^2 derived from the radar-backscattered power. *Right panel*: C_n^2 derived from the radar spectral width. C_n^2(balloon) is the blue solid line in both panels.

undergoes a continuous equalization with the environment. This process changes the temperature and water vapor pressure of the air parcels. Their potential temperature and specific humidity are preserved. Consequently, the resulting inhomogenieties in refractive index are best characterized by the differences in potential temperature and specific humidity between the regions exchanging the air parcels. This quantity is M [*Ottersten*, 1969a, b]. On the other hand *Tatarski* [1961] defines M as the index of refraction that an air parcel would attain if brought adiabatically to standard pressure, assuming that the specific humidity of the air parcel maintains its value. We plot M^2 in Figure 6.2. We offer one caveat. Because of the dependence of M on humidity and potential temperature, both of which vary considerably, it is not accurate to interpret C_n^2 as a direct measure of turbulence intensity. ε is a more direct measure of turbulence intensity.

6.2 Measurement Comparison

We present the turbulence intensity computed from the *in situ* and radar data in Figure 6.3. In the left-hand panel of the figure, we plot C_n^2(radar) derived from the radar backscatter. We have smoothed C_n^2(balloon), the balloon measured C_n^2, to the vertical resolution of the radar data. In the aspect-sensitive stratosphere, C_n^2(radar) is almost always larger than the *in situ* measurement. We believe this is due to contamination from the non-turbulent scatter. The agreement is better in the upper troposphere, where the atmosphere is more isotropic. An exception is seen for altitudes below 13 km, where C_n^2(balloon) is about an order of magnitude larger than C_n^2(radar).

Since we can use the spectral width to calculate the turbulence energy dissipation rate via (6.6a), we can use that with (6.7) to backward calculate the effective C_n^2 as predicted by the spectral width method. We plot this result on the right-hand panel of Figure 6.3. We see that the spectral width method is able to capture most of the peak features in C_n^2(balloon), except between 13-15 km, where C_n^2(balloon) is over-estimated by 4-10 dB.

6.3 Discussion

6.3.1 Turbulence Parameter Measurement Comparison

Looking at our turbulence parameter computed from the radar backscatter, as shown in the left panel of Figure 6.3, we suspect that contributions from quasi-specular echoes in the radar backscatter power yielded C_n^2(radar) that is larger than C_n^2(balloon) by 10-20 dB. This contamination is stronger in the stratosphere than the troposphere, possibly due to the increased stability in the former. Using C_n^2(balloon) as a reference, we see that the quasi-specular echo contamination is more prominent in C_n^2(radar) derived from the vertical beam than it is for the oblique beam signals. The 10 dB difference between C_n^2(balloon) and C_n^2(radar) in favor of C_n^2(balloon) for altitudes between 11 km and 13 km reveals a limitation in measuring C_n^2 from the

radar backscatter. We suspect that a number of intense turbulence patches exist in this altitude range, as revealed by C_n^2(balloon), but these patches do not fill the entire radar range volume. Therefore, a radar measures an equivalent patch of turbulence filling the entire range volume that is a factor of 10 smaller than C_n^2(balloon). In other words, via (6.2), the filling factor (F) is 0.1.

The spectral width gives us C_n^2(radar) that is a slightly better estimate of C_n^2(balloon) in the stratosphere; however, there are still instances where the spectral width underestimates C_n^2(balloon). One possible explanation is that the turbulence is too weak to be measured accurately by the radar spectral width. Alternatively, one may suggest that that we did not adequately remove the shear and beam broadening effects present in the Doppler spectrum, although this seems unlikely to account for a 5-10 dB difference. Furthermore, the beam broadening effects are very small when the vertical beam data are used, given the narrowness of the radar beam. It is also possible that at these altitudes the balloon and the radar do not share a common volume. In other words, the balloon has drifted away from the radar site such that the *in situ* probes and radar probe different parcels of air.

This is perhaps an appropriate place for us to comment on some caveats on using a radar to measure turbulence parameters. A radar operates in the frequency band of 2-100 MHz generally use pulse resolutions on the order of hundreds of meters. They achieve continuous coverage in height and time, which is especially important for intermittent turbulence, as a single balloon-borne *in situ* probe measurement is very likely to miss many cases of strong, short-lived turbulence; yet such bursts of activity are the very thing that can cause the most severe aircraft damage. A radar's ability to examine gross features of turbulence in an altitude region which is inaccessible to radiosondes is its strength.

Radars are ideal for long-term observations of atmospheric turbulence but have their shortcomings. For example, it is difficult to use the radars to make any precise

measurement of atmospheric turbulence, due to the poor spatial resolution. For example, detailed study of turbulence has shown that turbulence is extremely intermittent [*Tennekes*, 1973]. The turbulence parameters ε and C_n^2 can vary by a factor of 100 or so in short time intervals. In other words, a radar can only measure an average turbulence intensity of a parcel of air. Balloon-borne probes, on the other hand, can make measurements with high-resolution but they cannot observe the atmosphere continuously, due to economic reasons. Recently, such instruments as blimps, kites, and powered parachutes, which are designed to carry aloft an instrument package, have been developed for repeatable *in situ* measurements. However, these measurements are currently restricted to the planetary boundary layer. Further developments of radar and *in situ* probe technology are needed. The multiple-instrument approach is perhaps the currently most accurate way of observing the atmosphere.

When we make radar measurements of the turbulent energy dissipation rate, we assume that the turbulence fills the radar pulse volume. However, there is a tendency for the radar to pick out the stronger layers, due to radar's poor sensitivity to regions of small turbulence. A radar will often not even recognize a truly laminar region, due to overflow of the pulse from neighboring turbulent regions. Furthermore, a small active region that completely fills a small resolution volume may be only one of the many intermittent patches within a larger turbulent region, and the steady state and spatially homogeneous assumptions used to derive turbulent energy balance equation may be violated. On the other hand, it is also possible a layer to be transparent to the radar. This occurs when the potential temperature gradient in the turbulent layer is near zero.

Balloon measurements are imperfect. For example, we would expect a layer to be quite active because of the low Richardson number, but it does not show strongly in the C_n^2 profile because the turbulence is embedded in a layer which is almost adiabatic (either driven that way by turbulence or pre-existing that way before the turbulence

was created). As a consequence, a parcel of air in this layer will show no (or at least little) deviation in temperature from its surroundings when displaced vertically, thereby producing a zero value for the temperature perturbations and, therefore, C_T^2. This is a weakness of using thermosondes to look for mechanically turbulent layers; they cannot see layers embedded in an adiabatic temperature profile and these are often the strongest and most active layers [*Hocking and Mu*, 1997].

Despite these shortcomings, there is a demand for additional knowledge about turbulent energy dissipation rates in the lower atmosphere, for the purposes of mesoscale modeling, weather forecasting, and the airborne laser (ABL) program. Hence, a mean estimate of the turbulent energy dissipation rate will be adequate.

6.3.2 M^2 and Radar Backscatter

On a side note, M is an indication of the static stability of the medium. Since humidity is negligible in the upper troposphere and the stratosphere, as seen from (6.8), M^2 is determined almost entirely by the temperature gradient. M^2 is large when the atmosphere is stable and small when the lapse rate is more nearly adiabatic. M^2 profile in Figure 6.2 compares well to the SNR profile from the vertical direction displayed in Figure 5.1. This follows well with the radar equation developed by *Gage et al.* [1981]

$$P_R = \frac{\alpha^2 P_T A_e^2}{4\lambda^2 r^2} M^2 (\Delta r)^2 . \tag{6.9}$$

P_R is the mean received power, α is the array efficiency, P_T is the peak transmitted power, A_e is the array effective area, and Δr is the pulse width. Comparing Figures 6.2 with 5.1, we see M^2 increases by about 10 dB going from 10-16 km to 16-20 km and then decreases for $z > 20$ km, a trend identical to the SNR from the vertical direction. The good correlation between the SNR and M^2, and hence $\Delta\theta/\Delta z$, and the low

turbulent activity at locations of strong backscatter indicate that the scatterers causing aspect sensitivity in the stratosphere are stable, stratified layers.

6.4 Conclusion

In this chapter, we compared the turbulence parameter C_n^2 as measured by a VHF radar with *in situ* balloon-borne instruments. We find that both methods of radar measurement of C_n^2, from the backscatter and the spectral width, have their limitations; the latter approach provides a more accurate measure of C_n^2. Errors that may contribute to an overestimate of C_n^2 are more easily removed from the radar spectral width. Radar backscatter, due to the contribution of Fresnel scatter/reflection, overestimates C_n^2, particularly in the lower stratosphere where Fresnel scatter/reflection appears to be the dominant cause of radar backscatter.

The goal of this thesis is to understand the temperature structures that cause aspect sensitivity. We recall the collocation of aspect-sensitive echoes with vertical potential temperature steps, and the similarity between the latter with temperature structures created during a Kelvin Helmholtz instability (KHI). We now turn our attention to a discussion of KHI in the lower atmosphere. Specifically, we want to examine the relationship between KHI and the observed temperature structures and how this result will impact our understanding of the vertical structure of the atmosphere and the cause of aspect sensitivity. This is our focus for the next two chapters.

Chapter 7

Kelvin-Helmholtz Instability in the Lower Atmosphere

It is challenging to obtain the measurements needed to fully understand the scattering mechanisms in the middle atmosphere. While a radar can offer continuous measurements of the atmosphere, the spatial resolution is poor, typically on the order of hundreds of meters. This is at least an order of magnitude larger than the temperature structures observed by *in situ* probes. In some recent observations [e.g., *Dalaudier et al.*, 1994; *Muschinski*, 1996], balloon-borne sensors have been launched from sites near or collocated with the radar to offer *in situ* information on the radar target. However, since only few balloons can be launched, this offers us a limited insight into the scattering mechanisms.

Direct numerical simulation (DNS), where the Navier-Stoke equation is solved directly, provides an alternative approach to the investigation and potential identification of the underlying dynamical structures observed using radar and *in situ* measurement techniques. It has been suggested that instabilities, such as the Kelvin-Helmholtz instability (KHI), which occur in the atmosphere, may play a part in the

observed radar backscatter [*Chilson et al.*, 1997; *Werne and Fritts,* 1999, 2000a, b; *Gibson-Wilde et al.*, 2000]. *Gibson-Wilde et al.* [2000] presented a study using a direct numerical simulation of KH billow-induced turbulent structures in predicting the VHF radar backscatter in the mesosphere.

There are many reasons that encouraged us to examine KHI. We have an interest in atmospheric instabilities in general as dynamic and convective instabilities are two mechanisms that contribute significantly to the dissipation of larger scale motions, e.g., gravity waves and tidal motions, and the generation of lower and middle atmospheric turbulence, which are likewise expected to play a significant role in the vertical transport of heat and atmospheric constituents [e.g., *Fritts et al.*, 1984]. KHI is the most common dynamic instability seen in the atmosphere and is often manifested in the atmosphere as a series of KH billows. The instability is due to enhanced velocity shears and/or a local minimum of the static stability either in the mean flow or associated with low-frequency wave motion. In contrast, convective instabilities occur when the lapse rate becomes superadiabatic through the action of gravity waves or localized heating.

KHIs have not been adequately observed by radars or *in situ* probes. Previously published radar observations of KHI lacked the information needed to conclude that specific turbulent layers observed by VHF radar in the stratosphere are KHI-induced. Furthermore, there is considerable evidence that KHI may play a part in generating the turbulence in the free atmosphere. The temperature structure of KHI at the late stage its evolution, which is a vertical temperature step, is observed in temperature soundings, as seen in Chapters 3 and 4. This motivates us to investigate KHI.

In this chapter, our goal is to examine the relationship between KHI and the observed temperature structures presented in Chapters 3, 4, and 5. Specifically, we want to show that KHI is a possible explanation for the *in situ* observed potential temperature steps and the associated VHF radar backscatter. Our approach includes a

comparison between *in situ* and radar observations of turbulence and temperature structures with the scaled temperature fields from a direct numerical simulation of a KHI. Two sets of balloon data are used, one with a very high-resolution sensor flown over Wichita, KS, and the other with a lower height resolution flown over the Jicamarca Radar Observatory (JRO) near Lima, Peru. We support this simulation-observation comparison with the available radar observation. Comparisons of this type can be quite powerful. We can take several cuts through the DNS and produce results that mimic an actual sensor making an *in situ* measurement of the atmosphere. This has an advantage over constructing analytic predictions of the atmospheric phenomenon via a sensor response. A balloon sensor, during its ascent, only makes one cut through a given structure whereas many passes are needed to compile the data needed to statistically analyze the temporal and spatial evolution of such structures. In contrast, one can easily compute the statistics of the simulated dataset. Furthermore, such techniques are very useful in uniting such disparate datasets as balloon temperature profiles and radar backscatter measurements and provide insights into the processes responsible for VHF scatter in the stratosphere.

We organize our discussion as follows. We first present the properties of the numerically simulated turbulent region, along with the dimensionalization relevant to the lower atmosphere. Some pages are devoted to a brief discussion of the *in situ* dataset from Wichita and JRO. As the numerical simulation was computed in a normalized grid space, paragraphs are devoted to the procedure needed to dimensionalize the simulation. The DNS calculated temperature is then compared with the *in situ* temperature measurements from Wichita and Peru. We also examine the evolution of a KH billow as observed by a VHF radar and *in situ* probes. The effects of KHI on radar backscatter are considered.

7.1 Direct Numerical Simulation of KHI

We are interested in the role that Kelvin-Helmholtz instabilities (KHI) play in the atmosphere, particularly in the creation of temperature structures, turbulence generation, wave excitation, transport of constituents, and radar backscatter [e.g., *Muschinski et al.*, 1999; *Gibson-Wilde et al.*, 2000]. The highest resolution direct numerical simulation (DNS) of KHI currently available, as presented by *Werne and Fritts* [1999] and *Werne et al.* [2000a, b] forms the basis of this study.

The simulation is implemented in non-dimensional space. The non-dimensional fluid dynamics equations were solved under Boussinesq's approximation, which assumes

1) Density fluctuations consist of small deviations from equilibrium and are negligible with regard to acceleration or inertial effects.
2) Velocity fluctuations are small enough to make nonlinear effects negligible.
3) Vertical scale of motion or vertical wavelength is much less than the scale height of the atmosphere.

Furthermore, the simulation ignores viscous effects and assumes that the wavelengths are small enough to allow one to ignore acoustic effects. The variations of density are assumed to be much smaller than variations of vertical velocity with respect to height.

The initial potential temperature profile is

$$\theta(t = 0, z) = \beta z \tag{7.1}$$

and horizontal velocity profile is

$$U(t = 0, z) = U_0 \tanh(z/L), \tag{7.2}$$

where β is the potential temperature gradient, U_0 is the maximum velocity across the initial shear region, and L is the half depth of the initial shear layer. The vertical extent of the instability is dependent on the vertical extent of the velocity profile. Under these conditions, the equations of motion are:

$$\partial_t \vec{u} + \vec{\omega} \times \vec{u} = Re^{-1} \nabla^2 \vec{u} - \vec{\nabla} P + Ri\theta \vec{z} \tag{7.3}$$

$$\partial_t \theta + \vec{u} \cdot \vec{\nabla} \theta = Pe^{-1} \nabla^2 \theta \text{ , and} \tag{7.4}$$

$$\vec{\nabla} \cdot \vec{u} = 0 \tag{7.5}$$

Equations (7.3)–(7.5) express momentum, heat, and mass conservation for the system; $\vec{u}$ = (u, v, w) and $\vec{x}$ = (x, y, z) are velocity and position vectors; $\vec{\omega} = \vec{\nabla} \times \vec{u}$ is the vorticity; and θ is the potential temperature. All quantities are non-dimensional, using characteristic time, length, and temperature scales: h/U_0, h, βh. $Ri = N^2/\max(\partial_z u)^2$, $Re = U_0 h/\nu$, and $Pe = hU_0/\kappa$ are the Richardson, Reynolds, and Peclet numbers. κ is the thermal diffusivity and ν is the kinematic viscosity. Ri = 0.05 and Re = Pe = 2500 are used for the 3D solutions presented here. Equality of Re and Pe implies the Prandtl number (Pr) = ν/κ =1, which is near the value for air ($Pr_{air} \approx 0.7$), while $Ri < 0.25$ indicates dynamic instability for the stratified layer [*Miles*, 1961]. The definitions of Re, Pe, and Pr are discussed in detail in Appendix C.

Boundary conditions are periodic in horizontal directions and stress-free on the top and bottom boundaries of the numerical domain. Solutions are obtained with a pseudo-spectral Galerkin algorithm with field variables represented spatially by Fourier series. The hybrid implicit-explicit, 3rd-order Runge-Kutta time-stepping suggested by [*Spalart et al.*, 1991] is implemented with a Courant-Friedrichs-Lewy (CFL) criterion of 0.68.

Motion is initiated with the most rapidly growing asymptotic linear eigenmode ($\lambda \approx 4\pi$ but slightly dependent on Re) superposed with a Kolmogorov noise spectrum added to the velocity field. Vorticity amplitudes for these perturbations are 0.07 and 0.014, respectively. To accommodate the eigenmode and the anticipated "secondary instability" [*Klaassen and Peltier*, 1985, 1991; *Palmer et al.*, 1994], horizontal dimensions of $x_o \times y_o = 12.56 \times 4.2$ are used. Sufficient remoteness of top and bottom boundaries is established with 2D tests, and z_o = 25 is chosen.

Spatial resolution is varied during the evolution so that small-scale features are always properly represented. With $Re = 2500$, as many as $1000 \times 360 \times 2000$ spectral modes are required. For comparison with naturally occurring shear layers (for which the final full layer depth L is measured, but h is not), the layer Reynolds number $Re_L = \Delta UL/\nu$, based on the velocity difference ΔU across the layer and L, is roughly $Re_L \approx 3\times10^4$. This should be compared to mesospheric [*Lübken*, 1992], stratospheric [*Ierkic et al.*, 1990], and oceanic [S*eim and Gregg,* 1994] observations of $Re_L \approx 10^4$, 3×10^6, and 3×10^6, respectively.

The simulation provides velocity and potential temperature information within a space defined by 1000 streamwise (x-direction), 350 spanwise (y-direction), and 2000 vertical (z-direction) grid points, which translate to dimensions of $(4\pi, 4.2, 25)L$ [*Gibson-Wilde et al.*, 2000; *Werne et al*., 2000a, b]. We dimensionalize the simulated data by choosing the value of U_0, β, and L.

Simulations are carried out on the Cray T3E's at the U.S. Army Engineer Research Development Center (ERDC) and the Naval Oceanographic Office (NAVO) Major Shared Resource Centers (MSRC's) as part of the Air Force AirBorne Laser (ABL) project. 500 processors where used for the largest runs.

The computed solutions illustrate the evolution of turbulent KH billow breakdown, from the growth of the initial 2D vortex, to subsequent secondary instability in the form of streamwise-aligned vortex tubes created by roll-ups of vortex sheets, to the generation of a turbulent cascade to smaller length scales as streamwise and spanwise vortex tubes mutually interact. After ≈10 buoyancy periods ($t \approx 300$ in our non-dimensional units), stratification overcomes the dynamical motion, and the flow restratifies [*Werne and Fritts*, 1999; *Werne and Fritts*, 2000a].

Figure 7.1 presents three cross-sectional views of the DNS temperature field at $t = 200$ with a linear variation in gray-scale shading. The temperature field in the interior of the turbulent region is well-mixed and the strong vertical and horizontal tempera-

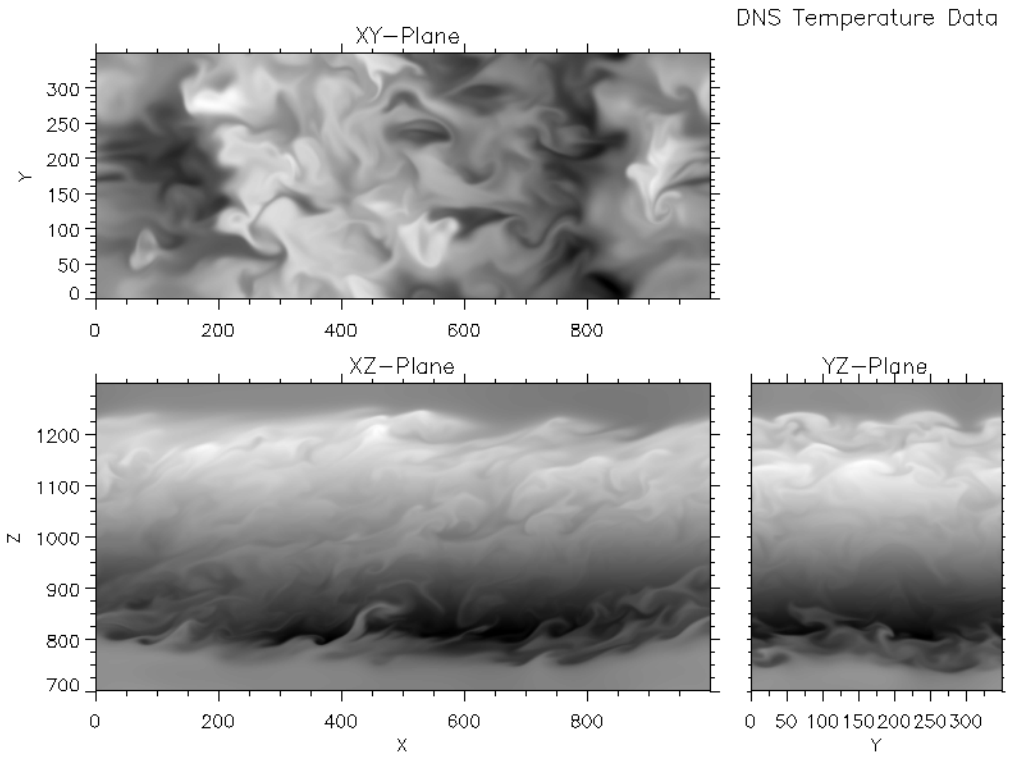

Figure 7.1: High-resolution cross-section of DNS temperature field at $t = 200$ showing views from above (top panel), along the streamwise direction (main panel), and along the spanwise direction (right panel). The initial linear temperature profile βz is removed to enhance contrast in the lower two panels.

ture variations exist at the edges of the layer. We use this simulation to understand the observed potential temperature steps. In order to compare our simulated KH flow with atmospheric observations, we must ascribe dimensions, i.e., dimensionize, to the non-dimensional DNS results. We do this in the following section. *Gibson-Wilde et al.* [2000] conducted a similar comparison with observations of mesospheric dynamics where the Reynolds number is comparable with that simulated. The stratospheric cases examined here, however, possess much higher values of *Re*, indicating the viscosity of the simulated flow is higher than we would prefer. Nevertheless, as the numerical solutions manage to separate production and dissipation ranges sufficiently to develop an inertial sub-range, allowing us to compute turbulence intensity and dissipation rates, the computed solutions are suitable for the analysis presented here

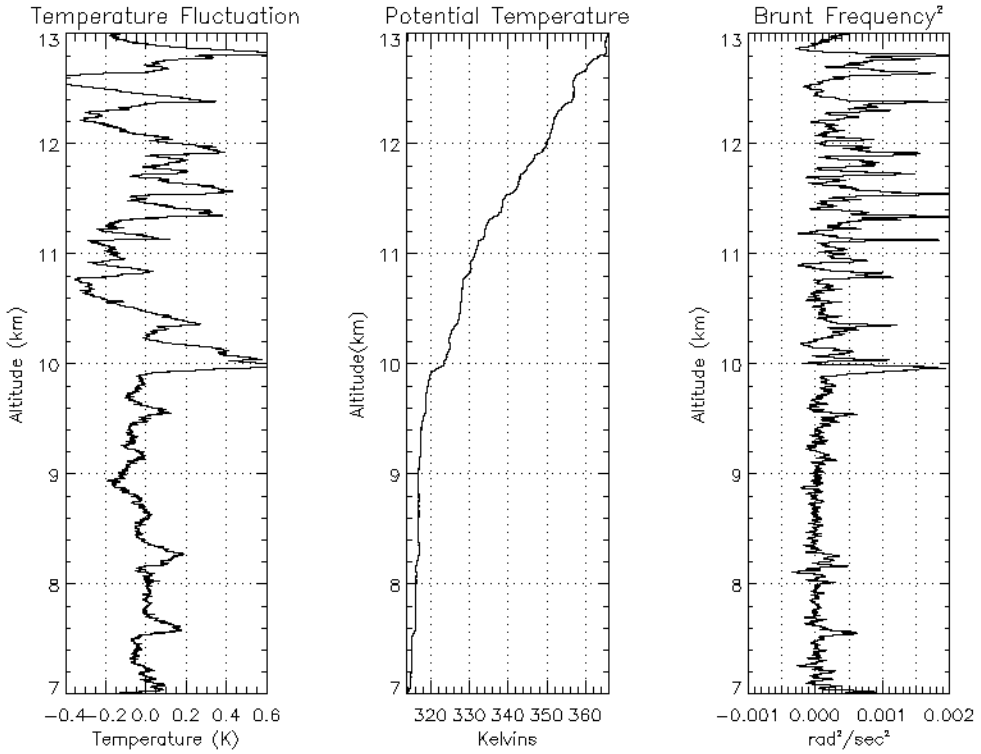

Figure 7.2: *Left panel*: High-resolution temperature fluctuation as measured by a high-resolution temperature sensor over Wichita, KS, on 5 March 1995. Asymmetrical structures, which are characterized by a sudden increase in temperature followed by a gradual decrease, that are prevalent in the dataset. *Center panel*: Potential temperature derived from the radiosonde temperature measurement. The tropopause is at ~10 km. *Right panel*: Square of the Brunt-Väisälä frequency (N^2).

[*Werne and Fritts*, 1999; *Werne and Fritts*, 2000a, b]. This is a significant improvement over earlier simulations of stratified shear turbulence which did not achieve an inertial subrange. The presence of an inertial range means that production and dissipation ranges are well separated such that we can calculate dissipation rates and turbulence intensity from the velocity and temperature information. The application of this non-dimensional simulation to the stratosphere is detailed in the following section.

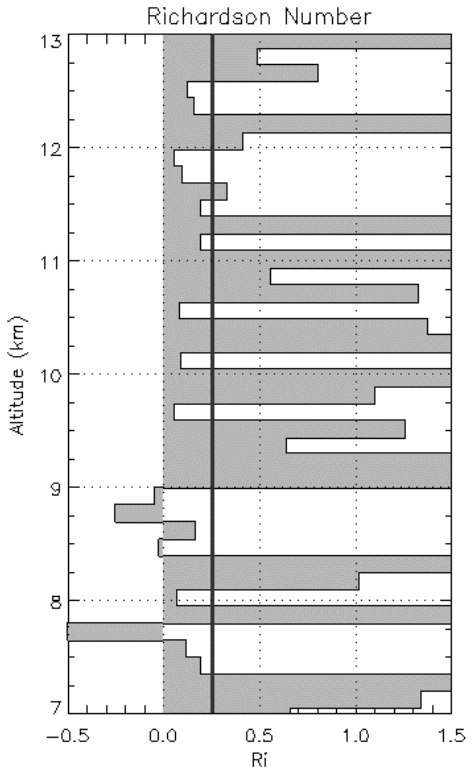

Figure 7.3: Gradient Richardson number (*Ri*). Dark line indicates *Ri* = 1/4, the boundary of stability.

7.2 Data Presentation and Comparison

We present the comparison between the *in situ* temperature observation and the structures predicted by the numerical simulation. In this discussion, we consider the temperature sounding from Wichita and Peru.

7.2.1 Comparison Between DNS and Wichita Dataset

We revisit the high-resolution measurement of the lower atmospheric temperature fluctuations made at Wichita, KS, on 5 March 1995 [*Walters*, 1995]. We reproduce a section of this dataset in Figure 7.2. The saw-tooth temperature structures (or edges) mark the edges of the nearly vertical potential temperature steps; the temperature gradient at the center of the step is small, very close to the marginally stable value for convective instability. We plot in Figure 7.3 the gradient Richardson number (*Ri*) as

defined by equation (3.3). When we compare Figures 7.2 and 7.3, a correspondence is seen between the center temperature steps with low Richardson numbers (*Ri*).

7.2.1.1 Dimensioning Process

We describe here the dimensioning process required to compare the DNS with the observed features. We will first scale, i.e., dimensionalize, the numerical simulation to the temperature step near 15.85 km observed at Wichita, KS, as seen in Figure 7.4. The parameters needed to scale the simulation to the observations are the half-depth of the initial shear layer (h) (This is, by definition of the simulation, a fourth of the final vertical depth of the instability, i.e., $L = 4h$ [*Werne and Fritts*, 1999].), the background potential temperature gradient (β [K/km]), and the background horizontal velocity (U_0).

The potential temperature profile has been dimensionalized based on a mean potential temperature θ_0 determined from the radiosonde observation. In this case, it is 409 K. The initial potential temperature gradient (β) is related to the velocity and length scales, the acceleration due to gravity (g = 9.8 m/s^2), and the Richardson number by

$$\beta = \frac{Ri\theta_0}{g}\left(\frac{U_0}{h}\right)^2. \qquad (7.6)$$

The parameters β, U_0, h are chosen self-consistently to represent the balloon data segment, constrained by the dimensionless parameter *Ri*. There are two ways to approach the dimensionalization of the DNS. One option is to tune U_0 and h until β matches exactly with the observation. The other is to estimate U_0 and h as best we can from the data and then compute β from (7.6). For the Wichita data, due to the poor height resolution of the wind measurement, we choose the first method here. From the observation in Figure 7.2, we see that the vertical depth of the temperature step is 160 m, which, based on Figure 4 of *Werne and Fritts* [1999], indicates $h \sim 40$ m. The

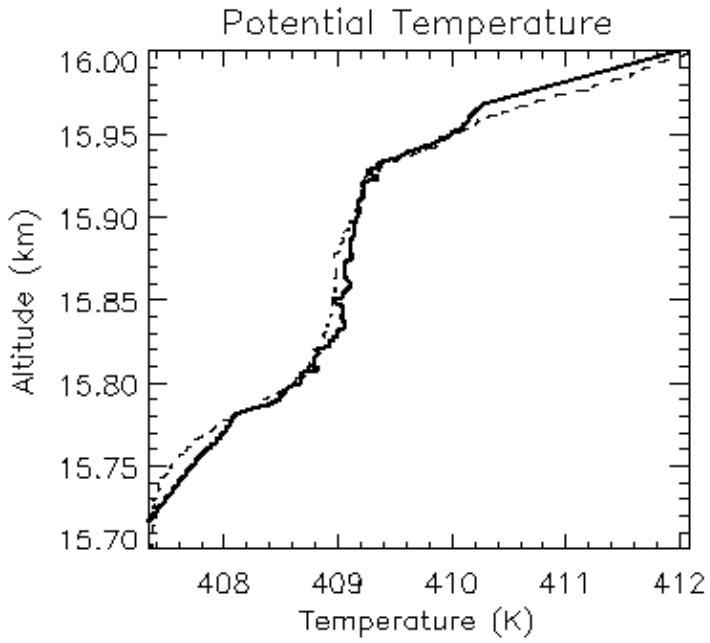

Figure 7.4: Comparison between the balloon-measured potential temperature from Wichita, KS, on 5 March 1995 and the potential temperature profile calculated via the numerical simulation. Dashed line is the measured profile; solid line is the simulated profile.

mean potential temperature at the center of the turbulent region is ~409 K. Choosing β = 12 K/km gives us the best comparison. This implies that, via (7.5), U_0 = 3 m/s, which compares well with the meridional component of the wind; see Figure 3.5. The scaling factors yield a spatial resolution in all three dimensions of 3.34 cm between grid points. This resolution is very close to the vertical resolution of ~5 cm of the balloon measurement. The full horizontal extent of the initial billow is $4\pi h \approx 500$ m.

Using our estimates for U_0 and h, we can estimate the kinematic viscosity:

$$\nu = \frac{U_0 h}{Re}. \tag{7.7}$$

With Re = 2500, we estimate ν = 0.048 m^2/sec, which is ~560 times larger than a typical stratospheric value of $\nu = 8.54 \times 10^{-5}$ m^2/sec at 16 km altitude [*U.S. Standard Atmosphere*, 1976]. The disparity between ν for the simulated and actual atmospheres demonstrates the limitations of the DNS.

7.2.1.2 Comparison Between Observation and DNS

We compare the measured potential temperature structure measured at Wichita with the temperature structure predicted from the simulation. We have chosen a profile at x = 2.5 and t = 200 (both non-dimensional). With h = 40 m and U_0 = 3 m/s, the dimensionalized time is 200 h/U_0 = 44 minutes; in other words, we are examining a temperature structure formed 44 minutes after the initial formation of the KHI. This corresponds to 20% of the billow length and 7 buoyancy periods. We present in Figure 7.4 the result of the comparison between the Wichita observation with the simulation. Good agreement is seen between the simulation and the observation, not only in the region where the potential temperature gradient is near zero, but also in the way the temperature step merges back to the background atmospheric temperature. This is perhaps remarkable as the simulation can only describe the atmosphere in a limited fashion.

Another way to evaluate the quality of the comparison is to check buoyancy period of the observation and the simulation. For the stratosphere over Wichita, as seen in Figure 7.2, the buoyancy period, i.e., 1/N, where N is the Brunt-Väisälä frequency, is ~6 minutes. An alternative way to define the buoyancy period is

$$T = \frac{2\pi}{\sqrt{Ri}} \frac{h}{U_0}. \tag{7.8}$$

For the dimensionalized simulation profile, with Ri = 0.05, h = 40 m. and U_0 = 3 m/s, T = 6.2 minutes, which is comparable to the observation. A difference between the observed and simulated buoyancy period indicates that Ri that trigged the observed KHI is not 0.05, as it is for the simulation.

We want to emphasize that we have selected a snapshot of the simulation representing a point in the evolution displaying the layered structure produced by the

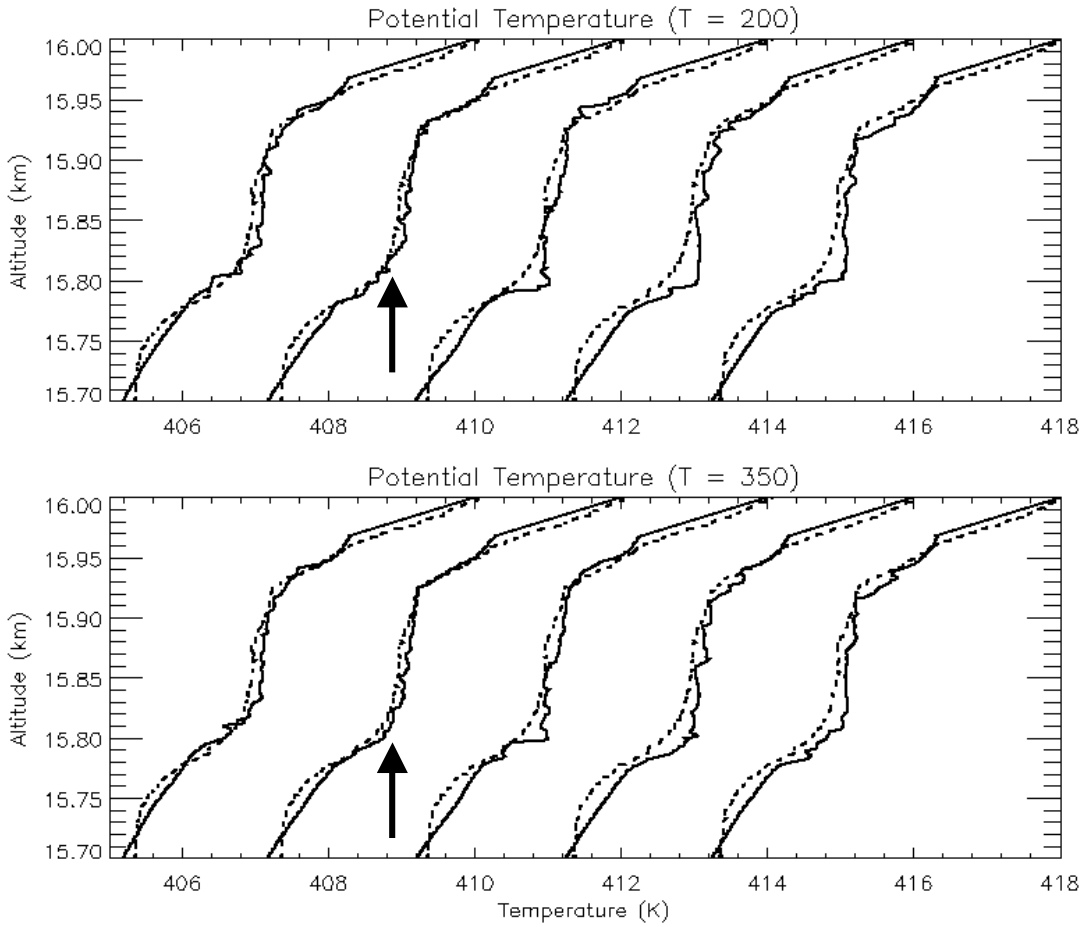

Figure 7.5: Comparison between the Wichita potential temperature profile with the simulation. We select the vertical profile at five different locations along the streamwise direction in the simulation: x = 0, 200, 400, 600, and 800 at two different normalized times, t = 200 (*top panel*) and 350 (*lower panel*). Each set of comparison results is separated by 2 K. Dashed line is the measured profile; solid line is the simulated profile.

turbulent event; the layered structure is a dominant structure seen throughout much of the simulation and not something that appears sporadically. To show this, we have chosen to compare the Wichita potential temperature profile at five different locations (at x = 0, 2.5, 5, 7.5, and 10) along the streamwise direction of the simulation at two different non-dimensional times (t = 200 and 350). We show this comparison result in Figure 7.5 with each comparison separated by 2 K. The arrows indicate the comparison result seen in Figure 7.4. The comparison indicates that the vertical

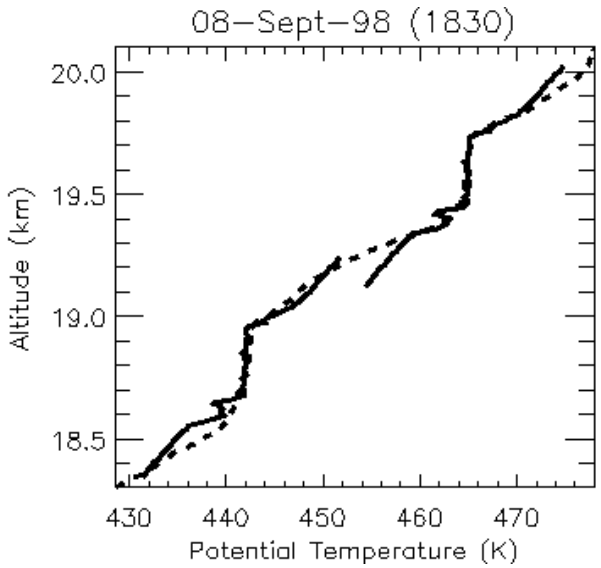

Figure 7.6: Comparison between the balloon-measured potential temperature from JRO on 8 September 1998 and potential temperature profiles calculated via the numerical simulation. Dashed line is the measured profile; solid lines are the simulated profiles.

profile of layered structure in the simulation compares well with the observation, independent of the location or the time-step in the simulation. A detailed time evolution of the simulation showing changes in the simulated temperature is discussed in *Werne and Fritts* [1999, 2000a, b].

7.2.2 Comparison Between DNS and JRO Dataset

We compare the measured potential temperature on 8 September 1998 from Peru with the simulation results in Figure 7.6. Since two measured temperature steps show a strong similarity, we will dimensionalize the KH billow to one of the temperature steps; we choose the one centered at 18.8 km for our purpose. Since we have a higher resolution wind measurement, we scale the simulation to the observation by choosing h and U_0 and then use (7.6) to compute β. The half-depth of the initial shear layer h was 80 m, corresponding to the full vertical extent of a billow of 350 m. We estimate the velocity scaling factor U_0 to be ~4 m/s from the measured wind profile. The mean

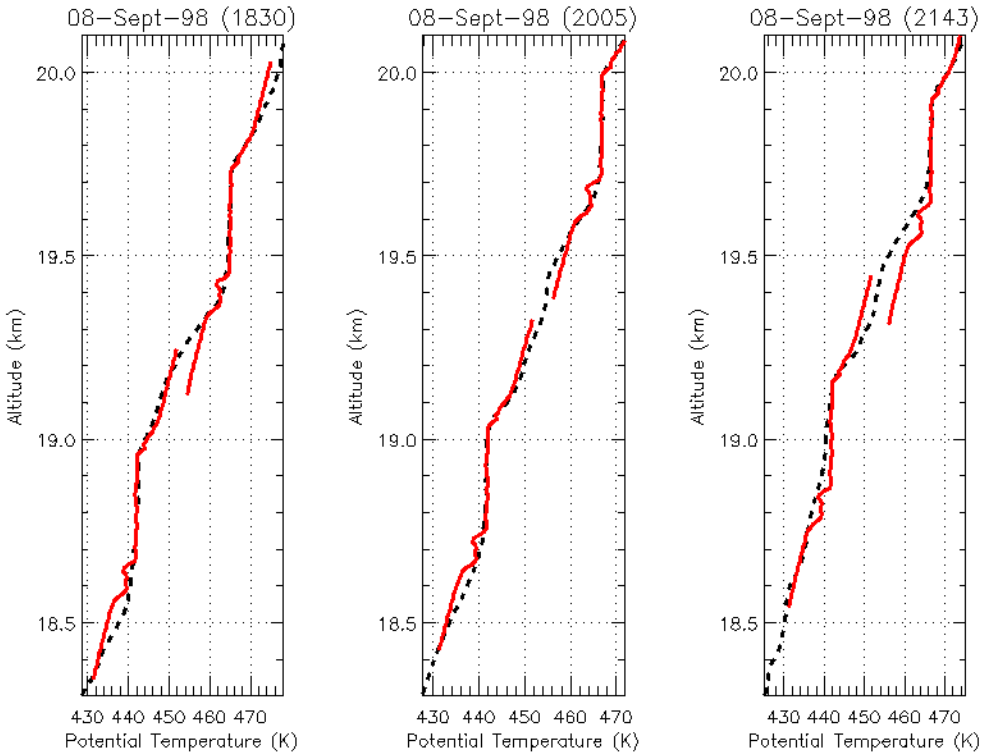

Figure 7.7: Comparison between the balloon-measured potential temperature from 8 September 1998 and potential temperature profiles calculated via the DNS technique. The dashed lines are the measured profiles; the red solid lines are the DNS profiles. The DNS data is averaged horizontally over a region of area 9 m x 9 m. Potential temperature as measured on the evening of 8 September 1998. The balloons were launched at 1830, 2005, and 2143 LT. We use the same dimensionalization parameters as the ones used to produce the results seen in Figure 7.6.

potential temperature at the center of the turbulent region was 440 K. The resulting potential temperature gradient (β) is 22.4 K/km, which is comparable to the measured value. The scaling factors yield a spatial resolution in all three dimensions of 9.05 m between grid points. We again see good agreement between the observation and simulation. Similar results are seen when we compare the simulation with temperature steps observed at 2005 LT and 2143 LT and present the result in Figure 7.7.

7.2.3 Potential Temperature Steps

The potential temperature profile in Figures 7.4, 7.6, and 7.7 exhibit potential temperature steps where the potential temperature gradient is near zero, indicating a neutrally stable atmosphere that is homogeneously mixed. The edges of these potential temperature steps correlate to asymmetric structures that were captured by the high-resolution sensor. These structures are characterized by a sudden increase followed by a gradual decrease in temperature. We zoom in on an example of the potential temperature steps measured at Wichita, along with the associated temperature fluctuations, and plot them in Figure 7.8. This is from the measurements at Wichita, KS, as discussed in Chapter 3. In this figure, we shown an example of three successive close-ups of the sharp temperature gradient (indicated by the box) in the stratosphere where a gradient of 230 K/km is detected. A temperature gradient of 175 K/km is seen in the tropospheric example plotted in Figure 7.9.

Just as they exist in mid-latitudes, as seen in the Wichita dataset, potential temperature steps are also prevalent in the equatorial region, as seen in the MIST campaign dataset. Potential temperature steps are observed in almost all of the temperature soundings made during the MIST campaign. In Figure 7.10, we present four representative profiles where potential temperature steps are observed. Again, the vertical depths of these steps are on the order of hundreds of meters. It must be emphasized that during the MIST campaign, the balloon observations indicate that many of the stratified features, as indicated by the potential temperature steps, are present over JRO.

The good comparison between the simulation and the observed temperature steps seems to suggest that KHI is a mechanism that acted on a parcel of air such that the content of the parcel has been homogenized and well mixed. It is possible that many mechanisms may be able to create potential temperature steps, but the dynamic instability known as KHI is one of them. We also see that the depths of the tempera-

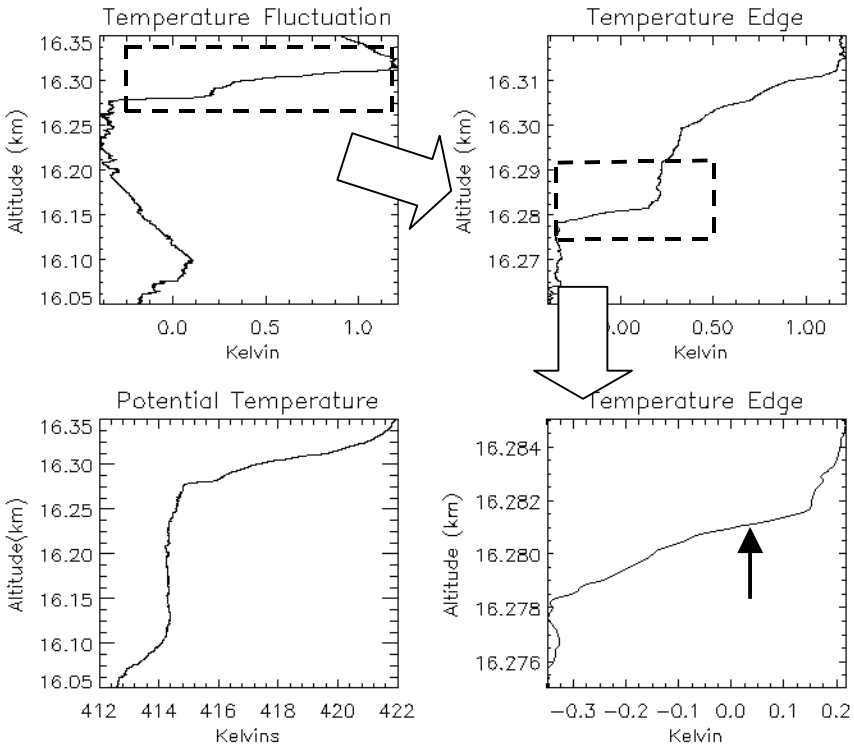

Figure 7.8: Three successive close-ups from the stratospheric temperature structure seen in the upper left-hand panel. Potential temperature is also plotted. Temperature gradient indicated by the solid arrow on the lower right-hand panel has a thickness of ~1 m and an associated temperature change of 0.225 K, which gives us a gradient of 225 K/km. The measurement was made at Wichita, KS.

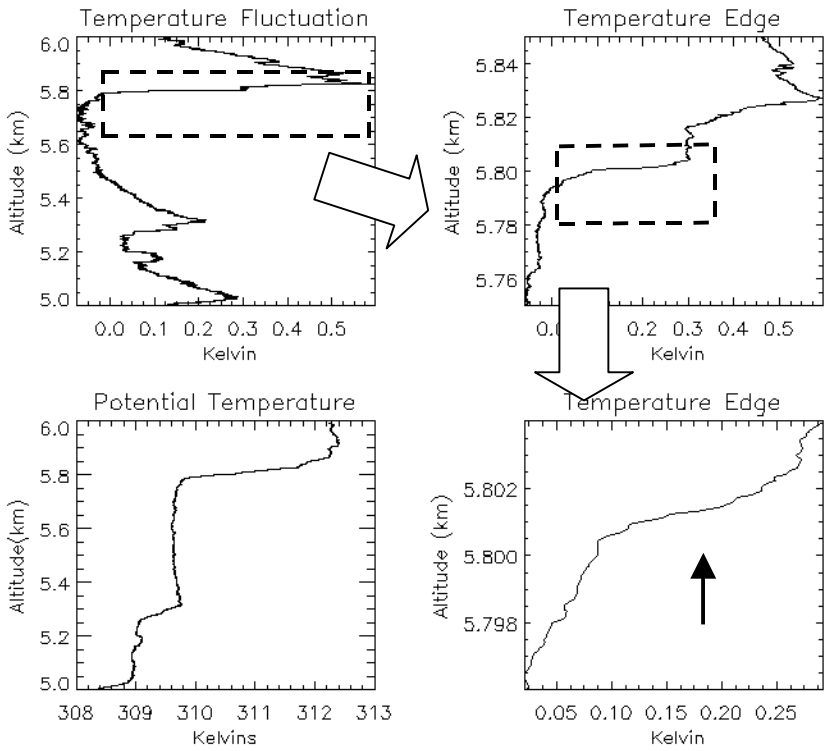

Figure 7.9: Three successive close-ups from the tropospheric temperature structure, plotted in the same format as Figure 7.8. Temperature gradient indicated by the solid arrow on the lower right-hand panel has a thickness of 0.63 m and an associated temperature change of 0.11 K, which gives us a gradient of 175 K/km. The measurement was made at Wichita, KS.

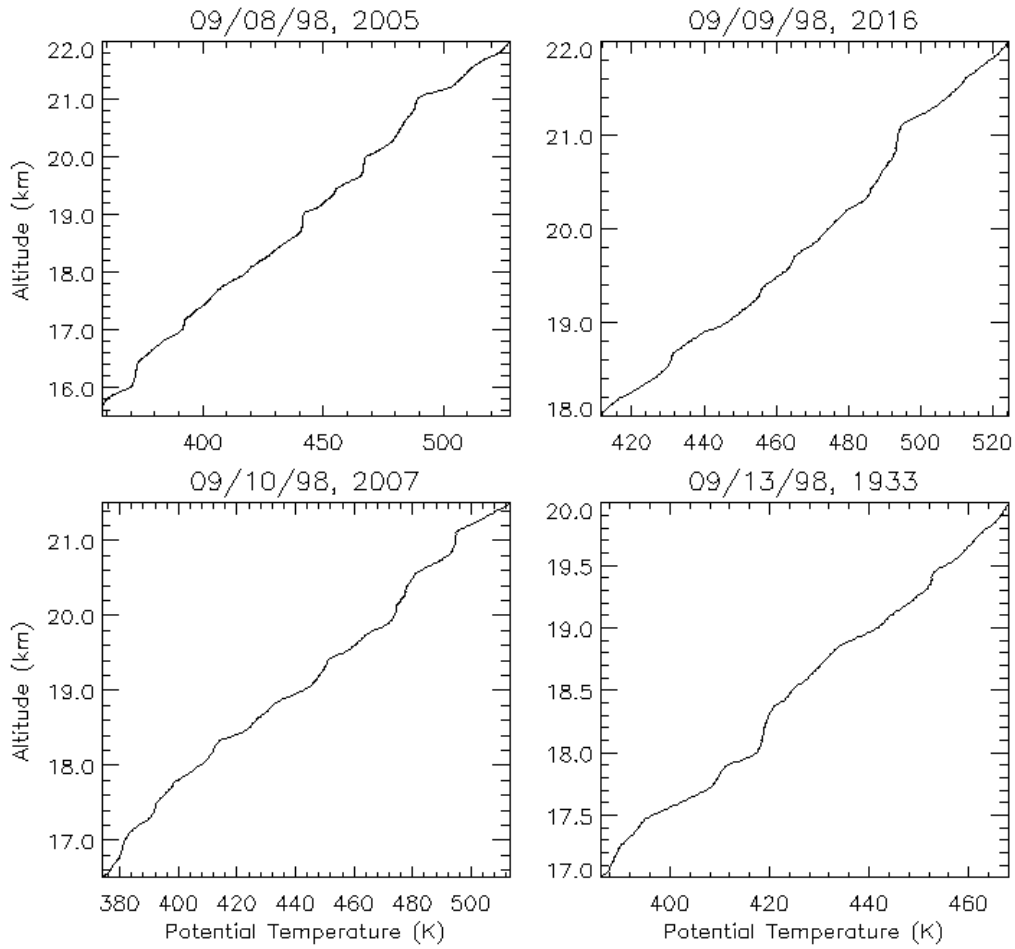

Figure 7.10: Four other examples of the lower stratospheric temperature profile measured at the Jicamarca Radio Observatory (JRO) during the MIST campaign. Numerous examples of potential temperature steps are seen.

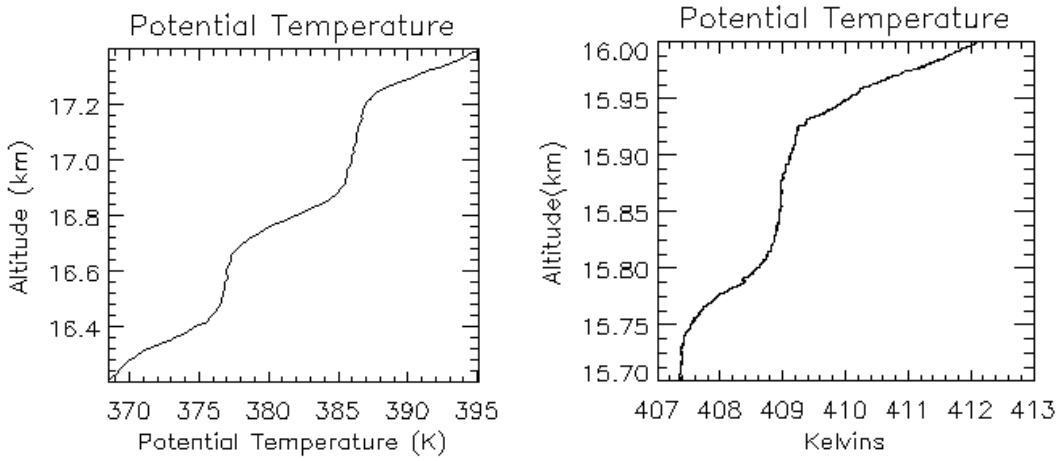

Figure 7.11: *Right panel*: Potential temperature steps observed at the Jicamarca Radio Observatory on 7 September 1998 at 2012 LT. *Left panel*: Potential temperature steps observed at Wichita, KS.

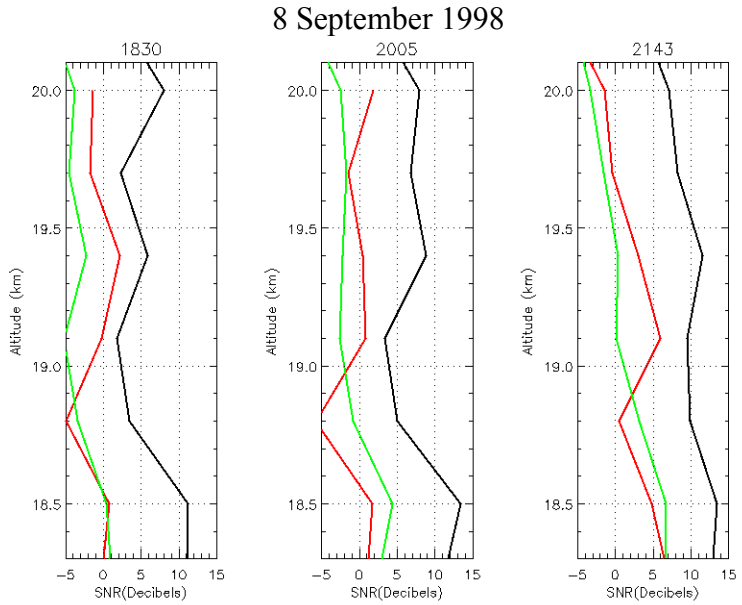

Figure 7.12: Radar backscatter measured on 8 September 1998 at the Jicamarca Radio Observatory (JRO). The green line is the SNR of the north beam, the red solid line is from the west beam, and the solid line is from the vertical beam.

Table 7.1. Summary of potential temperature step parameters as observed in the stratosphere for 7-10 September 1998 at the Jicamarca Radio Observatory. The values of step depth (S) are approximately related to the half depth of the initial shear layer (L) through $L = S/4$.

Launch date	Launch time (LT)	Step center (km)	Step depth (m)	$\Delta\theta/\Delta z$ (K/km)
09/07/1998	1830	15.9	100	14.3
		16.5	200	17.4
		17.0	200	17.5
		19.1	300	32.4
		19.8	400	32.8
	2012	16.55	300	21.5
		17.1	200	29.5
		18.2	800	26.8
		19.95	500	27.2
09/08/1998	1830	16.25	500	31.5
		17.1	200	23.8
		18.75	500	22.4
		19.6	400	22.0
	2005	16.25	500	32.3
		17.1	200	29.5
		18.95	300	22.1
		19.95	300	21.8
	2143	16.25	400	18.5
		19.85	300	21.8
09/010/1998	1830	16.9	300	19.6
		18.05	280	19.2
		19.05	200	17.2
		19.7	400	17.0

ture steps are non-uniform but are on the order of a few hundred meters. Some temperature steps, such as the ones near 20 km, approached a depth of 1 km. These structures resemble the ones seen at Wichita. This is clarified in Figure 7.11 where we plot the JRO observed potential temperature steps next to a potential temperature step observed at Wichita.

The centers of the temperature steps move with time, perhaps an indication of inertial wave activity and/or diurnal tide activity [*Larsen and Cornish*, 1989; *Riggin et al.*, 1999]. As discussed in Chapter 2, KHI may excite low frequency motions that

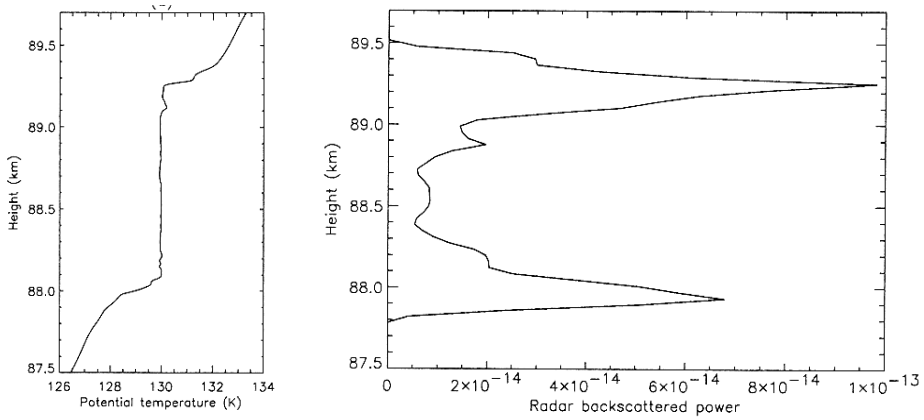

Figure 7.13: *Left panel*: High-resolution potential temperature profile through the center of the simulated KHI. *Right panel*: Simulated 50 MHz backscattered power. The range resolution was 37.6 m [After *Gibson Wilde et al.*, 2000].

would affect the location of temperate steps. It must be emphasized that during the MIST campaign, the balloon observations indicate that many stratified features, as indicated by the potential temperature steps, are present over JRO. These features often persist in successive bal loon launches, as seen in Table 7.1, where we have indicated the temperature step location, the step depth, and the background $\Delta\theta/\Delta z$.

We present in Figure 7.12 the average SNR between 1830-1900 LT (left panel) and 2005-2035 LT (center panel), and 2143-2213 LT (right panel). We recall from our previous discussions of KHI that the edges of a KH layer are responsible for high backscatter. *Gibson-Wilde et al.* [2000] demonstrated this by computing the radar backscatter from a DNS of a KHI. We reproduce their result in Figure 7.13. However, comparing Figure 7.7 with 7.12, it is not obvious that the SNR increases at the edges of the temperature steps. We suspect that the 300 m height resolution of the radar is too large to allow the radar to resolve the fine details observed in the *in situ* measurement.

7.3 Observations of KHI at Jicamarca Radio Observatory

During the MIST campaign, we were fortunate to observe what we believe to be an evolving KHI. In this section, we present the radar and balloon data for that event.

7.3.1 Radar Observations: 8-10 September 1998

Figure 7.14 presents the radar observations on the evening of 8 September 1998. The backscatter characteristics were briefly discussed analyzed in Chapters 4 and 5. We focus our attention on the atmospheric structure as observed by the vertically pointing beam. The figure contains the Doppler moments: radial velocity and spectral width, as well as the backscatter power from the vertical direction. The SNRs from the oblique directions are also included. We restrict the data presentation to the upper troposphere, as the dynamics observed in this region is our focus.

A periodic billow structure is seen centered at ~11 km starting around 2030 LT. The structure is slightly anisotropic, as backscatter from the oblique directions exhibit the same structure but less intensely by about 3-5 dB. The vertical extent of this structure increases to ~2 km in a period of 2 hours, extending from 10 km to 12 km. This has the appearance of a Kelvin-Helmholtz instability (KHI), as seen in previous KHI observations by *Gossard et al.* [1971], *Chapman and Browning* [1997], and *Czechowksy and Rüster* [1997] which we display in Figures 2.6, 2.7, and 2.8, respectively.

Comparing the spectral width with SNR, we see that, near 11 km, the appearance of the periodic echoes is associated with the increase of the spectral width; as the billow grows, the region of large spectral width broadens also. This is also associated with the periodic behavior in the radial velocity in the vertical direction, which indicates that the air parcel is oscillating in the vertical direction.

Unfortunately, the radar was turned off on 8 September before we were able to see further evolution of the billow structure. However, we can find out what happens to

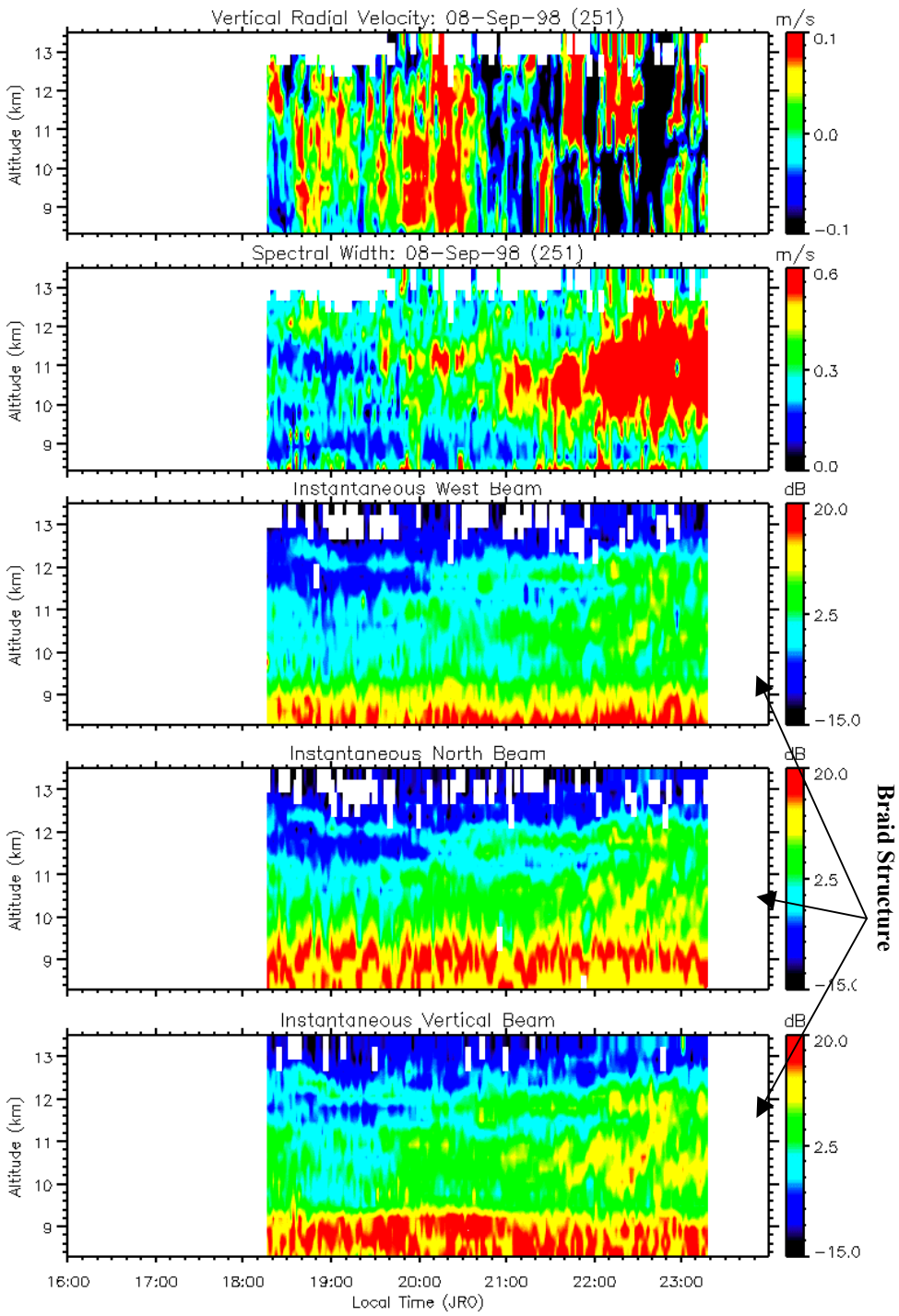

Figure 7.14: Signal measured by the Jicamarca VHF radar in its multi-beam configuration on 8 September 1998. We present the data measured in the vertical direction. From top to bottom: radial velocity in the vertical direction; spectral width in the vertical direction; radar backscatter from the west, north, and vertical direction. The signal above 21 km is noise. Strong signal seen near and below 9 km is caused by ground clutter. Regions where SNR < -5 dB are omitted.

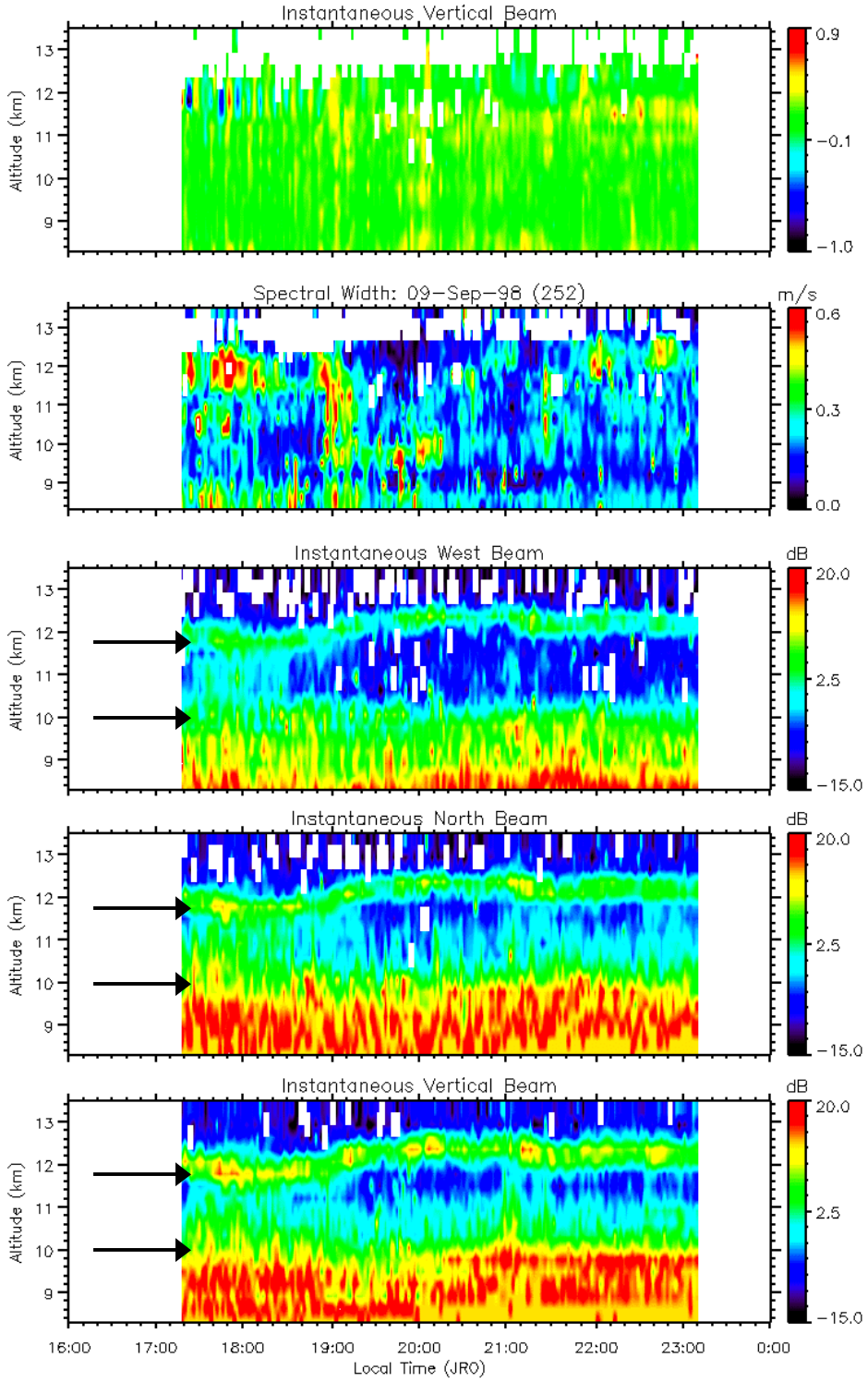

Figure 7.15: Same as Figure 7.14, but for 9 September 1998. Arrows indicate the scattering layers.

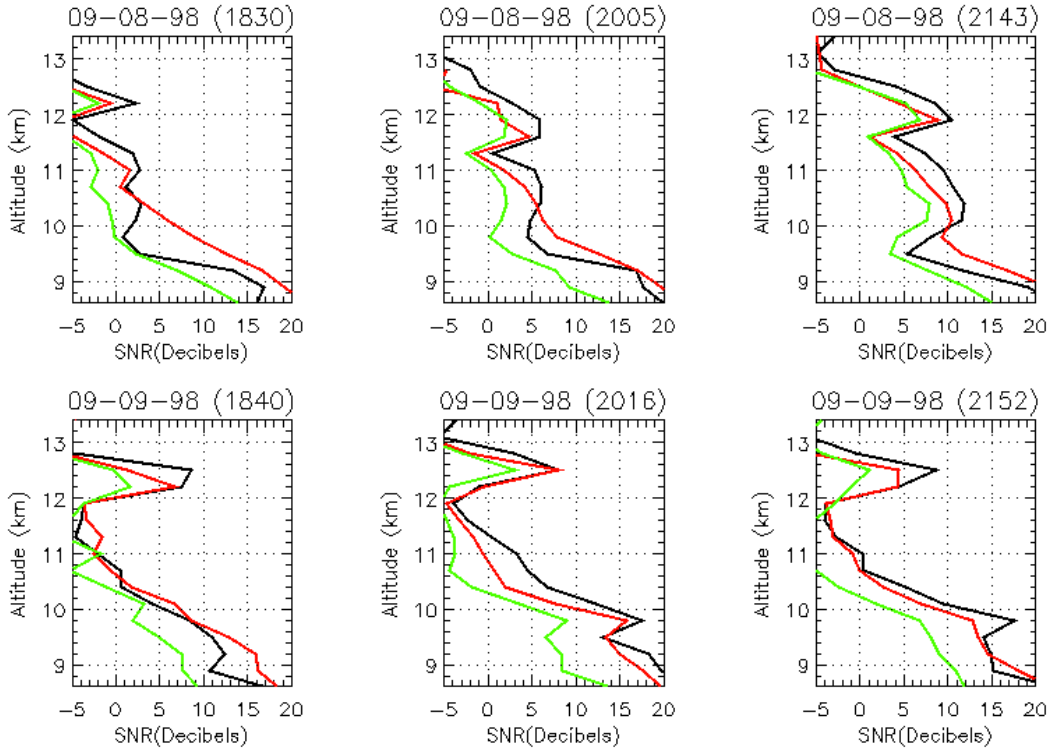

Figure 7.16: *Top panel*: Average SNR profiles from 8 September 1998. *Bottom panel*: Average SNR profiles from 9 September 1998. The green line is the SNR from the north direction, the red solid line is the SNR from the west beam, and the black line is the SNR from the vertical beam.

this structure by the radar data on 9 September 1998. We plot this in Figure 7.15. For the scattering characteristic observed on 9 September 1998 near ~11 km, the billow signature has disappeared and is replaced by a scattering layer near 12 km, which seems to mark the upper boundary of the billow observed on the previous evening. We suspect that there is another scattering layer near 10 km; however, the atmospheric signal is inseparable from the signal from the ground clutter and receiver recovery problems. The scattering layer has a long lifetime. Throughout this observation period, the scattering layers remain relatively unchanged, when one would suspect that diffusion and other mechanisms would act on the layer and smooth out the structure. The scattering layers may also have been fossilized. We are tacitly assuming that the structures observed on September 8 and 9 are related to each other. The

characteristics of the radar backscatter and temperature structure observed in these two days are too coincidental to be caused by separate events. We will examine this in a later section.

On this evening, the atmosphere is relatively quiet, aside from the local turbulent patches seen in the upper troposphere. The radial velocity in the vertical direction does not indicate any obvious periodic motion of the atmosphere. Any indication of the periodic behavior associated with what appears to be the KH billow seen in 8 September 1998 have disappeared. The radar data on 10 September 1998 (see Chapter 4, Figure 4.12) reveal structures do not seem to be related to those observed on 8 and 9 September 1998. Taking in context, the radar data suggest that the periodic echo structures observed on 8 September 1998 develop into two thin scattering layers and are not seen on 10 September 1998. A better understanding of the structure evolution may evolve from the *in situ* data.

The development of the billow structure and its remains are perhaps more clearly seen in Figure 7.16 where we examine 30-minute averages of the SNR. Looking at the data from 8 September 1998 in Figure 7.4, the SNR strength reflects the growth of the billow structure. At 2143 LT, approximately 2 hours into the billow evolution, we see that the SNR near the billow region has increased by ~10 dB. Turning our attention to Figure 7.15, we see a peak in SNR near 12.5 km. Another peak is seen slightly below 10 km but less obviously because of the ground clutter and receiver recovery problems experienced at the lower range gates.

7.3.2 Balloon Data: 8-10 September 1998

We were fortunate to have balloons launched at the time that the billow structure was evolving. The *in situ* measurements provided by the balloon will help us understand the structure and dynamics of the evolving billow. We plot in Figure 7.17 the potential temperature (θ), C_n^2, and wind information measured via the balloons

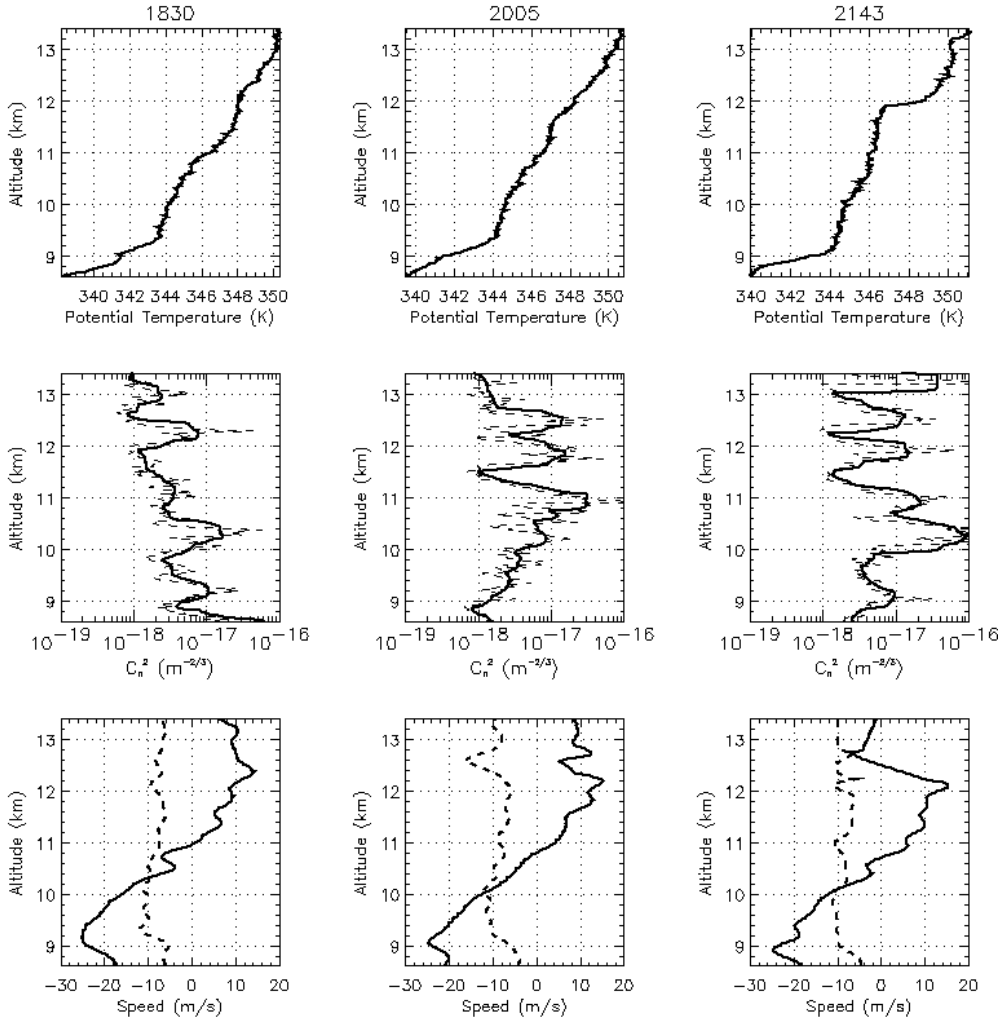

Figure 7.17: *In situ* measurement made near the altitude of the billow structure on the evening of 8 September 1998. Balloons were launched at 1830, 2005, and 2143 LT. *Top panel*: Potential temperature. *Center panel*: Dashed line is the measured C_n^2. The solid line is the C_n^2 averaged to a 300 m height resolution. *Bottom panel*: The meridional wind (solid line) and the zonal wind (dashed line).

launched on 1830 LT, 2005 LT, and 2143 LT, 8 September 1998. Keep in mind that the balloon, traveling at ~5 m/s, needs ~20 minutes to reach the neighborhood of ~11 km. In other words, if we are looking at the balloon data from 1830 LT, the corresponding radar data is near 1850 LT. We limit our analysis from 8.6 to 13.4 km, the altitude range relevant in the understanding of the evolving billow structure.

Towards the end of the evening, the potential temperature data indicate the development of a potential temperature step. This development correlates with the growth of the billow structure which is detected by the radar. Potential temperature profiles from 1830 LT and 2005 LT are similar to previously observations made on 7 September. As the billow structure begins near 2000 LT and starts to grow in size and intensity, its effect is seen in the formation of a potential temperature step centered ~10.5 km, extending vertically from 9 km to 12 km.

The billow activity is also indicated by the turbulence parameter. We consider the *in situ* measurement of C_n^2, which is a measurement of the temperature fluctuation as caused by turbulence. We plot this in the center row of Figure 7.18. The solid line is the C_n^2 smoothed to 300 m, the height resolution of the radar; the dashed line is the actual measurement. C_n^2 grows steadily in time, especially near 10-11 km, in accordance to the instability growth; C_n^2 at several locations measured from the 2143 LT launch is nearly a magnitude larger than the 1830 LT launch.

The lower panel of Figure 7.17 plots the wind information. A large vertical shear in the meridional component exists in the same altitude range of the billow structure seen in the RTI plot. The shear persists throughout this evening. *In situ* temperature structures, taken in context with the radar data, seem to indicate that the observed wind shear is related to the atmospheric dynamics observed by the radar as well as the *in situ* temperature and turbulence probes.

Figure 7.18 depicts the structure ~1 day after the start of the instability. The temperature steps observed at 2143 LT on 8 September have evolved into a

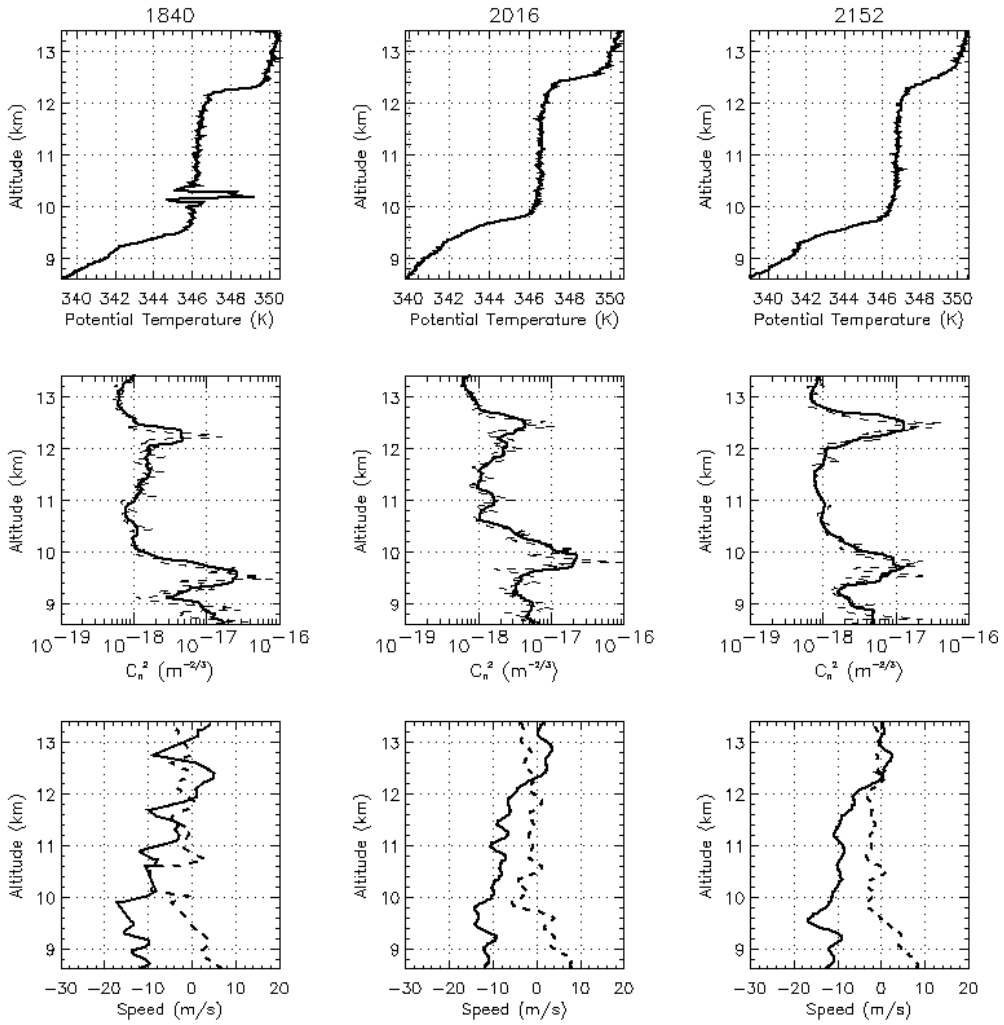

Figure 7.18: The same as Figure 7.17 but for the evening of 9 September 1998.

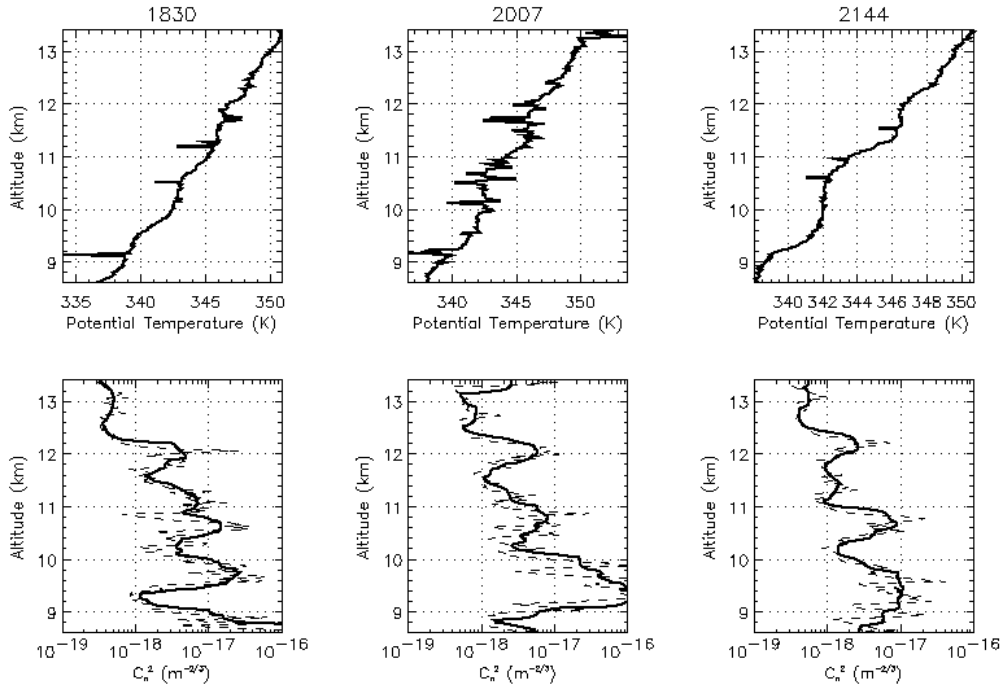

Figure 7.19: *In situ* measurement made near the altitude of the billow structure on the evening of 10 September 1998. Balloons were launched at 1840, 2016, and 2152 LT. *Top panel*: Potential temperature. Sharp fluctuations in the potential temperature profile are caused by a glitch in the temperature sensor.

temperature step centered near 11 km with a 2 km vertical extent. The fluctuations seen near 10.2 km in the 1840 LT flight is caused by an instrument glitch. The air parcel in the temperature step behaves adiabatically, i.e., the potential temperature gradient is nearer to zero than it was observed at 2143 LT in the previous evening. This means that this parcel of air, extending >2 km in the vertical direction, is well mixed. The large temperature gradient at the edges of the steps would create a large temperature gradient that would appear as a scattering layer in the RTI plot seen in Figures 7.15 and 7.16. Between the 1840 LT and the 2016 LT flight, the temperature steps have been advected upward by ~300 m, possible by some low-frequency atmospheric motion originating from inertial gravity wave and/or tides [*Larsen and Cornish*, 1989; *Riggin et al.*, 1999]. The observed instability may also be responsible

for generating the low-frequency motion that modulates the location of the temperature step.

The homogeneous mixing of the atmosphere is indicated by the potential temperature steps and also by the *in situ* measurement of C_n^2. C_n^2, a measure of the refractive index fluctuation, and thereby the temperature fluctuation, of the atmosphere, is small in the adiabatic portion of the temperature step and increases at the edges. This double peaked C_n^2 structure is seen in the backscatter power profile as the scattering layer at ~12 km and perhaps one near 10 km.

Winds observed in this altitude were nearly constant, contrary to what it was 24 hours ago. On this evening, the wind was ~-10 m/s in the meridional direction and ~0 m/s in the zonal direction. The structures revealed in the balloon measurement on 10 September 1998, as seen in Figure 7.19, are not obviously related to the structures seen on the previous two evenings. Wind data was not available in this altitude range on this evening.

7.3.3 Discussion

We believe that the structure observed near ~11 km on 8 September 1998 is a KHI. We were fortunate to observe its evolution by both a VHF radar, which provides us quasi-continuous observation of the atmosphere, and *in situ* probes, which provide the atmospheric thermodynamic variables and turbulence intensity. The radar observation gives us a visual presentation of the evolving instability while *in situ* probes reveal the small-scale structures within the instability.

From a visual inspection, the structure observed on 8 September resembles previous observations of KHI [e.g., *Gossard et al.*, 1971; *Singh et al.*, 1999]. We can vividly discern the cat-eye shaped billow structure that is indicative of KHI. The active turbulence associated with the initial stages of the KHI development is also seen in the radar spectral width. Furthermore, the scattering layers seen on 9 September are

what one expects by probing, via a radar, the structures created at the end of a KHI evolution. We recall from our KHI discussion in Chapter 2 that active mixing associated with the instability creates an adiabatic, well-mixed layer of air with sharp transitions at the edges to as the adiabatic layer merges with the background atmosphere. The vertical profile of the adiabatic layer is a potential temperature step. We see this in the *in situ* data from September 9 seen in Figure 7.18. The formation of the temperature step is seen in the previous evening. The backscatter caused by the sharp change in the refractive index at the edges of the temperature step is observed in the evening of 9 September 1998. What we are surprised by is the long duration of this structure. *Browning* [1971] observed billows that persist longer than 4 hours. The billow observed at JRO lasts much longer than that, at least 24 hours. We investigate this in the following section.

7.4 The Lifetime of KHI

The temperature step centered near 11 km and its associated C_n^2 and SNR profiles seen on 9 September are related to the KH event that took place 24 hours earlier. One may be hesitant to believe the long life time of such a structure. We have two possible explanations for this. It is possible that the remnant of the KH event observed on 8 September is fossilized and remains in the background atmosphere. It is also possible that the turbulent eddy diffusion rate is small enough to yield a long lifetime for the structure. We examine both possibilities. Appendix A provides the background in turbulence theory needed for this discussion. Our discussion here comes from a variety of sources, among them *Tatarski* [1961], *Tennekes and Lumley* [1972], *Cho* [1993], and references therein.

7.4.1 Eddy Diffusion

We want to determine the lifetime of a turbulent eddy. In other words, the amount of time needed for eddy diffusion to destroy an eddy of scale size l. In eddy diffusion, mass is transferred through the mixing of turbulent eddies within the fluid. No longer are the properties carried by the 3D random walk of molecules. Consider a passive tracer of turbulence, ξ. Good candidates are potential temperature and potential refractive index. For a turbulent eddy of scale l, the rate of generation of mean square tracer fluctuations is

$$\frac{\partial\left\langle\left|\xi_l\right|^2\right\rangle}{\partial t} \sim \frac{\left\langle\left|\xi_l\right|^2\right\rangle}{\tau_l}. \tag{7.9}$$

τ_l is a typical lifetime associated with the eddy. In the inertial range of turbulence, the rate of generation of fluctuations is equal to the rate at which the smaller scale fluctuations of size around $l_K = \upsilon^{3/4}\varepsilon^{-1/4}$, the Kolmogorov microscale, are lost due to viscous effects. Energy is generated at larger scales and propagates down through the smaller scales until the scales become so small, and associated shear so large, that viscous forces damp out the motions. Thus, within the inertial range kinetic energy is not created or destroyed – it simply propagates down the scales at a rate of

$$\varepsilon_\xi \approx \frac{\left\langle\left|\xi_l\right|^2\right\rangle}{\tau_l}. \tag{7.10}$$

The loss rate via eddy diffusion is

$$\varepsilon_\xi \sim D_\xi\left|\nabla\overline{\xi_l}\right|^2, \tag{7.11}$$

D_ξ being the turbulent diffusion coefficient appropriate to ξ. $\overline{\xi_l}$ is the mean (time averaged) value of ξ at height z. Thus, combining (7.10) and (7.11) and for simplicity, assuming only a vertical gradient of $\overline{\xi}$, we have

$$\varepsilon_{\xi} \approx \frac{\left\langle \left| \xi_l \right|^2 \right\rangle}{\tau_l} \approx D_{\xi} \left(\frac{d\overline{\xi_l}}{dz} \right)^2 . \tag{7.12}$$

A velocity

$$v_l \sim l/\tau_l \tag{7.13}$$

can also be associated with the scale l, where v_l is the typical velocity associated with these scales. In other words, an eddy of dimension l would have a velocity around v_l and a lifetime around τ_l.

Since ξ_l, the fluctuation of the tracer at scale l, is proportional to the RMS velocity $\sqrt{v_l^2/2}$, we can then, along with (7.12) and (7.13), say

$$\frac{\left\langle v_l^2 \right\rangle / 2}{\tau_l} = \frac{\left\langle v_l^2 \right\rangle}{2} \frac{v_l}{l} \approx \varepsilon_d \approx \upsilon \left| \nabla \sqrt{\left\langle v_\eta^2 \right\rangle / 2} \right|^2 , \tag{7.14}$$

i.e.

$$\begin{pmatrix} \text{Energy generated per} \\ \text{unit mass per unit time} \end{pmatrix} \approx \begin{pmatrix} \text{Energy loss} \\ \text{rate} \end{pmatrix} \approx \begin{pmatrix} \text{Energy lost due} \\ \text{to viscosity} \end{pmatrix} \tag{7.15}$$

Since this is a dimensional result, the factors of 2 are dropped. Thus,

$$\varepsilon_d = \frac{v_l^3}{l} . \tag{7.16}$$

This, combined with (7.13), yields

$$\tau_l = \varepsilon_d^{-1/3} l^{2/3} = l^2 / D_{\xi}. \tag{7.17}$$

Thus, τ_l, the lifetime of a turbulent eddy of scale size l, is dependent on the scale l and the turbulent diffusion coefficient.

The eddy diffusivity can be approached in two ways: one is based on dimensional analysis, another on the use of a turbulence parameter. Theoretical justifications of these approaches are beyond the scope of this thesis. However, we want to evaluate the different formulations of the eddy diffusivity provided in literature. We approach this via computing the eddy diffusion parameters using *in situ* measurements.

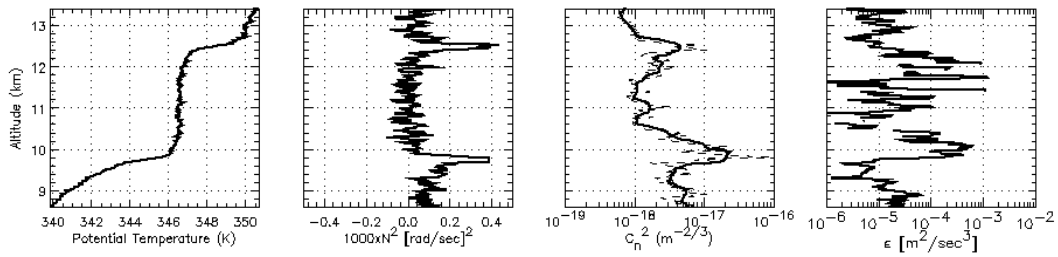

Figure 7.20: *In situ* measurement made near the altitude of the billow structure on the evening of 9 September 1998. Balloon was launched at 2016 LT. From left to right: Potential temperature; square of the Brunt-Väisälä frequency; C_n^2; turbulent dissipation rate (ε).

By analogy between molecular and eddy diffusion, the eddy diffusivity can be expressed as

$$D_\xi = l\, v_l\,, \tag{7.18}$$

where l is a characteristic length scale and v_l is the characteristic turbulent velocity. Taking into account the energy dissipation rate ε_d and the Richardson number, (7.18) can be expressed as [*Bertin et al.*, 1997]

$$D_\xi = \frac{\varepsilon_d}{3N^2}\,. \tag{7.19}$$

Let us consider how long it would take for eddy diffusivity to destroy a vertical potential temperature step. We plot in Figure 7.20 N^2 and the energy dissipation rate computed from the *in situ* measurement of the thermodynamic parameters on the 2016 LT flight. According to the radiosonde measurements, $N^2 = 4.0\times10^{-4}$ [rad/sec]^2 and $\varepsilon \sim 10^{-3}$ [W/kg] and yield a typical value of $D_\xi \sim 0.833$ m^2/s. When doing this calculation, one must convert the units of N^2 from [rad/sec]^2 to [1/sec]^2. The edge of the temperature step has a length scale on the order of 300 m, as seen in Figure 7.20. Diffusion theory tells us that the lifetime (τ_l) of a turbulent eddy of scale size l is

$$\tau_l = \varepsilon^{-1/3} l^{2/3} = l^2/D. \tag{7.20}$$

In this case, $\tau_I \sim 30$ hours. This calculation assumes that the flux Richardson number (*Rf*) to be 0.25. By definition, *Rf* is defined as the quotient between the gradient Richardson number (*Ri*) and the Prandtle (*Pt*) number. In general, *Rf* is in the range 0.15-0.25 while *Ri* is strongly varying. As a consequence, the *Pt* number is strongly variable as well, ranging from 0.1 to 20 within a turbulent layer. The ratio of these two numbers yields a somewhat constant *Rf*.

7.4.2 Fossil Turbulence

The basic ideas and evidence for fossil turbulence in the ocean and atmosphere have been in print for decades, starting with *Woods* [1969]. The term fossil turbulence refers to remnants of turbulence in fluid which is no longer turbulent. Fossil turbulence is easily observed by pouring cold cream into hot coffee. The initial turbulence is generally dampened to internal wave motions before mixing is complete, leaving the fossil milk (and temperature) turbulence at the bottom of the cup. Skywriting and high altitude jet contrails are also familiar examples of fossil turbulence in stably stratified fluids.

Fossil turbulence is not turbulence but is the remains of it; it begins with kinetic energies on the order of the original turbulence and decays with time. The physical process leading to fossil turbulence is that buoyancy forces remove turbulent kinetic energy at large scales, but no comparable mechanism removes the large scale fluctuations of scalar fluid properties, such as temperature, produced by the original turbulence. Internal restratification will remove some scalar fluctuations if the initial turbulence is weak or has operated for only a short time. As the Reynolds number of the initial patch of turbulence increases, a much wider range of fossil scalar fluctuations will exist after the turbulence is dampened; the persistence time of the fossil should increase correspondingly.

Consider the evolution of an isolated patch of actively turbulent fluid embedded in a stably stratified region of non-turbulent fluid. Density variations are assumed to be entirely due to variations in temperature. The following scenario unfolds after the source of kinetic energy is removed from the turbulent mixing of a high Schmidt number scalar. Begin with a turbulent patch of length scale L_p imbedded in a non-turbulent, stably stratified region with an ambient vertical gradient in the scalar. With no energy input, the velocity fluctuation spectrum starts to decay and the inertial subrange shrinks as the inner scale moves to longer lengths. The size of the patch grows due to the entrainment of ambient fluid. The Batchelor scale of the scalar variance spectrum also shifts to larger scales, but the level of the spectrum rises because the difference in the scalar quantity between fluid entrained at the top and bottom increases as the patch grows.

We summarize here the fossilization process as described by *Gibson* [1980, 1986]. Fossilization begins when the inertial forces of the largest turbulent eddies in the patch become equal to the buoyancy forces of the surrounding stably stratified medium, i.e., when L_p grows to l_{LS}, the buoyancy scale. (In fossil turbulence literature, the buoyancy scale is often referred to as the Ozmidov scale.) Complete fossilization is reached when the viscous dissipation subsides to $\varepsilon = 24.5\nu N^2$ [*Stillinger et al.*, 1983] and the Batchelor scale has reached the fossil Batchelor scale $l_{BF} = D^{1/2}N^{-1/2}$ [*Gibson*, 1986].

Gibson [1980] gives a scalar fossil "decay time" of

$$\tau_F = \varepsilon_0^{1/3}\nu^{-1/3}N^{-5/3}, \tag{7.21}$$

where ε_0 is the energy dissipation at the onset of fossilization which lies between the ε of the original turbulence and $\varepsilon_F = 24.5\nu N^2$ which occurs at complete fossilization. The time τ_F can be taken as the minimum persistence time for fossil scalar turbulence with $Sc > 1$, since the fossil should last longer if it is dependent on the scalar

molecular diffusivity. Recent discussions on this topic can be found in *Gibson et al.* [1999].

Is fossil turbulence an explanation of the observed temperature structure lifetime? To answer this, we want to compute the decay time (τ_F) of the fossil turbulence and offer a convincing argument that what we have is fossil turbulence. We examine the atmospheric parameters near the scattering layer located slightly above 12 km. Again, we choose a value of $N^2 = 0.210^{-3}$ [rad/sec]^2 and $\varepsilon = 10^{-4}$[m^3/sec^3]. According to *U. S. Standard Atmosphere* [1976], ν near 11 km is $0.8\text{x}10^{-4}$ m^2/s. Using these values, we compute τ_F to be ~6 hours. We suspect that, if we had *in situ* measurements from earlier in the evening, we would measure a larger ε, giving us a longer decay time. This supports the persistence of the scattering layer. We have thus examined two possible mechanisms, fossil turbulence and eddy diffusion, that would permit a potential temperature step to persist (see Figure 7.8), with the latter to be the most reasonable mechanism.

7.5 Discussion and Conclusion

The study of KHI in the atmosphere by visual observations of clouds or billow patterns using ground based weather and FM-CW radars [e.g., *Eaton et al.*, 1995; *Chilson et al.*, 1997] or using instrumented aircrafts [e.g., *Nielson*, 1992] has been reported numerously in the literature. VHF radar observations have also been reported both in the lower atmosphere and mesosphere heights [*Czechowksy and Rüster*, 1997; *Singh et al.*, 1999]. Recent *in situ* measurements from JRO and Wichita, KS, suggest that KH event occur more often than previously realized.

However, observation techniques have their limitations. Radar techniques offer measurements over a wide range of altitude with good time resolution but the height resolution is poor. On the other hand, *in situ* measurements capture the vertical temperature structures at one snap shot in time. Numerical simulations can be used to

compensate for the experimental measurement shortfalls. For the case of a KH billow, very high-resolution computer simulations provide the opportunity to focus on the evolution of individual billows, their subsequent transition to turbulence and dissipation of energy. Using the simulation to interpret the experimental data offers us insight into the physical phenomenon.

In situ measurements capture the signature of a KHI structure at the end of its evolution-a potential temperature step, as observed in the three balloon flights of 9 September 1998 plotted in Figure 7.7. In other words, the balloon data provide three snapshots in the evolution of KH billows, more specifically, near the decaying stage of the evolution. We can see the edges of the potential temperature steps being smoothed out by turbulence and other dissipative processes. This effect is particularly dramatic for the potential temperature step centered at ~19 km at 2143 LT. Furthermore, this work has brought to light the observations of persistent regions of strong radar backscatter, as seen in Figure 7.12, which are collocated with the temperature steps.

A wide range of vertical scales of turbulent regions is suggested by *Coulman et al.* [1995] and *Luce et al.* [1995] and the measurements presented here, as summarized in Table 7.1. However, the sporadic nature of balloon flights leads to difficulties in determining a statistical description of the occurrence of turbulent events. Can we use longer-term measurements, such as radar observations to give a statistical measure of these events? Clearly resolution is a key issue. It is necessary to develop a relation between the smallest scale features (O(10m)) and those at resolvable scales (O(100m)). To do this, the concept of self-similarity is needed. Self-similarity is the property we associate with fractals - the object appears the same regardless of the scale at which it is viewed. We see in the Wichita dataset observations of self-similar structures in the form of internal, smaller-scale vertical structure of the potential temperature steps. The measurements indicate that (major) potential temperature steps with vertical extent ~300 m contain within them smaller (minor) steps, self-similar in

nature, with individual vertical extents of 30 m. Clearly the VHF radar vertical resolution is not sufficient to resolve such structures; yet, these structures, with their steep temperature gradients, are likely to contribute most to the observed radar backscatter. *In situ* observations may help us understand these structures, if the instrument provides measurements with adequate vertical resolution. We believe that a combination of radar observations, direct measurements, and DNS is needed to help us understand the physics of these self-similar potential temperature steps.

It appears that KHIs are more common than is suggested by visual observations of billow clouds. The common occurrence of KHI in the lower stratosphere could be relevant to the suggestion of *O'Sullivan and Dunkerton* [1995] that KHI, created by inertia-gravity waves, may be one of the most important mechanisms for cross-isentropic transport and vertical mixing of constituents in the lower stratosphere.

We see self-similar structures in the balloon observations made at JRO. Figures 7.8, 7.9, and 7.10, illustrate the similarity between neighboring potential temperature steps. The DNS scaling performed for the step centered at 18.75 km results in a potential temperature profile which also 'fits' the step at 19.6 km altitude. Since the value of kinematic viscosity will remain approximately constant from 18.5 km to 20.0 km, we suggest that the similarity between the steps is evidence for a common generation mechanism. The existence of a height sequence of critical wind shear levels necessary for the generation of these features cannot be confirmed with the current dataset. However, both the VHF radar observations and the estimation of the total vertical wind shear of the horizontal wind from balloon data provide evidence for localized large wind shears in this height region.

This chapter has aimed to clarify issues regarding the cause of the potential temperature steps observed in the Wichita and MIST campaign datasets. The good agreement between the observation and the KHI simulation indicates that KHI is one mechanism responsible for the creation of such homogeneous mixing in the

atmosphere. This allows us to identify of KH billow structures in future atmospheric datasets. We emphasize the importance of the use of multiple measurement techniques, such as radar and balloon-borne probes, to obtain unambiguous temperature and wind velocity determinations. The availability of the simulated KH billow is extremely valuable. With it, for the first time, we can confirm the observed potential temperature steps and vertical shears of the horizontal velocity can be interpreted in terms of KH structure.

In addition, we also examined in this chapter the evolution of a KHI as observed by both *in situ* probes and VHF radar. The initial evolution of the KHI is indicated by an increase in SNR and spectral width. The formation of a potential temperature step is also visible. This temperature step remains 24-hours after the beginning of the KHI evolution, and perhaps longer. This may be a result of the low background eddy diffusivity. It is also possible that the temperature steps are fossilized, which gives its long lifetime. In the next chapter, we want to apply our understanding of the potential temperature steps to the observed radar backscatter in the lower atmosphere.

Chapter 8

Radar Backscatter Calculation

As we have seen in the previous chapters, the lower atmosphere is aspect-sensitive; that is, radar backscatter decreases with an increase in tilt angle, with the strongest signal coming from the vertical direction [e.g., *Röttger*, 1980a, b; *Hooper and Thomas*, 1998]. We presented an example of this in Chapter 4 where we discussed an investigation of aspect sensitivity at the Jicamarca Radio Observatory (JRO). The implication is that horizontally stratified sheets of varying index of refraction exist with vertical scales comparable to the wavelength. One of our goals in this thesis is to understand the scattering mechanisms that cause aspect sensitivity based on a wavelet analysis of the high-resolution balloon measurements of atmospheric temperature. We predict the radar backscatter based on the wavelet decomposition of an *in situ* atmospheric temperature in the lower atmosphere. As we have seen in Chapter 3, localized structures such as the temperature gradients at the edges of the potential temperature steps are best characterized via wavelet transforms. We want to show in this chapter that, given the wavelet transform of a high-resolution temperature measurement, the wavelet coefficients can be used to calculate the Fresnel reflection coefficient. This wavelet-based scattering model assumes that the temperature layers

have an infinitely long horizontal correlation length. Our approach is similar to that applied by *Alcala* [1998] and *Alcala and Kelley* [2001] to the problem of VHF backscatter from the polar mesosphere summer echoes (PMSE).

We briefly digress from our scattering calculation and consider the wavelet analysis of the temperature structure predicted by a numerical simulation of the Kelvin-Helmholtz instability (KHI). We examine the wavelet spectrum, i.e., the relationship between wavelet coefficients and scale size, of the high-resolution data and compare it to the simulation. This behavior is then used to compute the radar backscatter from a low-resolution *in situ* temperature measurement again assuming that the scatterer has an infinite horizontal correlation length. Corrections to this scattering calculation are made taking into account the finite horizontal correlation length of the scatterers.

This chapter is organized as follows. In the next section, we demonstrate the advantages of wavelets for radar backscattering calculation. This wavelet approach is then applied on the high-resolution temperature measurement and the result is presented. We then develop the wavelet spectrum from the high-resolution dataset and the numerical simulation in an attempt to identify something of a universal wavelet coefficient behavior. This result allows us to predict radar scattering from a low-resolution *in situ* temperature measurement. We conclude this chapter by discussing a radar backscatter calculation using a low-resolution temperature data with the help with the wavelet spectrum. This result is compared with the measured backscatter at UHF and VHF.

8.1 Scattering Calculation from High-Resolution Data

The temperature profile that we analyzed in Chapter 3 is unique in its high height resolution. It is the only temperature sounding, as far as we are aware of, where the height resolution is less than 1 m which is less than the Bragg scale for a 50 MHz

radar. This dataset is therefore a good candidate to be used to predict radar backscatter. We will show that the wavelet transform, with its ability to characterize sharp temperature gradients, makes it ideal to be incorporated in the scattering calculation.

8.1.1 Fresnel Reflection From Horizontally Stratified Media

In this scattering calculation, we assume that the scattering layers do not vary with time. We also neglect the effects of advection by winds in the neutral atmosphere. These assumptions require that the timescales of any changes in the layer are much longer than the integration period (typically >> 1 minute) used to process the radar data.

Consider a plane wave impinging on a layer filled with a dielectric different from vacuum. We define the reflection coefficient ρ as the ratio of the incident electric field to the reflected electric field. Given a horizontally stratified refractive index layer between *z1* and *z2* with a refractive index profile $n(z)$, the reflection coefficient is [*Wait*, 1962],

$$\rho = \frac{1}{2}\int_{z2}^{z1}\left[\frac{1}{n(z)}\frac{d}{dz}n(z)\right]e^{-2jk_o z}\,dz\,. \tag{8.1}$$

One can model $n(z)$ as

$$n(z) = n_0 + \Delta n(z), \tag{8.2}$$

where n_0 is a constant background refractive index and $\Delta n(z)$ is the local fluctuation in refractive index dependent on water vapor and dry air fluctuations in the lower atmosphere and free electron density in the middle/upper atmosphere [e.g., *Gage and Balsley*, 1980]. Typically, $n_0 = 1$ and $\Delta n(z) << 1$. Substituting this expression into (8.1), we obtain

$$\rho \approx \frac{1}{2}\int_{z2}^{z1}\left[\frac{d}{dz}\Delta n(z)\right]e^{-2jk_o z}dz\,. \tag{8.3}$$

For completeness, let us examine some insights revealed by (8.3) regarding the relationship between $\Delta n(z)$ and ρ. ρ is related to the shape of $\Delta n(z)$. In general, if $\Delta n(z)$ contains gradients, the steeper the gradient of the refractive index, the larger the reflection coefficient. For a smooth profile of refractive index, a longer wavelength radar will see a larger reflection coefficient than a shorter wavelength radar.

We want to consider the effect of the layer shape on the calculation of the reflection coefficient in (8.3). The most basic shape used to model the layer profile is the step function, first introduced in undergraduate physics and electrical engineering courses. Although this is a good model for boundaries between different media, its applicability for modeling gradients within the same medium is questionable as diffusion inhibits the formation of such sharp edges. In recognition of this problem, various authors attempted to use other models for the layer shape [*Hocking*, 1987; *Woodman and Chu*, 1989]. One particularly common model is the constant gradient, which gives a linear profile for the refractive index.

It is important, though, that the function we use to model the refractive index irregularities is smooth. We consider, in some detail, just how the discontinuity in the derivative of the modeling function can change the wavelength dependence of the fluctuation spectrum. For mathematical conveniences, we will ignore the effect of the shape of the radar pulse width to ρ. We can represent $\Delta n(z)$ via a Taylor expansion,

$$\Delta n(z+h) = \Delta n(z) + h\frac{d\Delta n(z)}{dz} + \frac{1}{2}h^2\frac{d^2\Delta n(z)}{dz^2} + \frac{1}{6}h^3\frac{d^3\Delta n(z)}{dz^3} + \cdots \tag{8.4}$$

We can rearrange the terms in (8.4) to obtain an expression for the derivative of $\Delta n(z)$,

$$\frac{d\Delta n(z)}{dz} = \frac{\Delta n(z+h) - \Delta n(z)}{h} - \frac{1}{2}h\frac{d^2\Delta n(z)}{dz^2} - \frac{1}{6}h^2\frac{d^3\Delta n(z)}{dz^3} - \cdots \tag{8.5}$$

When we substitute this expansion into (8.3), we derive a new expression for the reflection coefficient.

$$\rho \approx \frac{1}{2}\int_{z2}^{z1}\left[\frac{\Delta n(z+h)-\Delta n(z)}{h}\right] e^{-2jk_o z}\, dz - \frac{1}{2}\int_{z2}^{z1}\left[\frac{1}{2}h\frac{d^2\Delta n(z)}{dz^2}+\frac{1}{6}h^2\frac{d^3\Delta n(z)}{dz^3}\right] e^{-2jk_o z}\, dz \quad (8.6)$$

The first term in (8.6) is the constant gradient profile used by many authors for partial reflection calculations [e.g., *Gage and Green*, 1978; *Woodman and Chu*, 1989; *Luce et al.*, 1995]. The second term shows the contribution of the second and higher derivatives to the non-smooth $\Delta n(z)$. The higher-order derivative terms act to diminish ρ. When h is zero, we obtain the standard formula for the step function profile. However, as h increases, the ability of the modeling function to estimate the proper reflection coefficient will depend on the number of continuous derivatives, or the smoothness. If $\Delta n(z)$ were not smooth, the second term of (8.6) would therefore be undefined; this leads to an over estimate of ρ. We conclude from this exercise that, if we want to compute ρ from an *in situ* measurement of $\Delta n(z)$, the function we use to model $\Delta n(z)$ must be smooth.

We model the refractive index fluctuations specified by the derivative of a Gaussian, first proposed by *Hocking* [1987] and then used by *Alcala* [1998] and *Alcala and Kelley* [2001] for calculating theoretical PMSE echoes by an electron density profile measured by a sounding rocket. The model is the wavelet that we used in the wavelet analysis discussed in Chapter 3. It satisfies the smoothness requirement. In other words, this model does not introduce discontinuities that may lead to an over-estimate of radar backscatter. Since we can use wavelets to decompose localized structures, if we can relate the reflection coefficient to the wavelet coefficient, the result of the wavelet transform, we can than compute ρ from the wavelet coefficients. To do this, we follow *Alcala* [1998] and *Alcala and Kelley*

[2001] and define $\Delta n(z_o)$, an index fluctuation centered at an altitude z_o at a scale size h as

$$\begin{aligned}\Delta n(z) &= n_o \sqrt{h}\,\frac{d}{dz} e^{-(z-z_o)^2/4h^2} \\ &= -n_o \frac{1}{\sqrt{h}}\left(\frac{z-z_o}{2h}\right) e^{-(z-z_o)^2/4h^2}\end{aligned}, \tag{8.7}$$

with the reflection coefficient [*Alcala*, 1998]

$$\rho(z_o) \approx -4\sqrt{\pi}\,(k_o h)^2 \left(\frac{n_o}{\sqrt{h}}\right) e^{-(d_o/2\sigma_r)^2}\; e^{-4k_o^2 h^2}\; e^{-2jk_o z_o}, \tag{8.8}$$

where d_o is the distance between z_o and the center of a range gate and σ_r is the half-power half width of the radar beam. $\rho(z_o)$ was derived assuming that all reflections are Fresnel reflections. In other words, the structures causing the reflection have a horizontal extent larger than the first Fresnel zone. We now can use wavelets to help us predict radar backscatter from an *in situ* measurement of $n(z)$.

We apply (8.8) to scattering from multiple layers in a given range gate. We will assume the Born approximation which says that the incident wave is not affected by the scatterer and multiple reflection is negligible. The total refractive index fluctuation of N layers is simply the sum of the fluctuations from each layer. Extending this concept to a scattering calculation, the total reflection coefficient from N layers is

$$\rho_{total} = \sum_{i=0}^{N-1} \rho_i(z_{oi}) \tag{8.9}$$

where ρ_i is the reflection coefficient caused by layer i centered at z_{oi} [*Alcala*, 1998; *Alcala and Kelley*, 2001]. The summation arises because the reflection coefficient, and, therefore, the reflected electric field, is a linear function of the refractive index fluctuations.

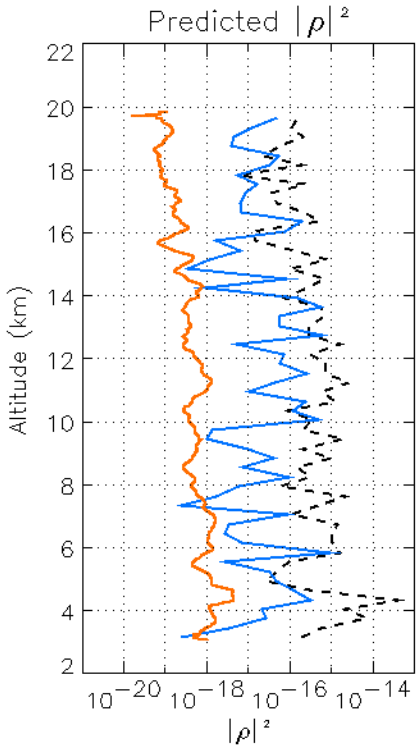

Figure 8.1: Predicted square of the magnitude of the reflection coefficient that a radar may observe giving the present temperature sounding. Black dashed line is reflection coefficient calculated using a piecewise derivative of $n(z)$. Our wavelet model of a refractive index perturbation yielded the result colored in blue. Red line marks the predicted power backscatter from isotropic turbulence computed C_n^2 derived from the *in situ* measurement of temperature.

We apply this wavelet-based scattering calculation to the high-resolution Wichita dataset and present the result of the scattering calculation in Figure 8.1 (blue line). In this calculation, we assume that our radar is operating at 50 MHz with a range resolution of 300 m. What we have done in this calculation is to first wavelet decomposed a 300 m segment of the temperature profile using the derivative of a Gaussian as the wavelet basis. The wavelet coefficients, the result of the wavelet decomposition at each scale, indicate the contribution of the wavelet basis to the temperature profile. Via (8.8), we can relate the wavelet coefficients to the Fresnel reflection coefficient. Each data point in the blue line is therefore the square of the sum of the Fresnel reflection coefficients computed from the 300 m segment of

temperature data. VHF radars have been used to measure the Fresnel reflection coefficient in the troposphere the lower stratosphere [e.g., *Green and Gage*, 1980; *Dalaudier et al.,* 1989, 1994]. $|\rho|^2$, based on our calculation, compares well with the measured results discussed in Chapter 2.

Black dashed line shows the reflection coefficient calculated using a piecewise derivative of the index of refraction derived from the *in situ* temperature profile. In other words, we have computed a 300 m segment of $\Delta n(z_o)$ and used (8.3) to compute ρ. We interpret the greater reflection coefficient from the piecewise derivative to be a result of contributions of discontinuities in the measured $\Delta n(z)$. We see differences of 10s of dBs between this result and the wavelet-based method. This is not a surprising result. *Woodman and Chu* [1989] established precedence by examining the reflection coefficient of two scattering models: one with a constant gradient while the second has a Gaussian profile. If the scattering layer were $1/2\lambda$ thick, the power calculated using the linear profile is 39 dB larger than that from the Gaussian profile. Thus, we can see that the discontinuous higher-order derivatives can greatly overestimate the backscattered power from larger-scale layers.

Red line is the predicted radar backscatter caused by turbulence. We examine this because in aspect sensitivity experiments, as one tilts the radar beam off-vertical, after a while, the radar backscatter, as a function of zenith angle, stops decreasing and becomes constant. This happens when turbulence backscatter is equal to Fresnel scattering. Since we can use the high-resolution temperature measurement from Wichita to compute C_n^2 (see Chapter 3), a predicted turbulence backscatter can hence be computed. We want to compare this with our prediction of $|\rho|^2$. As mentioned in Chapter 5, when considering turbulence backscatter, one assumes that turbulence fills the radar range volume and then compute a volume reflectivity (η). In this study, since we have already made a postulation of ρ based on Fresnel scatter from the steep edges in the dataset, we use (5.3) to convert the turbulence volume scatter (η) to an

effective $|\rho|^2$. To perform the conversion, we have taken the parameters of the MU Radar, with λ_o = 6 m, Δr = 300 m, and A_e = 8330 m^2. We use the MU radar because the MU radar and the observations made at mid-latitudes, e.g., Wichita, KS. Furthermore, the MU radar has been used to measure the aspect sensitivity of the lower atmosphere [*Tsuda et al.*, 1997]. The computed turbulence backscatter would therefore be what the MU radar would have measured based on the atmosphere characterized by the Wichita balloon sounding. In terms of radar backscatter, the contribution from turbulence component is clearly well below the contribution from edge component, which is characteristic of the aspect sensitivity of radar scatter from the atmosphere.

In Figure 8.2, we plot the difference between the reflected power we calculated for Fresnel scattering and the value of turbulent scatter we predicted for the MU radar under the same atmospheric condition as measured by the balloon flight; the backscatter is expressed in decibels. Similar to experimental observations seen in Chapter 4, the ratio of vertical Fresnel scatter power in the lower stratosphere to the isotropic component is about 20 dB and about 10 dB in the troposphere. We suspect that the higher aspect sensitivity in the stratosphere is related to the greater stability of that part of the atmosphere. Our prediction compares well with previous measurements. *Hooper and Thomas* [1995, 1998] made radar observations in Wales of the backscattered signal in the vertical direction and at zenith angles of 4.2º, 6º, 8.5º, and 12º. The radar operates at a frequency of 46.5 MHz. At a zenith angle of 12º, the backscattered power is approximately 10 dB below the vertical power at 6 km and 20 dB less at 14 km. *Tsuda et al.* [1997], using the MU radar in Japan, studied the characteristics of specular echoes reflected from stratified layers in the troposphere and lower stratosphere. The echo power was largest in the vertical direction, decreased by about -10 dB at 6º off-vertical, and then gradually decreased to a constant level between -15 and -25 dB down at $\theta > 20º$, where θ is the zenith angle.

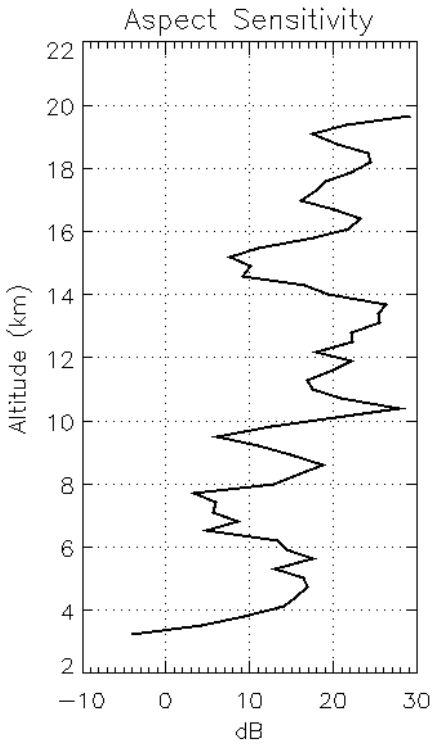

Figure 8.2: Difference between the predicted radar backscatter from Fresnel scatter versus that from turbulent scatter that the MU radar would observe using this temperature sounding. We have used C_n^2 computed from the higher order difference to calculate the equivalent reflection coefficient of isotropic turbulence. Fresnel scattering is about 15 dB more effective than turbulence scattering in the troposphere and 25 dB in the stratosphere.

This constant level is interpreted as the isotropic turbulence scattering level. However, the Jicamarca Radio Observatory cannot make this kind of measurement, as the radar can only tilt a few degrees off-vertical.

8.2 Scattering Calculation from Low-Resolution Data

Changes in the atmospheric scalar parameters, such as temperature and electron density, lead to changes in the refractive index, resulting in radar backscatter. We showed that, for a given *in situ* measurement of an atmospheric scalar parameter, one can use the results of the wavelet transform to compute the Fresnel reflection coefficient. We base our calculations on the fact that radar scattering is caused by

sharp gradients of a passive scalar parameter, e.g., the temperature gradients seen in the Wichita dataset. These coherent and localized structures will have components that persist over multiple scale sizes. In Chapter 3, we exploited this property to isolate these gradients via a wavelet-based edge-tracking algorithm. In the previous section, we modeled the refractive index fluctuation by an appropriate wavelet basis function and computed a closed-form expression of the reflection coefficient. In the our case, the wavelet basis is the first derivative of a Gaussian. This allows us to relate the reflection coefficient to the wavelet coefficients generated from the wavelet transform of the measured scalar parameter.

Backscatter is caused by structures on the Bragg scale, i.e., $\lambda/2$ or even smaller features [*Briggs and Vincent*, 1973]. For a signal sampled at sampling interval T, the smallest scale that a wavelet transform can resolve in that signal is $2T$. Hence, in order to compute the backscatter coefficient using wavelets, the signal must be sampled at a sampling interval of one-half the Bragg wavelength or smaller; this condition guarantees the isolation, via the wavelet transform, of the Bragg scale component of the refractive index structure, as was the case for the Wichita dataset. However, temperature data measured by a typical radiosonde, such as the ones used at JRO, fail to meet this condition; the sampling interval of the temperature profile is about 10-15 m. One cannot effectively apply the wavelet-based algorithm to this temperature data to predict the expected radar backscatter since the smallest scale resolvable by the wavelet transform is 30 m, an order of magnitude larger than the Bragg scale.

8.2.1 Wavelet Coefficient Model

We bypass this roadblock by returning to Figure 3.9 and revisiting our wavelet analysis result. The temperature gradient near 3.705 km contain structures ranging from large scales (~50 m) to scales near the Nyquist period, which is approximately

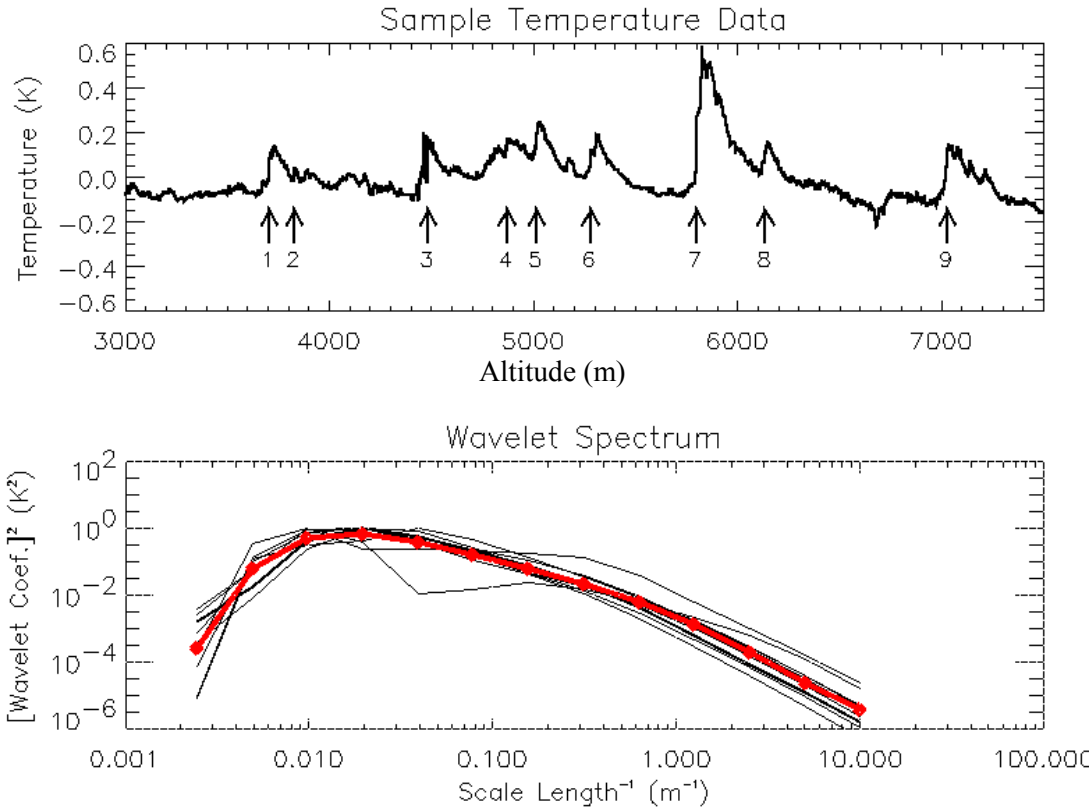

Figure 8.3: *Top panel*: A segment of the high-resolution temperature data measured at Wichita. Sharp temperature gradients, or edges, are indicated by the arrows. *Lower panel*: Normalized wavelet spectrum, i.e., square of the wavelet coefficient versus the scale size for the indicated temperature gradients. Red line is the least square fit of the spectrum.

~10 cm. This is seen visibly in the scalogram, which is similar to the Fourier spectrogram, shows us the spatially-varying localized energy spectrum. Other examples of temperature gradients exhibit similar scalogram structures. We want to characterize the wavelet coefficient behavior at a temperature gradient. To do this, we examine nine temperature edges that we have selected from the Wichita dataset; see the top panel of Figure 8.3. We plot in the lower panel the normalized wavelet spectrum, i.e., the relationship between squared amplitude of the wavelet coefficient and scale size. For each temperature gradient, the wavelet coefficients exhibit a similar dependence on scale sizes.

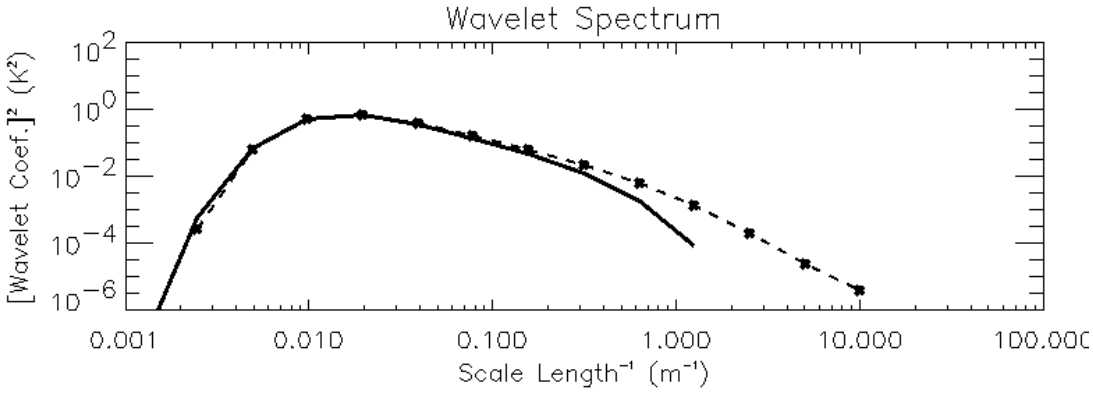

Figure 8.4: Normalized wavelet spectrum of troposphere temperature structure. Dashed-starred line is the wavelet spectrum computed from temperature edges in the simulation. Solid line is the wavelet spectrum predicted from the *in situ* data.

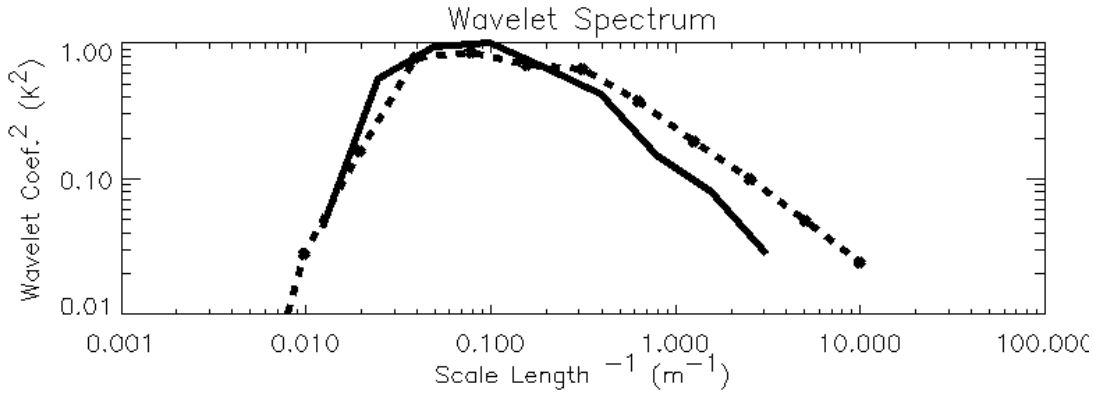

Figure 8.5. *Dashed-starred line*: Normalized wavelet spectrum, i.e., the square of the wavelet coefficient versus scale size for the temperature gradients, which we call edges, in the lower stratosphere measured at Wichita. *Solid line*: Wavelet spectrum computed from temperature edges computed by the simulation.

We have shown in Chapter 7 good agreement between the measured potential temperature step and the vertical profile of a computer simulation of a Kelvin-Helmholtz instability (KHI). To show perhaps the universality of this wavelet coefficient behavior, we perform the similar wavelet analysis on the simulated data plotted in Figure 7.4 and plot the result as the solid line in Figure 8.4. We have reproduced the wavelet spectrum from Figure 8.3 as the star-dashed line. The shape is very similar for scales down to approximately three meters, after which the *in situ* data maintains a higher amplitude. This is very near the Nyquist scale for the simulation and here we assume the *in situ* data to be more reliable. We see the similar result for the temperature structures observed in the stratosphere; see Figure 8.5. In this calculation, we only examine the edges where the temperature gradient is steeper than 15 K/km. This wavelet spectrum is another indication that the edge components of the data, i.e., the sharp temperature gradients, are localized coherent structures persisting over multiple scale sizes.

The wavelet analysis result, as presented in the form of the wavelet spectrum, reveals a similarity between the measured and simulated potential temperature step. In addition, the wavelet spectrum seems to manifest a universal characteristic. This is a new result. Once the wavelet spectrum is known, we only need information on the large scales as the spectrum would provide the needed information at the small scales which we need to use a low-resolution temperature profile to predict radar backscatter. We examine the validity of this statement in the following section.

8.2.2 Scattering Calculation

We now have a hypothetical functional dependence between the wavelet coefficient and the vertical scale for a temperature structure as demonstrated in Figures 8.3 and 8.4. We can apply this to the wavelet coefficient of the low-resolution data and

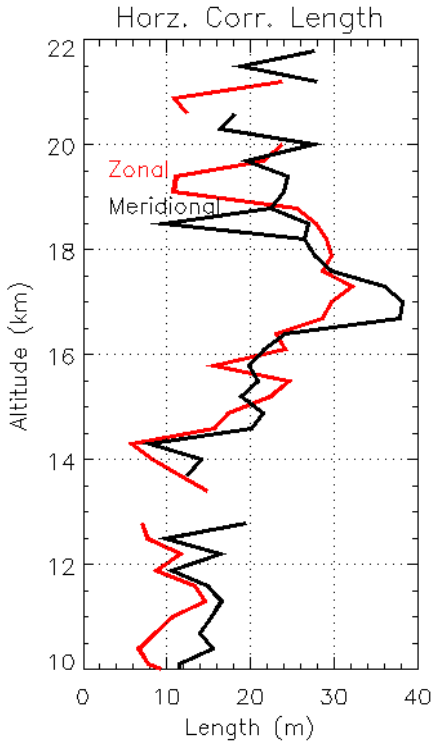

Figure 8.6: Horizontal correlation length in the zonal (red) and meridional (black) directions computed from the radar data for 1830-1910 LT on 8 September 1998. Horizontal correlation length increases from ~15 m in the troposphere to ~25 m in the stratosphere.

extrapolate the wavelet coefficients from a scale of 30 m to 3 m, the Bragg wavelength for the 50 MHz Jicamarca radar. We then compute the square of the Fresnel reflection coefficient, $|\rho|^2$, via (8.8) and (8.9) as described in section 8.1.1. In this scattering calculation, we temporarily assume that the scatterer has an infinite horizontal correlation length, or at least a length larger than the Fresnel radius, which is about 200 m at 17 km. We find that this approximation causes a substantial overestimate of $|\rho|^2$ and that the finite horizontal correlation length must be taken into account. In the experiment described in Chapter 4 in which the radar emitted beams pointing in the vertical and slightly off-vertical directions, the measured aspect sensitivity can be used to estimate this correlation length. We plot in Figure 8.6 the horizontal correlation length (ζ) as measured by JRO on 8 September 1998 near 1830. As in

Chapter 5, we see that ζ is typically 25 m in the stratosphere and about half that size in the troposphere. These two values differ by a factor of two which corresponds to a factor of sixteen in scattering strength in the Rayleigh regime. Thus, edge scatter is stronger at stratospheric heights than in the upper troposphere, even though the vertical gradient scales must be comparable, since scatter is observed at 50 MHz.

Alcala and Kelley [2001] make a correction to the scattering calculation by developing an expression comparing $|\rho|^2$ from a scatterer of finite horizontal correlation length with scatterer of an infinite horizontal correlation length. The ratio is

$$\frac{|\rho(\zeta)|^2}{|\rho(\infty)|^2} = \left[\frac{8k_o A^2 h^2}{\sqrt{z^2 + 64k_o^2 A^4 h^4}} \right]^2 \tag{8.10}$$

where $k_o = 2\pi/\lambda_{\text{radar}}$, $A = \zeta/h$, z is the range to the scatterer, and $h \approx 0.2\lambda$ is the vertical scale length of the most effective backscatter [*Briggs and Vincent*, 1973]. As a consistency check, we see that as ζ increases, $|\rho(\zeta)|^2 / |\rho(\infty)|^2$ the ratio of $|\rho|^2$ approaches unity. We then define a "corrected" $|\rho|^2$ as

$$|\rho|^2_{\text{corrected}} = \frac{|\rho(\zeta)|^2}{|\rho(\infty)|^2} |\rho|^2_{\text{original}} \tag{8.11}$$

where $|\rho|^2_{\text{original}}$ is the $|\rho|^2$ computed for a scatterer with an infinite horizontal correlation length. In this calculation, ζ is the root-mean-squared (RMS) of the correlation length in the zonal and meridional direction. We compute $|\rho(\zeta)|^2 / |\rho(\infty)|^2$ and plot the result in Figure 8.7. Solid line is the ratio at z = 18 km while the dashed line is for z = 13 km. The plot indicates that, for $\zeta < 25$ m and $h = 0.2\lambda$ for a 50 MHz radar, if we do not account for the finite horizontal length of the scatterers, we would over estimate the reflected power by a factor of ten or more!

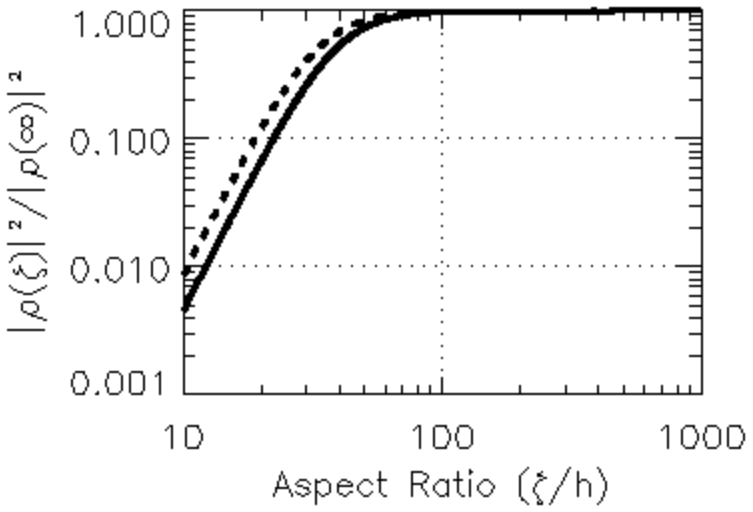

Figure 8.7: Ratio between the reflection coefficients of two scatterers as a function of the aspect ratio. One scatterer has a finite horizontal correlation length, the other infinite. Solid line is for z = 18 km; the dashed line is for z = 13 km.

In Figure 8.8, we compare the radar-measured $|\rho|^2$ to $|\rho|^2_{\text{corrected}}$, computed from the simultaneously measured temperature profile using (8.11) and (8.12). We also include in the figure the predicted $|\rho|^2_{\text{corrected}}$ computed from the low-resolution temperature profile via wavelets, taking into account the finite horizontal correlation length of the scatterer. We see, perhaps not surprisingly, good agreement in the stratosphere the measured $|\rho|^2$ and $|\rho|^2_{\text{corrected}}$. The agreement is not as good in the troposphere although the edge scattering does decrease dramatically, nearing the value of turbulent scatter.

The radar return ceases to be aspect-sensitive when the radar return from Fresnel scattering is equal to or less than the turbulence scattering. It is known that the middle atmosphere is not aspect-sensitive for UHF radars such as the 430 MHz radar at Arecibo Observatory (AO) [e.g., *Woodman and Guillen*, 1974]. We can check this using our wavelet calculation, and we plot the results in Figure 8.9. Red lines are the predicted $|\rho|^2_{\text{corrected}}$ for 430 MHz, calculated based on two different assumptions.

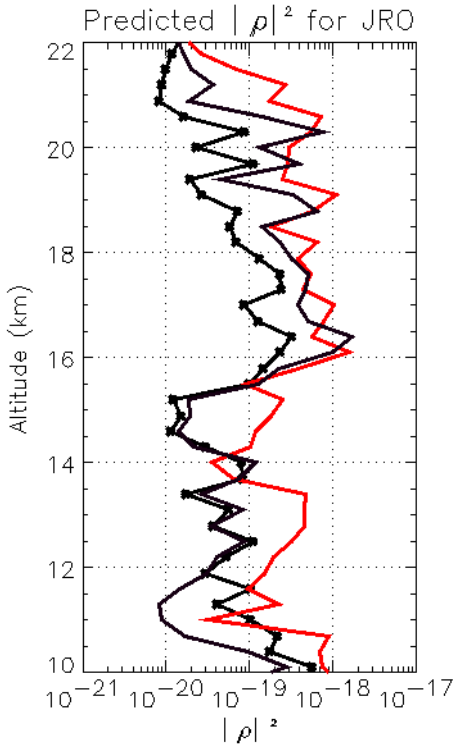

Figure 8.8: Fresnel coefficient as measured by JRO compared to the reflection coefficient computed from the temperature profile. Solid-starred line is the square root of the sum of the squares of the reflection coefficient computed from the off-vertical beams; solid line is the reflection coefficient computed from the vertical beam signal. Red-line is the predicted scattering computed from the low resolution temperature profile, adjusted to the horizontal correlation length computed from the radar data.

Solid red line is $|\rho|^2_{\text{corrected}}$ calculated under the assumption that the horizontal correlation length at UHF frequencies has the same ratio to the wavelength as we find at VHF frequencies; in other words, the scatterer has a horizontal correlation length of about 3 m. On the other hand, assuming that the horizontal correlation length at UHF is equal to that at VHF (25 m) gives us the result plotted as the red solid-dotted line. Black dashed line is the equivalent $|\rho|^2$ computed from the turbulence volume reflectivity. C_n^2 used was obtained from the balloon data taken over the Jicamarca Radio Observatory but is representative of the atmosphere in general and suitable for the estimates made here [e.g., *Coulman et al.*, 1995; *Walters*, 1995]. Since we know

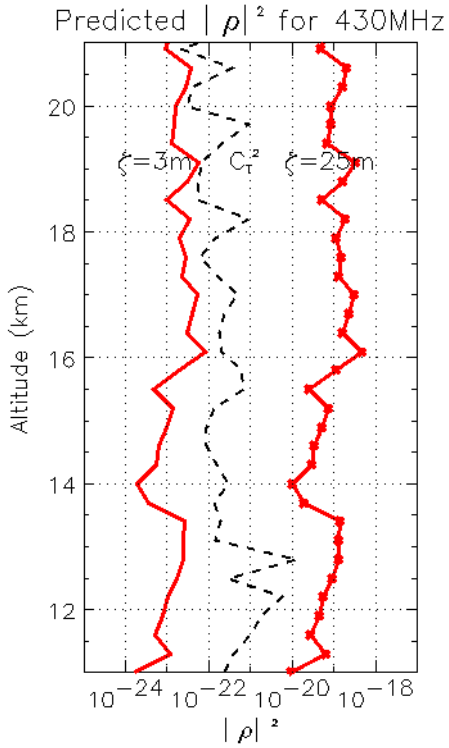

Figure 8.9: Scattering prediction for a radar at 430 MHz, using the temperature profile in Figure 8.8. Solid red line assumes that the horizontal correlation length of the scatterers is about 3 m. An assumption of 25 m yields the result plotted as the solid-dotted red line. Dashed line is the predicted turbulence scattering using the *in situ* measurement of C_n^2 made by the balloon.

that aspect sensitivity is not measured at UHF, we predict that the horizontal correlation length is at most slightly larger than 3 m. Thus, our extrapolated wavelet spectrum describes the character of the temperature steps quite well.

8.3 Discussion and Conclusion

In this chapter, we calculate the Fresnel reflection coefficient using the wavelet coefficients from a high-resolution temperature measurement and find the values to be in good agreement with the experimentally measured values. The turbulent scatter is found using C_n^2 computed from the high-resolution temperature measurement via the higher order structure function. We compare the computed turbulent scatter with the calculated Fresnel scatter to determine the theoretical aspect sensitivity a 50 MHz

radar may observe the conditions given by the balloon sounding. The ratio between the Fresnel scatter and the turbulent scatter is around 10 dB in the troposphere and over 20 dB in the stratosphere. Our calculation compares well with published observations of aspect sensitivity.

We find that both the measured and DNS predicted potential temperature steps display a similar wavelet coefficient behavior at the edges of the steps. This universal character of the wavelet spectrum allows low-resolution data to be extrapolated in order to predict the radar backscatter. Indeed, when this approach is applied to low-resolution temperature data measured at a VHF radar site, good agreement is found between the measured backscatter strength and the predicted backscatter, provided the finite horizontal correlation length is taken into account. Furthermore, the good agreement between the wavelet spectrum of the observation and the simulation predicted temperature structure is additional evidence that the observed potential temperature steps are caused by a late time evolution of a Kelvin-Helmholtz instability. We show that potential temperature steps have a definite effect on radar backscatter at VHF. An accurate backscatter prediction for a VHF radar requires the knowledge of the horizontal correlation length of the scatterer. Although we do not have direct measurement of the correlation length of the scatterer, we can compute one based on the measured aspect sensitivity. Our computation also indicates the required scatterer horizontal correlation length, upper bound only, to yield the near-isotropy of the radar backscatter in the middle atmosphere at 430 MHz.

Chapter 9

Conclusions

In this chapter, we recapitulate the important results from this thesis. We also comment on how our own work has hopefully expanded the understanding of the structures in the lower atmosphere, particularly the temperature structures that maybe responsible for aspect-sensitive scatter. There are undoubtedly many questions that have not been answered and new one s that have emerged as a result of our new work. We briefly go over them as well as providing suggestions on how they may be addressed.

9.1 Concerning Our Observations

In this thesis, we presented two datasets of lower atmosphere observations. In one, a high-resolution temperature sensor measured lower atmospheric temperature structures at Wichita, KS. The second dataset originates from a multi-instrument campaign at the Jicamarca Radio Observatory where we probed the lower atmosphere with theVHF radar and radiosondes. After numerous pages of analysis and discussion, what have we learned from these?

9.1.1 Balloon Data

Looking at the *in situ* measurements, one common signature seen in the lower atmosphere both at equatorial and mid-latitudes is the potential temperature step. The vertical extent of these steps ranges from tens of meters to hundreds of meters. In one observation at the Jicamarca Radio Observatory on 9 September 1998, a step with a vertical extent of ~2 km was observed. These regions of adiabatically mixed air are bordered by sharp temperature gradients that mark the boundaries between the temperature step and the background atmosphere. The adiabatic region is further indicated by a low value of N^2, Ri, and C_n^2. High-resolution *in situ* temperature measurements indicate that the temperature gradients at the edges can be particularly steep (> 40 K/km).

The balloon-borne turbulence sensor used at Wichita, KS, provided high-resolution temperature fluctuation measurements. Edges of the potential temperature step appear as ramp-cliff, saw tooth shaped structures. The cliffs mark the edges of the temperature step while the ramp corresponds to the near zero potential temperature gradient portion of the step. These structures are not only measured in laboratory turbulence, but also in the boundary layers [e.g., *Taylor*, 1958; *Kaimal and Businger*, 1970].

Wavelets seem to be a promising tool for the study of coherent structures in the atmosphere. In particular, following the footsteps of *Alcala et al.* [2001], we use wavelets to isolate the coherent fluctuations, i.e., the ramp-cliff structures, from the dataset. This helps us prove that the measured temperature is composed of the coherent structures, background isotropic turbulence, and instrument noise. Fourier analysis of the residual signal indicates the presence of isotropic turbulence. The latter statement is supported by the comparison of C_n^2 found from the Fourier analysis of the residual signal and C_n^2 determined via the higher order structure function.

Wavelet analysis of the high-resolution temperature measurement reveals the small-scale structures that exist at the sharp temperature gradients. Structures as small as ~10 cm are seen at some of the sharpest gradients. It is reasonable to suggest that these small-scale structures, which are concentrated at sharp temperature gradients, are responsible for clear-air echo from the lower atmosphere, and perhaps also the aspect sensitivity measured at VHF.

Self-similarity is the property we associate with fractals - the object appears the same regardless of the scale at which it is viewed. We see in the Wichita data set self-similar structures in the form of internal, smaller-scale vertical structure of the potential temperature steps. Potential temperature steps with vertical extent ~300 m contain within them smaller steps, self-similar in nature, with individual vertical extents of 30 m.

We also see self-similar structures in the balloon observations made at JRO. The temperature steps observed on 8 September 1998 illustrate the similarity between neighboring potential temperature steps. This similarity is evidence for a common generation mechanism. The existence of a height sequence of critical wind shear levels necessary for the generation of these features cannot be confirmed with the current dataset.

9.1.2 Radar Data

VHF radar measurement of the lower atmosphere made at the Jicamarca Radio Observatory (JRO) near Lima, Peru, indicates strong echoes in the lower atmosphere, particularly in the lower stratosphere. The duration of the scattering events is longer than the observation hours. These scattering layers are on the order of 1 km thick; they can be thinner but are not observable with a radar with a 300 m height resolution. These scattering layers are aspect-sensitive (AS). In other words, the radar backscatter from the vertical direction is larger, by 10-15 dBs, than the backscatter from a

direction ~2.5° off-vertical. Aspect sensitivity is stronger in the stratosphere than the troposphere.

If we model the scatterer as an ellipsoid with a Gaussian refractive index profile in both the vertical and the horizontal direction, we can use the measured aspect sensitivity (AS) to compute the horizontal correlation length of such a scatterer. At JRO, the horizontal correlation length increases with increasing aspect sensitivity, going from ~15 m in the troposphere to ~25 m in the stratosphere. These values are roughly 10 % of the Fresnel scale for the VHF radar at that height.

It is insightful to interpret the radar backscatter in the context of the *in situ* measurement of the atmospheric thermodynamic parameters. We detect in the troposphere what may be called isotropic turbulence scatter. This is not only indicated by the weaker aspect sensitivity measured at these heights, but also the comparison between the measured backscatter with the predicted turbulence backscatter. Furthermore, the data suggest that, especially in the stratosphere, the temperature gradients at the edges of the potential temperature steps cause the measured radar backscatter.

Aspect sensitivity increases with the increase in atmospheric stability. The atmospheric thermodynamic parameters provided by the *in situ* probes indicate an extremely stable stratosphere and a turbulent troposphere.

The availability of the *in situ* measurement of C_n^2 gives us an opportunity to validate the effectiveness of deriving C_n^2 from radar parameters, mainly, the signal-to-noise ratio (SNR) from the oblique direction and the spectral width. At the Jicamarca Radio Observatory, we find that both radar parameters provide a relatively good indication of C_n^2. However, it is not uncommon for the radar to over-estimate the atmospheric C_n^2 by an order of magnitude or more. There are two causes for this: Fresnel reflection/scatter and non-turbulence spectral width broadening effects. The latter is minimized because of the beam size and low wind velocities at JRO. It is,

however, very difficult to separate the non-turbulent component of the backscattering from its turbulent counterpart. The bottom line is that, for the Jicamarca radar, the spectral width seems to provide the better estimate of atmospheric C_n^2.

Radar observations reveal a small portion of a larger picture where gravity waves and mean wind structures interact with Bragg-scale features to produce a complex environment. This complexity is suggested by some radar observations of descending scattering layers, associated with the downward phase progression of gravity waves and/or diurnal and semi-diurnal tides [*Hooper and Thomas*, 1998; *Riggin et al.*, 1999]. Vertical movement of the center of the temperature steps is also seen. However, the vertical motion is on the order of a radar range gate; the radar does not have adequate vertical resolution to measure the rate of vertical phase propagation over time periods of several hours.

9.2 Concerning Kelvin-Helmholtz Instability

There has been a growing interest to understand the roles that dynamic instabilities, such as the Kelvin-Helmholtz instability (KHI), play in the atmosphere, particularly in their effects on the vertical transport of chemicals, turbulence generation, wave excitation, and radar backscatter [e.g., *Muschinski et al.*, 1999; *Gibson-Wilde et al.*, 2000]. The vertical potential steps observed at Wichita, KS, and JRO spurred our interest in KHI. These temperature structures resemble the vertical profile of a late-time Kelvin-Helmholtz instability (KHI). We find excellent agreement between the temperature steps from balloon data and the numerical simulation of a KHI. Considering the frequency with which these temperature steps are observed in the JRO and Wichita dataset, KHI events seem to occur more often than previously indicated. This is important, as this indicates that KHI plays a major role in the creation of turbulent layers in the atmosphere, which will affect the vertical transport of aerosols and other atmospheric constituents.

Wavelet analysis also reveals a similarity between the measured and the DNS predicted potential temperature step. For both datasets, the wavelet spectrum at the edges of the step displays an almost identical wavelet coefficient behavior except at small scales, as a result, we believe, to the limitations of the ability of the numerical simulation to model the atmosphere. This seemingly universal characteristic of the wavelet spectrum affirms the resemblance between the observed potential temperature and the vertical structure of the KHI simulation.

This thesis addressed issues regarding the identification of KH billow structures in stratospheric datasets. We emphasize the importance of the use of multiple measurement techniques, such as radar and balloon-borne probes, to obtain unambiguous temperature and wind velocity determinations. The availability of the numerical simulation is extremely valuable. With it, for the first time, we can confirm that the observed potential temperature steps and vertical shears of the horizontal velocity can be interpreted in terms of KH structure. Furthermore, the availability of the DNS has allowed us to confirm the observation of a KHI in its development and decay phase.

The remnant of a KHI structure is long lived. This is best exemplified by the KHI event seen near 11 km on 8-9 September 1998. Adiabatic layers that form at the end of a KHI evolution seem to persist for nearly a day, perhaps more. We examined two possible explanations for this: fossil turbulence and eddy diffusion. The persistence of the adiabatic layer at the late stages of the KHI evolution may be explained by low eddy diffusivity.

9.3 Concerning the Radar Backscatter Controversy

Although it has been a little over twenty years since the first observation, the radar community has yet to reach an agreement on the cause of aspect sensitivity. Three major theories have been developed to explain aspect sensitivity: Fresnel reflection,

Fresnel scatter, and anisotropic turbulence. Regarding this controversy, based on the VHF and *in situ* observations made at JRO, our results seem clear. Our correlation lengths are much too large to be explained by anisotropic turbulence according to the theory presented by *Hocking and Hamza* [1997] and too small for a Fresnel reflection mechanism.

For mathematic conveniences, people have modeled the scatterers as circular pan-cake like structures with a Gaussian profile in the vertical and horizontal direction [e.g., *Luce et al.*, 1995; *Hooper and Thomas*, 1998]. However, we cannot envision in good faith the atmosphere creating such a structure. As an alternate explanation, there is strong evidence that suggests that the late time evolution of a Kelvin-Helmholtz instability (KHI) plays a major role in the lower atmosphere backscatter. As the instability decays into a stratified layer of adiabatically mixed air, the edges of that layer, because of the sharp temperature gradients that exist there, will contain Bragg scale components responsible for VHF backscatter. In the observations at JRO, potential temperature steps, which are tell-tale signs of KHI, are seen along with strong aspect-sensitive radar backscatter. If the KHI has the right dimensions, it is possible that it has structures that lead to an aspect-sensitive echo.

9.4 Concerning Scattering Calculation

We believe that the steepest gradients, i.e., the cliff component of the ramp-cliff structures, which are the edges of the potential temperature steps, cause the strongest scatter. If the height resolution of the temperature profile were less than one-half of a Bragg wavelength, and we model the change in the refractive index as a wavelet, we can predict the VHF scatter based on the wavelet coefficients of the high-resolution temperature measurement. A predicted turbulent scatter is found using C_n^2 computed from the higher order structure function. We compare the computed turbulent scatter to the calculated Fresnel scatter to determine theoretical aspect sensitivity a 50 MHz

radar may observe the conditions given by the balloon sounding. The predicted aspect sensitivity compares well with published observations of aspect sensitivity by, e.g., *Hooper et al.* [1995, 1998] and *Tsuda et al.* [1997], from around 10 dB in the troposphere and over 20 dB in the stratosphere.

The universal wavelet spectrum behavior at a temperature gradient at the edge of a potential temperature step allows us to extrapolate a low-resolution temperature measurement to a resolution equal to or smaller than the Bragg scale. We use this approach to compute the Fresnel backscatter from the low-resolution temperature data at JRO. We again find good agreement between the measured backscatter strength and the predicted backscatter, provided we take into account the finiteness of the horizontal correlation length. Assuming an infinitely long horizontal correlation lengths leads us to overestimate the backscatter by a factor of ten or more. What is more important is perhaps the relationship between KHI and radar backscatter. The resemblance between the simulated and observed potential temperature step, and effect of the edges of the step on the radar backscatter indicate that the scatter mechanisms may be generated by KHI. Our scattering calculation also confirms the near-isotropy of the radar backscatter in the middle atmosphere at 430 MHz.

9.5 Unanswered Questions and Future Works

At the end of this thesis, although we understand a little more of the scatter mechanisms in the lower atmosphere, there is still a lot that we do not know. *In situ* measurements from JRO and Wichita do indeed suggest that KHI events occur more often than previously observed. However, the limited observation time and height resolution of the radar places a ceiling in our ability to resolve the small-scale structures of the KHI. One limitation of the JRO experiments was the short radar observation period. Radar observations of a developing KHI, from the beginning to end, coupled with *in situ* measurements of the atmospheric thermodynamic

parameters, winds, and turbulence intensity. This type of observation will help us understand the development of the instability and its effect on the radar backscatter.

Furthermore, *in situ* measurements of atmospheric temperature reveal a wide range of vertical scales. Total vertical motions of the temperature steps and the scattering layers are on the order of a radar range gate; a radar does not have adequate vertical resolution to measure the rate of vertical phase propagation over time periods of several hours. The sporadic nature of balloon flights with sufficiently high resolution leads to difficulties in determining a statistical description of the occurrence of turbulent events. Long-term measurements via a radar are needed to give a statistical measure of these events. However, the height resolution of a radar must be high, as the smallest scale features are on the order of tens meters.

More work needs to be done in terms of comparing the simulated KHI with the observed temperature structure. We have compared the direct numerical simulation (DNS) of a KHI to the *in situ* measurement of potential temperature. The preliminary results shown in this thesis are encouraging. However, we did not have a chance to compare in detail the radar backscatter predicted from a simulation KHI to an observed KHI. Furthermore, we need to try to explain the frequent appearance of the KHI structures, as seen in the temperature profiles. The self-similarity seen in the temperature structures measured at JRO and Wichita also deserve investigation. A combination of radar observations, direct measurements, DNS, and fractal analysis are needed to help us understand the physics of these self-similar potential temperature steps.

We need to apply the DNS to the study of lower atmospheric turbulence. As high-resolution *in situ* instruments are expensive and radars with height resolution on the order of tens of meters are unable to reach the lower stratosphere, numerical simulation may be the only approach to investigate quantitatively turbulent structures in the atmosphere and to test the extraction of turbulence from radar and *in situ*

observations. In order to assess the role of turbulence in the real atmosphere, we need to quantify the rates of occurrence of intermittent turbulent events. In previous radar measurements of the turbulent energy dissipation rate, assumptions of the turbulence either filling the radar pulse volume or remaining confined in a layered structure are inevitable [*Hocking*, 1999**,** and references therein]. The use of the DNS in concert with the observation will minimize these assumptions.

Further experimental investigations are thus needed for a better understanding of the 3-D temperature field. A better knowledge of the morphology of the fine scale refractive index structure will allow a complete understanding of aspect sensitivity about the aspect sensitivity at VHF frequencies. A 2-D sounding of the temperature sheets would improve the knowledge about their horizontal structures and would lead to a global understanding of the partial reflection contribution at vertical incidence. Such a description would be very useful to get an insight on the generation, evolution, and destruction mechanisms of the sheets which are presently largely unknowns. A better knowledge of the vertical enhancement mechanism can be obtained by an improvement of the radar system. However, we believe that real insight into the dynamic and structure of the atmosphere will be achieved via multiple-instruments observations, the interpretation of which is supported by numerical simulations of atmospheric dynamics and instabilities.

Appendix A

Turbulence Primer

Turbulent motion affects practically every aspect of the atmosphere. The role played by turbulence in the atmosphere can be classified into two categories: momentum transport and scalar mixing. In transporting momentum, turbulent motions behave in a manner roughly analogous to molecular viscosity, reducing differences in velocity between different regions of the flow. Small-scale turbulence is essential to energy and mass transport vertically in the air column.

Scalar mixing refers to the homogenization of fluid properties such as temperature by random molecular motions. Molecular mixing rates are proportional to spatial gradients, which are greatly amplified due to the stretching and kneading (i.e., stirring) of fluid parcels by turbulence. This is because of the slow rate of molecular diffusion process in which individual air molecules are exchanged between sections of the atmosphere with different properties. In the air, the vertical flux of properties such as horizontal air velocity, temperature, and constituent concentration are primarily dependent upon turbulence. Turbulence greatly enhances this exchange by moving larger parcels of air greater distances instead of individual molecular scales.

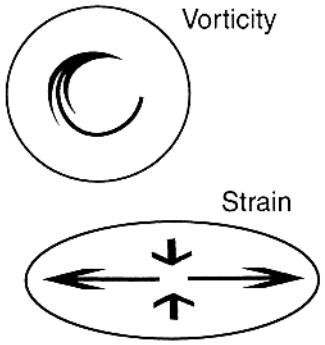

Figure A.1: Schematic representation of vortices and strain, in terms of the effect they have on an initially circular fluid parcel in two-dimensional flow. Vorticity rotates the parcel without changing its shape. Strain stretches the parcel in one direction and compresses it in orthogonal direction (to conserve mass). Flow in the neighborhood of a point following the motion can always be decomposed into a vortical component and strain component. In three dimensions the geometry is more complex, but the concepts are the same.

This appendix will describe the simple, classical picture of stationary, homogeneous, isotropic turbulence, focusing primarily on the commonly seen Fourier spectrum description. We will also discuss the structure function, from which we get the structure function coefficient, a commonly used turbulence parameter. We show how this type of turbulence representation ties back in with the Fourier formalism of the turbulence theory.

A.1 Turbulence Mechanisms

The main mechanisms that drive turbulence at the smallest scales are described in terms of strain and vorticity. They are quantities that represent the tendency of the flow at any point to deform and to rotate fluid parcels, respectively. We present a graphical representation of strain and vorticity in Figure A.1. A major and recent insight is that vorticity and strain are not distributed randomly in a turbulent flow, but rather are concentrated into coherent regions, each of which is dominated by one type of motion or the other [*Werne and Fritts*, 2000a, b].

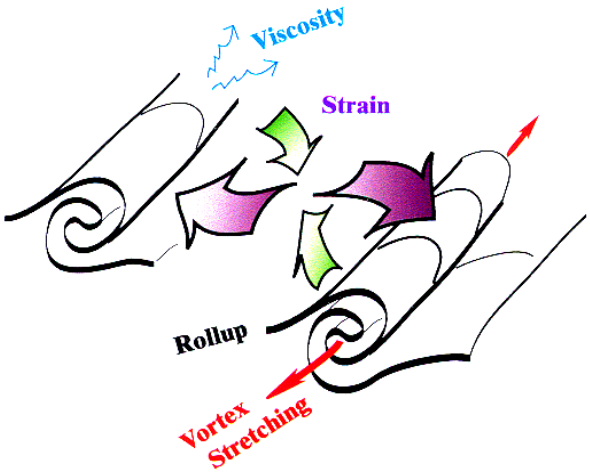

Figure A.2: Schematic illustration on line vortices and strained regions in a turbulent flow. Fluid parcels in the vortex interiors rotate with only weak deformation. In contrast, fluid parcels moving between the vortices are rapidly elongated in the direction of the purple arrows and compressed in the direction of the green arrows.

The first mechanism we consider is vortex rollup due to shear instability. We depict this situation in Figure A.2. This process results in a vorticity concentration of dimension close to unity, i.e., a line vortex. The process of vortex stretching reinforces line vortices. When a vortex is stretched by the surrounding flow, its rotation rate increases to conserve angular momentum. Opposing these processes is molecular viscosity, which both dissipate vorticity and fluxes away from strongly rotational regions.

Turbulence may thus be visualized as loosely tangled spaghetti of line vortices, which continuously advect each other in complex ways [*Werne and Fritts*, 2000a]. At any given time, some vortices are being created via rollup, some are growing due to vortex stretching, and some are decaying due to viscosity. Many, however, are in a state of approximate equilibrium among these processes, so that they appear as long-lived, coherent features of the flow. Mixing is not accomplished within vortices themselves; in fact, these regions are relatively stable, like the eye of hurricane. Instead, mixing occurs mainly in regions of intense strain that exist between any two,

nearby vortices that rotate in the same sense. It is in these regions that fluid parcels are deformed to produce amplified gradients and consequent rapid mixing.

Although the essential structures of turbulence are not complex, they combine in a bewildering range of sizes and orientations that defies typical analysis methods. Because of this, turbulence is most usefully understood in statistical terms. Although the statistical approach precludes detailed prediction of flow evolution, it does give access to the rates of mixing and property transport, which are of primary importance in most applications. Statistical analysis focus on the various moments of the flow fluid, defined with respect to some averaging operation. The average may be taken over space and/or time, or it may be an ensemble average taken over many flows begun with similar initial conditions. Analyses are often simplified using three standard assumptions. The flow statistics are assumed to be

- Stationary (invariant with respect to translations in time),
- Homogeneous (invariant with respect to translations in space), and/or
- Isotropic (invariant with respect to rotations).

Much of our present understanding pertains to this highly idealized case. We based our discussion on the classical theory of Kolmogorov. Our description will focus on the power spectrum that describe the variability of kinetic energy and scalar variance. The spectrum provides insight into the physical processes that govern motion and mixing at different spatial scales. This theory, based on a heuristic argument and simple dimensional considerations, is adequate in introducing the ideas of turbulent advection of scalar quantities. It has been proven to be remarkable accurate in the description of turbulence in the atmosphere and many other fluid media. The basic scenario is thus:

1. Energy from large-scale mean flows and waves are converted to three dimensional turbulent eddies via instabilities.

2. Vortex stretching mechanisms transfer the eddy kinetic energies to smaller eddies.
3. Small eddies become so small that molecular viscosity begins to destroy them.

Let us explain this scenario in more physical terms. Suppose that turbulence is generated by a steady, homogeneous, isotropic stirring force whose spatial variability is described by k_{LS}. Suppose further that turbulence is allowed to evolve until equilibrium is reached between forcing and viscous dissipation, i.e., the turbulence is statistically stationary. This is a non-linear process, where a spectral flux, or cascade, of energy is induced. The energy cascade starts at the source of the turbulence. Turbulent fluctuations in the atmospheric fluid velocity can be induced by a number of mechanisms. Perhaps dominant among these mechanisms in the lower atmosphere are dynamics and convective instabilities and breaking gravity waves. In either case, turbulence is produced. Because the largest scales of fluctuations have velocity shears too small for molecular viscosity to be an important sink of energy, the turbulent velocity fluctuations cascade to smaller and smaller scales until molecular viscosity can act actively. The energy cascade is directed primarily (though not entirely) towards smaller scales, i.e., large-scale motions interact to create smaller-scale motions. The resulting small eddies involve sharp velocity gradients, and are therefore susceptible to viscous dissipation. Thus, while kinetic energy resides mostly in large-scale motions, primarily small-scale motions dissipate it. Turbulence can be envisioned as a pipeline conducting kinetic energy through wave number space: in at the large scales, down the spectrum, and out again at the small scales, all at a rate ε defined as,

$$\varepsilon = -\frac{d}{dt}\frac{1}{2}\left[\overline{u'^2 + v'^2 + w'^2}\right], \tag{A.1}$$

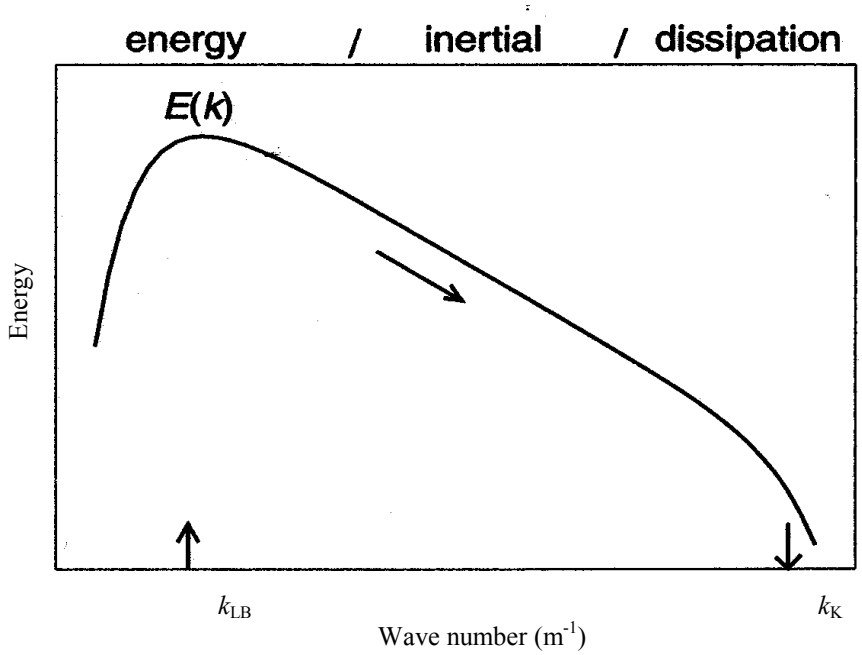

Figure A.3: Theoretical wave number spectrum of kinetic energy and kinetic energy dissipation for stationary, homogeneous, isotropic turbulence forced at k_{LB}. Approximate locations of the energy containing, inertial, and dissipation subranges are indicated, along with the Kolmogorov wave number. Axes are logarithmic. Numerical values are omitted here for clarity.

where $\overline{u'^2+v'^2+w'^2}$ is the total mean square velocity fluctuations, and $\frac{1}{2}\overline{u'^2+v'^2+w'^2}$ is therefore the mean kinetic energy per unit mass at any instant in time [*Batchelor*, 1953]. The overbar refers to a spatial average.

A.2 Kinetic Energy Spectrum

The kinetic energy spectrum is often divided conceptually into three sections. Figure A.3 shows a typical wave number spectrum of kinetic energy. The energy containing subrange encompasses the largest scales of motion, while the dissipation subrange includes the smallest scales. If the range scales were larger enough, there may exist an intermediate range in which the form of the spectrum is independent of both large-scale forcing and small-scale viscous effects. This intermediate range is called the inertial subrange. In this picture of the Kolmogorov energy cascade, for high

Reynolds numbers, the inertial subrange is the range of the one dimensional energy wave number spectrum in which there are no sources or sinks of energy, but only cascade from lower to higher wave numbers (large to small scales); the energy spectrum depends on the energy dissipation rate (ε). This subrange follows a -5/3 power law. The form of energy spectrum in this subrange is

$$E(k) = C_0 \varepsilon^{2/3} k^{-5/3}, \tag{A.2}$$

where $C_0 \approx 1.5$ is a constant [*Tennekes and Lumley*, 1972]. This power law spectral form indicates that motions in the inertial subrange are self-similar, i.e., their geometry is invariant under coordinate dilations. Once scales are reached that are small enough to allow viscosity to play a significant role in diffusing velocity fluctuations, the energy falls off much more rapidly with increasing wave number.

We define k = 1/(scale size), as it is in the convention of most turbulence literature. The existence of an inertial subrange in the atmosphere depends on the relationship between the Kolmogorov microscale

$$l_K = \upsilon^{3/4} \varepsilon^{-1/4}, \tag{A.3}$$

where υ is the kinematic viscosity and the Lumley-Shur buoyancy scale [*Lumley*, 1964]

$$l_{LS} = N^{-3/2} \varepsilon^{1/2}. \tag{A.4}$$

l_K is a scale within the viscous range of the turbulence; it represents a typical scale at which energy transfer by scale-cascade and energy dissipation rate, are comparable. l_{LS} is the scale related to large eddies in the buoyancy range. In actuality, the inertial subrange exists between $C_K l_K$ and $C_{LS} l_{LS}$ where the constants are found empirically to be $C_K \approx 12.8$ [*Hill and Clifford*, 1978], and $C_{LS} \approx 10.1$ [*Weinstock*, 1978]. At scales lager than $C_{LS} l_{LS}$, a fraction of the turbulent energy will be lost to the potential energy of stratification, and thus the energy spectrum becomes dependent not only on ε and k but also on buoyancy parameters [e.g., *Weinstock*, 1978]. Thus, a $k^{-5/3}$ inertial subrange can only exist for $C_K l_K < C_{LS} l_{LS}$. In the Earth's atmosphere, this condition is

roughly satisfied up to ~100 km, so a turbulent inertial subrange exists in the lower atmosphere, specifically at the Bragg scale for VHF radars [*Hocking*, 1985]. At length shorter than the inner scale, $C_K l_K$, viscosity damps out the velocity fluctuations and the energy spectrum falls off exponentially with k [*Corrsin*, 1964].

A.3 Passive Scalars and Mixing

These ideas of universal spectral forms can be extended to the spectrum of a passive scalar additive mixed by turbulence fairly straightforwardly. Now let us suppose that the fluid possesses some scalar property ξ, such as temperature or the concentration of some chemical species, and that this scalar is dynamically passive, i.e., its presence does not affect the flow. Suppose also that there is a source of large-scale variations in ξ, e.g., an ambient temperature gradient. As the turbulence folds and kneads ξ, i.e., mixes ξ, typical gradients of ξ will also increase and, therefore, become susceptible to erosion by molecular diffusion.

For this passive scalar, the diffusion coefficient D_ξ takes place of the dynamic viscosity ν as the damping parameter. The velocity fluctuations of the isotropic turbulence will mix the passive scalar. The scalar variance is destroyed at a rate χ_ξ, which is equal (in equilibrium) to the rate at which the variance is produced by the large eddies. χ_ξ is analogous to (A.1). We defineχ_ξ to be

$$\chi_\xi = -\frac{1}{2}\frac{d}{dt}\overline{\xi^2} = D_\xi \overline{\nabla \xi^2} \tag{A.5}$$

In other words, just as the energy dissipation rate, (A.5), summarizes how successfully turbulence draws energy from the mean flow and deposit it to viscous heating, the variance dissipation rate represents how successfully the turbulent mixing draws variance from the mean flow and deposits it to molecular diffusion.

Thus, turbulent mixing proceeds in a manner similar to the energy cascade discussed above. However, there is an important difference between the two

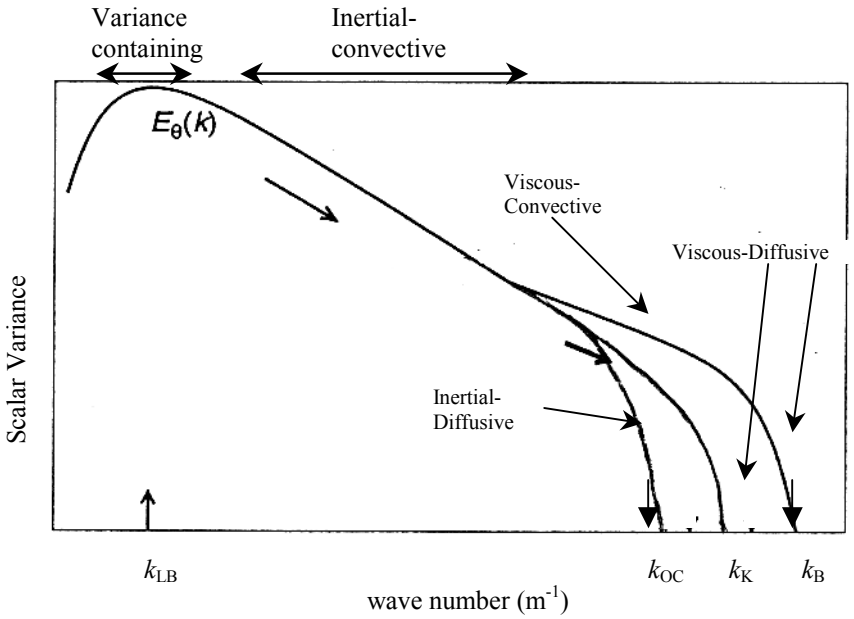

Figure A.4: Theoretical wave number spectrum of scalar variance and dissipation for stationary wave number k_{LB}. Approximate locations of the variance containing, inertial convective, inertial diffusive, viscous convective, and discus diffusive subrange, along with the Kolmogorov wave number k_K, the Batchelor wave number, k_B, the Obukhov-Corrsin wave number k_{OC}. Axes are logarithmic. Numerical values are omitted here for clarity.

phenomena. Unlike energy, scalar variance is driven to small scales by a combination of two processes. First, scalar gradients are compressed by the strain fields between the turbulent eddies. Second, the eddies themselves are continuously redistributed towards smaller scales, as the energy cascades from large scales to small scales. Figure A.4 shows the equilibrium scalar variance spectrum. Most of the variance is contained in the larger scales, which are separated from small scales by an inertial convective subrange, so called because temperature variance is convected by motions in the inertial subrange of the energy spectrum. Here, the spectrum of the inertial convective subrange can be expressed as

$$E_\xi(k) = C_\xi^2 \chi_\xi \varepsilon^{-1/3} k^{-5/3} \qquad \text{(A.6)}$$

C_ξ^2 is the second order structure function coefficient, which we will discuss in detail in a later section.

The shape of the spectrum at small scales is very different from that of the energy spectrum. Because the scale at which viscosity begins to destroy the velocity fluctuations may be different from the scale at which diffusivity of the additive, D_ξ, starts to dampen the scalar fluctuations, $E_\xi(k)$ at high wave numbers, i.e., small scales, will in general have a more complex form that is dependent on a key ratio is the Schmidt number defined as

$$Sc = \frac{\upsilon}{D_\xi}. \tag{A.7}$$

$Sc = 1$ for a typical atmosphere. Two additional scales also become important: the Obukhov-Corrsin scale [*Obukhov*, 1949; *Corrsin*, 1951]

$$l_{OC} = D_\xi^{3/4}\varepsilon^{-1/4} \tag{A.8}$$

and the Batchelor scale [*Batchelor*, 1959]

$$l_B = \nu^{1/4}D_\xi^{1/2}\varepsilon^{-1/4}. \tag{A.9}$$

For $Sc << 1$, we get two subranges in the scalar energy scale delineated by l_{OC}: the inertial-convective subrange with a $k^{-5/3}$ slope where the additive follows the inertial subrange turbulence of the fluid, and the inertial-diffusive subrange where the scalar fluctuations are damped out by diffusion even though the fluid is maintaining turbulent eddies. For $Sc >> 1$ two subranges appear to be divided by l_B in addition to the inertial-convective subrange: the viscous-convective subrange with a k^{-1} dependence where the scalar fluctuations are not yet affected by diffusion but the fluid fluctuations have been dissipated by viscosity, and the viscous-diffusive subrange where the additive inhomogenieties are finally smeared out by diffusion. Figure A.4 illustrates the various wave number subranges described above. From a dimensional point of view, the scalar spectrum can be expressed as

$$E_\xi(k) = C_\xi \chi_\xi \varepsilon^{-1/3} k^{-5/3} f(kl_K, Sc), \tag{A.10}$$

where $f(kl_K, Sc)$ is a non-dimensional function that describes the spectral behavior at high wave numbers.

In summary, the energy and temperature spectra exhibit many similarities. Energy (temperature variance) is input at large scales, cascade down the spectrum by inertial (convective) processes, and finally dissipated by molecular viscosity (diffusion). The main difference between the two spectra occurs at high wave numbers for the scalar spectrum.

A.4 Structure Function

The second order structure function (D_ξ^2) is defined as

$$D_\xi^2(\boldsymbol{r}_1, \boldsymbol{r}_2) = \langle [\xi(\boldsymbol{r}_1) - \xi(\boldsymbol{r}_2)]^2 \rangle, \tag{A.11}$$

where ξ is an atmospheric scalar parameter such as temperature or index of refraction, $\boldsymbol{r}_1$ and $\boldsymbol{r}_2$ are position vectors of two points in space, and $\langle\rangle$ implies an ensemble average. The radar and optics community applies heavily the structure function to gauge atmospheric turbulent intensity [e.g., *Walters*, 1998; *Hocking*, 1999, and references therein]. In this application, inertial subrange turbulence is subtly assumed. However, its relationship to the more well known –5/3 power law is not obvious. Most users accept by faith that (A.11) parameterizes the inertial subrange turbulence. We want to take the time to revisit the derivation that relates the second order structure function to the –5/3 power law.

We organize the discussion as follows. We first discuss the origins of the necessity of the structure function in the measurement of atmospheric turbulence. We then, via some mathematic derivations, relate the structure function to the -5/3 power law. The discussion will be heavily inundated with mathematics. However, we do hope that, via this discourse, the reader will gain a familiarity with the structure function.

A.4.1 Why Structure Functions?

It should be noted that D_ξ^2 is a very rough approximation of actual meteorological fields as homogeneous and isotropic random fields. Atmospheric turbulence always contains larger scale components which usually destroy the homogeneity and isotropy of the fields. Moreover, these components cause the meteorological fields to be non-stationary. Thus, there is a close relation between the non-stationary, inhomogeneities, and anisotropy of the meteorological field of an atmospheric variable; basically they are due to the same causes. Therefore, in analyzing the spatial structure of meteorological fields (and some others) it is appropriate to apply the method of the structure function.

A.4.2 Definition

The difference between the value of the field $\xi(\boldsymbol{r})$ at two points $\boldsymbol{r}_1$ and $\boldsymbol{r}_2$ is chiefly affected only by inhomogenieties of the field $\xi(\boldsymbol{r})$ with dimensions which do not exceed the distance $|\boldsymbol{r}_2 - \boldsymbol{r}_1|$. If the distance is not too large, the largest inhomogenieties have no effect on $\xi(\boldsymbol{r}_1) - \xi(\boldsymbol{r}_2)$ and therefore the structure function,

$$D_\xi^2(\boldsymbol{r}_1, \boldsymbol{r}_2) = \langle[\xi(\boldsymbol{r}_1) - \xi(\boldsymbol{r}_2)]^2\rangle, \tag{A.12}$$

can only depend on $|\boldsymbol{r}_2 - \boldsymbol{r}_1|$. It defines the basic characteristic of a random process with stationary increments. Roughly speaking, $D_\xi^2(\boldsymbol{r}_1, \boldsymbol{r}_2)$ characterizes the intensity of $\xi(\boldsymbol{r})$ with periods which are smaller than or comparable with $|\boldsymbol{r}_2 - \boldsymbol{r}_1|$.

The random field $\xi(\boldsymbol{r})$ is called locally homogeneous in the region G if the distribution functions of the random variable $\xi(\boldsymbol{r}_2) - \xi(\boldsymbol{r}_1)$ are invariant with respect to shifts of the pair of points $(\boldsymbol{r}_1, \boldsymbol{r}_2)$, as long as these points are located in G. The mean value of $\langle\xi(\mathbf{r}_2) - \xi(\boldsymbol{r}_1)\rangle$ and the structure function of a locally homogeneous random field depend only on $|\boldsymbol{r}_2 - \boldsymbol{r}_1|$,

$$D_\xi^2(\boldsymbol{r}_2 - \boldsymbol{r}_1) = \langle[\xi(\boldsymbol{r}_1) - \xi(\boldsymbol{r}_2)]^2\rangle. \tag{A.13}$$

A locally homogeneous random field is called locally isotropic in the region G if the distribution function of the quantity are invariant with respect to rotation and mirror reflections of the vector $\boldsymbol{r}_2 - \boldsymbol{r}_1$, as long as the points ($\boldsymbol{r}_1$, $\boldsymbol{r}_2$) are located in G [*Tatarski*, 1961]. The structure function of a locally isotropic random field depends only on $r = |\boldsymbol{r}_2 - \boldsymbol{r}_1|$.

$$D_\xi^2(r_2 - r_1) = \langle[\xi(r_1) - \xi(r_2)]^2\rangle = D_\xi^2(r). \tag{A.14}$$

A.4.3 Structure Function and Spectral Density

To relate the structure function to the variance spectrum $E_\xi(k)$, we need to present a relationship between the structure function and a 3D spectrum. Consider locally homogeneous random field $f(\boldsymbol{r})$ with stationary increments can be presented as [*Tatarski*, 1961],

$$f(\boldsymbol{r}) = f(0) + \int_{-\infty}^{\infty}\int\int \left(1 - \exp\left(j\boldsymbol{k}\cdot\boldsymbol{r}\right)\right) d\varphi\left(\boldsymbol{k}\right). \tag{A.15}$$

Here, $f(0)$ is a random variable, and the random amplitude $d\varphi(\boldsymbol{k})$ obeys the condition

$$\overline{d\varphi(\boldsymbol{k}_1)\, d\varphi^*(\boldsymbol{k}_2)} = \delta(\boldsymbol{k}_1 - \boldsymbol{k}_2)\Phi(\boldsymbol{k}_1)\, d\boldsymbol{k}_1 d\boldsymbol{k}_2, \tag{A.16}$$

where $\Phi(\boldsymbol{k}) \geq 0$ is the spectral density of the random field $f(\boldsymbol{r})$ and * denotes complex conjugation. Substituting the expansion (A.15) in (A.13) and using the relation (A.16), *Tatarski* [1961] shows that

$$\begin{aligned} D_\xi^2(\boldsymbol{r}_2 - \boldsymbol{r}_1) &= \langle[\xi(\boldsymbol{r}_1) - \xi(\boldsymbol{r}_2)]^2\rangle = \langle[\xi(\boldsymbol{r}_1) - \xi(\boldsymbol{r}_2)]\,[\xi^*(\boldsymbol{r}_1) - \xi^*(\boldsymbol{r}_2)]\rangle \\ &= 2\int_{-\infty}^{\infty}\int\int \left(1 - \cos\left(\boldsymbol{k}\cdot\boldsymbol{r}\right)\right)\Phi_\xi\left(\boldsymbol{k}\right) d\boldsymbol{k}\,. \end{aligned} \tag{A.17}$$

In the case where the field $\xi(\boldsymbol{r})$ is locally isotropic, and $D_\xi^2(\boldsymbol{r}_2 - \boldsymbol{r}_1) = D_\xi^2(r)$ and $\Phi(\boldsymbol{k}) = \Phi(k)$. In this case

$$D_\xi^2(\boldsymbol{r}_2 - \boldsymbol{r}_1) = 8\pi\int_0^{\infty}\left(1 - \frac{\sin(kr)}{kr}\right)\Phi_\xi\left(k\right)k^2\, dk\,. \tag{A.18}$$

We want to focus our attention on $\Phi_\xi(k)$. Since the structure function is related to the spectral density $\Phi_\xi(k)$ of a locally isotropic random field, and if we can relate $\Phi_\xi(k)$ to the variance spectrum $E_\xi(k)$, then we have successfully connected the structure function with the Fourier formalism of Kolmogorov's turbulence theory. To solve for $\Phi_\xi(k)$, we simplify the situation in (A.18) and consider a locally isotropic field along any line in space. *Tatarski* [1961] invokes the correlation function for an isotropic field and shows that given a locally isotropic field along any line in space, the structure function $D_\xi^2(\boldsymbol{r})$ can be expanded as

$$D_\xi^2(r) = 2\int_{-\infty}^{\infty}(1-\cos(k\cdot r))V(k)dk\,, \tag{A.19}$$

where

$$\Phi_\xi(k) = -\frac{1}{2\pi k}\frac{dV(k)}{dk}. \tag{A.20}$$

At this point, a small digression is needed before we arrive at an expression for $\Phi_\xi(k)$. Via dimensional analysis, the structure function in (A.14) can be re-expressed as

$$D_\xi^2(r) = C_\xi^2 r^p,\ (0 < p < 2), \tag{A.21}$$

where C_ξ^2 is the structure function coefficient and $r = |\boldsymbol{r}_2 - \boldsymbol{r}_1|$. This is only valid in the inertial subrange, where $l_K < r < l_{LS}$. A detailed derivation of this can be found in *Hall* [1991]. Our goal is to compute $V(k)$ and in turn get $\Phi_\xi(k)$. Consider the spectral density

$$V(k) = A|k|^{-(p+1)}, \tag{A.22}$$

where $A > 0$ and $0 < p < 2$. Substituting (A.22) into (A.19) and carrying out the integration, we obtain

$$D_\xi^2(r) = \frac{2\pi A}{\Gamma(p+1)\sin\left(\frac{\pi p}{2}\right)}k^{-p}. \tag{A.23}$$

Via the duality principle, it is easy to see that the structure function (A.21) corresponds to the one dimensional spectral density function

$$\mathrm{V}(k) = \frac{\Gamma(p+1)}{2\pi}\sin\left(\frac{\pi p}{2}\right)C_\xi^2 k^{-(p+1)}. \tag{A.24}$$

We use the relation (A.20) to find the three-dimensional spectral density $\Phi_\xi(k)$

$$\Phi_\xi(k) = -\frac{1}{2\pi k}\frac{dV(k)}{dk} = \frac{\Gamma(p+2)}{4\pi^2}\sin\left(\frac{\pi p}{2}\right)C_\xi^2 k^{-(p+3)}. \tag{A.25}$$

For $p = 2/3$, we have

$$\Phi_\xi(k) = \frac{\Gamma\left(\frac{8}{3}\right)\sin\left(\frac{\pi}{3}\right)}{4\pi^2}C_\xi^2 k^{-11/3} = 0.033 C_\xi^2 k^{-11/3}. \tag{A.26}$$

$\Phi_\xi(k)$ then represents the *density* of the fluctuations in ξ at wave number k for the inertial range.

Let us tie this result back to $E_\xi(k)$. A three dimensional spectrum $E_\xi(k)$, depending only on the scalar wave number $k = |\boldsymbol{k}|$, is obtained by integrating $\Phi_\xi(k)$ on a spherical shell of radius k. The result is

$$E_\xi(k) = \frac{1}{2}\oint \Phi_\xi(\boldsymbol{k})k^2 d\Omega, \tag{A.27}$$

where $d\Omega$ is an element of solid angle. $E_\xi(k)$ is then the spectrum of the variance of ξ, since

$$\int_{-\infty}^{\infty} E_\xi(k)dk = \frac{1}{2}\left\langle \xi^2 \right\rangle. \tag{A.28}$$

In the isotropic case, Φ_ξ depends only on k, and hence

$$\begin{aligned} E_\xi(k) &= 2\pi k^2 \Phi_\xi(k) \\ &= 0.209 C_\xi^2 k^{-5/3}. \end{aligned} \tag{A.29}$$

A.5 Turbulence Spectrum and Radar Backscatter

As we have presented at several places in this thesis, turbulent fluctuations cause refractive index variations that produce scattering that can be observed via high-power

radar systems. Scattering typically derives from structures with scale size equal to one-half of the transmitted wavelength; this is the Bragg wavelength. It is necessary to have turbulent structure of this dimension in order to obtain an echo [*Crane*, 1980]. In an effort to understand clear-air turbulence (CAT) echoes, it is important to understand the theory of turbulence and its effect on radar backscatter. *Tatarski* [1961] has studied the effect of atmospheric refractive index fluctuations on amplitude scintillations of electromagnetic waves theoretically. He assumed a medium which is locally homogeneous and isotropic, consisting of relatively small-scale blobs of different refractive index varying between scale sizes l_o (inner scale of turbulence) and L_o (outer scale of turbulence). The intensity of the refractive index fluctuations in the scale range l_o and L_o is expressed by the refractive index structure function which has been shown experimentally, under certain circumstances, to follow a two-third law [e.g., *Wyngaard et al.*, 1971; *Hocking*, 1985]. The amplitude of radio scintillations has been shown by *Tatarski* [1961] to be proportional to the magnitude of the refractive index structure parameter C_n^2, a measure of refractive index fluctuations induced by the turbulence. It characterizes the small-scale variability of the temperature and humidity in the inertial subrange of turbulence, where the turbulence is considered isotropic and homogeneous [*Panofsky*, 1968; *Balsley et al.*, 1980; *Gage et al.*, 1980; *Coulman et al*., 1995].

High-resolution measurements (<10 m) of atmospheric structures are achieved by *in situ* probes carried aloft by such vehicles as balloons, aircrafts, blimps, powered parachutes, and kites. As we have shown in the thesis, one way to understand the mechanism(s) that cause the clear-air radar backscatter is to compare the measured radar backscatter with the prediction computed from an *in situ* atmospheric measurement. In Chapter 5, we use the *in situ* measured C_n^2, the refractive index structure function parameter to compute the volume reflectivity defined as,

$$\eta(\lambda) \approx 0.38 C_n^2 \lambda^{-1/3} \quad [\mathrm{m}^2/\mathrm{m}^3] \tag{5.2}$$

where λ is the wavelength of interest. In this discussion, we want to show how one derives (5.2) from turbulence theory by examining the relationship between $\eta(\lambda)$ and the Fourier spectrum of the refractive index field, and how, with the assumption of isotropy, $\eta(\lambda)$ can be related to C_n^2, a parameter that can be directly measured in the atmosphere via a turbulence sensor. Furthermore, we want to examine the difference between the atmospheric measurements with an *in situ* probe and by radar backscattering.

Consider the Fourier transform of a three dimensional atmospheric field, e.g., refractive index. How a radar and an *in situ* measures this three-dimensional field is different. While an *in situ* instrument will be able to measure the Fourier modes in the direction that the sensor is moving, it will also receive contributions from Fourier modes in all direction. On the other hand, the radar would only receive contributions of the Fourier modes at the Bragg scale ($\lambda/2$) in the radar pointing direction. We examine this difference, particularly in the context of radar scattering and the derivation of (5.2).

It should be pointed out that turbulent motion alone is not suffice to degrade radio wave propagation; to produce refractive index fluctuations, turbulence in the presence of a temperature gradient (and a humidity gradient at radio frequencies) is necessary. In addition to turbulent scatter, enhanced VHF echoes that arise from stable, horizontally stratified atmospheric structure when the radar beam is directed vertically offer a means of studying atmospheric stability. This mechanism requires a spatial coherence of refractive index structure *transverse* to the radar wave vector. As seen in our discussion of aspect sensitivity in this thesis, the problem of VHF echoes is a complex one [*Coulman et al.*, 1995; *Dalaudier et al.*, 1994].

Much of the work discussed in this paper is based on the Kolmogorov theory of inertial range isotropic turbulence, [e.g., *Batchelor*, 1959; *Tatarski*, 1961, 1971]. Some improved theories have recently been developed [e.g., *Hill and Clifford*, 1978;

Weinstock, 1978; *Sykes and Lewellen*, 1982; *Hocking*, 1985, 1999], but it is not always necessary to use such sophisticated models to study turbulent processes in the middle atmosphere. Radars in the frequency band of 2-100 MHz generally use pulse resolutions of between 100 m and several kilometers. Therefore, in most cases, these radars cannot be used to obtain new information about the detailed structure of turbulence. Rather, these radars are able to examine gross features of turbulence in an altitude region which is inaccessible to other, higher resolution techniques, and this is their strength. These radars are generally only used to examine gross features such as the temporal and spatial variability of turbulence, and mean turbulent energy dissipation rates [*Hocking*, 1985].

We organize our discussion as follows. We first develop the relationship between the one-dimensional and the three-dimensional Fourier spectrum of the refractive index. In our derivations, a conscious effort is made to relate the Fourier spectrum of the refractive index to $\eta(\lambda)$, the volume reflectivity of the radar as we are interested in the radar backscatter caused by changes in refractive index. By invoking the assumption of isotropic turbulence, we show how $\eta(\lambda)$ can be related to C_n^2 via the one-dimensional Fourier spectrum of the refractive index.

A.5.1 Turbulence Theory

Tatarski [1961, 1967] first considered the relationship between radar observations of the intensity of the refractive index fluctuations produced by clear air turbulence and the structure and intensity of the turbulence. He developed a relationship between the scattering cross-section per unit volume observed by a radar (expressed as C_n^2) and the power spectral density of the refractive index fluctuations in the inertial-convective subrange of turbulence, where the turbulence is homogeneous and isotropic, at a scale size equal to half the radar wavelength. He further extended the relationship to include the mean gradients of the temperature, humidity, and wind and a parameter of

the turbulence, the outer scale for inertial subrange. *Ottersten* [1969b] went further to postulate that the scattering cross section per unit volume within an isotropic turbulence depends primarily on the eddy dissipation rate or the intensity of turbulence and only secondarily on the mean gradients in the stably stratified region at or above the tropopause where the effect of the humidity fluctuations is negligible. *Van Zandt et al.* [1978] proposed a model for the estimation of C_n^2 which included the effect of the layer structure of turbulence with layers thinner than the vertical dimension of the radar resolution volume but assumed that the outer scale parameter was constant. *Crane* [1977] developed a model which includes the effect of the layer structure and the expectation that the eddy dissipation rate and the outer scale are parameters of the turbulence which are not fixed.

We will begin our discussion with the elementary relationship between the turbulence affected refractive index and radar backscatter. According to *Ottersten* [1969a], the general expression connecting random refractive-index variations to the radar reflectivity, η, or radar cross section per unit scattering volume, is

$$\eta(\boldsymbol{k}) = (\pi^2/2)k^4\phi_n(\boldsymbol{k}). \tag{A.30}$$

The direction of the radian vector wave number $\boldsymbol{k}$ is the radar radial direction; the absolute value $k = |\boldsymbol{k}|$ is related to the radar wavelength λ_R through $k = 4\pi\lambda_R^{-1}$. The space spectrum $\phi_n(\boldsymbol{k})$, or spatial power-spectral density, is a three-dimensional representation of the refractive index field and is obtained by a Fourier transform of the three-dimensional refractive index covariance function. The normalization used is

$$\left\langle n'^2 \right\rangle = \int_{-\infty}^{\infty} \phi_n(\boldsymbol{k}) d\boldsymbol{k} \,. \tag{A.31}$$

where n' denotes the deviation from the spatial mean value of the refractive index and the angle brackets denote spatial average; the integration is carried out over the entire wave-number space.

A.5.2 Refractive Index Power Spectrum

In the derivation of (A.30), multiple scattering is neglected, and the linear dimension of the scattering volume is assumed to be large compared with the radar wavelength but small compared with the first Fresnel zone. It is further assumed that the refractive-index field is weakly stationary and locally homogeneous within the scattering volume.

$\phi_n(\boldsymbol{k})$ resolves the refractive index field into an infinite number of Fourier modes directed along all direction in space and forming a continuum of different wave numbers. Only one of these Fourier modes contributes to the radar backscattering. The radar samples the space spectrum at the particular mode whose direction coincides with the radar radial direction and whose wave number corresponds to the space scale $L = 2\pi k^{-1} = 0.5\lambda_R$, which is the Bragg condition for reflection from periodic structures.

The continuum of Fourier modes $\phi_n(k\boldsymbol{i})$ along a given direction specified by the unit vector $\boldsymbol{i}$ is not equivalent to the one-dimensional spectrum $S_n^{\,1}(k)$ that a discrete sensor, e.g., the temperature probe carried by a balloon, would measure when moving along the direction $\boldsymbol{i}$. The sensor will be sensing not only the Fourier modes that are confined to the direction of the sensor motion but will receive contributions from Fourier modes in all directions. Thus, there is a basic difference between the measurement of refractive index variation with a sensor and by radar backscattering, which, in general, prevents the comparison of sensor measurements along one direction with radar data obtained in the same direction.

There exists considerable confusion about the various conventions for spectral representations of homogeneous random fields that have resulted in misinterpretations of the relationships between the refractive index spectrum measured by radar and *in situ* measurement [*Ottersten*, 1969a; *Gage and Balsley*, 1980; *Hocking*, 1985; *Hooper and Thomas*, 1998; *Hocking*, 1999]. One reason for this is the convention of

introducing a so-called three-dimensional spectrum of the refractive index, $E_n(k)$, that is a function of the scalar wave number k. The $E_n(k)$ is the integral of $\phi_n(\boldsymbol{k})$ over spherical shells of radii k:

$$E_n(k) = k^2 \int_{4\pi} \phi_n(\boldsymbol{k}) d\Omega(\boldsymbol{k}). \tag{A.32}$$

The integral extends over all directions of $\boldsymbol{k}$. $E_n(k)$ contains contributions from all Fourier modes of wave number k regardless of the direction of the wave number $\boldsymbol{k}$. In particular, if the field is isotropic, $\phi_n(k)$ depends only on k and $E_n(k) = 4\pi k^2 \phi_n(\boldsymbol{k})$, which, together with (A.30), gives

$$\eta(k) = (\pi/8) k^2 E_n(k). \tag{A.33}$$

This formulation is valid for locally isotropic fields. It is important to distinguish the three-dimensional scalar spectrum $E_n(k)$ and the one-dimensional $S_n^{\alpha}(k)$ that a discrete sensor would measure when moving through air along a direction α.

A.5.3 One-Dimensional Spectrum

The one-dimensional spectrum $F_n^x(k_x)$, which describes the refractive index field along the x-axis in a coordinate system x, y, z in real space, is obtained by integration of the space spectrum $\phi_n(k)$ along the k_x and k_y axis in the coordinate system k_x, k_y, k_z, in wave number space:

$$F_n^x(k_x) = \int\int_{-\infty}^{\infty} \phi_n(\boldsymbol{k}) dk_y dk_z \,. \tag{A.34}$$

The normalization convention here is $< n'^2 > = \int_{-\infty}^{+\infty} F_n^x(k_x) dk_x = \int_0^{+\infty} S_n^x(k_x) dk_x$, where $S_n^x(k_x) = 2F_n^x(k_x)$ is the measurable one-dimensional spectrum of refractive index fluctuations along the x-axis, and $S_n^x(k_x)$ is non-zero only for positive k_x values. Similarly, one-dimensional spectrum $F_n^{\alpha}(k_{\alpha})$ describes the field in an arbitrary direction α. In general, the various $F_n^{\alpha}(k_{\alpha})$ are different. By defining, $F_n^{\alpha}(k_{\alpha})$ over the whole real axis α, we let the various k_{α} attain positive as well as negative values, as opposed to the wave numbers in the three dimensional spectrum.

For a given direction α, the value of the one-dimensional real spectrum $S_n^{\alpha}(k_\alpha)$, $k_\alpha > 0$, at a given value of k_α, contains contributions not only from the particular Fourier mode in the direction α and of wave number k_α but includes, in addition, contributions from an infinite number of Fourier modes directed along all directions in space. Each of these Fourier modes has a wave number that is larger than k_α and that is uniquely determined by the direction of the Fourier mode such that this wave number, when projected onto the direction α, will appear to be of wave number k_α. Of the Fourier modes directed perpendicular to the direction α, only those of infinite wave number contributes to $S_n^{\alpha}(k_\alpha)$. *Bolgiano* [1963] described this accumulation of Fourier modes into one-dimensional spectrum as an aliasing of all smaller components (higher wave numbers) in other directions to a single component in the direction of observation of the one-dimensional spectrum. This ambiguity in the very nature of one-dimensional spectrum prohibits the identification of a particular wave number k_α in the one-dimensional spectrum with physical eddy sizes equal to $2\pi|k_\alpha|^{-1}$ [*Ottersten*, 1969b] This is the reason why reflection coefficient calculated from one-dimensional spectrum $S_n^{\alpha}(k_\alpha)$, $k_\alpha > 0$, along the direction α, cannot readily be interpreted in terms of radar backscattering along the direction α, which, as pointed out earlier, singles out the particular Fourier mode that is directed along the direction α and whose wave number fits the relation $k = 4\pi\lambda_R^{-1}$.

A.5.4 Isotropic Field

For an isotropic field, the situation is simplified because $\phi(\mathbf{k}) = \phi(k)$ and all one-dimensional spectrum $F^{\alpha}(k_\alpha)$ in various directions are identical; the general relations (A.34) reduce to (A.35) or the differential form (A.36)

$$F_n^{\alpha}(k_\alpha) = \int_{|k_\alpha|}^{\infty} 2\pi k \phi_n(k) dk \,, \qquad \text{(A.35)}$$

$$\frac{dF_n^{\alpha}(k_{\alpha})}{dk_{\alpha}} = -2\pi k_{\alpha}\phi_n(|k_{\alpha}|) \tag{A.36}$$

Further, $E_n(k) = 4\pi k^2 \phi_n(k)$ which, substituted in (A.37) and (A.38), respectively, gives relationships between the one-dimensional and the three dimensional spectrum for the isotropic case:

$$F_n^{\alpha}(k_{\alpha}) = \int_{|k_{\alpha}|}^{\infty} (2k)^{-1} E_n(k) dk \tag{A.37}$$

$$\frac{dF_n^{\alpha}(k_{\alpha})}{dk_{\alpha}} = -(2k_{\alpha})^{-1} E_n(|k_{\alpha}|) \tag{A.38}$$

Equations (A.35) through (A.38) all testify to the fact that isotropy implies that the one-dimensional spectral density $F_n{}^{\alpha}(k_{\alpha})$ always decreases with increasing wave number $|k_{\alpha}|$. Therefore, directly measured (one-dimensional) spectrum $S_n{}^{\alpha}(k_{\alpha})$, $k_{\alpha} > 0$, that displays positive slopes or humps provide direct evidence of a non-isotropic field.

With $S_n{}^{\alpha}(k) = 2F_n{}^{\alpha}(k)$ representing the measurable one-dimensional spectrum of refractive index fluctuations, we may use (A.36) in (A.30) or (A.38) in (A.33) to obtain

$$\eta(k) = -(\pi/8)k^3[\mathrm{d}S_n{}^{\alpha}(k)/\mathrm{d}k]. \tag{A.39}$$

Superscript α not only denotes a one-dimensional spectrum but also represents any direction because no direction is unique in an isotropic field; k attains positive values only. Equation (A.39) is the proper expression to use for the comparison of the radar reflectivity of refractive index fluctuations with direct measurements of one-dimensional refractive index spectrum, provided that the refractive index field is known to be isotropic for $k = 4\pi\lambda_R^{-1}$, the wave number determining the backscattering. As observed earlier, (A.39) is always non-negative because of the isotropy. In general, for anisotropic turbulent, the radar backscattering cannot be readily

interpreted in terms of one-dimensional refractive index spectrum and the general expression (A.30) must be used and information about the anisotropy is necessary before one-dimensional and three-dimensional spectrum can be related with connections of type (A.35).

We confine the remaining discussion to isotropic fields. A useful approach is to approximate the one-dimensional refractive index spectrum with a power law, $S_n^{\alpha}(k) \approx k^{-p}$, $p>0$ as required by isotropy, implying

$$[\mathrm{d}S_n^{\alpha}(k)/\mathrm{d}k] = -pk^{-1}S_n^{\alpha}(k) \tag{A.40}$$

$$E_n(k) = pS_n^{\alpha}(k) \tag{A.41}$$

and

$$\phi_n(k) = (p/4\pi)k^{-2}S_n^{\alpha}(k). \tag{A.42}$$

We thus have with (A.40) in (A.39)

$$\eta(k) = p(\pi/8)k^2S_n^{\alpha}(k), \tag{A.43}$$

which also may be obtained with (A.41) in (A.34) or (A.42) in (A.30). Equation (A.34) is a useful expression for the comparison of radar reflectivity to direct measurements of one-dimensional refractive index spectrum. We observe the similarity between (A.34) and (A.33), the only difference between the spectra being the factor of p, as seen in (A.40); p determines the slope of the one-dimensional spectrum $S_n^{\alpha}(k)$, which follows the same power law as the so-called three-dimensional spectrum $E_n(k)$.

A.5.5 Inertial Subrange

When an inertial subrange is present, the particular spectral power law within this range for the field of any conservative, passive quantity distributed by the turbulence is the –5/3 law, and we have E_n and $S_n^{\alpha} \approx k^{-5/3}$, whereas $\phi(\mathrm{k}) \approx k^{-11/3}$ [*Tatarski*, 1961]. For radars with wavelengths from meters to centimeters, the spatial scale $L = 2\pi k^{-1} = 0.5\lambda_R$ determining the backscattering will generally fall within the inertial subrange,

particularly if the radar returns originate from regions of violent mixing and intense turbulence. With (A.43) we finally arrive at

$$\eta(k) = (5/3)(\pi/8)k^2 S_n^{\alpha}(k), \tag{A.44}$$

an expression that is recommended for the comparison of radar reflectivity with instrument measurements.

The structure function is defined as the mean square difference of the values of a variable at the distance r apart [*Panofsky*, 1968; *Walters*, 1995]. More specifically, the structure function D_X is of the form

$$D_X(\boldsymbol{r}_1, \boldsymbol{r}_2) = \langle [X(\boldsymbol{r}_1) - X(\boldsymbol{r}_2)]^2 \rangle, \tag{A.45}$$

where X is an atmospheric scalar parameter such as the temperature or index of refraction, $\boldsymbol{r}_1$ and $\boldsymbol{r}_2$ are position vectors of two points in space, and $\langle\rangle$ implies an ensemble average, arise in the theory of wave propagation through random media, e.g., turbulence.

Although the (A.45) is a tensor, it is frequently possible to assume local isotropy and homogeneity so that D is a function of the scalar difference between $\boldsymbol{r}_1$ and $\boldsymbol{r}_2$

$$D_X(\boldsymbol{r}_1, \boldsymbol{r}_2) = D_X(|\boldsymbol{r}_2 - \boldsymbol{r}_1|). \tag{A.46}$$

The structure function may follow a power law allowing one to write

$$D_X(|\boldsymbol{r}_2 - \boldsymbol{r}_1|) = C_X^2 \, r^m, \tag{A.47}$$

where

$$|\boldsymbol{r}_2 - \boldsymbol{r}_1| = r \tag{A.48}$$

and $0 < m \leq 2$. The structure parameter C_X^2 is proportionality constant. Over sufficiently small regions, of the order of millimeters to meters in size, which the turbulence is locally homogeneous and isotropic, the atmosphere can have a Kolmogorov structure function dependence with $m = 2/3$. Within these constraints, a passive additive such as the atmospheric index of refraction, the structure parameter becomes

$$C_n^2 = \frac{\left\langle [n(\boldsymbol{r}_2) - n(\boldsymbol{r}_1)]^2 \right\rangle}{r^{2/3}} \tag{A.49}$$

The structure function and the one-dimensional spectrum are equivalent representations and contain the same information about the turbulent field in the inertial subrange, with the spectral –5/3 power law corresponding to the 2/3 law in the structure function. When k is the radian wave number corresponding to the spatial scale $2\pi k^{-1}$, we have [*Ottersten*, 1968]:

$$S_n^{\alpha}(k) \approx \frac{1}{4} C_n^2 k^{-5/3} \tag{A.50}$$

which, with (A.44), gives

$$\eta(\lambda) \approx 0.38 C_n^2 \lambda^{-1/3} \tag{A.51}$$

where the structure constant C_n^2 represents a measure of the variability of the refractive index field within the inertial subrange. Equation (5.2) is hence proven. Most works give the constant 0.39 in (A.51), although 0.38 is the more accurate value [*Ottersten*, 1969a, b]. The relations (A.51) and (A.44) are tied in several works where the factor 5/3 in (A.44) is missing. *Smith and Rogers* [1963] derived equation (A.51) directly from the basic relation (A.30) and the space spectrum $\phi_n(k)$ given by the expression

$$\phi_n(k) \approx 0.033 C_n^2 k^{-11/3} \tag{A.52}$$

which is applicable for isotropic turbulence in the inertial subrange [*Tatarski*, 1961] Equation (A.52) corresponds to (A.47) with m = 2/3 and may be obtained with (A.50) in (A.42) and p = 5/3.

The refractivity structure constant C_n^2 is related to the mean square fluctuations of radio index of refraction $\overline{(\Delta n)^2}$ by

$$C_n^2 = 5.45 \, \overline{(\Delta n)^2} \, L_o^{-2/3} \tag{A.53}$$

where L_o is the outer scale of turbulence [e.g., *Balsley and Gage*, 1980]. By substitution of equation (A.53) into (A.51) we find

$$\eta(\lambda) = 2.07\ \overline{(\Delta n)^2}\ L_o^{-2/3}\lambda^{-1/3}. \qquad \text{(A.54)}$$

The gross structure of turbulence in the free atmosphere is intermittent in time and inhomogeneous in space with active turbulence confined to thin horizontal layers. Within the turbulent layers the small-scale structure of turbulence approaches a locally homogeneous and isotropic condition and approximately conforms to inertial range turbulence theory. In view of the inhomogeniety of the gross structure it is useful to distinguish between local and volume measures of turbulence. For example, the radar measure a volume average $\overline{C_n^{\,2}}$ which is related to the local $(C_n^2)_{turb}$ by

$$\overline{C_n^{\,2}} = F\,(C_n^2)_{turb}, \qquad \text{(A.55)}$$

where F is the fraction of the observed volume which is turbulent [*Van Zandt et al.*, 1978, *Balsley and Gage*, 1980].

A.5.6 Conclusion

In this section, we discussed how isotropic turbulence affect radar backscatter and how the parameter C_n^2 is used as a measurement of turbulence intensity. We presented the arguments that one would follow to show how C_n^2 is related to η, the volume reflectivity.

Appendix B

Antenna Near Field

When examining the electric and magnetic fields generated by an antenna, one generally assumes that the distance between the observer and the antenna is large. This so called "far-field" approximation allows one to approximate the propagating electric and magnetic fields as plane waves. This approximation fails when one is close to the antenna, as it is the case for the scattering regions observed by the vertical beam of the Jicamarca Radio Observatory (JRO). In this section, we will first examine the far-field and the near-field regions of the antenna and then apply the results to the vertical beam generated by the Jicamarca VHF radar.

B.1 Antenna Near Field

As noted in the lectures on electro-magnetic wave propagation and the radar equation, electromagnetic radiation expands spherically and the power density at a long range (R) from the transmitting antenna. In other words

$$P_E = \frac{P_t G_t}{4\pi R^2}, \tag{B.1}$$

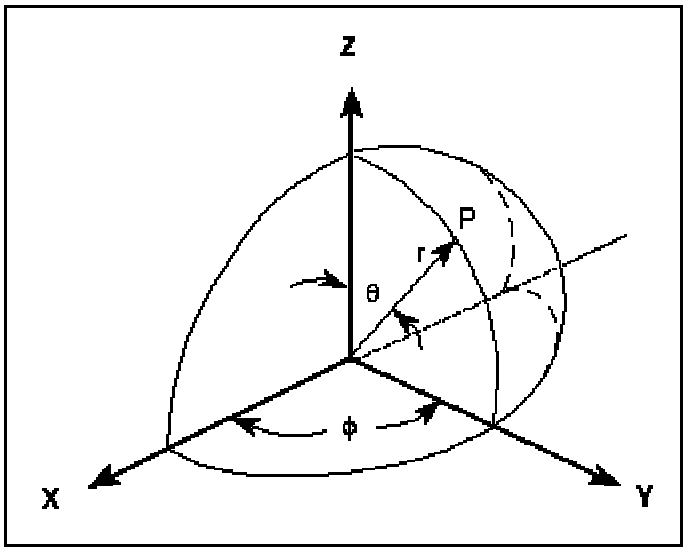

Figure B.1: Spherical radiation to point "P" from an idea point source.

where P_E is the power from the expanding radiation, P_T is the transmitted power, and G_T is gain of the transmitting antenna. When the range is large, the spherical surface of uniform power density appears flat to a receiving antenna which is very small compared to the surface of the sphere. This is why the far field wave front is considered planar and the rays approximately parallel. Also, it is apparent that at some shorter range, the spherical surface no longer appears flat, even to a very small receiving antenna.

The distance where the planer, parallel ray approximation breaks down is known as the near field. The crossover distance between near and far fields (R_{ff}) is taken to be where the phase error is $1/16^{th}$ of a wavelength, or about 22.5°. R_{ff} is defined to be

$$R_{ff} = \frac{2D^2}{\lambda}, \tag{B.2}$$

where λ is the wavelength and D is the largest dimension of the transmitting antenna.

If the same size antenna is used for multiple frequencies, R_{ff} will increase with increasing frequency. However, if various size antennas are used for different frequencies and each antenna is designed with D as a function of λ ($\lambda/2$ to 100λ), then

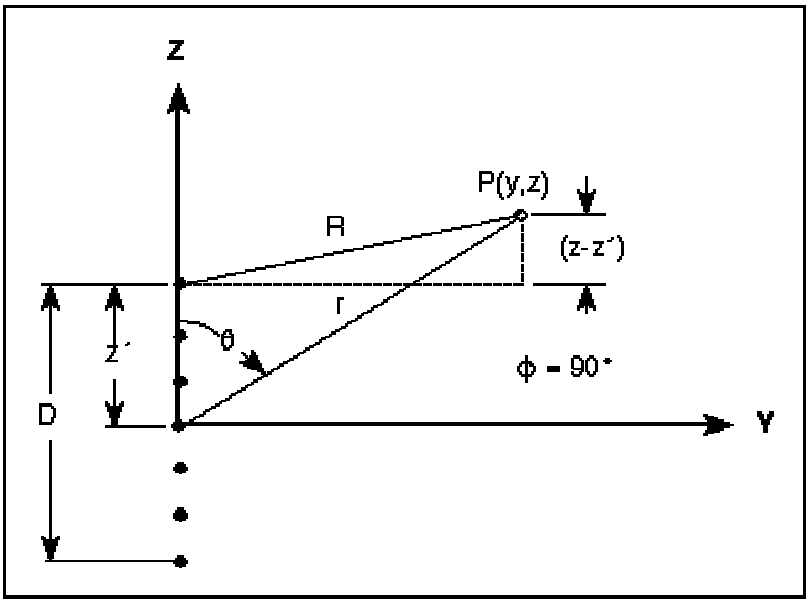

Figure B.2: Near field geometry of point "P" for a non-ideal radiator with dimension *D*.

R_{ff} will vary from *c/2f* to *20000c/f*. In this case, R_{ff} will decrease with increasing frequency. For example: a 10λ antenna at 3 GHz has a *D* of 100 cm and corresponding R_{ff} of 20 m, while a 10λ antenna at 30 GHz has a *D* of 10 cm and corresponding R_{ff} of 2 m.

While the above analogy provides an image of the difference between the near and far fields, the relationship must be defined as a characteristic of the transmitting antenna. Actual antennas, of course, are not ideal point source radiators but have physical dimensions. If the transmitting antenna placed at the origin of Figure B.1 occupies distance *D* along the Z-axis and is boresighted along the Y-axis (ϕ = 90), then the geometry of point *P* on the sphere is represented in two dimensions by Figure B.2. For convenience, the antenna is represented by a series of point sources in an array.

When point *P* is close to the antenna, as in Figure B.2, then the difference in distance of the two rays *r* and *R* taken respectively from the center of the antenna and

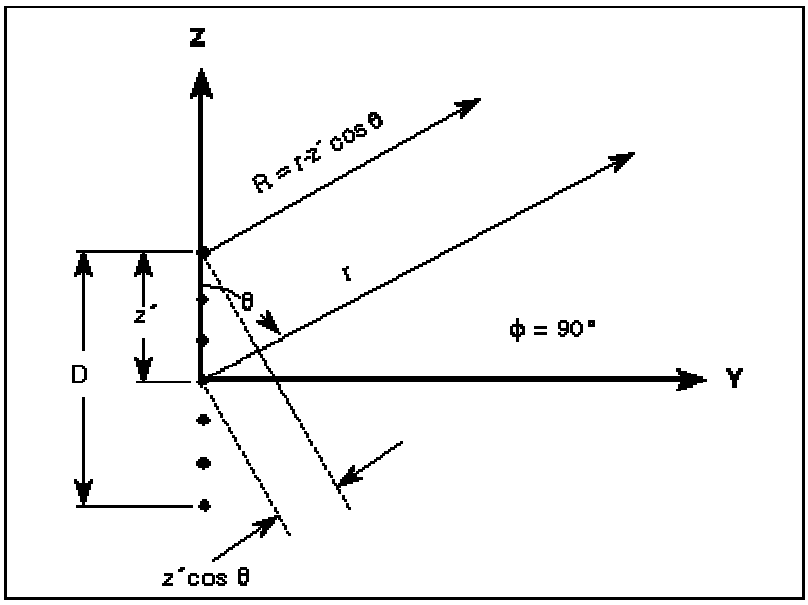

Figure B.3: Far field parallel ray approximation for calculations.

the outer edge of the antenna varies as point *P* changes. Derivation of equation (B.2) is given as follows. From Figure B.2, the following applies:

$$r^2 = z^2 + y^2 \tag{B.3}$$

$$z = r\cos\theta \tag{B.4}$$

$$y = \mathrm{r}\sin\theta \tag{B.5}$$

and

$$R = \sqrt{y^2 + (z - z')^2} = \sqrt{y^2 + z^2 - 2zz' + (z')^2}\,. \tag{B.6}$$

Substituting (B.3) and (B.4) into (B.6)

$$R = \sqrt{r^2 - 2r\cos\theta z' + (z')^2}\,, \tag{B.7}$$

which puts point *P* into spherical coordinates. Equation (B.7) can be expanded by the binomial theorem which for the first three terms, reduces to:

$$R = r - z'\cos\theta + \frac{(\sin\theta z')^2}{2r} + \cdots \tag{B.8}$$

In the parallel ray approximation for far field calculations (Figure B.3) the third term of (B.8) is neglected.

The distance where the far field begins (R_{ff}) (or where the near field ends) is the value of r when the error in R due to neglecting the third term of equation (B.8) equals 1/16 of a wavelength. R_{ff} is usually calculated on boresight, so that $\theta = 90°$ and the second term of equation (B.8) equals zero ($\cos 90° = 0$). Therefore, from Figure B.3, where D is the antenna dimension, R_{ff} is found by equating the third term of (8) to $1/16^{th}$ of a wavelength.

$$\frac{(z' \sin\theta)^2}{2R_{ff}} = \frac{\lambda}{16}. \tag{B.9}$$

For $\sin(\theta = 90°) = 1$ and $z' = D/2$, (B.9) becomes

$$\frac{(D/2)^2}{2R_{ff}} = \frac{\lambda}{16} \tag{B.10}$$

and

$$R_{ff} = \frac{16(D/2)^2}{2\lambda} = \frac{2D^2}{\lambda} \tag{B.11}$$

Equation (B.11) is the standard equation for calculating the far field given in all references.

The power density within the near field varies as a function of the type of aperture illumination and is less than would be calculated by equation (B.1). Thus, in the antenna near field there is stored energy. The complex radiation field equations have imaginary terms indicating reactive power.

B.2 Study of the Near-Field of An Array Antenna

As discussed in the previous section, the plane-wave characteristic of the electromagnetic field in the far-field region of an antenna is well known. The

interpretation of radar backscatter in the far-field region is straight forward, as the electric/magnetic field is proportional to *1/R* while power is proportional to $1/R^2$. Complications arise when one examines the radar backscatter in the near-filed region of the antenna, where the plane-wave approximation fails.

In this section, we want to examine the transmitted electromagnetic field in the near-field region of an array antenna. This issue is important for the lower atmospheric (z < 30 km) observations made in the vertical direction by the Jicamarca VHF radar, as the near field of the antenna extends out to 30 km. In this numerical study of the near-field region of an antenna array, we will first examine the near-field of an antenna array composed of N dipoles and then apply our results to the Jicamarca VHF radar.

B.2.1 Methodology

The Jicamarca VHF radar is composed of half-wave dipoles. In this calculation, we consider the general situation of an antenna array composed of N half-wave dipoles. The electric field generated by each dipole is defined by

$$E_\theta \sim \frac{\cos\left((\pi/2)\cos\theta\right)}{\sin\theta}\frac{1}{R}, \tag{B.12}$$

where R is the distance away from the antenna and θ is the angle measured from the axis of the dipole. From antenna theory, the E-field at a point (x, y, z) is obtained by

$$E_\theta(x, y, z) = \sum_{i=1}^{N} g_i E_{\theta i} \exp\left[\phi_i + 2\pi \frac{R_i}{\lambda}\right], \tag{B.13}$$

where $E_{\theta i}$ is the dipole located at (x_i, y_i, 0), g_i is the amplitude of dipole i, and ϕ_i is the phase of dipole i [*Elliot,* 1981]. We define R_i as the distance between dipole i and (*x, y, z*) as

$$R_i = \sqrt{(x - x_i)^2 + (y - y_i)^2 + z^2}\ . \tag{B.14}$$

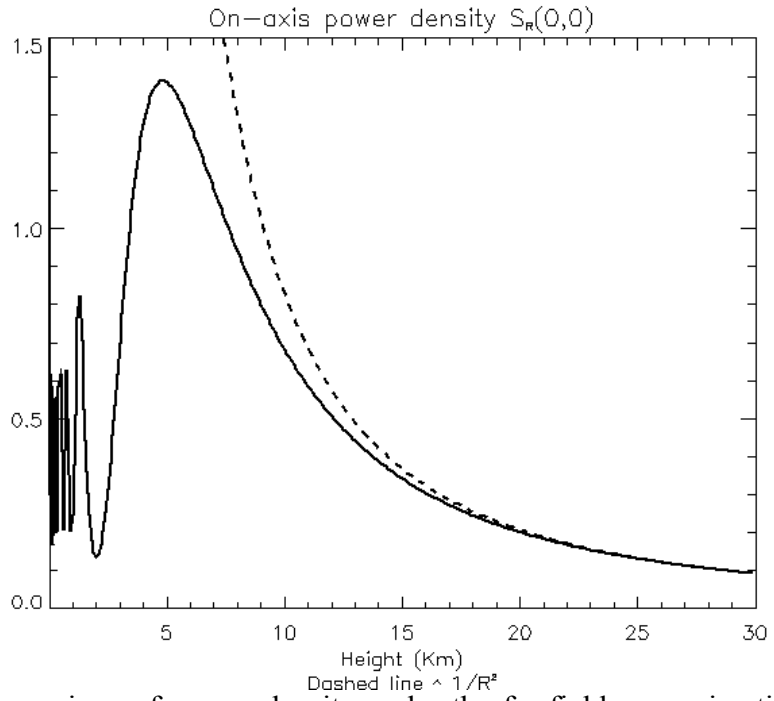

Figure B.4: Comparison of power density under the far-field approximation (dashed line) with the computed value (solid line) along the axis of the antenna beam in the vertical direction. For z > 10 km, the power density based on the far-field approximation differs from the actual value by 10 % or less.

In the following section, we show the results for the Jicamarca antenna array which is composed of 144×144 half-wave dipole array [*Ochs*, 1965].

B.2.2 Results

We implement our calculation assuming equal phase and amplitude, i.e., ϕ_i and g_i are constant, for each dipole. We present in Figure B.4 the behavior of the power at (0, 0, z). For z > 10 km, the power density based on the far-field approximation differs from the actual value by 10 % or less. This gives us confidence that the near-field effects of the Jicamarca antenna will not affect the quality of the radar data, and hence, aspect sensitivity measurements, near 10 km.

In Figure B.5, we present the relative phase as a function of height. The relative phase is an indication of the validity of the plane wave approximation: the smaller the

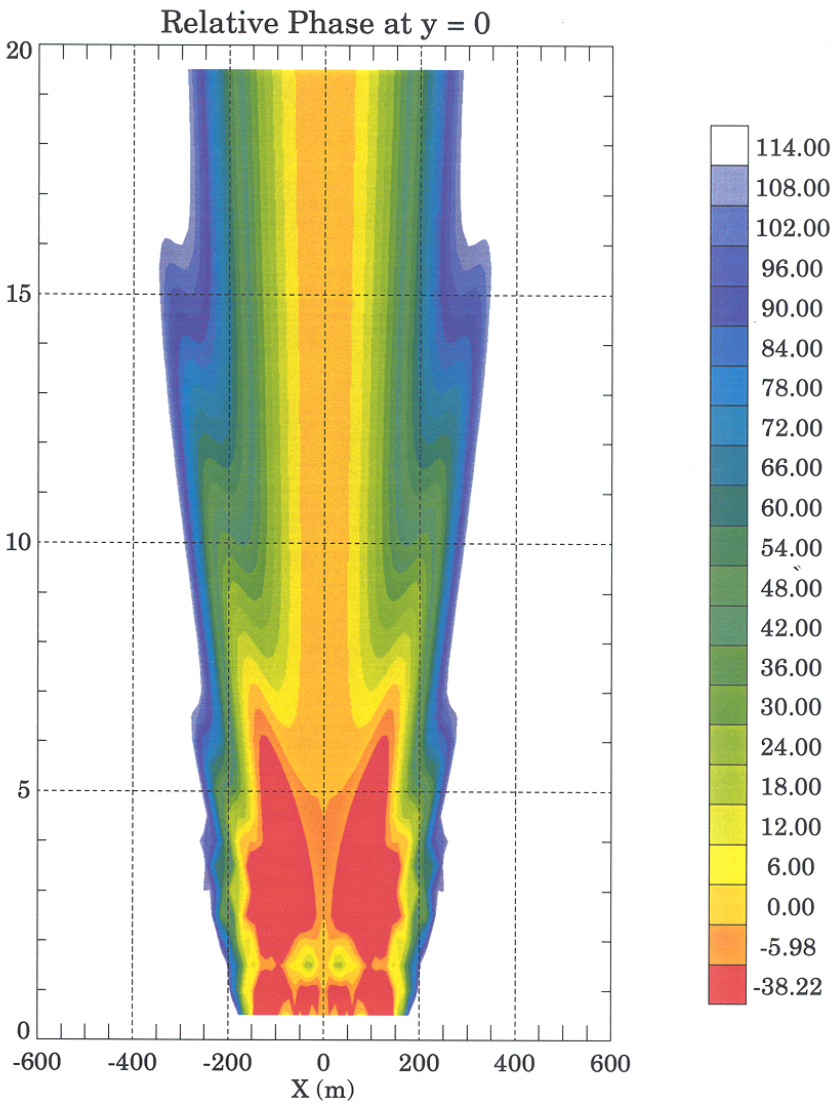

Figure B.5: Relative phase as a function of height. The smaller the value of relative phase, the similar is the wave front to a plane wave.

value of relative phase, the similar is the wave front to a plane wave. We see that the plane wave approximation is value in the center of the radiation of for heights above 10 km.

Appendix C

The Numbers Game

In this section, we will discuss various *numbers* that are of interest in fluid dynamics. Numbers are, by definition, dimensionless quantities which somehow embody physically important characteristics of the systems being studied. More often than not, they indicate the relative importance of various processes, and appear as the ratio of either terms or time scales. The reason for describing a system in terms of these numbers is that often the character of computational model output tends to depend more on the ratio of terms rather than their absolute value. So, for example, when faced with modeling the behavior of a system over a wide range of velocities and diffusivities, we may find that we need only perform experiments over a range of the ratio of two terms (the Peclet number) rather than doing every conceivable velocity and diffusivity combination. In this section, we will list some of the more important numbers, along with typical values and what they mean.

C.1 The Reynolds Number

The Reynolds number, often referred to as *Re*, is a measure of the relative importance of inertial to viscous terms. The higher the Reynolds number, the more likely to be turbulent the flow, and the lower the number, the more likely the flow will be laminar. The Reynolds number is defined as

$$Re = \frac{uL}{\nu}, \tag{C.1}$$

where the denominator is the kinematic viscosity, u is the fluid velocity, and L is a length scale. This may also be regarded as the ratio of the (molecular) diffusive time scale to the advective time scale. For most fluids (the atmosphere, oceans, etc.), the Reynolds number is of the order of several thousand or greater. Thus, most fluids are in a state of turbulent flow.

Reynolds number, in fluid mechanics, is a criterion of whether fluid (liquid or gas) flow is absolutely steady (streamlined, or laminar) or, on the average, steady with small unsteady fluctuations (turbulent). Whenever the Reynolds number is less than about 2,000, flow in a pipe is generally laminar, whereas, at values greater than 2,000, flow is usually turbulent. Actually, the transition between laminar and turbulent flow occurs not at a specific value of the Reynolds number but in a range usually beginning between 1,000 to 2,000 and extending upward to between 3,000 and 5,000.

C.2 The Peclet Number

The Peclet number (*Pe*) is a measure of the relative importance of advection to diffusion. Diffusion here is turbulent diffusion. The higher the Peclet number, the more important is advection. It is given by

$$Pe = \frac{uL}{\kappa} \tag{C.2}$$

and can be arrived at by non-dimensionalizing the advection-diffusion equation. This number may also be thought of as the ratio between the diffusive with the advective time scales.

The trick, though, is in the seemingly arbitrary choice of the length scale L. Clearly, the bigger L becomes, the higher the Peclet number becomes. This is equivalent to saying that given enough time, advection always wins out over diffusion.

This is because while the displacement of a particle increases linearly with time with advection, it only increases as the square root of time with diffusion. This can be seen by thinking about diffusion as a random walk experiment (which is what it mathematically is). But it does boil down to this implicit ambiguity that the Peclet number (and hence the apparent relative role of advection and diffusion) depends on the spatial scale of the system being studied.

C.3 The Richardson Numbers

The atmosphere, particularly at the upper troposphere and heights above that, is in general stably stratified. That is, heavy air is overlain by lighter air. If the reverse were true, then the air column would be gravitationally unstable, and vertical motions (convection) would result that would erase the condition. For turbulent displacement to occur vertically in a stratified air column, the fluid particles must overcome the vertical density (buoyancy) gradient. Thus, one would expect that the ability of the air column to resist this vertical turbulence will be related to the vertical density gradient (also referred to as the rate of buoyancy production). One model of the origin of the energy required to produce turbulent motions is the vertical shear in the horizontal velocity. That is, if the horizontal velocity is changing with height, the different layers traveling at different speeds tend to "rub" against one another, and there must be an overall dissipation occurring to maintain the velocity gradient. This dissipation scales as the square of the velocity gradient, so that defines a Richardson Flux number (Ri_f) as

$$Ri_f = \frac{\gamma g}{\nu \rho_o} \frac{\partial \rho / \partial z}{\left(\partial u / \partial z\right)^2}, \tag{C.3}$$

where γ is the thermal conductivity, ν is the kinematic viscosity, g is the gravitational constant and u is the horizontal velocity. This is the ratio of buoyancy production to

turbulent kinetic energy. Another important quantity is the gradient Richardson number (Ri_g), which is defined by

$$Ri_g = \frac{g \,\partial\rho/\partial z}{\rho_o \left(\partial u/\partial z\right)^2} = \frac{N^2}{\left(\partial u/\partial z\right)^2} \tag{C.4}$$

where N^2 is the square of the Brunt-Väisälä frequency. In situations where Ri_g decreases much below 1, turbulent diffusion becomes important, and can grow to a point where the system mixes vigorously. Laboratory experiments indicate that a critical Ri_g of 0.25 is a good approximation for most systems. In the text, Ri_g is referred to as Ri.

C.4 Various Other Numbers

Various other numbers crop up in different circumstances. Ones that appear in this thesis are the Prandtl number (Pr) and the Schmidt number (Sc). The former is the ratio of viscosity to thermal diffusion

$$Pr = \frac{\nu}{\gamma} \tag{C.5}$$

and the latter is the ratio of viscosity to molecular diffusion (D)

$$Sc = \frac{\nu}{D} \tag{C.6}$$

These are often used to compare model or flux calculations between different situations or chemical species.

Bibliography

Alcala, C. M., *Radar Scattering from Nonturbulent Layers in the Summer Polar Mesosphere*, Ph. D. Thesis, Cornell University, 1998.

Alcala, C. M., M. C. Kelley, and J. Ulwick, Nonturbulent layers in polar summer mesosphere: 1. Detection of sharp gradients using wavelet analysis, *Submitted to Radio Sci.*, *in press*, 2001.

Alcala, C. M., and M. C. Kelley, Nonturbulent layers in polar summer mesosphere: 2. Application of wavelet analysis to VHF scattering, *Radio Sci.*, *in press*, 2001.

Andrews, D., J. Holton, and C. Leovy, *Middle Atmospheric Dynamics*, Academic Press, 1987.

Antoine, J.-P., Wavelet analysis: a new tool in physics, *Wavelets in Physics*, ed., J. C. van den Berg, Cambridge Univeristy Press, 1999.

Antonia, R. A., and J. D. Atkinson, A ramp model for turbulent temperature fluctuations, *Phys. Fluids*, *19*, 1273-1278, 1976.

Antonia, R. A., A. J. Chambers, C. A. Friehe, and C. Q. Van Atta, Temperature ramps in the atmospheric surface layers, *J. Atmos. Sci.*, *36*, 99-108, 1977.

Axford, D. N., An observation of gravity waves in shear flow in the lower stratosphere, *Q. J. R. Meteorol. Soc.*, *96*, 273-286, 1970.

Axford, D. N., On an observation of turbulent waves on the tropopause surface, *Q. J. R. Meteorol. Soc.*, *99*, 438-449, 1973.

Bader, M. J, G. S. Forbes, J. R. Grant, R. B. E. Lilley, and A. J. Waters, Images in weather forecasting. A practical guide for interpreting satellite and radar imagery, Cambridge University Press, 1995.

Balsley, B. B., and D. Farley, Partial reflections: A source of weak VHF equatorial spread-F echoes, *J. Geophys. Res.*, *80*, 4735-4737, 1975.

Balsley, B. B., and K. S. Gage, The MST radar technique: Potential for middle atmospheric studies, *Pure. Appl. Geophys.*, *118*, 452-493, 1980.

Balsley, B. B., and K. S. Gage, On the vertical-incidence VHF backscatter power profile from the stratosphere, *Geophys. Res. Lett.*, *8*, 1173-1175, 1981.

Balsley, B. B., and V. L. Peterson, Doppler-air measurements of clear air atmosphere turbulence at 1290 MHz, *J. Appl. Meteorol.*, *20*, 266-274, 1981.

Balsley, B. B., The MST technique-a brief review, *J. Atmos. Terr. Phys.*, *43*, 495-509, 1981.

Balsley, B. B., J. W. Birks, M. L. Jensen, K. G. Knapp, J. B. Williams, and G. W. Tyrrell, Vertical profiling of the atmosphere using high-tech kites, *Environ. Sci. Technol.*, *28*, 422-427, 1994.

Barat, J., Some characteristics of clear-air turbulence in the middle atmosphere, *J. Atmos. Sci.*, *39*, 2553-2565, 1982.

Barat, J., and F. Bertin, Simultaneous measurement of temperature and velocity fluctuations within clear-air turbulence layers: analysis of the estimate of dissipation rate by remote sensing techniques, *J. Atmos. Sci.*, *41*, 1613-1619, 1984.

Batchelor, G. K., The application of similarity theory of turbulence in the atmospheric diffusion, *Quart. J. Roy. Meteorol. Soc.*, *76*,1333-146, 1950.

Batchelor, G. K., *The Theory of Homogeneous Turbulence*, Cambridge University Press, 1959.

Bean, B. R., and E. J. Dutton, *Radio Meteorology, Natl. Bur. Stand., Monogr. 92, Supt. Doc.*, U.S. Govt. Printing Office, Washington D.C., 1966.

Bertin, F., J. Barat, and R. Wilson, Energy dissipation rates, eddy diffusivity, and the Prandtl number: An in situ experimental approach and its consequences on radar estimates of turbulent parameters, *Radio Sci.*, *32*, 791-804, 1997.

Bertin, F, P. F. J. van Velthoven, P. Bassemoulin, R. Ney, and M. Massebeuf, Wave-turbulence interactions observed in the lower stratosphere by the PROUST UHF radar and GPS radiosoundings, *J. Atmos. Solar-Terr. Phys.*, *61*, 663-673, 1999.

Bohne, A. R., Radar detection of turbulence in precipitation environments, *J. Atmos. Sci.*, *40*, 1137-1142, 1978.

Bolgiano, R., Jr., The general theory of turbulence-turbulence in the atmosphere, in *Winds and Turbulence in the Stratosphere, Mesosphere and Ionosphere*, ed., K. Rawer, North-Holland, 1968.

Booker, H. G., and W. E. Gordon, A theory of radio scattering in the troposphere, *Proc. IEEE*, *38*, 401-412, 1950.

Bradshaw, P., *An Introduction to Turbulence and Its Measurement*, Pergamon, 1975.

Briggs, B. H., and R. A. Vincent, Some theoretical considerations on remote probing of weakly scattering irregularities, *Aust. J. Phys.*, *26*, 805-814, 1973.

Brown, J. H., E. Dewan, A. Murphy, and P. Thomas, Study of possible solar heating effects on thermosonde probes-error analysis, *Report # AFGL-TR-89-0178,* ERP 1034, Air Force Geophys. Lab., Hanscom Air Force Base, MA, USA, 1989.

Brown, W. O. J., S. Fukao, and M. Yamamoto, Multiple antenna FDI observations on the MU radar, *Proc. 7th Workshop on Tech. and Sci. Aspects of MST Radar*, ed., B. Edwards, SCOSTEP, Boulder, CO, 384-387, 1996.

Browand, F. K., and C. D. Winant, Laboratory observations of shear-layer instability in a stratified fluid, *Boundary Layer Meteorol.*, *5*, 65-77, 1973.

Browning, K. A., and C. D. Watkins, Observations of clear air turbulence by high power radars, *Nature*, *227*, 260-263, 1970.

Browning, K. A., G. W. Bryant, J. R. Starr, and A. McPherson, Simultaneous measurements of clear air turbulence by high-power radar and instrumented aircraft, *Nature*, *228*, 1065-1067, 1970.

Browning, K. A., Structure of the atmosphere in the vicinity of large-amplitude Kelvin-Helmholtz billows, *Q. J. R. Meteorol. Soc.*, *97*, 283-299, 1971.

Browning, K. A., J. R. Starr, and A. J. Whyman, Measurements of air motion in regions of clear air turbulence using high-power Doppler radar, *Nature*, *239*, 267-269, 1972.

Browning, K. A., G. W. Bryant, J. R. Starr, and D. N. Axford, Air motion within Kelvin-Helmholtz billows determined from simultaneous Doppler radar and aircraft measurement, *Q. J. R. Meteorol. Soc.*, *99*, 608-618, 1973.

Bufton, J. L., P. O. Minott, M. W. Fitzmaurice, and P. Titterton, Measurements of turbulence profiles in the troposphere, *J. Opt. Soc. Am.*, *62*, 1068-1070, 1972.

Bufton, J. L., Correlation of microthermal turbulence data with meteorological soundings in the troposphere, *J. Atmos. Sci.*, *30*, 83-87, 1873.

Cadet, D., Energy dissipation within intermittent clear air turbulence patches, *J. Atmos. Sci.*, *34*, 137-142, 1977.

Chakrabarty, D. K., G. Beig, J. S. Sidhu, H. Chakrabarty, R. Narayanan, N. K. Modi, S. R. Das, and P. Chakrabarty, Measurement of the eddy diffusion coefficient in the middle atmosphere from a balloon at low altitude, *J. Atmos. Terr. Phys.*, *49*, 975-980, 1987.

Chapman, D., and K. A. Browning, Radar observations of wind-shear splitting within evolving atmospheric Kelvin-Helmholtz billows, *Q. J. R. Meteorol. Soc.*, *123*, 1433-1439, 1997.

Chau, J. L., and B. B. Balsley, Interpretation of angle-of-arrival measurements in the lower atmosphere using spaced antenna radar systems, *Radio Sci.*, *33*, 517-522, 1998a.

Chau, J. L., and B. B. Balsley, A statistical comparison of VHF techniques to study clear-air vertical velocities in the lower atmosphere using the Jicamarca radar, *Radio Sci.*, *33*, 1565-1583, 1998b.

Chau, J. L., R. J. Doviak, A. Muschinski, and C. L. Holloway, Tropospheric measurements of turbulence and characteristics of Bragg scatterers using Jicamarca VHF radar, *Radio Sci.*, *35*, 179-193, 2000.

Chen, J. S., J. Y. Liu, and Y. H. Chu, Effects of anisotropy and power spectrum of refractivity irregularities on the determination of layer thickness and layer position using the frequency domain interferometry technique, *Radio Sci.*, *32*, 437-451, 1997.

Chilson, P. B., A. Muschinski, and G. Schmidt, First observations of Kelvin-Helmholtz billows in an upper level jet stream using VHF frequency domain interferometry, *Radio Sci.*, *32*, 1149-1160, 1997.

Chimonas, G., and J. R. Grant, Shear excitation of gravity waves, I, Modes of a two-scale atmosphere, *J. Atmos. Sci.*, *41*, 2269-2277, 1984a.

Chimonas, G., and J. R. Grant, Shear excitation of gravity waves, II, Upscale scattering from Kelvin-Helmholtz waves, *J. Atmos. Sci.*, *41*, 2278-2288, 1984b.

Cho, J. Y. N., Inertio-gravity wave parameter estimation from cross-spectral analysis, *J. Geophys. Res.*, *100*, 18727-18737, 1995.

Cho, J. Y. N., *Radar Scattering from the Summer Polar Mesosphere: Theory and Observation*, Ph. D. Thesis, Cornell University, 1993.

Chu, Y. H., J. K. Chao, C. H. Liu, and J. Röttger, Aspect sensitivity at tropospheric heights measured with vertically pointed beam of the Chung-Li VHF radar, *Radio Sci.*, *25*, 539-550, 1990.

Corrsin, S., On the spectrum of isotropic temperature fluctuations in isotropic turbulence, *J. Applied Phys.*, *22*, 469-473, 1951.

Corrsin, S., Further generalizations of Onsager's cascade model for turbulence spectra, *Phys. Fluid*, *7*, 1156-1159, 1964.

Cot, C., and J. Barat, Wave-turbulence interaction in the stratosphere: a case study, *J. Geophys. Res.*, *91*, 2749-2756, 1986.

Coulman, C. E., J. Vernin, Y. Coqueugniot, and J. L. Garcia, Outer scale of turbulence appropriate to modeling refractive index structure profiles, *App. Opt.*, *27*, 155-160, 1988.

Coulman, C. E., J. Vernin, and A. Fuchs, Optical seeing-mechanism of formation of thin turbulent laminae in the atmosphere, *Appl. Opt.*, *34*, 5461-5474, 1995.

Crane, R. K., Measurements of clear air turbulence in the lower stratosphere using the Millstone Hill *L*-band radar, preprints, *14th Radar Meteorological Conference*, Amer. Meteorol. Soc., Boston, MA, 101-106, 1970.

Crane, R. K., A review of radar observations of turbulence in the lower atmosphere, *Radio Sci.*, *15*, 177-193, 1980.

Czechowsky, P., I. M. Reid, and R. Rüster, VHF radar measurements of the aspect sensitivity of the summer polar mesopause echoes over Andenes, Norway, *Geophys. Res. Lett.*, *15*, 1259-1262,1988.

Czechowsky, P., and R. Rüster, VHF radar observations of turbulent structures in the polar mesopause region, *Ann. Geophys.*, *15*, 1028-1036, 1997.

du Castel, F., *Tropospheric Radio Wave Propagation Beyond the Horizon*, Pergamon, Tarrytown, NY, 1966.

Dalaudier, F., M. Crochet, and C. Sidi, Direct comparison between in situ and radar measurements of temperature fluctuation spectra: A puzzling result, *Radio Sci.*, *24*, 311-324, 1989.

Dalaudier, F., C. Sidi, and M. Crochet, Direct evidence of "sheets" in the atmospheric temperature field, *J. Atmos. Sci.*, *51*, 237-248, 1994.

Daubechies, I., Orthonormal bases of compactly supported wavelets, *Commun. on Pure and Appl. Math.*, *XLI*, 901-996, 1988.

Davis, P. A., and W. R. Reiter, Resonant parallel shear instability in the stably stratified planetary boundary layer, *J. Atmos. Sci.*, *33*, 1287-1300, 1976.

Doviak, R. J., and D. S. Zrnic, Reflection and scatter formula for anisotropically turbulent air, *Radio Sci.*, *19*, 325-336, 1984.

Dutton, J. A., and H. A. Panofsky, Clear air turbulence: a mystery may be unfolding, *Science*, *167*, 937-944, 1970.

Eaton, F. D., S. A. McLaughlin, and J. R. Hines, A new frequency-modulated continuous wave radar for studying planetary boundary layer morphology, *Radio Sci.*, *30*, 75-88, 1995.

Ehernberger, L. J., High altitude turbulence encountered b the supersonic YF-12A airplane, *Proc. 6th Conf. on Aerospace and Aeronautical Meteorol.*, American Meteorol. Soc., Boston, MA, 305-312, 1974.

Eliot, R. S., *Antenna Theory and Design*, Prentice-Hall, 1981.

Farge, M., N. K.-R. Kevlahan, V. Perrier, and K. Schneider, Turbulence analysis, modeling and computing using wavelets, *Wavelets in Physics*, ed., J. C. van den Berg, Cambridge Univeristy Press, 1999.

Foufoula-Georgiou, E., and P. Kumar, Wavelet analysis in geophysics: An introduction, *Wavelets in Geophysics*, ed., Foufoula-Georgiou, E., and P. Kumar, Academic Press, 1994.

Friis, H. T., A. B. Crawford, and D. C. Hogg, A reflection theory for propagation beyond the horizon, *Bell Sys. Tech. J.*, *36*, 627-644, 1957.

Frisch, A. S., and J. A. Businger, A study of convective elements in the atmospheric surface layer, *Boundary Layer Meteorol.*, *3*, 301-328, 1973.

Frisch, A. S., and S. F. Clifford, A study of convection capped by a stable layer using Doppler radar and acoustic echo sounders, *J. Atmos. Sci.*, *31*, 1622-1628, 1974.

Fritts, D. C., Shear excitation of atmospheric gravity waves, II, Nonlinear radiation from a free shear layer, *J. Atmos. Sci.*, *41*, 524-537, 1984.

Fritts, D. C., M. A. Geller, B. B. Balsley, M. L. Chanin, I. Hirota, J. R. Holton, S. Kato, R. S. Lindzen, M. R. Schöberl, R. A. Vincent, and R. F. Woodman, Research status and recommendations from the Alaska workshop on gravity waves and turbulence in the middle atmosphere, *Bull. Am. Meteorol. Soc.*, *65*, 149-159, 1984.

Fritts, D. C., and P. K. Rastogi, Convective and dynamical instabilities due to gravity wave motions in the lower and middle atmosphere: Theory and observation, *Radio Sci.*, *20*, 1247-1277, 1985.

Fritts, D. C., T. L. Palmer, Ø. Andreassen, and I. Lie, Evolution and breakdown of Kelvin-Helmholtz billows in stratified compressible flows. Part I: Comparison of two and three dimensional flows, *J. Atmos. Sci.*, *53*, 3173-3191, 1996.

Fukao, S., T. Sato, S. Kato, R. M. Harper, R. F. Woodman, and W. E. Gordon, Mesospheric winds and waves over Jicamarca on May 23-24, 1974, *J. Geophys. Res.*, *84*, 4379-4386, 1979.

Gage, K. S., and J. L. Green, Evidence for specular reflection from monostatic VHF radar observation of the stratosphere, *Radio Sci.*, *13*, 991-1001, 1978.

Gage, K. S., and B. B. Balsley, On the scattering and reflection mechanisms contributing to clear air radar echoes from the troposphere, stratosphere, and mesosphere, *Radio Sci*., *15*, 243-257, 1980.

Gage, K. S., J. L. Green, and T. E. Van Zandt, Use of Doppler radar for the measurement of atmospheric turbulence parameters from the intensity of clear air echoes, *Radio Sci.*, *15*, 407-416, 1980.

Gage, K. S., D. A. Carter, and W. L. Ecklund, The effect of gravity waves in specular echoes observed by the Poker Flat MST radar, *Geophys. Res. Lett.*, *8*, 599-602, 1981.

Gamage, N., and C. Hagelberg, Detection and analysis of microfronts and associated coherent events using localized transforms, *J. Atmos. Sci.*, *50*, 750-756, 1993.

Gibson, C. H., Internal waves, fossil turbulence, and composite ocean microstructure spectra, *J. Fluid Mech.*, *168*, 89-117, 1986.

Gibson, C. H., Fossil two-dimensional turbulence in the ocean, in *Turbulent Shear Flows*, *7*, Ed. F. Durst, W. C. Reynolds, Springer-Verlag, 63-78, 1991.

Gibson, C. H., Fossil turbulence revisited, *J. Marine Sys.*, *21*. 147-167, 1999.

Gibson-Wilde, D., J. Werne, D. Fritts, and R. Hill, Direct numerical simulation of VHF radar measurements of turbulence in the mesosphere, *Radio Sci.*, *35*, 783-798, 2000.

Gossard, E. E., D. R. Jensen, and J. H. Richter, An analytical study of the tropospheric structure as seen by high-resolution radar, *J. Atmos. Sci.*, *28*, 794-805, 1971.

Gossard, E. E., J. E. Gaynor, R. J. Zamora, and W. D. Neff, Fine structure of elevated stable layers observed by sounder and in situ tower sensors, *J. Atmos. Sci.*, *42*, 2156-2169, 1985.

Gossard, E. E., and A. S. Frisch, Relationship of the variances of temperature and velocity to atmospheric stability-Application to radar and acoustic sounding, *J. Clim. Appl. Meteorol.*, *26*, 1021-1036, 1987.

Green, J. L., K. S. Gage, and T. E. Van Zandt, Atmospheric measurements by VHF pulsed Doppler radar, *IEEE Trans. Geosci. Electron.*, *17*, 262-280, 1979.

Green, J. L., and K. S. Gage, Observations of stable layers in the troposphere and stratosphere using VHF radar, *Radio Sci.*, *15*, 395-405, 1980.

Greene, M. T., High achiever, *Nature*, *407*, 947, 2000.

Gurvich, A. S., and A. I. Kon, Aspect sensitivity of radar returns from anisotropic turbulence irregularities, *J. Electromagn. Waves Appl.*, *7*, 1343-1353, 1993.

Hagelberg, C. R., and N. K. Gamage, Applications of structure preserving wavelet decompositions to intermittent turbulence, a case study, *Wavelets in Geophysics*, ed., Foufoula-Georgiou, E. and P. Kumar, Academic Press, 1994.

Hall, T. M., *Radar Observations and Dynamics of the Polar Summer Mesosphere*, Cornell University, 1991.

Hardy, H. R., D. Atlas, and K. M. Glover, Multiwavelength backscatter from the clear atmosphere, *J. Geophys. Res.*, *71*, 1537-1552, 1966.

Hardy, K. R., and I. Katz, Probing the clear atmosphere with high power, high-resolution radar, *Proc. IEEE*, *57*, 468-480, 1969.

Hardy, K. R., R. J. Reed, and G. K. Mather, Observation of Kelvin-Helmholtz billows and their mesoscale environmental by radar, instrumented aircraft, and a dense radiosonde network, *Q. J. R. Meteorol. Soc.*, *99*, 279-293, 1973.

Haug, A., E. V. Thrane, K. Bjørnå, A. Brekke, and O. Holt, Observations of unusually strong partial reflections in the auroral D-region during an absorption event, *J. Atmos. Terr. Phys.*, *39*, 1333-40, 1977.

Hicks, J. J., and J. K. Angel, Radar observation of breaking gravitational waves in the visually clear atmosphere, *J. Appl. Meteorol.*, *7*, 114-121, 1968.

Hill, R. J., and S. F. Clifford, Modified spectrum of atmospheric temperature fluctuations and its application to optical propagation, *J. Opt. Soc. Am.*, *68*, 892-899, 1978.

Hines, C. O., Internal atmospheric gravity waves at ionospheric heights, *Can. J. Phys.*, *38*, 1441-1481, 1960.

Ho, K. L., N. D. Mavrokoulakis, and R. S. Cole, Determination of the atmospheric refractive index structure parameter from refractivity measurements and amplitude scintillation measurements at 36 GHz, *J. Atmos. Terr. Phys.*, *40*, 745-747, 1978.

Hocking, W. K., Angular and temporal characteristics of partial reflections from the D-region of the ionosphere, *J. Geophys. Res.*, *84*, 845-851, 1979.

Hocking, W. K., and R. A. Vincent, A comparison between HF partial reflection profiles from the *D*-region and simultaneous Langmuir probe electron density measurement, *J. Atmos. Terr. Phys.*, *44*, 843-854, 1982.

Hocking, W. K., and J. Röttger, Pulse-length dependence of radar signal strengths for Fresnel backscatter, *Radio Sci.*, *18*, 1312-1324, 1983a.

Hocking, W. K., On the extraction of atmospheric turbulence parameters from radar backscatter Doppler spectra, I, Theory, *J. Atmos. Terr. Phys.*, *45*, 89-102, 1983b.

Hocking, W. K., R. Rüster, and P. Czechowsky, Observation and measurement of turbulence and stability in the middle atmosphere with a VHF radar, *Rep. ADP 335*, Dept. of Phys., Univ. of Adelaide, Adelaide, S. Aust., 1984.

Hocking, W. K., Measurements of turbulent energy dissipation rates in the middle atmosphere by radar techniques: A review, *Radio Sci*., *20*, 1403-1422, 1985.

Hocking, W. K., R. Rüster, and P. Czechowsky, Absolute reflectivities and aspect sensitivities of VHF radio waves scatterers measured with the SOUSY radar, *J. Atmos. Terr. Phys.*, *48*, 131-144, 1986a.

Hocking, W. K., Observation and measurements of turbulence in the middle atmosphere with a VHF radar, *J. Atmos. Terr. Phys.*, *48*, 655-670, 1986b.

Hocking, W. K., Radar studies of small-scale structure in the upper and middle atmosphere and lower ionosphere, *Adv. Space Res.*, *7*, 327-338, 1987.

Hocking, W. K., Seasonal variation of turbulence intensities in the upper mesosphere and lower thermosphere measured by radar techniques, *Handbook for MAP*, *27*, SCOSTEP Secretariat, University of Illinois, Urbana, 427-438, 1989.

Hocking, W. K., S. Fukao, T. Tsuda, M. Yamamoto, T. Sato, and S. Kato, Aspect sensitivity of stratospheric VHF radio waves scatters, particularly above 15 km altitude, *Radio Sci*., *25*, 613-627, 1990.

Hocking, W. K., S. Fukao, M. Yamamoto, T. Tsuda, and S. Kato, Viscosity waves and thermal-conduction waves as a case of "specular" reflectors in the radar studies of the atmosphere, *Radio Sci.*, *26*, 1281-1303, 1991.

Hocking, W. K., Some new perspectives on viscosity and thermal conduction waves as a cause of specular reflections in radar studies in of the atmosphere, *Proceedings of the Seventh Workshop on Technical and Scientific Aspects of MST Radars*, 82-85, 1995.

Hocking, W. K., An assessment of the capabilities and limitations of radars in measurements of upper atmospheric turbulence, *Adv. Space Res.*, *17*, 37-47, 1996.

Hocking, W. K., and A. M. Hamza, A quantitative measure of the degree of anisotropy of turbulence in terms of atmospheric parameters, with particular relevance to radar studies, *J. Atmos. Solar-Terr. Phys.*, *59*, 1011-1020, 1997.

Hocking, W. K., and P. K. L. Mu, Upper and middle tropospheric kinetic energy dissipation rates from measurements of C_n^2-review of theories, *in situ* investigations, and experimental studies using the Buckland Park atmospheric radar in Australia, *J. Atmos. Solar-Terr. Phys.*, *99*, 1779-1803, 1997.

Hocking, W. K., The dynamical parameters of turbulence theory as they apply to middle atmosphere studies, *Earth Plan. Space*, *51*, 525-541, 1999.

Holton, J., *An Introduction to Dynamic Meteorology*. Academic Press, San Diego, 1992.

Hooper, D., and L. Thomas, Aspect sensitivity of VHF scatters in the troposphere in the troposphere and stratosphere from comparisons of powers in off vertical beams, *J. Atmos. Solar-Terr. Phys.*, *57*, 655-663. 1995.

Hooper, D. A., and L. Thomas, Complementary criteria for identifying regions of intense atmospheric turbulence using lower VHF radar, *J. Atmos. Solar-Terr. Phys.*, *60*, 49-61, 1998.

Hoppe, U. P., E. V. Thrane, T. A. Blix, F. J. Lübken, J. Y. N. Cho, and W. E. Swartz, Studies of polar mesosphere summer echoes by VHF radar and rocket probes, *Adv. Space. Res.*, *14*, 139-148, 1994.

Ierkic, H. M., R. F. Woodman, and P. Perillat, Ultrahigh vertical resolution radar measurements n the lower stratosphere at Arecibo, *Radio Sci.*, *25*, 941-952, 1990.

James. P. K., and K. A. Browning, An observational study of primary and secondary billows in the free atmosphere, *Q. J. R. Meteorol. Soc.*, *107*, 351-365, 1981.

Kaimal, J. C., and J. A. Businger, Case studies of a convective plume and dust devil, *J. Appl. Meteorol.*, *9*, 612-620, 1970.

Kelley, M. C., *The Earth's Ionosphere: Plasma Physics and Electrodynamics*, Academic Press, Inc., 1989.

Kilburn, C., S. Fukao, and M. Yamamoto, Extended period frequency domain interferometry observations at stratospheric and tropospheric heights, *Radio Sci.*, *30*, 1099-1109, 1995a.

Kilburn, C., S. P. Kingsley, S. Quegan, R. Rüster, and G. Schmidt, Super-resolution: A new technique for MST radar studies of atmospheric thin layers, *J. Atmos. Solar-Terr. Phys.*, *57*, 1135-1151, 1995b.

Klaassen, G. P., and W. R. Peltier, Evolution of finite amplitude Kelvin-Helmholtz billows in two spatial dimensions, *J. Atmos. Sci.*, *42*, 1321-1339, 1985.

Klaassen, G.P., and Peltier, W.R., The influence of stratification on secondary instability in free shear layers, *J. Fluid Mech.*, *227*, 71-106, 1991.

Klostermeyer, J., and R. Rüster, Radar observation and model computations of a jet stream-generated Kelvin-Helmholtz instability, *J. Geophys. Res.*, *85*, 2841-2846, 1980a.

Klostermeyer, J., and R. Rüster, Computation of acoustic-gravity waves, Kelvin-Helmholtz instabilities and wave-induced transport in realistic atmospheric models, *J. Geophys. Res.*, *85*, 2829-2839, 1980b.

Klostermeyer, J., and R. Rüster, Further study of a jet stream generated Kelvin-Helmholtz instability, *J. Geophys. Res.*, *86*, 6631-6637, 1981.

Knapp, K. G., B. B. Balsley, M. L. Jensen, H. P. Hanson, J. W. Birks, Observation of the transport of polluted air masses form the northeastern United States to Cape Sable Island, Nova Scotia, Canada, during the 1993 NARE summer intensive, *J. Geophys. Res.*, 103, 13,399-13,411, 1998.

Kropfli, R. A., I. Katz, T. G. Konrad, and E. B. Dobson, Simultaneous radar reflectivity measurements and refractive index spectra in the clear atmosphere, *Radio Sci.*, *3*, 991-994, 1968.

Lane, J. A., Radar echoes from clear air in relation to refractive-index variations in the troposphere, *Proc. IEEE*, *London*, *116*, 1656-1660.

Larsen, M. F., and C. R. Cornish, Observations of quasi-inertial period waves in the lower stratosphere over Arecibo, *Middle Atmosphere Program, Handbook for MAP*, *28*, 334-340, 1989.

Larsen, M. F., and J. Röttger, VHF radar measurements of refractivity layer tilt angles and associated vertical beam radial velocity corrections, *J. Atmos. Ocean. Technol.*, *8*, 477-490, 1991.

Lawrence, R. S., G. R. Ochs, and S. F. Clifford, Measurements of atmospheric turbulence relevant to optical propagation, *J. Opt. Soc. Am.*, *60*, 826-830, 1970.

Lesicar, D., and W. K. Hocking, Studies of seasonal behavior of the shape of mesospheric scatters using a 1.98 MHz radar, *J. Atmos. Solar-Terr. Phys.*, *54*, 295-309, 1992.

Lesicar, D., W. K. Hocking, and R. A. Vincent, Comparative studies of scatterers observed by MF radars in the southern hemisphere mesosphere, *J. Atmos. Solar-Terr. Phys.*, *56*, 581-591, 1994.

Lilly, D. K., and P. F. Lester, Waves and turbulence in the stratosphere, *J. Atmos. Sci.*, *31*, 800-812, 1974.

Linder, B. C., The nature of D-region scattering of vertical incidence radio waves I: Generalized statistical theory of diversity effects between spaced receiving antennas, *Australian J. Phys.*, *28*, 163-170, 1975a.

Linder, B. C., The nature of D-region scattering of vertical incidence radio waves II: Experimental observations using spaced antenna reception, *Australian J. Phys.*, *28*, 171-185, 1975b.

Lindzen, R. S., Stability of a Helmholtz velocity profile in continuously stratified infinite Boussinesq fluid: Application to clear air turbulence, *J. Atmos. Sci.*, *31*, 1507-1514, 1974.

Lindzen, R. S., Turbulence and stress owing to gravity waves and tidal breakdown, *J. Geophys. Res.*, *86*,9707-9714, 1981.

Lübken, F.J., On the extraction of turbulent parameters from atmospheric density fluctuations, *J. Geophys. Res.*, *97*, 20385-20395, 1992.

Luce, H., M. Crochet, F. Dalaudier, and C. Sidi, Interpretation of VHF ST radar vertical echoes from in situ temperature sheet observations, *Radio Sci.*, *30*, 1003-1025, 1995.

Luce, H., M. Crochet, C. Hanuise, M. Yamamoto, and S. Fukao, On the interpretation of the layered structures detected by mesosphere-stratosphere-troposphere radars in dual frequency domain interferometry mode, *Radio Sci.*, *34*, 1077-1083, 1999.

Luce, H., J. Röttger, M. Yamamoto, and S. Fukao, Scattering layer thickness and position estimated by radar frequency domain interferometry 1. Effects of the limited horizontal extent and advection of the scattering layers, *Radio Sci.*, *35*, 119-131, 2000a.

Luce, H., J. Röttger, M. Crochet, M. Yamamoto, and S. Fukao, Scattering layer thickness and position estimated by radar frequency domain interferometry 2. Effects of tilts of the scattering layer or radar beam, *Radio Sci.*, *35*, 1109-1127, 2000b.

Ludlam, F. H., Characteristics of billow clouds and their relation to clear-air turbulence, *Q. J. R. Meteorol. Soc.*, *93*, 419-435, 1967.

Lumley, J. L., The spectrum of nearly inertial subrange in a stably stratified fluid, *J. Atmos. Sci.*, *21*, 99-102, 1964.

Mallat, S., and W. L. Hwang, Singularity detection and processing with wavelets, *IEEE Trans. Inform. Theory*, *38*, 617-643, 1992.

Mallat, S., and S. Zhong, Characterization of signals from multiscale edges, *IEEE Trans. Patt. Anal. Machine Intel.*, *14*, 710-732, 1992.
Mestayer, P. G., C. H. Gibson, M. F. Coantic, and A. S. Patel, Local isotropy in heated and cooled turbulent boundary layer, *Phys. Fluids*, 19, 1279-87, 1976.

Metcalf, J. I., and D. Atlas, Microscale ordered motions and atmospheric structure associated with thin echo layers in stably stratified zones, *Boundary Layer Meteorol.*, *4*, 7-35, 1973.

Miles, J. W., On the stability of heterogeneous shear flows, *J. Fluid Mech.*, *10*, 496-508, 1961.

Misme, P., F. du Castel, and J. Voge, Refléxions partielles dans l'atmosphere et propagation á grande distance, Premi è re partie: Mesures météorologiques, *Ann. Télécommun*, *13*, 209-214, 1958.

Muschinski, A., Possible effect of Kelvin-Helmholtz instabilities on VHF radar observations of the mean vertical wind, *J. Appl. Meteorol.*, *35*, 2210-2217, 1996.

Muschinski, A., P. Sullivan, D. Würtz, R. Hill, S. Cohn, D. Lenschow, and R. Doviak, First synthesis of wind-profiler signals on the basis of large-eddy simulation data, *Radio Sci.*, *34*, 1437-1459, 1999.

Nastrom, G. D., Doppler radar spectral width broadening due to beamwidth and wind shear, *Ann. Geophys.*, *15*, 786-796, 1997.

Nielson, J. W., In situ observation of Kelvin-Helmholtz waves along a frontal inversion, *J. Atmos. Sci.*, *49*, 369-386, 1992.

O'Sullivan, D., and T. J. Dunkerton, Generation of inertia-gravity waves in a simulated life cycle of baroclinic instability, *J. Atmos. Sci.*, *52*, 3695-3716, 1995.

Obukhov, A. M., Structure of the temperature filed in turbulent flows, *Izvestiya Akademii Nauk SSSR*, *Geohr. Geophys. Ser.*, *13*, 58, 1949.

Ochs, G. R., The Large 50MC/S Dipole Array at Jicamarca Radio Observatory, *NBS Report 8772*, U. S. Department of Commerce, 1965.

Ottersten, H., Theoretical aspects of CAT detection by radar, *Proc. 13th Radar Meteorol. Conf.*, American Meteorological Society, Boston, 1968.

Ottersten, H., Radar backscattering from turbulent clear atmosphere, *Radio Sci.*, *4*, 1251-1255, 1969a.

Ottersten, H., Atmospheric structure and radar backscattering in clear air, *Radio Sci.*, *4*, 1179-1193, 1969b.

Palmer, R. D., M. F. Larsen, R. F. Woodman, S. Fukao, M. Yamamoto, T. Tsuda, and S. Sato, VHF radar interferometry measurements of vertical velocity and the effect of tilted refractivity surface on standard Doppler measurements, *Radio Sci.*, *26*, 417-427, 1991.

Palmer, R. D., M. F. Larsen, E. I. Sheppard, S. Fukao, M. Yamamoto, T. Tsuda, and S. Sato, Post-statistic steering wind estimation in the troposphere and lower stratosphere, *Radio Sci.*, *28*, 261-271, 1993.

Palmer, T. L., D. C. Fritts, and Ø. Andreassen, Evolution and breakdown of Kelvin-Helmholtz billows in stratified compressible flows. Part II: Instability structure, evolution, and energetics, *J. Atmos. Sci.*, *53*, 3192-3212, 1996.

Palmer, R. D., M. F. Larsen, S. Fukao, and M. Yamamoto, On the relationship between aspect sensitivity and spatial interferometric in-beam incidence angles, *J. Atmos. Solar-Terr. Phys.*, *60*, 37-48, 1998.

Panofsky, H. A., The structure constant for the index of refraction in relation to the gradient of index of refraction in the surface layer, *J. Geoph. Res.*, *73*, 6047-6049, 1968.

Patnaik, P. C., F. S. Sherman, and G. M. Corcos, A numerical simulation of Kelvin-Helmholtz waves of finite amplitude, *J. Fluid Mech.*, *73*, 215-240, 1976.

Peltier, W. R., J. Halle, and T. L. Clark, The evolution of finite-amplitude Kelvin-Helmholtz billows, *Geophys. Astrophys. Fluid Dyn.*, *10*, 53-87, 1978.

Pfister, L., W. Starr, R. Craig, M. Löwenstein, and M. Legg, Small-scale motions observed by aircraft in the tropical lower stratosphere: evidence for mixing and its relationship to large scale flows, *J. Atmos. Sci.*, *43*, 3210-3225, 1986.

Reid, I. M., Radar observations of stratified layers in the mesosphere and lower thermosphere (50-110 km), *Adv. Space. Res.*, *10*, 107-119, 1990.

Reiter, E. R., and A. Burns, The structure of clear-air turbulence derived from 'TOPCAT' aircraft measurements, *J. Atmos. Sci.*, *23*, 206-212, 1966.

Riggin, D. M., E. Kudeki, Z. Feng, M. F. Sarango, Jicamarca Radar Observations of the diurnal and semidiurnal tides in the troposphere and the lower stratosphere, Submitted to *J. Geophys. Res.*, 1999.

Robinson, F. L., and T. F. Konrad, A comparison of the turbulent fluctuations in clear air convection measured simultaneously aircraft and Doppler radar, *J. Appl. Meterol.*, *13*, 481-487, 1974.

Röttger, J., and C. H. Liu, Partial reflection and scattering of VHF radar signals from clear atmosphere, *Geophys. Res. Lett.*, *5*, 357-360, 1978.

Röttger, J., and R. A. Vincent, VHF radar studies of tropospheric velocities and irregularities using spaced antenna techniques, *Geophys. Res. Lett.*, *5*, 917-920, 1978.

Röttger, J., and G. Schmidt, High resolution VHF radar sounding of the troposphere and stratosphere, *IEEE Trans. Geosci. Electron.*, *GE-17*, 182-189, 1979.

Röttger, J., Reflection and scattering of VHF signals from atmospheric refractivity structures, *Radio Sci.*, *15*, 259-276, 1980a.

Röttger, J., Structure and dynamics of the stratosphere and mesosphere revealed by VHF radar investigation, *Pure Appl. Geophys.*, *118*, 494-527, 1980b.

Röttger, J., and H. M. Ierkic, Postbeam steering and interferometry applications of VHF radar to study winds, waves, and turbulence in the lower and middle atmosphere, *Radio Sci.*, *20*, 1461-1480, 1985.

Röttger, J., and C. La Hoz, Characteristics of polar mesosphere summer echoes (PMSE) observed with the EISCAT 224 MHz radar and possible explanations of their origin, *J. Atmos. Terr. Phys.*, *52*, 893-906, 1990.

Röttger, J., C. H. Liu, J. K. Chao, A. J. Chen, C. J. Pan, and L. J. Fu, Spatial interferometer measurements with the Chung-Li VHF radar, *Radio Sci.*, *25*, 503-415, 1990.

Rüster, R., and J. Klostermeyer, VHF radar observations of a Kelvin-Helmholtz instability in a subtropical jet stream, *Geophys. Astrophys. Fluid Dyn.*, *26*, 107-116, 1983.

Saito, N., Simultaneous noise suppression and signal compression using a library of orthonormal bases and the minimum description length criterion, *Wavelets in Geophysics*, ed., Foufoula-Georgiou, E., and P. Kumar, Academic Press, 1994.

Salby, M. L., *Fundamentals of Atmospheric Physics*, Academic Press, San Diego, CA, 1996.

Sato, T., and R. F. Woodman, Fine altitude resolution observations of stratospheric turbulent layers by the Arecibo 430 MHz radar, *J. Atmos. Sci.*, *39*, 2546-2552, 1982.

Sato, T., T. Tsuda, S. Kato, S. Morimoto, S. Fukao, and I. Kimura, High-resolution MST observations of turbulence by using the MU radar, *Radio Sci.*, *20*, 1452-1460, 1985.

Saxton, J. A., J. A. Lane, R. W. Meadows, and P. A. Matthews, Layer structure of the troposphere, *Proc. Inst. Electr. Eng.*, *111*, 275-283, 1964.

Schilling, V. K., and U. Janssen, Particle dispersion due to dynamical instabilities in the lower stratosphere, *Beitr. Atmos. Phys.*, *65*, 259-273, 1992.

Scinocca, J. F., The mixing of mass and momentum by Kelvin-Helmholtz billows, *J. Atmos. Sci.*, *52*, 2509-2530, 1995.

Seim, H. E., and Gregg, M.C., Detailed observations of a naturally occuring shear instability, *J. Geophys. Res.*, *99*, 10049-10073, 1994.

Sheen, D. R., C. H. Liu, and J. Röttger, A study of signal statistics of VHF radar echoes from clear air, *J. Atmos. Terr. Phys.*, *47*, 675-684, 1985.

Singh, S., K. K. Mahajan, and R. K, Choudhary, Detection of Kelvin-Helmholtz instability with the Indian mesosphere-stratosphere-troposphere radar: A case study, *J. Geophys. Res.*, *104*, 3937-3945, 1999.

Smith, P. L., and R. R. Rogers, On the possibility of radar detection of clear-air turbulence, *Proc. 10th Weather Radar Conf.*, p. 316, American Meteorological Society, Boston: 1963.

Smith, R. B., Kelvin-Helmholtz instability in severe down slope wind flow, *J. Atmos. Phys.*, *48*, 1319-1324, 1991.

Spalart, P. R., R. D. Moser, and M. M. Rogers, Spectral methods for the Navier-Stokes equations with one infinite and two periodic directions, *J. Comput. Phys.*, *96*, 297-324, 1991.

Sreenivasan, K. R. and R. A. Antonia, Skewness of temperature derivatives in turbulent shear flows, *Phys. Fluids*, *20*, 1986-1988, 1977.

Stillinger, D. C., K. N. Helland, and C. W. Van Atta, Experiments on the transition of homogeneous turbulence to internal waves in a stratified fluid, *J. Fluid Mech.*, *131*, 91-122, 1983.

Sykes, R. I., and W. S. Lewellen, A numerical study of breaking Kelvin Helmholtz billows using a Reynolds-stress turbulence closure model, *J. Atmos. Sci.*, *39*, 1506-1520, 1982.

Tatarski, V. I., *Wave Propagation in a Turbulent Medium*, translated from Russian by R. A. Silverman, McGraw-Hill, New York: 1961.

Tatarski, V. I., *Wave Propagation in a Turbulent Atmosphere*, Nauka, Moscow: 1967. (English translation, *The Effects of the Turbulent Atmosphere on Wave Propagation*, available from National Technical Information Service, Springfield, Va., 1971)

Taylor, R. J., Thermal structures in the lowest layers of the atmosphere, *Aust. J. Phys.*, *11*, 168-176, 1958.

Tennekes, H., and J. L. Lumley, *A First Course in Turbulence*, MIT Press, Cambridge, 1972.

Thorpe, S. A., Turbulence in stably stratified fluids, A review of laboratory experiments, *Boundary Layer Meterol.*, *5*, 95-119, 1973.

Thorpe, S. A., Transitional phenomena and the development of turbulence in stratified fluids: A review, *J. Geophys. Res.*, *92*, 5231-5281, 1987.

Torrence, C., and G. P. Compo, A Practical Guide to Wavelet Analysis, *Bull. Amer. Meteor. Soc.*, *79*, 61-78, 1998.

Tsuda, T., T. Sato, K. Hirose, S. Fukao, and S. Kato, MU radar observations of the aspect sensitivity of the backscattered VHF echo power in the troposphere and lower stratosphere, *Radio Sci.*, *21*, 971-980, 1986.

Tsuda, T., P. T. May, T. Sato, S. Kato, and S. Fukao, Simultaneous observations of reflection echoes and refractive index gradient in the troposphere and lower stratosphere, *Radio Sci.*, *23*, 655-665, 1988.

Tsuda, T., T. E. Van Zandt, and H. Saito, Zenith-angle dependence of VHF specular reflection echoes in the lower atmosphere, *J. Atmos. Solar-Terr. Phys.*, *59*, 761-775, 1997.

U. S. Standard Atmosphere, U.S. Committee on Extension to the Standard Atmosphere, *Tech. Rep.*, U. S. Government Printing Office, Washington, 1976.

van den Berg, J. C., *Wavelets in Physics*, Cambridge Univeristy Press, 1999.

Van Atta, C. W., Effect of coherent structures on structure functions of temperature atmospheric boundary layer, *Archives of Mech.*, *29*, 161-171, 1977.

Van Zandt, T. E., J. L. Green, K. S. Gage, and W. L. Clark, Vertical profiles of refractivity turbulence structure constant: comparison of observations by the Sunset radar with a new theoretical model, *Radio Sci*., *13*, 819-829, 1978.

Van Zandt, T. E., J. L. Green, W. L. Clark, and J. R. Grant, Buoyancy waves in the troposphere: Doppler radar observations and a theoretical model, *Geophys. Res. Lett.*, *6*, 429-432, 1979.

Van Zandt, T. E., and R. A. Vincent, Is VHF Fresnel reflectivity due to low frequency buoyancy waves?, *Handbook for MAP*, *9*, 78-80, SCOSTEP Secr., Univ. of Ill., Urbana, 1983.

Vincent, R. A., The interpretation of some observations of radio wave scattered from the lower ionosphere, *Aust. J. Phys.*, *26*, 815-827, 1973.

Vincent, R. A., and Belrose, J. S., The angular distribution of radio waves partially reflected form the lower ionosphere, *J. Atmos. Terr. Phys.*, *40*, 35-47, 1978.

Vincent, R. A., and J. Röttger, Spaced antenna VHF radar observations of tropospheric velocities and irregularities, *Radio Sci.*, *15*, 319-335, 1980.

Wait, J., *Electromagnetic Waves in Stratified Media*, Pergamon Press, Oxford, 1962.

Walters, D. L., Measurements of optical turbulence with higher order structure functions, *Appl. Opt.*, *34*, 1591-1597, 1995.

Waterman, A. T., T. Z. Hu, P. Czechowsky, and J. Röttger, Measurements of anisotropic permittivity structure of upper troposphere with clear air radar, *Radio Sci.*, *20*, 1580-1592, 1985.

Weinstock, J., Vertical turbulent diffusion in a stably stratified fluid, *J. Atmos. Sci.*, *35*, 1022-1027, 1978.

Weinstock, J., Using radar to estimate dissipation rates in thin layers of turbulence, *Radio Sci.*, *16*, 1401-1406, 1981.

Werne, J., and D. C. Fritts, Stratified shear turbulence: Evolution and Statistics, *Geophys. Res. Lett.*, *26*, 439-442, 1999.

Werne, J., and D.C. Fritts, Anisotropy in a stratified shear layer, *Phys. Chem. Earth*, *in press*, 2000a.

Werne, J. and D. C. Fritts, Structure functions in stratified shear turbulence, *Proceedings of the 10th DOD HPC User Group Conference*, Albuquerque, NM, *in press*, 2000b.

Witkin, A., Scale space filtering, *Proc. Int. Joint Conf. Artificial Intel.*, 1019, 1983.

Woodman, R. F., Inclination of the geomagnetic field measured by an incoherent scatter technique, *J. Geophys. Res.*, *76*, 178-184, 1971.

Woodman, R. F., and A. Guillen, Radar observations of winds and turbulence in the stratosphere and mesosphere, *J. Atmos. Sci.*, *31*, 493-505, 1974.

Woodman, R., P. Kugel, and J. Röttger, A coherent integrator decoder for the SOUSY-VHF Radar, *Radio Sci.*, *15*, 233-242, 1980.

Woodman, R. F., Turbulence in the middle atmosphere: A review, *Middle Atmospheric Program, Handbook for MAP*, *2*, SCOSTEP Secretariat, Univeristy of Illinois, Urbana, 293-310, 1981.

Woodman, R. F., and P. K. Rastogi, Evaluation of effective eddy diffusive coefficients sing radar observations of turbulence in the stratosphere, *Geophys. Res. Lett.*, *11*, 243-246, 1984.

Woodman, R. F., and Y. H. Chu, Aspect sensitivity measurements of VHF backscatter made with the Chung-Li radar: Plausible mechanisms, *Radio Sci*., *24*, 113-125, 1989.

Woods, J. D., On Richardson's number as a criterion for laminar-turbulent-laminar transition in the ocean and atmosphere, *Radio Sci*, *4*, 1289-1298, 1969.

Worthington, R. M., and L. Thomas, The measurement of gravity wave momentum, flux in the lower atmosphere using VHF radar, *Radio Sci.*, *31*, 1501-1517, 1996.

Worthington, R. M., and L. Thomas, Long-period unstable gravity-waves and associated VHF radar echoes, *Ann. Geophys.*, *15*, 813-822, 1997.

Worthington, R. M., R. D. Palmer, and S. Fukao, An investigation of tilted aspect-sensitive scatterers in the lower atmosphere using the MU and Aberystwyth VHF radars, *Radio Sci.*, *34*, 413-426, 1999a.

Worthington, R. M., Calculating the azimuth of mountain waves, using the effect of tilted fine-scale stable layers on VHF radar echoes, *Ann. Geophys.*, *17*, 257-272, 1999b.

Wyngaard, J. C., Y. Izumi, and S. A. Collins, Jr., Behavior of the refractive-index structure parameter near ground, *J. Opt. Soc. Am.*, *61*, 1646-1650, 1971.

Yaglom, A. M., *Correlation Theory of Stationary and Related Random Functions I and II*, Springer-Verlag, New York, 1987.

Yamanaka, M. D., S. Ogino, S. Kondo, T. Shimomai, S. Fukao, Y. Shibagaki, Y. Maekawa, and I. Takayabu, Inertio-gravity waves and subtropical multiple tropopauses: vertical wavenumber spectra of wind and temperature observed by the MU radar, radiosondes and operational rawinsonde network, *J. Atmos. Solar-Terr. Phys.*, *58*, 785-805, 1994.

Young, J. R. C., Breaking gravity waves on a jet stream over the North Pacific, *Weather*, *26*, 306-307, 1971.